New MR Imaging Techniques in Epilepsy

Udo Carl Wieshmann

A thesis submitted to the University of London for the degree of

Doctor of Philosophy

June 1999

Epilepsy Research Group
Department of Clinical Neurology
Institute of Neurology
University College London
Queen Square
London WC1N 3BG
United Kingdom

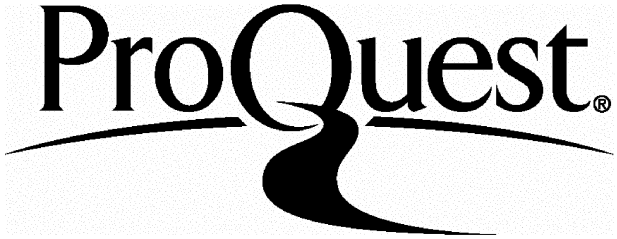

Abstract

This thesis is concerned with the application of three magnetic resonance (MR) techniques in epilepsy: i.) Fluid attenuated inversion recovery prepared (FLAIR) imaging, ii.) diffusion imaging including diffusion tensor imaging (DTI) and iii.)serial and high resolution imaging of the hippocampus.

I assessed the clinical value of fast FLAIR in epilepsy in a study involving 128 patients and of 3D FLAIR in a study involving 10 patients. The conspicuity of neocortical lesions and hippocampal sclerosis was increased. New lesions were detected in 5% of patients. The extent of low grade tumours was best assessed on 3D fast FLAIR images. Fast FLAIR was inferior to standard MR techniques for identifying and heterotopia.

I applied newly developed, experimental diffusion imaging techniques. In eight studies using different diffusion imaging techniques involving a total of 50 patients and 54 control subjects I investigated the mobility of water molecules in the human epileptic brain in vivo. I used spin echo diffusion imaging in two studies, echo planar imaging (EPI) based DTI in four studies and EPI diffusion imaging in a patient during focal status epilepticus. Finally, in a preliminary study I attempted to use EPI diffusion imaging as a contrast to visualise transient changes associated with frequent lateralizing spikes. Our findings were: i.) diffusion is increased in hippocampal sclerosis suggesting a loss of structural organization and expansion of the extracellular space, ii.) displaying the directionality (anisotropy) of diffusion is superior to standard imaging to visualise tracts, iii.) anisotropy is reduced in the pyramidal tract in patients with hemiparesis and iv.) in the optic radiation in patients with hemianopia after temporal lobectomy suggesting wallerian degeneration, v.) both developmental and acquired structural abnormalities have a lower anisotropy than normal white matter, vi.) diffusion abnormalities in blunt head trauma are widespread and may include regions which are normal on standard imaging, indicating microstructural damage suggestive of diffuse axonal injury, vii.) focal status epilepticus can be associated with a reduced diffusion in the affected cortex, viii.) diffusion imaging may be useful as a contrast for event-related (spike triggered) functional MR imaging.

With serial MRI I demonstrated hippocampal volume loss in a patient after generalized status epilepticus and with high resolution imaging of an anatomical specimen and a control subject I showed hippocampal layers on MR images.
The results presented in this thesis emphasised the flexibility of MR imaging and its ability to demonstrate abnormalities in vivo. FLAIR imaging is now part of the clinical work up of patients with epilepsy. Diffusion imaging has been shown to be superior to standard imaging to visualise tracts which has far-reaching implications for neurological applications. Diffusion imaging also provides an exciting window to study cerebral microstructure in vivo. Serial imaging allows for the first time the visualisation of temporal changes and high resolution imaging has the prospect of demonstrating hippocampal layers in vivo. MR imaging is a constantly progressing technique. It is hoped that this thesis will help to formulate hypotheses for new MR experiments to study the relationship of dysfunction and structural abnormalities.

Contributions of the author to the thesis

I familiarized myself with the basic principles of MR imaging and new MR techniques. I was awarded with a student stipend by the International Society for Magnetic Resonance in Medicine to attend the fourth international meeting and an MR course on new imaging and spectroscopy developments in 1996. I actively gathered information on new developments in MR in leading international groups in this and subsequent meetings.

At the MRI Unit at Chalfont I was involved in:

- discussing the development of new techniques with regard to potential applications in epilepsy in the team
- applying new techniques for the first time on volunteers (including myself) after the development phase
- assessing the initial images for artifacts and potential clinical applications
- providing feedback to physicists which often resulted in modifications and improvements
- designing of studies to assess the feasibility and potential clinical utility
- obtaining ethical approval
- recruiting control subjects and patients
- obtaining informed consent
- presenting results at MR meetings and neurological conferences
- writing scientific papers

Acknowledgments

I would like to thank my supervisor Prof Simon Shorvon for all his help and advise in developing the work described in this thesis, answering my questions and reading my written efforts.

Thanks also to Dr Mark Symms, Dr Chris Clark, Dr Gareth Barker, Dr Florence Franconi, Dr Louis Lemieux, Dr Samantha Free, Dr John Mottershead, Dr John Stevens, Dr Brian Kendall, Dr J Duncan, Phillipa Bartlett, Kim Birnie and David MacManus for their support.

I would also like to thank the other members of the Epilepsy Research group who have answered my questions and the staff at the National Society for Epilepsy and the patients for their generous support and participation in the numerous studies.

I would like to thank Sofia Eriksson who continues the work on diffusion imaging at the National Society for Epilepsy for her co-operation.

It has been a pleasure to work with them.

I would like to thank my wife her for support.

This research has been kindly funded by an European Community Fellowship, by the National Society for Epilepsy and by the European Neurological Society, by the guarantors of Brain, by the Institute of Neurology and by the International Society for Magnetic Resonance in Medicine. The Glaxo Wellcome scanner and the MRI Unit are supported by the National Society for Epilepsy.

Table of Contents

	Page
Abstract	2
Contributions of the author to the thesis	4
Acknowledgements	5
Table of Contents	6
List of Figures	15
List of Tables	24
List of Abbreviations	25

Chapter 1

Epilepsy and Magnetic Resonance Imaging

1.1 Epileptic Seizures and Epilepsy	26
1.1.1 Definition of Epileptic Seizures and Epilepsy	26
1.1.2 Frequency, Etiology and Structural Changes in Epilepsy	26
1.1.3 Changes associated with an ictal event	27
1.1.4 Methods in Epilepsy	28
1.2 MR Imaging	30
1.2.1 Introduction	30
1.2.2 Nuclear Magnetic Resonance	32
1.2.3 T1 and T2 relaxation	33
1.2.4 T2-relaxation and Diffusion*	36
1.2.5 MR echoes	37
1.2.6 Modifying contrast	38
1.2.7 Limitation of MR studies	39
1.2.8 Creating an MR image	39
1.2.9 Fast MR imaging	40
1.2.9.1 Fast Spin Echo Imaging	41
1.2.9.2 Echo Planar Imaging	41
1.2.10 Three dimensioned acquisitions	41

1.2.11 Resolution and signal intensity 42
1.2.12 Artefacts in MR imaging 42
1.3 MR imaging in Epilepsy 45
1.3.1 Introduction 45
1.3.2 The current role of MR imaging in Epilepsy 47
1.3.3 Important pathologies 48
1.3.3.1 Hippocampal sclerosis 48
1.3.3.2 Malformations of cortical development 49
1.3.3.3 Granulomas 50
1.3.3.4 Cavernomas 50
1.3.3.5 Other pathologies 50
1.3.3.6 Transient changes 51
1.3.3.7 No abnormalities detected on standard MR imaging 51
1.4 Technical advances in recent years in Epilepsy 51
1.4.1 Three D gradient echo acquisition technique in epilepsy 51
1.4.2 Fast spin echo (FSE) acquisition technique in epilepsy 52
1.4.3 Off resonance imaging in epilepsy 52
1.4.4 Functional Magnetic Resonance Imaging in epilepsy 52
1.4.5 Other MR techniques in epilepsy 53
1.5 New MR techniques in epilepsy discussed in this thesis 53
1.5.1 Aim of the thesis 53
1.5.2 FLAIR imaging in epilepsy 54
1.5.3 MR imaging of the hippocampus 54
1.5.4 Diffusion imaging in epilepsy 55
1.6 Summary 55
1.7 References 56

Chapter 2

Fluid Attenuated Inversion Recovery prepared (FLAIR) Imaging in Epilepsy

2.1 FLAIR Imaging 66

2.1.1 Introduction 66

2.2 FLAIR Imaging in Epilepsy with a fast FLAIR sequence 67

2.2.1 Introduction 67

2.2.1 Material and methods 68

2.2.1.1 Patients and controls 68

2.2.1.2 MR imaging 68

2.2.2 Results 69

2.2.2.1 Controls 69

2.2.2.2 Patients 70

2.2.2.2.1 Neocortical lesions detected by the standard protocol 70

2.2.2.2.2 Dysgenetic lesions detected by the standard protocol 70

2.2.2.2.3. Normal standard MR imaging 71

2.2.2.2.4 Hippocampal sclerosis 76

2.2.3 Discussion 79

2.2.4 Conclusion 82

2.3 Fast Fluid-attenuated Inversion-Recovery Imaging: First Experience with a 3D Version in Epilepsy 82

2.3.1 Introduction 82

2.3.2 Methods 84

2.3.3 Results 85

2.3.4 Discussion 90

2.3.5 Conclusion 92

2.4 References 92

Chapter 3

Diffusion Imaging in Epilepsy

3.1 Introduction 97

3.1.1 Principles of diffusion 97

3.1.2 Effect of diffusion on the NMR signal 99

3.1.3 Pulsed gradient spin echo technique 99

3.1.4 Diffusion in bounded systems 103

3.1.4.1 Restricted and hindered diffusion 103

3.1.4.2 Anisotropic diffusion and the diffusion tensor 104

3.1.4.3 Diffusion in biological systems 105

3.1.5 MR diffusion imaging 106

3.1.5.1 History of diffusion imaging 106

3.1.5.2 Diffusion tensor imaging 106

3.1.5.3 Measurements of magnitude and directionality of diffusion 107

3.1.5.4 Problems of in vivo diffusion imaging 108

3.1.5.5 Single shot EPI in diffusion imaging 110

3.2 Diffusion Imaging of Neurological Disease 111

3.2.1 Experimental studies 111

3.2.2 Clinical applications of diffusion imaging 113

3.3 Water Diffusion in the Human Hippocampus in Epilepsy 113

3.3.1 Introduction 113

3.3.2 Methods 114

3.3.2.1 Subjects 114

3.3.2.2 Measurement of ADC and AI 115

3.3.2.2 Measurement of T2 time and hippocampal volume 117

3.3.2.3 Statistical analysis 118

3.3.3 Results 118

3.3.3.1 Control subjects 118

3.3.3.2 Patients 119

3.3.3.2.1 Correlation of T2 time and volume with ADC_{av} and AI 119

3.3.3.2.2 Outliers 121
3.3.4 Discussion 123
3.3.5 Conclusion 125
3.4 Diffusion-weighted MRI Demonstrates Abnormal Pyramidal Tract in Hemiparesis 125
3.4.1 Introduction 125
3.4.2 Methods 125
3.4.2.1 Subjects 125
3.4.2.2 MR imaging 126
3.4.3. Results 127
3.4.3.1 Standard MR imaging 127
3.4.3.2 DWI 128
3.4.4 Discussion 130
3.4.5 Conclusion 131
3.5 Anisotropy of Water Diffusion in Corona Radiata and Cerebral Peduncle in Patients with Hemiparesis - a Diffusion Tensor Imaging Study 132
3.5.1 Introduction 132
3.5.2. Methods 132
3.5.2.1 Subjects 132
3.5.2.2 DTI parameters 133
3.5.3 Results 134
3.5.3.1 T2-weighted images and mean diffusivity maps 134
3.5.3.2 FA measurements 134
3.5.4 Discussion 138
3.5.5 Conclusion 140
3.6 Wallerian Degeneration in the Optic Radiation after Temporal Lobectomy Demonstrated in vivo with Diffusion Tensor Imaging 141
3.6.1 Introduction 141
3.6.2 Methods 141

3.6.2.1 Subjects 141
3.6.2.2 DTI parameters 142
3.6.2.3 Quantitative assessment of tracts (MR Tractrography) 142
3.6.3 Results 143
3.6.3.1 Standard MR imaging 143
3.6.3.2 DTI 143
3.6.3.3 MR Tractography 144
3.6.4. Discussion 146
3.6.5 Conclusion 147
3.7 Reduced Anisotropy of Water Diffusion in Structural Cerebral Abnormalities demonstrated with Diffusion Tensor Imaging 147
3.7.1 Introduction 147
3.7.2 Methods 148
3.7.2.1 Patients 148
3.7.2.2 DTI parameters 148
3.7.3 Results 149
3.7.4 Discussion 152
3.7.5. Conclusion 154
3.8 Blunt Head Trauma associated with widespread Water Diffusion Changes 154
3.8.1 Introduction 154
3.8.2 Methods 154
3.8.2.1 Patient 154
3.8.2.2 DTI parameters 155
3.8.3 Results 155
3.8.4 Discussion 157
3.8.5. Conclusion 157
3.9 Diffusion changes in status epilepticus 157
3.9.1 Introduction 157
3.9.2 Methods 158
3.9.2.1 Patient 158

3.9.2.2 DWI parameters 158
3.9.3 Results 159
3.9.4 Discussion 161
3.9.5. Conclusion 162
3.10 EEG-correlated diffusion-weighted fMRI in epilepsy - a preliminary study 163
3.10.1 Introduction 163
3.10.2 Methods 163
3.10.3 Results 164
3.10.4 Discussion and conclusion 165
3.11 References 166

Chapter 4

More MR Imaging of the Hippocampus

4.1 Introduction 179
4.2 Image contrast and hippocampal volumetric measurements 179
4.2.1 Introduction 179
4.2.2. Methods 181
4.2.2.1 Hippocampal measurements 181
4.2.2.2 Repeatability 182
4.2.2.3 Contrast 183
4.2.3 Results 184
4.2.4 Discussion 187
4.2.5 Conclusion 188

4.3 The development of hippocampal atrophy; a serial MRI study in a patient who developed epilepsy after generalized status epilepticus 188
4.3.1 Introduction 188
4.3.2.Case report 188
4.3.3. Methods 189

4.3.3.1 Scanning parameters 189
4.3.3.2 Quantification of hippocampal volumes 189
4.3.3.3 Co-registration and substraction of serial MRI scans 190
4.3.4 Results 190
4.3.4.1 Visual inspection of MRI images 190
4.3.4.2.Quantification of hippocampal volumes 191
4.3.4.3. Co-registration and substraction of serial MRI scans 192
4.3.5 Discussion 194
4.3.6 Conclusion 194

4.4 Hippocampal Layers on High Resolution Magnetic Resonance Images: Real or Imaginary? 195
4.4.1 Introduction 195
4.4.2. Methods 195
4.4.2.1 MR experiments 196
4.4.2.1.1 Scanning a hippocampal specimen at 7 Tesla 196
4.4.2.1.2 Scanning a hippocampal specimen at 1.5 Tesla 196
4.4.2.1.3 Scanning the hippocampus in vivo at 1.5 Tesla 196
4.4.2.1.4 Comparison with the histological appearance 197
4.4.3 Results 197
4.4.4 Discussion 200
4.4.5 Conclusion 203
4.5 References 203

Chapter 5
Conclusions

5.1 Introduction 207
5.2 Summary of thesis and future work 207
5.2.1 Epilepsy and magnetic resonance imaging 207
5.2.2 FLAIR imaging in epilepsy 208

5.2.4 Diffusion imaging in epilepsy 210
5.2.3 More MR imaging of the hippocampus 217
5.3 Conclusion 218
5.4 References 220

6 Appendix

Publications associated with this thesis

6.1 Publications associated with FLAIR Imaging in Epilepsy 223
6.1.1 Articles 223
6.1.2 Abstracts 223
6.2 Publications associated with Diffusion Imaging in Epilepsy 224
6.2.1 Articles 224
6.2.2 Abstracts 225
6.3 Publications associated with MR Imaging of the Hippocampus 227
6.3.1 Articles 227
6.3.2 Abstracts 227
6.4 Publications associated with Conclusions 228
6.4.1 Articles 228
6.4.2 Abstracts 229

List of Figures

(patient's right is left on coronal and axial MR images)

Figure 1.1 - Incident illustrating the strength of the main magnetic field b_0. Ferromagnetic equipment (oxygen cylinder) has been attracted by the magnet (1.5 Tesla). Courtesy of D. MacManus. (Page 32)

Figure 1.2 - T1 is the time for the longitudinal magnetization to regrow from 0 to $(1\text{-}e^{-1})$,or about 63% of its final value. T2 is the time for the transverse magnetization to decay to e^{-1}, or about 37% of its initial value. (Page 34)

Figure 1.3 -The relationship between T1 or T2 and molecular tumbling rate. (ω_L = Lamorfrequency). Adapted from Elster AD.[27] (Page 35)

Figure 1.4 - Spin echo sequence. TR = time to repeat, TE = time to echo, FID = free induction decay, t = time. (Page 37)

Figure 1.5 - Publications in epilepsy from 1884 to 1998. The number in brackets is the number of publications. (Source PubMed.) (Page 45)

Figure 1.6 - Publications about Epilepsy using Magnetic Resonance Imaging from 1984 to 1998. (Source PubMed.) (Page 46)

Figure 2.1 - sagittal FSE T2-weighted image of a normal control subject. CSF returns a high signal on the FSE T2-weighted images. (Page 67)

Figure 2.2 - Fast FLAIR images of the same control subject as in fig. 2.1. The signal from CSF is suppressed ("nulled"). (Page 67)

Figure 2.3 - Presumed DNT. Coronal spin echo T2-weighted image (top left), proton density weighted image (top right), T1-weighted image (bottom left) and fast FLAIR image (bottom right). A small cortical mass is shown in the right

posterior temporal lobe. The signal intensity change is most conspicuous on fast FLAIR. The patient had partial epilepsy. (Page 72)

Figure 2.4 - BAND HETEROTOPIA. Coronal spin echo T2-weighted image (top left), proton density weighted image (top right), T1-weighted image (bottom left) and fast FLAIR image (bottom right). A band of ectopic grey matter underlying the cortex ("double cortex") is shown (arrow). The abnormality is bilateral and fairly symmetric. The heterotopic grey matter is most conspicuous on the T1-weighted image and could be overlooked on fast FLAIR. The patient had partial epilepsy. (Page 73)

Figure 2.5 - NODULAR SUBEPENDYMAL HETEROTOPIA. Coronal spin echo T2-weighted image (top left), proton density weighted image (top right), T1-weighted image (bottom left) and fast FLAIR image (bottom right). Ectopic grey matter is shown adjacent to the right ventricle (arrow). The signal intensity of the ectopic grey matter is similar to normal greymatter and not more conspicuous on fast FLAIR. The patient had partial epilepsy. (Page 74)

Figure 2.6 - NORMAL STANDARD IMAGING. Coronal spin echo T2-weighted image (top left), proton density weighted image (top right), T1-weighted image (bottom left) and fast FLAIR image (bottom right). A small area returning a high signal is visible on fast FLAIR (arrow). Slight signal changes on the proton-density and T2-weighted images in this area are not clearly abnormal. The patient had frequent simple partial seizure with tingling on the right side, the EEG changes were in keeping with a left seizure focus. (Page 75)

Figure 2.7 - Left HIPPOCAMPAL SCLEROSIS. Coronal images of the hippocampal body. Spin echo T2-weighted image (top left), proton density weighted image (top right), T1-weighted image (bottom left) and fast FLAIR image (bottom right). The left hippocampus (arrow) is smaller than the right and returns a high signal on T2-weighted images. This is most conspicous on fast FLAIR since CSF signal has been suppressed. (Page 77)

Figure 2.8 - Left HIPPOCAMPAL SCLEROSIS. Coronal images of the hippocampal head. High resolution T1-weighted images (top) and fast FLAIR images (bottom). The left hippocampus is smaller than the right and returns a high signal on fast FLAIR. The patient had temporal lobe epilepsy and later underwent a left temporal lobe ectomy. Hippocampal sclerosis was histological confirmed. (Page 78)

Figure 2.9 - REFORMATTED 3D IRSPGR images (predominantly T1-weighted); the 3D data set has been rotated 360° in steps of 30 around the vertical axis. The cortex around the right calcarine sulcus is thicker than the cortex around the left calcarine sulcus but no clear-cut abnormality is visible. R=right, L=left, A=anterior, P=posterior (Page 87)

Figure 2.10 - REFORMATTED 3D fast FLAIR of the same patient. A lesion is clearly visible in the cortex above the anterior extremity of the right calcarine sulcus involving the isthmial gyrus. Note also Venetian blind artefacts at slab interfaces (best visible on reformatted images in the sagittal plane, which is orthogonal to the imaging plane). (Page 88)

Figure 2.11 - ADDITIONAL INFORMATION ON TUMOUR TEXTURE obtained with 3D fast FLAIR. Spin echo T2-image (top left), proton density weighted image (top right), T1-weighted image (bottom left) and 3D fast FLAIR image (bottom right). A lesion is shown in the right parietal lobe (arrow 1). Contrast is low on the proton density weighted image, T1- and T2-weighted images provide high contrast. However, both lesion and CSF (for example in the occipital horn of the left lateral ventricle, arrow 2) have similar signalintensities (low on T1- and high on T2-weighted images). FLAIR provides a high contrast for the lesion. The fact that the signal from the lesion is not suppressed on FLAIR indicates that the lesion is not a CSF filled cavity but a solid tumour. The patient had partial epilepsy. (Page 89)

Figure 3.1 - Classic description of diffusion. (Page 97)

Figure 3.2 - Pulsed gradient spin echo sequence. Diffusion gradients are applied before and after the 180° pulse. The gradient strength G, the duration of the gradient δ and the time between the leading edges of the diffusion gradients Δ determine the diffusion weighting of the sequence. (Page 100)

Figure 3.3 - Spin echo EPI sequence with pulsed diffusion gradients. Sagittal images of a control subject were acquired with increasing b values. Increasing b values results in signal attenuation. Signal attenuation is highest in regions of high diffusion (the CSF filled spaces). The slope of the curve represents the diffusion coefficient D (which becomes the apparent diffusion coefficient D* in biological systems, *see 3.1.4.3)* . (Page 102)

Figure 3.4 - Free and restricted diffusion. (Page 103)

Figure 3.5 - Experiment illustrating the influence of pulsatile brain motion on the apparent diffusion coefficient (ADC). A single shot EPI diffusion sequence was gated from the right common carotid artery. The diffusion sensitising gradient was applied in the frequency encoding (superior-inferior) direction. Average ADC maps of 24 experiments of a control subject are shown for different trigger delays (20ms, 70ms, 180ms, 230ms). For short trigger delays the ADC is arteficially high in midline structures (arrow). (Page 110)

Figure 3.6 - Box plots of the 24 measurments of the ADC in a region of interest (arrow in fig.3.5). Scanning parameters as in figure 3.5. For short trigger delays the ADC is arteficially high due to the pulsatile motion. For trigger delay 230ms the measured ADC equals the expected value (0.7×10^{-3} mm^2/s). (Page 111)

Figure 3.7 - Coronal maps of the apparent diffusion coefficient (ADC) of a control subject. Top left: ADC derived from measurements in the x-direction (ADC_x). Top right: ADC derived from measurements in the y-direction (ADC_y). Bottom left: ADC derived from measurements in the z-direction (ADC_z). Bottom

right: Map of the mean ADC of ADC_x, ADC_y and ADC_z (ADC_{av}). The arrowhead indicates the gradient direction (direction is into the imaging plane on ADC_z). (Page 117)

Figure 3.8 - Coronal maps of the ADC_{av} of the mesiotemporal region. A: patient with temporal lobe epilepsy, B: normal control. The signal is higher in the right hippocampus than in the left hippocampus in the patient, measurements revealed an elevated ADC_{av} on the right. (Page 119)

Figure 3.9 - Correlation of hippocampal T2-relaxation time and ADC_{av}. The triangles represent hippocampi of control subjects, the squares represent hippocampi of patients. (Page 120)

Figure 3.10 - Correlation of hippocampal volume and ADC_{av}. The triangles represent hippocampi of control subjects, the squares represent hippocampi of patients. (Page 121)

Figure 3.11 - Boxplot showing ADC_{av} in sclerotic hippocampi (HS), HS negative hippocampi of patients (no HS) and control hippocampi. Boxes contain the 50% of values falling between the 25th and 75th percentiles, and the "whiskers" lines that extend from the box to the highest and lowest values, outliers are indicated by dots. The line across the box is the median. (Page 122)

Figure 3.12 - Boxplot showing AI in sclerotic hippocampi (HS), HS negative hippocampi of patients (no HS) and control hippocampi. (For explanation see fig. 3.11) (Page 123)

Figure 3.13 - Top left: schematic drawing of a coronal section through the hemisphere. The pyramidal tract consists of projection fibres and forms the posterior limb of the internal capsule. Top right: Anisotropy map of a normal control subject. Bottom left: T1-weighted image of a patient with hemiparesis.

Bottom right: Anisotropy map of the same patient showing the abnormal pyramidal tract. (Page 129)

Figure 3.14 - Axial fractional anisotropy maps at three slice positions (midbrain level, through the basal ganglia and through the corona radiata). Top row: control subject. Bottom row: patient with a left hemiparesis. Myelinated structures are symmetrical in the control subject. 1 = right cerebral peduncle, 2 = right posterior limb of the internal capsule, 3 = subcortical white matter in the expected position of the right corona radiata. In the patient with a left sided hemiparesis anisotropy is reduced in the right cerebral peduncle, the right posterior limb of the internal capsule, and the right corona radiata. (Page 136)

Figure 3.15 - Fractional anisotropy measurements in the corona radiata (A) and the cerebral peduncle (B) in patients in dysfunctional and functional pyramidal tract and in control subjects. The anisotropy is reduced in the dysfunctional pyramidal tract in the corona radiata. At the level of the cerebral peduncle the anisotropy is significantly reduced only in three patients in the dysfunctional tract. All three had a severe hemiparesis. (Page 137)

Figure 3.16 - Schematic drawing of the right pyramidal tract (right posterior view). Adapted from Ferner and Staubesand. (Page 139)

Figure 3.17 - Top: Sagittal T1-weighted images. Bottom: Axial averaged maps of the fractional anisotropy of normal controls, showing myelinated pathways including the optic radiation overlayed with regions of significantly reduced anisotropy in the patients (scaled from blue = 2SD to yellow = 2SD-200). Left: patient 1, right amygdalo-corticetomy, no visual field defects. The optic radiation is normal. Middle: patient 2, right standard resection, clinically no visual field defect. Only the most medial fibres of the optic radiation are affected. Right: patient 3, left standard resection, clinically hemianopia to the right. Significant reductions of the anisotropy suggesting a breakdown of myelin are visible in the

left optic radiation exceeding the resection line. (Note that patients left is right on axial images.) (Page 145)

Figure 3.18 - Fractional anisotropy and mean diffusivity in structural abnormalities and in the white matter of control subjects. (Page 150)

Figure 3.19 - Structural abnormalities on DTI. T1-weighted images (left), maps of mean diffusivity (middle) and fractional anisotropy (right) are shown. Top row: A patient with traumatic brain damage affecting the right parital and frontal lobe (1). Middle row: A patient with polymicrogyria affecting the right hemisphere (2). Bottom row: A patient with a left temporal meningoma (3). The frational anisotropy is reduced in all structural abnormalities. However, mean diffusivity is only mildly increased in the patient with polymicorgyria. (Page 151)

Figure 3.20 - Diffusion tensor imaging and standard T1 weighted images in traumatic brain damage causing right quadrantanopia, impaired memory and epilepsy. T1-weighted images (top row) show brain atrophy. Maps of the mean diffusivity show widespread increase of the magnitude of diffusion (pixels with significantly *increased* mean diffusivity are shown in red). Maps of the anisotropy of diffusion (bottom row) show a decrease of the directionality of diffusion in myelinated structures including the right optic radiation (bottom left) and the forceps major of the corpus callosum (bottom right), (pixels with significantly *decreased* anisotropy are shown in red). Note that patient's right is left on images. (Page 156)

Figure 3.21 - DWI during status affecting the right leg. Top left: T2-weighted images during status. Top right: DWI during status. Bottom left: T2-weighted image after status. Bottom right: DWI after status. On DWI during status a high signal in the motor cortex of the right leg (indicating a decreased diffusion) and a low signal in the subcortical white matter (indicating an increased diffusion) is visible. Both changes resolved after status. (Page 161)

Figure - 3.22 fMRI (BOLD) activation map. Pixels with significant change are shown in red. (Page 164)

Figure - 3.23 - DWI (right) activation map. Pixels with significant change are shown in yellow and pink. (Page 164)

Figure 4.1 - Repeatability of hippocampal volumetric measurements. The difference (first minus second measurement) is plotted against the mean of both measurement for each hippocampus. Top: SPGR measurements. Bottom: IRSPGR measurements. (Page 185)

Figure 4.2 - Coronal SPGR (left) and IRSPGR (right) image taken though the hippocampal head. The inset (approximately 1.5 x magnification) shows mesio temporal structures. Note the higher grey matter-white matter contrast and the higher conspicuity of the alveus on IRSPGR. (Page 186)

Figure 4.3 - Axial T2-weighted images obtained during status in 1991. An abnormally high signal is visible in the mesio-temporal region bilaterally. (Page 191)

Figure 4.4 - Registration of serial MR scans using MRreg. Top: coronal T1-weighted image obtained 1 year after status epilepsy. Middle: coronal T1-weighted image obtained 4 years later and registered to the first scan. Bottom: difference image (B minus A). Dark pixels indicate loss of signal intensity suggestive of atrophy between A and B. Atrophy is visible in both hippocampi. There is also mild ventricular expansion. Windowing of the difference image: level=0, width=100. (Page 193)

Figure 4.5 - Left: schematic drawing of the hippocampal head. Right: Schematic drawing of the hippocampal body. The numbers indicate: 1=alveus, 2=pyramidal

cell layer, 3=stratum radiatum, 4=stratum lacunosum, 5=stratum moleculare, 6=dentate gyrus with granule cell layer, 7=fimbria, 8=temporal horn, 9=hippocampal fissure, 10=uncal fissure, 11=caudate nucleus, 12=lateral geniculate body, 13=subiculum. (Page 199)

Figure 4.6 - High resolution imaging of the hippocampal specimen at 7T. (Voxel size 0.064 x 0.064 x 1 = 0.004 mm^3.) Left: coronal sections of the hippocampal head. The background is dark and there are susceptibility artefacts at the edges because the specimen was scanned in air. The lines indicate hippocampal layers (from top to bottom) alveus, pyramidal cell layer, stratum radiatum, stratum lacunosum, stratum moleculare).Right: coronal sections of the hippocampal body. There is an artefact caused by air a small bubble. The lines indicate (from top to bottom) alveus, pyramidal cell layer, stratum radiatum, stratum lacunosum and stratum moleculare, granule cell layer of the dentate gyrus). (Page 199)

Figure 4.7 - High resolution imaging of the hippocampal specimen at 1.5 T. (Voxel size 0.156 x 0.156 x 1 mm = 0.024 mm^3.) Left: coronal section of the hippocampal head. The background is white because the specimen was scanned in formalin. Hippocampal layers can be identified.
Right: coronal section of the hippocampal body. The background is white because the specimen was scanned in formalin. Hippocampal layers can be identified but the granule cell layer of the dentate gyrus is difficult to identify. (Page 200)

Figure 4.8 - High resolution imaging of the hippocampus in vivo at 1.5 T. (Voxel size 0.47 x 0.47 x 2 mm = 0.0.442 mm^3.) Coronal FSE image showing the hippocampal body. The horizontal lines indicate layers presumably mainly representing alveus, pyramidal cell layer and stratum radiatum. The oblique line indicates a few pixels which are possibly representing the dentate gyrus.(Page 200)

Figure 4.9 - Histological picture of the anatomical specimen showing the layers in the hippocampal body. (Page 118)

List of tables

Table 1.1 Causes of Epilepsy 27

Table 1.2 Abnormal brain areas in partial epilepsy 29

Table 1.3 Scientific and technical milestones in MR imaging 31

Table 1.4 Adjusting imaging parameters to improve signal-to-noise ratio (SNR) 43

Table 1.5 MR artefacts 44

Table 1.6 Three dimensions to classification of studies of a diagnostic test 47

Tab. 2.1 Appearance of lesions associated with epilepsy on fast FLAIR 79

Table 2.2 Scanning parameters 85

Table 3.1 Experimental models of disease and development associated with diffusion changes 112

Table 3.2 Presumed aetiology of epilepsy, predominant seizure type and quantitative measurements. 114

Table 3.3 Mean fractional anisotropy in Corona Radiata and Cerebral Peduncle 135

Table 3.4 DTI measurements in structural abnormalities 152

Table 4.1 MR sequences used for hippocampal volumetric measurements 180

Table 4.2 Contrast to noise ratios of grey matter and white matter on SPGR and IRSPGR images 184

Table 4.3 Hippocampal volumetric measurements 191

List of Abbreviations

CSF	cerebrospinal fluid
DTI	diffusion tensor imaging
EEG	electroencephalogram
FLAIR	fluid-attenuated inversion-recovery
IRSPGR	Inversion recovery prepared spoilt GRASS
MR	magnetic resonance
NEX	number of excitations
PET	positron emission tomography
SE	spin echo
SPECT	single photon emission computed tomography
T	Tesla
TE	echo time
TEef	effective echo time
TI	inversion time
TR	repetition time

Chapter 1

Epilepsy and Magnetic Resonance Imaging

1.1 Epileptic Seizures and Epilepsy

1.1.1 Definition of Epileptic Seizures and Epilepsy

An epileptic seizure is defined as a recurrent, disorderly discharge of the nerve tissue.[1] Epilepsy is characterized by the recurrent occurrence of seizures without consistent provoking factors. For practical reasons epileptic seizures have been divided in focal and primary generalized seizures.[2] Epilepsy is a broad category of symptom complexes arising from any number of disordered brain functions that themselves may be secondary to a variety of pathologic processes, many of them being unknown. The classification of epilepsy has been dominated by clinical and electrographic correlation.[3] The structural or aetiological bases of epilepsy have been largely ignored, not least because, before the advent of MR imaging, there was no sensitive method for investigation. Epilepsy has both structural and functional features, and there is now a need to reevaluate clinical classification, in the broadest sense, in the light of the treatment by providing more specific clinical categorisation, allow more accurate prognostication and lead to prevention.[4]

1.1.2 Frequency, Etiology and Structural Changes in Epilepsy

The annual incidence of epilepsy has been estimated to lie between about 50 and 120 cases per 100,000 persons, and the prevalence between 5-10/1000 persons in a general population.[5] About 30% of patients have some additional neurological or psychiatric handicap. Age has a marked effect on incidence, and the age-related incidence of epilepsy follows a U-shaped pattern, falling from the highest incidence in the first two years to low levels in midlife and rising again to peak at 70 or 80 years.[6] Overall, most patients with epilepsy will enter remission. In a large population-based study 68% of patients with definite epilepsy achieved a 5 year remisson.

However, there is a higher than expected risk of death, especially in those with symptomatic epilepsy and about 30% the epilepsy is refractory to medical treatment.[7] Epileptic syndromes can be broadly divided into idiopathic and symptomatic epileptic syndromes. Idiopathic epilepsies are usually generalized and are believed to have a genetic background. Symptomatic epilepsies are those in which seizures are the consequence of an identifiable lesion or other specific etiology. Epilepsy has a wide range of causes, and indeed almost all grey-matter diseases can result in seizures (tab.1.1). When epilepsies are presumably symptomatic but currently of unknown specific etiology, they are termed cryptogenic.

Table 1.1

Causes of Epilepsy
Genetic and congenital abnormalities
Anoxic and perinatal injury
Trauma
Cerebral infection
Cerebrovascular disease
Cerebral tumour
Cerebral degenerative disorders
Cerebral inflamatory and immunological disorders
Toxins and drug withdrawal
Metabolic disorders

1.1.3 Changes associated with an ictal event

Epileptic seizures represent the clinical manifestations that result from excessive, synchronous, abnormal firing patters of neurons that are located predominantly in the cerebral cortex.[8,9] Many environmental and physiological factors modulate the probability of seizure occurrence: sleep deprivation, alcohol withdrawal and others. However, it is unknown how these perturbations translate into increased

epileptic susceptibility at the cellular level. In most patients, it is not possible to identify external or internal factors that explain why a seizure happened at a particular time. Changes that alter the neuronal excitability or the potential for synchronous interactions among neurons are undoubtedly important but remain to be specified in detail. There are two essential physiologic elements for seizure generation. The first is an abnormality of cellular excitability, arising from mechanisms that affect membrane depolarization and repolarization. The second is a "network defect" which derives from mechanisms underlying the development of aberrant neuronal integration, abnormal synchronization of neuronal populations, and propagation of the epileptic discharge within neural pathways. Seizures are associated with a number of physiological changes including a substantial increase in the cerebral blood flow.[10,11]

1.1.4 Methods in Epilepsy

Different zones play a role in seizure generation and propagation (tab.1.2). These include the irritative zone, the ictal onset zone, the epileptogenic lesion, the symptomatogenic zone, the functional deficit zone and the epileptogenic zone.[12] Several methods have been used for the detection of these zones.[13]

Table 1.2 Abnormal brain areas in partial epilepsy

Brain area	Definition	Measure
Irritative zone	Area of cortex that generates interictal spikes	EEG
Ictal onset zone	Area of cortex that initiates or generates seizures	EEG
Epileptogenic lesion	Structural pathology of the brain that is the direct cause of seizures	MRimaging, CT, tissue pathology
Symptomatogenic zone	Portion of the brain that produces the first clinical symptoms	EEG, behavioural observation, SPECT
Functional deficit zone	Cortical area producing nonepileptic dysfunction	Neurologic exam., neuropsychology, PET, SPECT
Epileptogenic zone	Total area of brain that is necessary to generate seizures and that must be removed to abolish seizures	Unknown

EEG allows the detection of cortical epileptic discharges[14] and is the method of choice for the detection of irritative zone and ictal onset zone. The method is limited by the fact that large areas of cortex are inaccessible for surface EEG recordings and that invasive recordings are prone to sampling errors.[15] Clinical observation is the most important method to localize the symptomatogenic zone and has been extensively used in video EEG telemetry.[16] SPECT allows ictal perfusion measurements and has been used to localize the symptomatogenic zone.[17] However, low temporal resolution, the unreliable timing of the injection of the tracer and artefacts limit the clinical use. PET studies can provide information about activation during seizures but are only possible in patients without head movement.[18,19]

The clinical examination and neuropsychological testing[20] are the most important methods to detect functional deficit zone. Interictal PET and SPECT studies have been widely used to detect the functional deficit zone.[21] Flow studies may be useful as an indirect marker of abnormal neuronal function. More importantly, receptor studies give insight into the mechanisms of seizure generation and PET remains the only non invasive method for receptor studies in humans.[22,23]

Structural neuroimaging is the method of choice for the detection of an epileptogenic lesion in vivo. Since the early days of neuroimaging it has been used in the diagnostic work up of patients. With advent of modern imaging in particular MR imaging structural neuroimaging has gained an important role in epilepsy.

1.2 MR Imaging

1.2.1 Introduction

MR imaging is a very powerful tool for the detection of abnormalities in vivo. A number of fundamental physical discoveries made it possible to use the physical properties of nuclei for image generation (tab.1.3). One of the most outstanding characteristic of MR imaging is its ability to alter the contrast between different tissues by changing the imaging parameters. This allows the detection of abnormal tissue and often gives information about the microstructure of tissue and function. The following paragraphs will explain some of the basic physical principles of MR signal and contrast generation in MR imaging.

Table 1.3Scientific and technical milestones MRimaging(adapted from Ref[24])

Scientific and technical milestones	Researcher (year)
Equations governing electric and magnetic fields	Maxwell (1873)
Statistical mechanics of atoms and molecules	Maxwell(1860),Bolzmann(1872), Gibbs(1878)
Radiowaves	Hertz (1887)
Superconductivity	Onnes (1911)
Atomic structure/atonic nuclei	Rutherford (1911)
Quantum theory	Bohr, Schrödinger, and others (1913-1926)
Nuclear magnetism	Pauli (1924)
Electron spin	Uhlenbeck and Goudsmit (1926)
NMR concept	Gorter (1936)
NMR observed in atomic beams	Rabi (1939)
NMR observed in solids and liquids	Bloch, Purcell (1946)
Equations for spin relaxation (T1, T2)	Bloch (1946)
NMR relaxation mechanism	Blombergen, Pound, Purcell (1948)
Spin echos	Hahn (1950)
High field superconductors	Matthias, Kunzler (1960)
Fourier transform NMR	Ernst, Anderson (1966)
X-ray computed tomography	Oldendorf (1961), Hounsfield (1973)
Whole-body NMR for medical diagnosis	Jackson (1968), Damadian (1972), Abe (1973)
Gradient fields for imaging (zeugmatography)	Lauterbur (1973)
Selective slice excitation	Mansfield (1974), Hoult (1977)
Human imaging using gradient fields	Aberdeen, Nottingham, EMI (1976-1979)
Whole body image using field focusing	Damadian (1978)
High field (1.5 T) whole-body magnets for human imaging	General Electric, Oxford Instruments (1981)
Widespread clinical applications with many submodalities	Many contributors (1980-present)

1.2.2 Nuclear Magnetic Resonance

Nuclear magnetic resonance is a process involving the absorption and emission of energy by nuclei.[2525,2626] Nuclei are subjected to a strong magnetic field b_0 (typically ranging from 0.5 Tesla to 4 Tesla) (fig. 1.1) and acquire a net nuclear magnetization (M). To induce an MR signal, a second magnetic field b_1, must be applied perpendicular to the main magnetic field b_0 and must rotate at the resonant radiofrequency. This is accomplished by using a radio frequency (RF) pulse. A RF pulse is an electromagnetic wave that results from the brief application of an alternating electric current through a transmitter coil. The RF pulse tips M, after

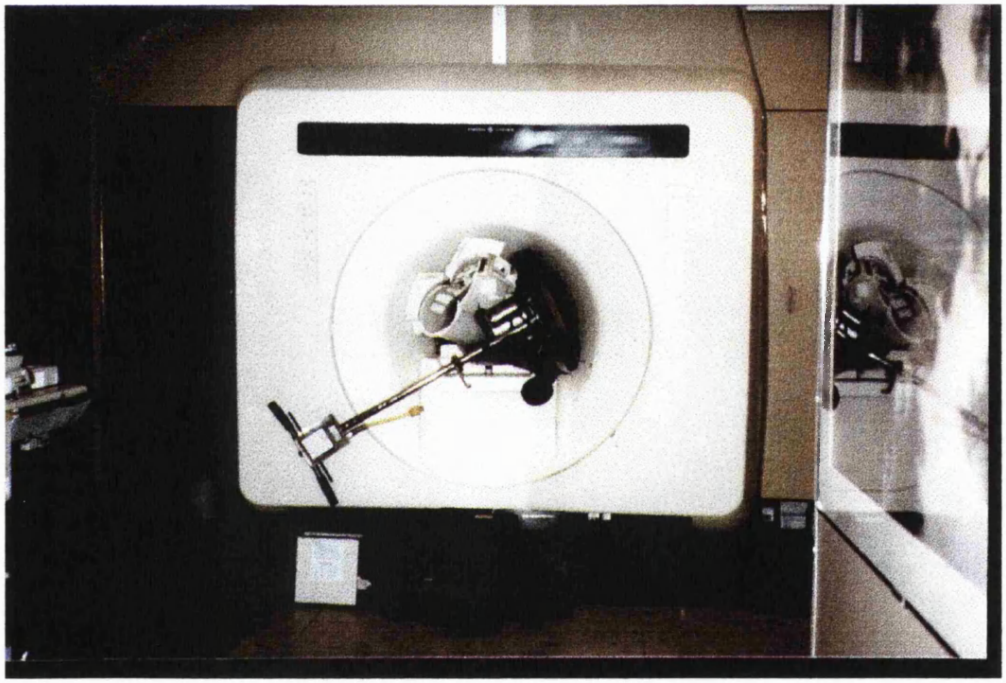

Figure 1.1 - Incident illustrating the strength of the main magnetic field b_0. Ferromagnetic equipment (oxygen cylinder) has been attracted by the magnet (1.5 Tesla). Courtesy of D. MacManus.

the pulse the spins (group of similar nuclei) seek to return to their initial alignment parallel to b_0 with equilibrium magnitude M_0. During this process, which is called relaxation, energy is released in form of radiofrequency waves. The resonance radiofrequency is specific for the nucleus at the given field strength (Lamor frequency). For example the Lamor frequency of protons at 1.5 Tesla is 64 MHz.

In MR imaging of the human body the strongest signal is obtained if the radiofrequency for nuclei of hydrogen nuclei (or protons) is chosen. Hydrogen nuclei are ubiquitous in the human body, they are predominantly bound in water and water accounts for about 70-80% of the total human bodyweight.[27]

1.2.3 T1 and T2 relaxation

Two time constants, T1 and T2, account for the reestablishment of thermal equilibrium of the nuclear magnetization following an RF pulse. T1 (or spin-lattice relaxation) describes the regrowth of longitudinal magnetization (M_z), whereas T2 (or spin spin relaxation) describes the decay of the transverse components (M_x and M_y). The T1 relaxation time represents the time required for M_z to increase to about 63% to its final value. The T2 relaxation time represents the time required for M_x or M_y to decay to about 37% of their maximum values (fig.1.2).

The practical implications of the relaxation process in medical imaging may be understood by considering the "tumbling rate" of water molecules in tissue. For

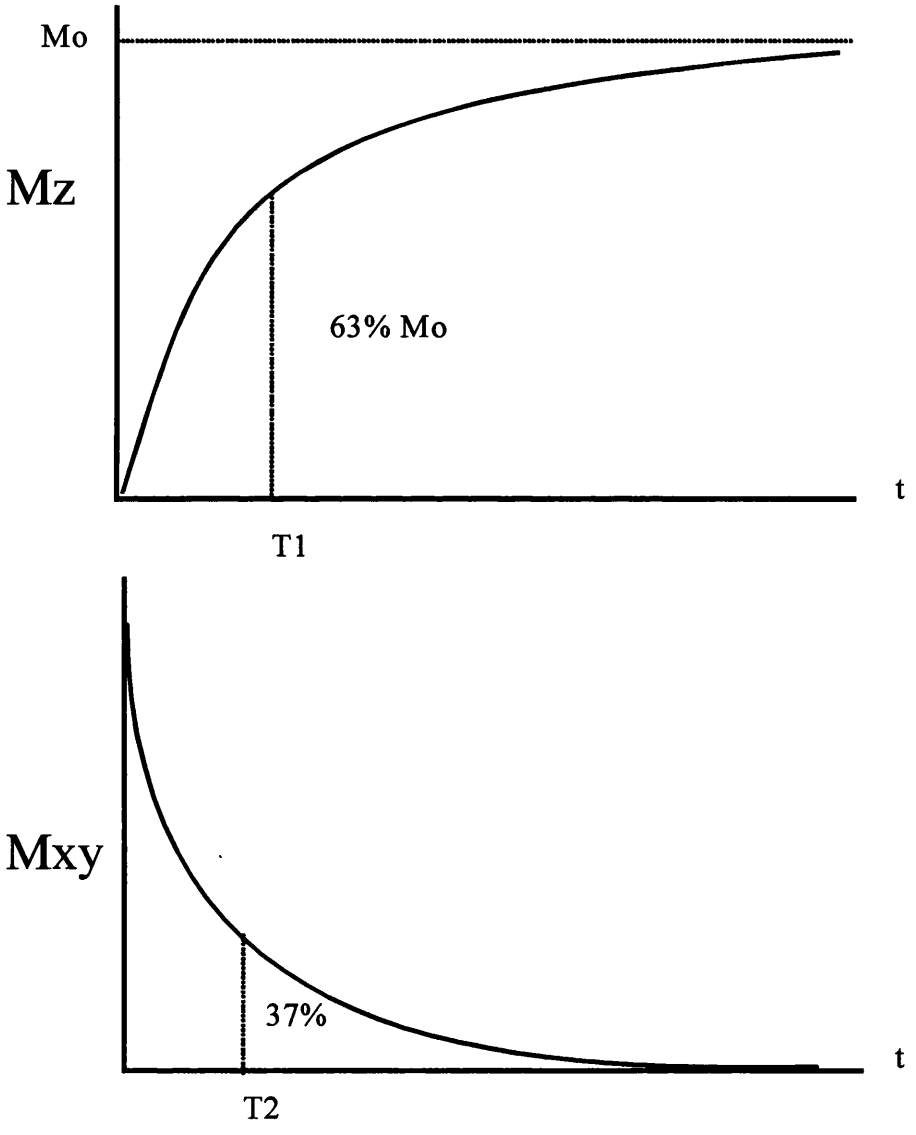

Figure 1.2 - T1 is the time for the longitudinal magnetization to regrow from 0 to $(1-e^{-1})$,or about 63% of its final value. T2 is the time for the transverse magnetization to decay to e^{-1}, or about 37% of its initial value.

effective T1 relaxation the molecule must tumble at frequencies close to Lamor frequency. The free water molecules tumbling faster relax ineffectively and therefore more slowly in Mz and have a long T1. The bound water molecules in biological tissue tumble close to Lamor frequency, relax effectively and therefore have a short T1. (At the other extreme, in the crystalline state molecules tumble much slower than Lamor frequency and have a long T1.)[28] The difference in T1 relaxation between these tissue water states forms the basis of an important tissue contrast in MR imaging.

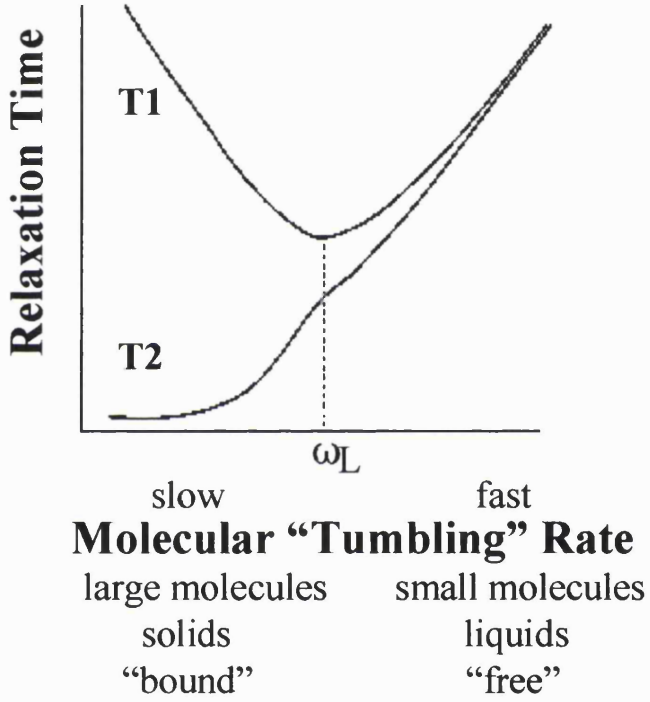

Figure 1.3 -The relationship between T1 or T2 and molecular tumbling rate. (ω_L = Lamorfrequency). Adapted from Elster AD.[27]

The behaviour of water in tissue also affects the T2 relaxation. Anything causing T1 relaxation also causes T2 relaxation, but T2 relaxation may occur without T1 relaxation because T2 relaxation can take place without energy dissipation. Therefore the numerical value of T2 is always less than or equal to T1; it is never greater. For most biological tissues, T1 values are typically 5 to 10 times longer

than T2 values. The bound water molecules have a short T2, free water molecules have a long T2 relaxation (fig.1.3). Several mechanisms affecting the T1 and T2 relaxation times in tissue have been identified. These include dipole-dipole interaction of molecules, J coupling, chemical exchange, diffusion, chemical shift anisotropy and others.[29]

T1 and T2 relaxation are tissue properties specific for a given tissue. However, there is at present no comprehensive theory for reliable predictions of T1 and T2 relaxation in tissue, because of the complex mechanisms affecting the T1 and T2 relaxation time.

1.2.4 T2-relaxation and Diffusion*

In any real nuclear magnetic resonance experiment the transverse magnetization decays much faster, this rate is denoted as T2* and can be considered as the observed T2. T2* results principally from inhomogeneties in the main magnetic field. The true T2 time can be calculated if the field inhomogeneties are known. These inhomogeneties may be the result of intrinsic defects in the magnet itself or of susceptibility-induced field distortions produced by tissue or haemoglobin.

Susceptibility artefacts caused by haemoglobin have been used as a source of contrast in functional MR imaging. (Blood oxygenation level dependent (BOLD) contrast.) Oxygenated haemoglobin has different susceptibility properties than deoxygenated haemoglobin. T2* relaxation time is dependent of the level of oxygenated haemoglobin weighted images. Local neuronal activation is associated with a local increase in local blood flow and the level of oxygenated blood overshoots the oxygen demand of the tissue at least under physiological conditions, resulting in a change in T2* relaxation. However, signal changes between rest and activated state are small (about 5% at 1.5 Tesla).[30] Diffusion (the molecular motion of water molecules) affects the magnitude of the MR signal. If a proton moves by diffusion throughout the course of an MR imaging experiment, it experiences an unrecoverable phase shift ("dispersion") resulting in signal attenuation as it travels through magnetic field gradients. This is a pure T2 effect

and can be used to quantify diffusion. Diffusion has been used as an independent contrast mechanism in MR imaging.[31,32]

1.2.5 MR echoes

Whenever a RF pulse is applied to a sample, a free induction decay (FID) signal is generated because the RF pulse tips some component of the longitudinal magnetization into the transverse plane. This signal (echo) can be recorded by a receiver coil. The FID signal persists until the phase coherence of the spins has been completely destroyed by T2* decay. The FID signal has the form of a rapidly decaying sine wave. In distinction to the FID, a spin echo (SE) is formed by the combined effect of two successive RF pulses. The first RF pulse tips part of the

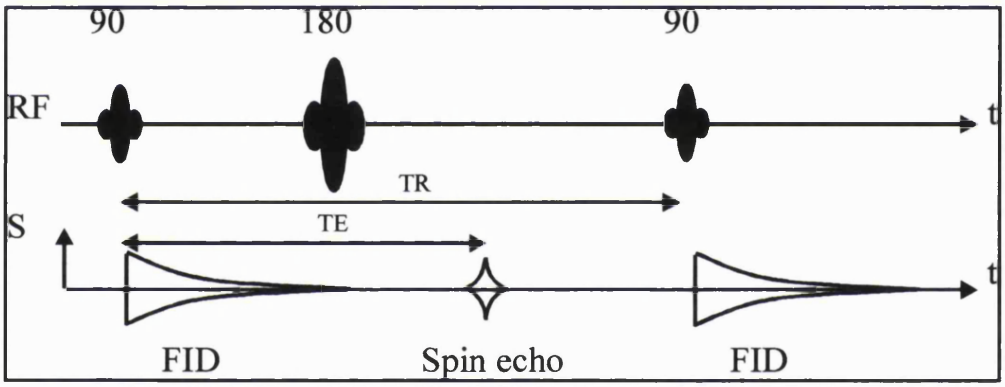

Figure 1.4 - Spin echo sequence. TR = time to repeat, TE = time to echo, FID = free induction decay, t = time.

longitudinal magnetization into the transverse plane and generates a short lasting FID signal. The second RF pulse refocuses the dephased components of the original FID into a SE (fig.1.4).[33] There are other methods of generating an echo including gradient echo and stimulated echo. A gradient echo arises from the action of a single RF pulse coupled with a gradient reversal.[34] If three or more RF pulses are applied a stimulated echo occurs. This technique is employed in MR spectroscopy under the name STEAM (stimulated echo acquisition mode). A repeating unit which is composed of a series of one or more radio frequency

pulses with the measurement of one or more signals is called a pulse sequence.

1.2.6 Modifying contrast

Modifying contrast is one of the most important characteristics of MR imaging. There are a number of different ways to modify contrast based on the physical principles of MR. In standard MR imaging contrast depends on the equipment parameter TR and TE which can be varied. The TR ("Time to Repeat") is the interval between two successive pulse cycles. The TE ("Time to Echo") is the time interval from one pulse (or a series of pulses in a more complicated pulse cycle) to the measurement of the MR signal.

Using a long TR reduces the effect of T1 relaxation in producing contrast and using a short TE reduces the effect of T2 in producing contrast. Varying TR and TE is therefore a strategy to modify the contrast on MR images. To produce a "T1 weighted" image a short TR pulse and a short TE should be used, to produce a "T2 weighted" image a long TR and a long TE should be used. To produce a "spin density" image, a long TR and a short TE is necessary. It should be kept in mind that the concept of T1 and T2 weighting is an oversimplification. In reality all MR images display tissue contrasts that depend complexly on spin density, T1, and T2 simultaneously.[35] Furthermore, different tissues in different parts of the image may have completely different "weightings".

There are a number of other strategies of varying contrast. The application of contrast material, usually gadolinium diethylenetriamine pentaacetic acid (GdDTPA), which shortens the T1 (and to a lesser extent the T2) relaxation time. The application of "diffusion gradients" in diffusion imaging which makes the sequence sensitive to the molecular motion of water (this is discussed in detail in chapter 4). The utilization of off-resonance (not Lamor frequency) saturation pulses to modify contrast.[36] The application of a physiological stimulus which is followed by a focal increase of the concentration of oxygenated haemoglobin resulting in a change in T2* in functional imaging. "Labeling spins" in perfusion imaging and other methods.

1.2.7 Limitation of MR studies

Theoretically, relaxation times of T1 and T2, diffusion, perfusion and magnetization transfer ratio can be measured accurately and reproducibly in the brain.[37,38,39] However, scanner performance and artefacts due to the subject (i.e. motion) can degrade both accuracy and reproducibility. Quality assessment and careful interpretation is crucial for quantitative MR studies in humans. Postprocessing studies like volumetry and fractal analysis are another examples for quantitative studies in MR imaging. In volumetry the volumes of structures are measured by detecting boundaries on images.[40] Fractal analysis provides a measure of the complexity of a structure.[41] Different manual, semiautomatic and automatic methods are available. All volumetric and fractal analysis methods have in common that the boundary detection is based on signal intensities. Thus the accuracy and reproducibility of volumetry and fractal analysis can be degraded by poor scanner performance or artefacts due to the subject like any other quantitative MR method.
Magnetic resonance spectroscopy and chemical shift imaging are other examples of quantitative MR techniques which will not be discussed in the thesis.

1.2.8 Creating an MR image

In MR imaging magnetic field gradients are used to attach spatial information to the MR signal. A magnetic field gradient is a quantitative change in magnetic field magnitude form one point in space to another. Gradients are characterized by the gradient strength (in mT/m), and their duration (in ms). Because of technical imperfections gradients cannot be switched on and off immediately. The slew rate defines the time required to reach maximum strength. Apart from imaging purposes gradients are used in diffusion imaging and as "crusher" gradients to eliminate eddy currents. When a gradient is imposed to the main magnetic field by sending a current through a gradient coil, the field strength is varied (slightly). Since it needs three points in space to localize a point in space, we need three

magnetic field gradients oriented along the major axes in space (and therefore three gradient coils). In order to produce an image, one gradient is used to locate the level of each plane and is known as the "slice select" or z gradient. The other two gradients are used to locate points of intensity within each plane. They are called "frequency" (or x) and "phase encoding" (or y) gradients. Signal arising from each part of an imaged object are thus spatially encoded by differences in frequency and phase. A Fourier transform (FT) allows an MR signal to be decomposed into a sum of sine waves of different frequencies, phases, and amplitudes. FT is used for image generation. The steps the scanner takes to achieve its goal of producing an image can be divided into three conceptual stages: 1. producing matrices where each row is a different repetition and each column is a point in time (k-space); 2. transforming these "repetition time" matrices into matrices where each column is a frequency point and each row is a phase encoding angle; and 3. performing a 2D Fourier transformation, which transforms these "phase-frequency" matrices into images, i.e., matrices whose rows and columns represent points on the x and y axis of the part being imaged.

1.2.9 Fast MR imaging

The way k-space is filled has important implications on the acquisition time and resolution. k-space is the matrix of data that is initially obtained when the signal in measured: each element in the matrix is the amplitude of the signal at a point in time corresponding to the element's column, and for a repetition corresponding to the element's row. Usually, the k-space matrix is obtained such that the columns on the left and the rows on the top are the most negative, the columns on the right and the rows on the bottom are the most positive, and zero lies somewhere at the centre. When this is the case, it turns out that the centrally located rows and columns affect the contrast of the final image, whereas the peripheral rows and columns affect the detail or resolution of the image. In other words, k-space is essentially partitioned into regions which specialise in either contrast of resolution. In half Fourier imaging k-space is only half filled, the other half is extrapolated

mathematically thus halving the acquisition time but also the signal to noise ratio.

1.2.9.1 Fast Spin Echo Imaging

Fast spin echo (FSE) imaging resembles a routine multiecho SE sequence in that it uses 180^0 refocusing pulses after a single 90^0 pulse to generate a train of echoes. The FSE technique, however changes the phase-encoding gradient for each of these echoes (the standard multiecho sequence collects all echoes in a train with the same phase encoding.) As a result of changing the phase encoding gradient between echos, multiple lines of k-space can be acquired within a given TR thus reducing acquisition time. The number of echoes acquired with in a given TR interval is known as the echo train length. Each echo train has been acquired with a different TE. However, the global image contrast is dictated by the echo train at which low order steps were performed (effective TE).

1.2.9.2 Echo Planar Imaging

In EPI all k-space is sampled by rapid gradient reversals and echo collection after a single set of RF pulses.Images can be obtained in 30 to 40ms therefore EPI holds the promise of "real time" MR imaging. Echoplanar imaging is used for forms of functional imaging in which a preparation sensitive to physiology is applied before the echoplanar readout. In order to spatially encode the signal after a single RF pulse imaging gradients have to be fast. Gradient coils must be able to generate 20 to 40 mT/m fields with rise times less than 200ms. Disadvantages of EPI include Chemical shift artefacts and acoustic noise. Various other k-space trajectories can be generated: zigzag, rectangular and spiral pattern.

1.2.10 Three dimensioned acquisitions

An alternative way of producing an image is 3DFT. In 3D FT imaging, the slice select gradient is no longer employed for each individual slice. Instead a single

slice is selected that is thick enough to contain the first and last slices of the desired imaging volume; and then each of the three orthogonal axes is encoded: frequency along the x axis and phase along the y and the z axis. The main advantage is that once the imaging volume is obtained, any number of sets of very thin contiguous slices in any direction may be produced. The main disadvantage is in increased acquisition time. Usually gradient echo sequences with short TR are used for this type of imaging.

1.2.11 Resolution and signal intensity

Each element of the image is a pixel. The pixel size and therefore the resolution of a MR image is determinated by the number of frequency encoding steps (N_x) and phase encoding steps (N_y) and the field of view (FOV). The in plane pixel dimensions for either 2DFT or 3DFT are $x=FOV_x/N_x$ and $y=FOV_y/N_y$. In 2DFT imaging the pixel depth equals the slice thickness. In 3DFT imaging the number of phase encoding steps in the z direction (N_z) = "slab thickness" needs to be known: $z=FOV_z/N_z$. Resolution is inversely correlated with signal intensity. The smaller the pixel the smaller the number of protons participating in the MR experiment the lower the signal. This can result in unacceptable signal to noise ratios. Averaging be may required to increase the signal to noise ratio (tab.1.4).

Table 1.4 (adapted from Ref[42])

Adjusting imaging parameters to improve signal-to-noise ratio (SNR)

Change in Parameter	Disadvantage/Trade-off
Increasing voxel size	Decreased spatial resolution
Increasing number of signal averages (number of excitations NEX)	Increased imaging time disproportionally to gain in SNR (doubling NEX increases SNR by $\sqrt{2}$)
Using narrow bandwidth technique	Limits number of slices available for a given repetition time (TR); increases chemical shift artefacts, increases motion artefacts.
Increasing interslice gap (reducing RF interference/cross talk)	May miss lesions
Using 3DFT instead of 2DFT acquistions	Increases imaging time; increases motion artefacts
Reducing systematic noise (flow compensation, gating, antialising)	Various time and hardware limitations dependent on strategy selected

1.2.9 Artefacts in MR imaging

A number of artefacts can affect the image quality. They are partly due to the signal to noise ratio of MR imaging but also to imperfections of the scanner. It is important that artefacts are recognized which can be particularly difficult if quantitative methods are used. Tab.1.5 lists typical artefacts.

Table 1.5 MR artefacts

Artefact	Cause	Appearance on images
erroneous T1 (too long or too short)	scanner imperfection	variation of signal intensity from scan to scan
too short T2	(scanner imperfection) poor refocusing of 180^0 pulse	variation of signal intensity from scan to scan
chemical shift artefacts	spatial misregistration due to different frequencies of protons bound in fat and in water	dark and bright bands around edges
truncation artefacts	finite sampling of frequencies in the Fourier transform	multiple fine bands at interfaces, pseudosyrinx
susceptibility artefacts	local distortions of the magnetic field caused by two juxtaposed materials of different magnetic susceptibility	image distortion and intensity changes at interfaces
wraparound	object exceeding the field of view	back of image attached to the front in the phase-encode direction
motion artefacts	change of the position of the scanned object	blurring, ghosts
zipper like artefacts	a) extraneous source (poor RF shielding of the scanner room) b) stimulated echos (imperfect slice selection profiles or improper RF transmitter adjustments)	a) band in phase encoding direction b) band in frequency encoding direction
herringbone artefacts	data error in Fourier transform	crisscross artefact
cross talk	imperfect slice profiles	increased noise

1.3 MR imaging in Epilepsy

1.3.1 Introduction

There is growing interest in MR imaging in epilepsy. About 10% of all publications in epilepsy from 1984 to 1998 have used MR imaging and there has been a continous increase in the number of publications per year (fig1.5). A substantial body of literature about MR imaging in epilepsy has developed since the first publications 15 years ago (fig1.6).[43,44] MR imaging is a developing technology and continuous assessment of new developments is important. Guidelines how to assess the clinical efficacy of a new technique have been proposed (tab.1.6). However, new MR techniques are often applied in a clinical environment without rigorous assessment. A study trying to evaluate the clinical efficacy of MR imaging in general has shown that only 5% of articles involved 30 or more patients and dealt with diagnostic accuracy, effect on diagnosis, or other more treatment related aspects of clinical efficacy.[45] Moreover, of this 5%, four

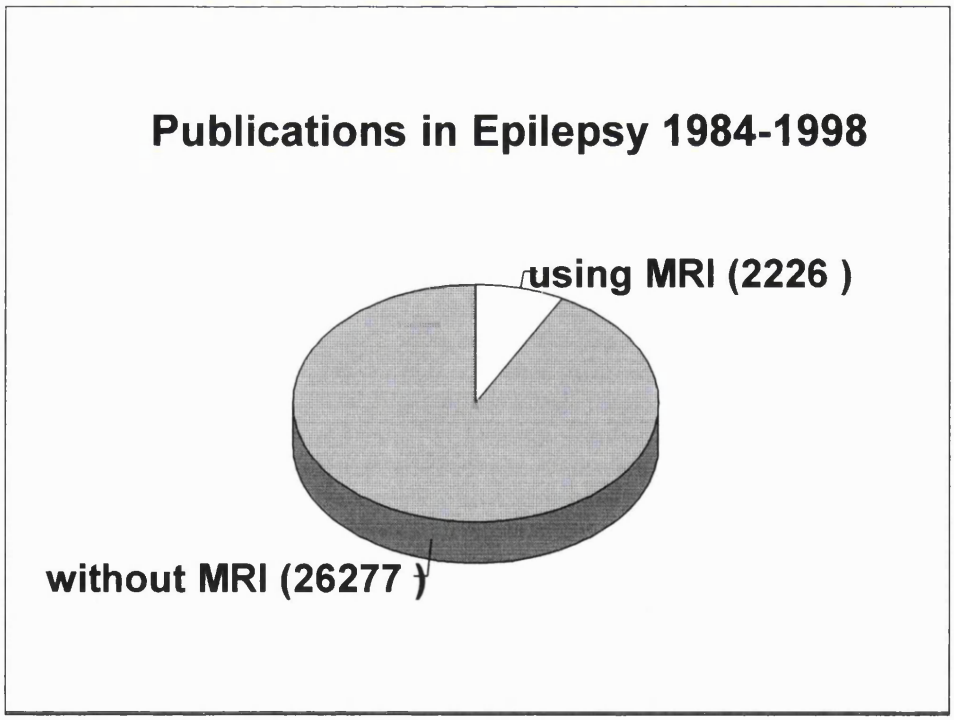

Figure 1.5 - Publications in epilepsy from 1884 to 1998. The number in brackets is the number of publications. (Source PubMed.)

fifth were rated in the lowest of four categories of methodologic quality and only one-seventh dealt with the effect of MR imaging on treatment or treatment plans. Studies about MR in epilepsy are no exception. For clinical purposes the impact of MR imaging on five issues is important: detection and diagnosis, pathophysiology and pathogenesis, treatment (both surgical and medical), prognosis and outcome and the prevention. The exact role of MR imaging in particular with regard to these issues has still to be defined.[46] With the development of new MR techniques the role of MR imaging continues to change and there is the need for assessment of the clinical value of new techniques. This thesis focusses on the role of MR imaging on detection and diagnosis to a lesser extent on pathogenesis and the consequences of treatment. The following paragraphs will give an update on the current role of MR imaging in epilepsy.

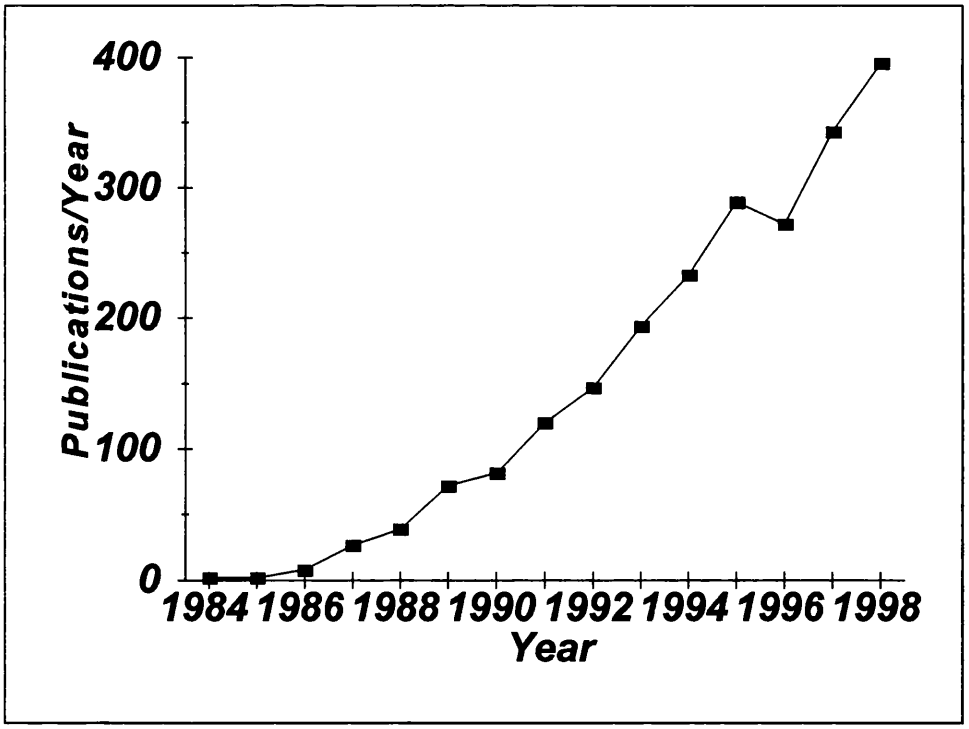

Figure 1.6 - Publications about Epilepsy using Magnetic Resonance Imaging from 1984 to 1998. (Source PubMed.)

Table 1.6 (adapted from Ref[44])

Three dimensions to classification of studies of a diagnostic test
1. What disease is being studied?
2. What level of clinical efficacy is addressed?
2.1. Technical capacity: A study showing the ability of a new test to measure or show certain findings in one or a few case-patients.
2.2. Diagnostic accuracy: A study with enough cases to calculate one or more accuracy statistics, such as sensitivity or specificity, with confidence intervals
2.3. Diagnostic impact: A study showing how the new test compares with an existing alternative or how the new test can replace or complement the alternative to improve accuracy in diagnosis
2.4. Therapeutic impact: A study showing how the new test leads to changes in the therapeutic planning, such as offering more accurate staging with associated changes in treatment for cancer patients
2.5. Patient outcomes: A study showing that use of the new test improves quality of life, leads to substantial relief, improvement in function, or decreased mortality.
3. Are the study methods adequate for internal validity and external generalizability?
Grade A: Studies with broad generalizability to most patients suspected of having the disease of concern, with no substantial flaws in research methods: a prospective comparison of a diagnostic test result with a well defined final diagnosis when assessing diagnostic accuracy or a large randomized control trial when assessing therapeutic impact or patients outcomes.
Grade B: Studies with narrower spectrum of generalizability, with only a few flaws that are well described so their impact on conclusions can be assessed, but still requiring a prospective study of diagnostic accuracy or a randomized trial for therapeutic effects or patient outcomes.
Grade C: Studies with several flaws in research methods, small sample sizes, or incomplete reporting. Often retrospective studies of diagnostic accuracy or effect and nonrandomized comparisons for therapeutic impact or patient outcomes.
Grade D: Studies with multiple flaws in research methods, obvious biases in selection of patients, or opinions without substantiating data.

1.3.2 The current role of MR imaging in Epilepsy

MR imaging demonstrates brain anatomy in lavish detail and has supplanted CT in the investigation of epilepsy.[47,48] Since the initial application to epilepsy,

standard MR imaging using T1- and T2-weighted sequences has been consistently superior to x-ray CT in terms of sensitivity and specificity for identifying structural abnormalities associated with epilepsy.[49,50,51,52,53,54,55] Using CT only 60% of MR imaging detected dysembryoblastic tumours (DNT), 40% of MR imaging detected cortical dysplasia and 30% of MR imaging detected subependymal heterotopias can be identified, HS and band heterotopia are usually undetectable on CT images.[56] Structural abnormalities can be detected in > 70% in patients with refractory seizures and candidates for epilepsy surgery[57] and in about 50% in less selected patients with MR imaging.[58] MR imaging is now the standard of reference in the evaluation of patients with epilepsy, particularly those with medically intractable seizures. CT retains a role, supplementary to MR imaging, in the recognition of intracranial calcifications that may not easily detected on MR images.

The rationale of imaging the brain of patients developing epilepsy is to identify underlying pathologies and to assist the formulation of syndrome-based and aetiological diagnoses.[59] For example hippocampal sclerosis either detected by MR imaging is part of the syndrome of mesio-temporal epilepsy. There is continuing interest in MR imaging in epilepsy research. MR imaging can be used to correlate the localization of structural abnormalities with the seizure semiology. Studies like this can contribute valuable information on the localisatory value of seizure symptoms[60] in particular in regions which are difficult to assess with surface EEG.[61]

1.3.3 Important pathologies

1.3.3.1 Hippocampal sclerosis

Hippocampal sclerosis (HS) is the single most common pathology underlying partial seizure disorders that do not respond to antiepileptic drug therapy, but which are amenable to surgical treatment.[62] Two thirds of patients with HS become seizure free after anterior temporal lobe resection. However, patients with morphogically normal hippocampus become only rarely seizure free after temporal

lobe resection.[63] Therefore the in vivo detection of HS is crucial importance for patients with temporal lobe epilepsy. By 1990 MR techniques had advanced sufficiently enough to allow the identification of HS on MR images.[64] HS is best identified on coronal images. Some authors recommend to scan the hippocampus perpendicular to its longitudinal axis to improve the visualisation of the hippocampus. MR imaging criteria of HS are hippocampal volume loss and a prolonged T2-relation time. Both volume loss and change in relaxation time can be either visually (qualitatively) or quantitatively assessed. Findings associated with HS, sometimes called secondary findings,[65] include loss of the internal architecture of the hippocampus on MR images, temporal lobe volume loss, dilatation of the temporal horn, narrowed collateral white matter, blurring of the grey matter white matter margin in the temporal neocortex, smaller fornix and atrophic mamillary bodies. They are variably accompanying features to the changes of HS but not reliable in their own right. Some of these features may be found in normal subjects.

Sensitivity and specificity of MR imaging with regard to the detection of HS are difficult to assess because a reliable histological goldstandard is only available in the highly selected minority of patients who undergo temporal lobectomy. However, patients with the clear-cut signs of HS on MR images have always histological signs of HS with cell loss in CA1. On the other hand endfolium sclerosis and mild cells loss in CA1 are usually undetectable on MR images.[66] Further improvement of the MR techniques may increase the sensitivity for HS. MR imaging is a good predictor of the outcome of temporal lobectomies. Patients who fulfill the MR criteria for unilateral HS have a 70% to 90% chance to be seizure free one year after temporal lobectomy, patients with normal MR images have only a 30% chance to be seizure free after temporal lobectomy.[67,68,69]

1.3.3.2 Malformations of cortical development

Malformations of cortical development (MCDs) are sometimes found in patients with epilepsy with or without a neurodevelopmental deficit. These abnormalities

are increasingly being recognized in patients with seizure disorders that were previously regarded as being cryptogenic. Gross abnormalities may be identified on x-ray CT, but are seen much more clearly on MR images. More subtle MCDs are difficult to detect or undetectable on x-ray CT but are readily detectable on MR images with T1-weighted contrast and high resolution. MCDs detectable with MR imaging include schizencephaly, agyria, diffuse and focal macrogyria, focal polymicrogyria, subependymal grey matter heterotopias, bilateral subcortical laminar heterotopia, tuberous sclerosis, focal cortical dysplasia and dysembryoblastic neuroepithelial tumours.[70]

1.3.3.3 Granulomas

Tuberculomas and cysticercosis are the most common identified causes of epilepsy in developing countries. Epilepsy is the most common manifestation of neurocysticercosis. Whilst X-ray CT will often demonstrate neurocysticercosis, MR is more sensitive in demonstrating various stages in the development of noncalcified cerebral cysticerosis lesions.

1.3.3.4 Cavernomas

Cavernomas are an important diagnostic group as surgical removal carries up to 70% chance of subsequent seizure remission. MR imaging is sensitive and specific for the detection of cavernomas since they have a characteristic appearance on MR images.

1.3.3.5 Other pathologies

Tumours, scars, cysts, ischaemic and traumatic lesions underlying and associated with epilepsy are well demonstrated with MR imaging.

1.3.3.6 Transient changes

Generally, single brief complex partial seizures do not appear to affect the signal on T2-weighted images. Partial status and generalized status may result in transient increased signal on T2-weighted images.[71,72,73,74,75] This finding needs to be differentiated from an underlying lesion such as a glioma or inflammatory process.

1.3.3.7 No abnormalities detected on standard MR imaging

This is the largest group in a non presurgical population. Patients with generalized epilepsy are MR negative on standard MR imaging including hippocampal volumetric measurements. However, patient with clear-cut partial seizures can be MR negative. Recent studies showed group differences in patients with epilepsy with generalized epilepsy compared to normal control groups. This is a very interesting a promising finding.[83] However, further evaluation of this finding is necessary.

1.4 Technical advances in recent years in Epilepsy

1.4.1 Three D gradient echo acquisition technique in epilepsy

There have been many technical advances made in recent years and these continue.[76] One of the most important advances was the 3D gradient echo acquisition technique which allows the generation of contiguous T1-weighted coronal images with high resolution (slice thickness < 2 mm). T1-weighted images provide a high contrast for grey matter and white matter thus resembling anatomical specimens. The relative brightness of white matter on T1-weighted images arises from myelin and is likely to be determinated by cholesterol of myelin.[77,78] Studies indicate that using coronal T1-weighted images with high resolution in the investigation of patients with epilepsy increases the sensitivity for

the detection of structural abnormalities, in particular for the detection of hippocampal sclerosis.[79] 3D T1 weighted data sets allow quantitative volumetric measurements.[80] Other experimental quantitative approaches in epilepsy include measurements of grey matter and white matter volume[81,82,83,84], morphometry of the temporal lobes,[85] curvilinear reconstruction of 3D MR images[86] and fractal analysis.[87] All methods detected differences between control subjects and patients with epilepsy. However, the numbers are small and diagnostic impact of these measurements has to be assessed.

1.4.2 Fast spin echo (FSE) acquisition technique in epilepsy

The use of the FSE technique to obtain high resolution coronal images with T2-weighted contrast was another important advance in epilepsy. Coronal fast spin echo images have been successfully used as an alternative the T1 weighted 3D gradient echo acquistion technique to identify hippocampal sclerosis.[88,89]

1.4.3 Off resonance imaging in epilepsy

Off resonance imaging has been used in the context of epilepsy in small studies in dysgenetic lesions[90] and hippocampal sclerosis.[91] In both studies abnormalities abnormal magnetization transfer rates have been demonstrated suggesting that the method can be used to identify abnormal tissue. A problem is that the difference between normal and abnormal grey matter is much smaller than the difference between normal white matter and demyelinated white matter.[92] Further studies with larger sample sizes are necessary for rigorous assessment.

1.4.4 Functional Magnetic Resonance Imaging (fMRimaging) in epilepsy

Functional imaging has been applied in various areas in recent years. One of the main roles of functional imaging in epilepsy could be the non invasive identification of the primary motor cortex and the dominant hemisphere in patients

with epilepsy who are candidates for epilepsy surgery.[93,94] Occasionally fMRI has been successfully used to identify regions of increased blood flow in partial seizures.[95] Using fMRI in combination with EEG recordings allows the registration of spikes but the technique is time consuming and therefore limited to cooperative patients.[96]

1.4.5 Other MR techniques in epilepsy

MR imaging provides a number of constrast which are yet to be applied in epilepsy. Hardware limitation currently limit the application of some. However, quantitation of proton density and characterization of the transverse magnetisation decay curve are possible and have potential importance in epilepsy. Proton density reflects the density of free water.[97] Measurements of the T2-relaxation time in the hippocampus are performed in addition to volumetric measurements.[98,99] The number of exponentials of the transverse magnetisation (T2) decay curve reflects the number of different water pools (for example intra cellular and extra cellular).[100] These parameters are likely to be altered if the celluar make-up changes in epilepsy during or after a seizure and are therefore of potential importance in epilepsy.

1.5 New MR techniques in epilepsy discussed in this thesis

1.5.1 Aim of the thesis

The aim of this thesis was to apply new MR techniques in epilepsy including fast FLAIR, serial and high resolution imaging of the hippocampus and diffusion imaging.

1.5.2 FLAIR imaging in epilepsy

The fluid attenuated inversion recovery (FLAIR) sequence combines cerebrospinal fluid (CSF) signal suppression with heavy T2-weighting. Lesions which have a signal intensity similar to CSF on conventional T2-weighted images become the brightest object on the CSF suppressed FLAIR images thus increasing the lesion conspicuity[101] which makes the sequence interesting for epilepsy.[102] Early applications of FLAIR were limited by the long acquisition time, but these have been reduced with the RARE readout in fast FLAIR[103] and with interleaved inversion pulses in OIL FLAIR.[104] We evaluated fast FLAIR in a large group of patients with epilepsy and also present initial experience with a 3D version of FLAIR in epilepsy.

1.5.3 MR imaging of the hippocampus

Quantitative measurements of the hippocampal volume are the most commonly used quantitative method in epilepsy. This method has undoubtedly contributed to the detection of hippocampal atrophy non-invasively and has kindled the interest of clinicians in MR imaging.[105,106,107,108] Various methods have been used and the exact role of volumetric measurements in the context of epilepsy remains to be assessed. In this thesis we present our own data regarding the repeatability of measurements of the hippocampal volume on different sequences. We applied hippocampal volumetric measurements in serial MR imaging in a patient who developed epilepsy after status epilepticus. Finally, we present an experiment on the microscopic structure of the hippocampus. Histologically hippocampal sclerosis is characterized by cell loss and gliosis affecting mainly the pyramidal cell layer in sector CA1 (or Sommers' sector).[109] To evaluate, if layers give contrast on MR images we performed MR experiments at different field strength using a hippocampal anatomical specimen and on a volunteer.

1.5.4 Diffusion imaging in epilepsy

Diffusion imaging is a technique which is sensitive to the molecular motion of water. Biological membranes restrict water diffusion in the human brain.[110] Microstructural changes associated with pathological processes including neuronal swelling, shrinkage or widening of the extracellular space or the loss of tissue organization all result intransient or permanent changes of diffusion and diffusion anisotropy.[111,112] Diffusion imaging is a promising technique in epilepsy because epileptic seizures are membrane associated events with may cause measurable diffusion changes.[113,114,115,116,117,118,119,120] Animal models of chronic epilepsy following status have demonstrated that persistent diffusion changes can also develop.[121] These persistent diffusion changes are likely to reflect the microstructural damage in such animals which include widened extracellular space, low neuronal densities, reduced dendritic branching and loss of cellular organization. In humans the technique is currently at an experimental state and still developing. In this thesis we provide our results on diffusion imaging in epilepsy.

1.6 Summary

- MR imaging is a rapidly devolping technique. Only a fraction of the different MR contrasts have been rigorously evaluated.
- MR techniques providing images with standard T1- and T2-weighted contrast allow the in vivo detection of structural abnormalities associated with epilepsy including hippocampal sclerosis.
- MR imaging assists the formulation of syndrome-based and aetiological diagnoses.
- In 1999 MR imaging demonstrates structural abnormalities in about 80% of highly selected presurgical patients but less frequently in non-selected patients.
- MR imaging has altered treatment and has prognostic value in patients who are candidates for epilepsy surgery.

- MR studies aimed at investigating brain function in epilepsy are experimental.

1.7 References

1. Jackson JH. On the anatomical, physiological and pathological investigation of epilepsies. West Riding Lunatic Asylum Medical Reports 3, 3.5. In: Taylor J. ed. *Selected writings of John Hughlings Jackson.* Hodder and Stoughton, London, 1931:90.

2. Commission on classification and terminology of the international league against epilepsy. Proposal for revised clinical and electroencephalographic classification of epileptic seizures. *Epilepsia* 1981;**22**:489-501.

3. Commission on classification and terminology of the international league against epilepsy. Proposal for revised classification of epilepsies and epileptic syndromes. *Epilepsia* 1989;**30**:389-399.

4. Shorvon SD. Magnetic resonance imaging in epilepsy: the clinical research questions. In: Shorvon SD, Fish DR, Andermann F, Bydder GM, Stefan H. *Magnetic resonance scanning and epilepsy.* Plenum Press, New York 1994:3-14.

5. Shorvon SD. Epidemiology, classification, natural history and genetic of epilepsy. *Lancet* 1990;**336**:93-96.

6. Hauser WA, Annegers JF, Kurland LT. Incidence of epilepsy and unprovoked seizures in Rochester, Minnesota: 1935-1984. *Epilepsia* 1993;**34**:453-468.

7. Cockerell OC, Johnson AL, Sander JW, Shorvon SD. Prognosis of epilepsy: a review and further analysis of the first nine years of the British national general practice study of epilepsy, a prospective population-based study. *Epilepsia* 1997;**38**:31-46.

8. Meldrum BS. Anatomy, physiology, and pathology of epilepsy. *Lancet* 1990;**336**:231-234.

9. Schwartzkroin PA. Cellular electrophysiology of human epilepsy. *Epilepsy Res* 1994;**17**:185-192.

10. Meldrum BS. Metabolic factors during prolonged seizures and their relation to nerve cell death. In: Delgado-Escueta AV, Wasterlain CG, Treiman DM, Porter RJ, eds. Advances in Neurology, Vol 34. Status Epilepticus. Raven Press, New York 1983:261-275.

11. Niehaus L, Wieshmann U. Cerebral blood flow velocity changes during simple partial motor seizures. *Electroenceph Clin Neurophysiol* 1996;**99**:323.

12. Talairach J, Bancaud J. Lesion, "irritative" zone and epileptogenic focus. *Confin Neurol* 1966;**27**:91-94.

13. Fish DR. The anatomical basis of the epilepsies and MRI: Implications for MRI. In: Shorvon SD, Fish DR, Andermann F, Bydder GM, Stefan H. *Magnetic resonance scanning and epilepsy.* Plenum Press, New York 1994:15-20.

14. Berger H. Über das Elektoenzephalogramm des Menschen. 1.-9. Mitteilung (1929-1938). Zusammenfassung: *Novo Acta Leopoldina, N.F.* 1938;**6**:173-309.

15. Quesney LF. Extratemporal epilepsy: clinical presentation, pre-operative EEG localization and surgical outcome. *Acta Neurol Scand* 1992;**140**(suppl):81-94.

16. Engel J Jr. Research on the human brain in an epilepsy surgery setting. *Epilepsy Res* 1998;**32**:1-11.

17. Newton MR, Berkovic SF, Austin MC, Rowe CC, McKay WJ, Bladin PF. Spect in the localisation of extratemporal and temporal seizure foci. *J Neurol Neurosurg Psychiatry* 1995;**59**:26-30.

18. Prevett MC, Duncan JS, Jones T, Fish DR, Brooks DJ. Demonstration of thalamic activation during typical absence seizures using H2(15)O and PET. *Neurology* 1995;**45**:1396-1402.

19. Koepp MJ, Richardson MP, Brooks DJ, Duncan JS. Focal cortical release of endogenous opioids during reading-induced seizures. *Lancet* 1998;**352**:952-955.

20. Baxendale SA, Thompson PJ, Van Paesschen W. A test of spatial memory and its clinical utility in the pre-surgical investigation of temporal lobe epilepsy patients. *Neuropsychologia* 1998;**36**:591-602.

21. Henry TR, Pennell PB. Neuropharmacological imaging in epilepsy with PET and SPECT. *Q J Nucl Med* 1998;**42**:199-210.

22. Koepp MJ, Hand KS, Labbe C, Richardson MP, Van Paesschen W, Baird VH, Cunningham VJ, Bowery NG, Brooks DJ, Duncan JS. In vivo [11C]flumazenil-PET correlates with ex vivo [3H]flumazenil autoradiography in hippocampal sclerosis. *Ann Neurol* 1998;**43**:618-626.

23. Richardson MP, Koepp MJ, Brooks DJ, Duncan JS. 11C-flumazenil PET in neocortical epilepsy. *Neurology* 1998;**51**:485-492.

24. Schenck JF, Leue WM. Instrumentation: magnets, coils, and hardware. In: Atlas SW: *Magnetic resonance imaging of the brain and spine.* Second edition. Lippincott-Raven Publishers, Philadelphia 1996:1-27.

25. Bloch F. Nuclear induction. *Phys Rev* 1946;**70**:460-474.

26. Bloch F, Hansen WW, Packard M. The nuclear induction experiment. *Phys Rev* 1946;**70**:474-485.

27. Morris P. *Nuclear magnetic resonance imaging.* Oxford University Press, Oxford 1986:313.

28. Elster AD. *Questions and answers in magnetic resonance imaging.* Mosby-Year Book, St Louis 1994:37.

29. Fullerton GD. Physiologic basis of magnetic relaxation. In: Stark DD, Bradley WG Jr eds. *Magnetic resonance imaging.* 2nd ed. Mosby-Year Book, St Louis 1992:88-108.

30. Bandettini PA, Wong EC, Binder JR, Rao SM, Jesmanowicz A, Aaron EA, Lowry TF, Forster HV, Hinks RS, Hyde JS. Functional MR imaging using the BOLD approach. In: LeBihan D. ed. *Diffusion and perfusion magnetic resonance imaging.* Raven Press, New York 1995: 335-349.

31. Stejskal EO, Tanner JE. Use of spin echo pulsed magnetic field gradient to study anisotropic restricted diffusion and flow. *J Chem Phy* 1965;**43**:3579-3603.

32. Taylor DG, Bushell MC. The spatial mapping of translational diffusion by the NMR imaging technique. *Phys Med Biol* 1985;**30**:345-349.

33. Hahn EL. Spin echoes. *Phys Rev* 1950;**80**:580-594.

34. Winkler ML, Ortendahl DA, Mills TC, Crooks LE, Sheldon PE, Kaufman L, Kramer DM. Characteristics of partial flip angle and gradient reversal MR imaging. *Radiology* 1988;**166**:17-26.

35. Elster AD. An index system for comparative parameter weighting in MR imaging. *J Comput Assist Tomogr* 1988;**12**:130-134.

36. Ulmer JL, Mathews VP, Hamilton CA, Elster AD, Moran PR. Magnetization transfer or spin-lock? An investigation of off-resonance saturation pulse imaging with varying frequency offsets. *Am J Neuroradiol* 1996;**17**:805-819.

37. Tofts PS, DuBoulay EPGH. Towards quantitative measurements of relaxation times and other parameters in the brain. *Neuroradiology* 1990;**32**:407-415.

38. Le Bihan D, Breton E, Lallemand D, Aubin M-L, Vignaud J, Laval-Jeantet M. Separation of diffusion and perfusion in intravoxel incoherent motion imaging. *Radiology* 1988;**168**:497-505.

39. Wolff SD, Balaban RS. Magnetization transfer contrast (MTC) and tissue water proton relaxation in vivo. *Magn Reson Med* 1989;**10**:135-144.

40. Jack CR Jr, Theodore WH, Cook M, McCarthy G. MRI-based hippocampal volumetrics: data acquisition, normal ranges, and optimal protocol. *Magn Reson*

Imaging 1995;**13**:1057-1064.

41. Free SL, Sisodiya SM, Cook MJ, Fish DR, Shorvon SD. Three dimensional fractal analysis of the white matter surface from magnetic resonance images of the human brain. *Cerebral Cortex* 1996;**6**:830-836.

42. Elster AD. *Questions and answers in magnetic resonance imaging.* Mosby-Year Book, St Louis 1994:109.

43. Oldendorf WH. The use and promise of nuclear magnetic resonance imaging in epilepsy. *Epilepsia* 1984;**25**(suppl 2):S105-S117.

44. Sostman HD, Spencer DD, Gore JC, Spencer SS, Holcomb WG, Williamson PD, Prichard J, Camputaro C, Greenspan RH, Mattson RH. Preliminary observations on magnetic resonance imaging in refractory epilepsy. *Magn Reson Imaging* 1984;**2**:301-306.

45. Kent DL, Haynor DR, Longstreth WT Jr, Larson EB. The clinical efficacy of magnetic resonance imaging in neuroimaging. *Ann Intern Med* 1994;**120**:856-871.

46. Spencer SS. MRI and epilepsy surgery. *Neurology* 1995;**45**:1248-1250.

47. Sitoh YY, Tien RD. Neuroimaging in epilepsy. *JMRI* 1998;**8**:277-288.

48. Duncan JS. Imaging and epilepsy. *Brain* 1997;**120**:339-377.

49. McLachlan RS, Nicholson RL, Black S, Carr T, Blume WT. Nuclear magnetic resonance imaging, a new approach to the investigation of refractory temporal lobe epilepsy. *Epilepsia* 1985;**26**:555-562.

50. Latack JT, Abou-Khalil BW, Siegel GJ, Sackellares JC, Gabrielsen TO, Aisen AM. Patients with partial seizures: evaluation by MR, CT, and PET imaging. *Radiology* 1986;**159**:159-163.

51. Lesser RP, Modic MT, Weinstein MA, Duchesneau PM, Luders H, Dinner DS, Morris. Magnetic resonance imaging (1.5 tesla) in patients with intractable focal seizures. *Arch Neurol* 1986;**43**:367-371.

52. Kuzniecky R, de la Sayette V, Ethier R, Melanson D, Andermann F, Berkovic S, Robitaille Y, Olivier A, Peters T, Feindel W. Magnetic resonance imaging in temporal lobe epilepsy: pathological correlations. *Ann Neurol* 1987;**22**:341-347.

53. Triulzi F, Franceschi M, Fazio F, Del Maschio A. Nonrefractory temporal lobe epilepsy: 1.5-T MR imaging. *Radiology* 1988;**166**:181-185.

54. Froment JC, Mauguiere F, Fischer C, Revol M, Bierme T, Convers P. Magnetic resonance imaging in refractory focal epilepsy with normal CT scans. *J Neuroradiol* 1989;**16**:285-291.

55. Cross JH, Jackson GD, Neville BG, Connelly A, Kirkham FJ, Boyd SG, Pitt MC, Gadian DG. Early detection of abnormalities in partial epilepsy using magnetic resonance. *Arch Dis Child* 1993;**69**:104-109.

56. Stevens JM. Imaging in epilepsy. *Clinical MRI* 1995;**5**:14-23.

57. Li LM, Fish DR, Sisodiya SM, Shorvon SD, Alsanjari N, Stevens JM. High resolution magnetic resonance imaging in adults with partial or secondary generalised epilepsy attending a tertiary referral unit. *J Neurol Neurosurg Psychiatry* 1995;**59**:384-387.

58. Wieshmann UC, Bartlett PA, Kendall BE, Stevens JM. The yield of MRI in clinical epilepsy referrals. *Neuroradiology* 1997;**39**:151.

59. Commission on neuroimaging of the international league against epilepsy. Recommendations for neuroimaging of patients with epilepsy. *Epilepsia* 1997;**38**:1255-1256.

60. Manford M, Fish DR, Shorvon SD. An analysis of clinical seizure patterns and their localizing value in frontal and temporal lobe epilepsies. *Brain* 1996;**119**:17-40.

61. Wieshmann UC, Niehaus L, Meierkord H. Ictal speech arrest and parasagittal lesions. *Eur Neurol* 1997;**38**:123-127.

62. Wolf HK, Campos MG, Zentner J, Hufnagel A, Schramm J, Elger CE, Wiestler OD. Surgical pathology of temporal lobe epilepsy. Experience with 216 cases. *J Neuropathol Exp Neurol* 1993;**52**: 499-506.

63. Duncan JS, Sagar HJ. Seizures characteristics, pathology, and outcome after temporal lobectomy. *Neurology* 1987;**37**:405-409.

64. Jackson GD, Berkovic SF, Tress BM, Kalnins RM, Fabinyi GC, Bladin PF. Hippocampal sclerosis can be reliably detected by magnetic resonance imaging. *Neurology* 1990;**40**:1869-75.

65. Bronen R. MR of mesial temporal sclerosis: how much is enough? *Am J Neuroradiol* 1998;**19**:15-18.

66. Van Paesschen W, Revesz T, Duncan JS, King MD, Connelly A. Quantitative neuropathology and quantitative magnetic resonance imaging of the hippocampus in temporal lobe epilepsy. *Ann Neurol* 1997;**42**:756-766.

67. Jack CR, Sharbrough FW, Cascino GD, Hirschorn KA, O'Brien PC, Marsh WR. Magnetic resonance image-based hippocampal volumetry: correlation with outcome after temporal lobectomy. *Ann Neurol* 1992;**31**:138-146.

68. Berkovic SF, McIntosh AM, Kalnins RM, Jackson GD, Fabinyi GCA, Brazenor GA, Bladin PF, Hopper JL. Preoperative MRI predicts outcome of temporal lobectomy. *Neurology* 1995;**45**:1358-1363.

69. Cascino GD, Jack CR, Parisi JE, Marsh WR, Kelly PJ, Sharbrough FW, Hirschorn KA, Trenerry MR. MRI in the presurgical evaluation of patients with frontal lobe epilepsy and children with temporal lobe epilepsy: pathologic correlation and prognostic importance. *Epilepsy Res* 1992;**11**:51-59.

70. Raymond AA, Fish DR, Sisodiya SM, Alsanjari N, Stevens JM, Shorvon SD. Abnormalities of gyration, heterotopias, tuberous sclerosis, focal cortical dysplasia, microdysgenesis, dysembryoplastic neuroepithelial tumour and dysgenesis of the archicortex in epilepsy. Clinical, EEG and neuroimaging features in 100 adult patients. *Brain* 1995;**118**:629-660.

71. Riela AS, Sires BP, Penry JK. Transient magnetic resonance imaging abnormalities during partial status epilepticus. *J Child Neurol* 1991;**6**:143-145.

72. Henry TR, Drury I, Brunberg JA, Pennell PB, McKeever PE, Beydoun A. Focal cerebral magnetic resonance changes associated with partial status epilepticus. *Epilepsia* 1994;**35**:35-41.

73. Tien RD, Felsberg GJ. The hippocampus in status epilepticus: demonstration of signal intensity and morphologic changes with sequential fast spin-echo MR imaging. *Radiology* 1995;**194**:249-256.

74. Cox JE, Mathews VP, Santos DD, Elster AD. Seizure-induced transient hippocampal abnormalities on MR: Correlation with positron emission tomography and electroencephalography. *Am J Neuroradiol* 1995;**16**:1736-1738.

75. Meierkord H, Wieshmann UC, Lehmann R, Niehaus L. Functional and structural consequences of status epilepticus demonstrated with MR imaging. *Acta Neurol Scand* 1997;**96**:127-132.

76. Stevens JM. New and developing MRI techniques in epilepsy. *Epilepsia* 1997;**38**(suppl.10):28-32.

77. Koenig SH, Brown RD, Spiller M, Lundbom N. Relaxometry of brain: why white matter appears bright in MRI. *Magn Reson Med* 1990;**14**:482-495.

78. Koenig SH. Cholesterol of myelin is the determinant of gray-white contrast in MRI of brain. *Magn Reson Med* 1991;**20**:285-291.

79. McBride MC, Bronstein KS, Bennett B, Erba G, Pilcher W, Berg MJ. Failure of standard magnetic resonance imaging in patients with refractory temporal lobe epilepsy. *Arch Neurol* 1998;**55**:346-348.

80. Cook MJ. Mesial temporal sclerosis and volumetric investigations. *Acta Neurol Scand* 1994;**152**(suppl):109-114.

81. Sisodiya SM, Free SL. Disproportion of cerebral surface areas and volumes in cerebral dysgenesis. MRI-based evidence for connectional abnormalities. *Brain* 1997;**120**:271-281.

82. Sisodiya SM, Free SL, Stevens JM, Fish DR, Shorvon SD. Widespread cerebral structural changes in two patients with gelastic seizures and hypothalamic hamartomata. *Epilepsia* 1997;**38**:1008-1010.

83. Sisodiya SM, Moran N, Free SL, Kitchen ND, Stevens JM, Harkness WF, Fish DR, Shorvon SD. Correlation of widespread preoperative magnetic resonance imaging changes with unsuccessful surgery for hippocampal sclerosis. *Ann Neurol* 1997;**41**:490-496.

84. Woermann FG, Sisodiya SM, Free SL, Duncan JS. Quantitative MRI in patients with idiopathic generalized epilepsy. Evidence of widespread cerebral structural changes. *Brain* 1998;**121**:1661-1667.

85. Lee JW, Reutens DC, Dubeau F, Evans A, Andermann F. Morphometry in temporal lobe epilepsy. *Magn Reson Imaging* 1995;**13**:1073-1080.

86. Bastos AC, Korah IP, Cendes F, Melanson D, Tampieri D, Peters T, Dubeau F, Andermann F. Curvilinear reconstruction of 3D magnetic resonance imaging in patients with partial epilepsy: a pilot study. *Magn Reson Imaging* 1995;**13**:1107-1112.

87. Cook MJ, Free SL, Manford MR, Fish DR, Shorvon SD, Stevens JM. Fractal description of cerebral cortical patterns in frontal lobe epilepsy. *Eur Neurol* 1995;**35**:327-335.

88. Tien RD, Felsberg GJ, Campi de Castro C, Osumi AK, Lewis DV, Friedman AH, Crain B, Radtke RA. Complex partial seizures and mesial temporal sclerosis: evaluation with fast spin-echo MR imaging. *Radiology* 1993;**189**:835-842.

89. Kim JH, Tien RD, Felsberg GJ, Osumi AK, Lee N, Friedman AH. Fast spin-echo MR in hippocampal sclerosis: correlation with pathology and surgery. *Am J Neuroradiol* 1995;**16**:627-636.

90. Sisodiya S, Barker G, Bartlett P, Tofts P, Shorvon S, Stevens S. Magnetization transfer contrast imaging of grey matter in cerebral dysgenesis. *Proceedings of the International Society for Magnetic Resonance in Medicine, fourth scientific meeting.* ISMRM, Berkeley, CA 1996:619.

91. Tofts PS, Sisodiya S, Barker GJ, Webb S, MacManus D, Fish D, Shorvon S. MR magnetization transfer measurements in temporal lobe epilepsy. *Am J Neuroradiol* 1995;**16**:1862-1863.

92. Gass A. Barker GJ, Kidd D, Thorpe JW, McManus D, Brennan A, Tofts PS, Thompson AJ, McDonald WI, Miller DH. Correlation of magnetization transfer ratio with clinical disability in multiple sclerosis. *Ann Neurol* 1994;**36**: 62-67.

93. Gaillard WD, Hertz-Pannier, Mott SH, Cuenod CA, LeBihan D, Theodore WH. Functional magnetic resonance imaging and language dominance in children. *Epilepsia* 1996;**37**(suppl 4):37.

94. Desmond JE, Sum JM, Wagner AD, Demb JB, Shear PK, Glover GH, Gabrieli JDE, Morrell MJ. Functional MRI measurement of language lateralization in Wada-tested patients. *Brain* 1995;**118**:1411-1419.

95. Detre J, Sirven J, O'Connor M, French J. Localization of subclinical ictal activity by functional magnetic resonance imaging: correlation with invasive monitoring. *Ann Neurol* 1995;**38**:618-624.

96. Allen PJ, Polizzi G, Krakow K, Fish DR, Lemieux L. Identification of EEG events in the MR scanner: the problem of pulse artifact and a method for its subtraction. *Neuroimage* 1998;**8**:229-239.

97. Tofts PS. Novel MR image contrast mechanisms in epilepsy. *Magn Reson Imaging* 1995;**13**:1099-1106.

98. Grünewald RA, Jackson GD, Connelly A, Duncan JS. MR detection of hippocampal disease in epilepsy: factors influencing T2 relaxation time. *Am J Neuroradiol* 1994;**15**:1149-1156.

99. Duncan JS, Bartlett P, Barker GJ. Measurement of hippocampal T2 relaxation time - development and implementation of new techniques. *Am J Neuroradiol* 1996;**17**:1805-1810.

100. Beaulieu C, Fenrich FR, Allen PS. Multicomponent water proton transverse relaxation and T2-discriminated water diffusion in myelinated and nonmyelinated nerve. *Magn Reson Imaging* 1998;**16**:1201-10.

101. Rydberg JN, Hammond CA, Grimm RC, Bradley JE, Jack CR, Huston J, Riederer SJ. Initial clinical experience in MR-imaging of the brain with a Fast Fluid-attenuated Inversion-Recovery Pulse Sequence. *Radiology* 1994;**193**:173-180.

102. Bergin PS, Fish DR, Shorvon SD, Oatridge A, deSouza NM, Bydder GM. Magnetic resonance imaging in partial epilepsy: additional abnormalities shown with the fluid attenuated inversion recovery (FLAIR) pulse sequence. *J Neurol Neurosurg Psychiatry* 1995;**58**:439-443.

103. De Coene B, Hajnal JV, Pennock JM, Bydder GM. MRI of the brain stem using fluid attenuated inversion recovery pulse sequences. *Neuroradiology* 1993;**35**:327-331.

104. Listerud J, Mitchell J, Bagley L, Grossman R. OIL FLAIR: optimized interleaved fluid-attenuated inversion recovery in 2D fast spin echo. *Magn Reson Med* 1996;**36**:320-325.

105. Jack CR, Theodore WH, Cook M, McCarthy G. MRI-based hippocampal volumetrics: data acquistion, normal ranges, and optimal protocol. *Magn Reson Imaging* 1995;**13**:1057-1064.

106. Luby M, Spencer DD, Kim JH, DeLanerolle N, McCarthy G. Hippocampal MRI volumetrics and temporal lobe substrates in medial temporal lobe epilepsy. *Magn Reson Imaging* 1995;**13**:1065-1071.

107. Trenerry MR, Westerveld M, Meador KJ. MRI hippocampal volume and neuropsychology in epilepsy surgery. *Magn Reson Imaging* 1995;**13**:1125-1132.

108. Cascino GD. Clinical observations with hippocampal atrophy. *Magn Reson Imaging* 1995;**13**:1133-1136.

109. Meencke HJ, Veith G. Hippocampal sclerosis in epilepsy. In: Lüders H ed. *Epilepsy surgery.* Raven Press, New York 1991:705-715.

110. Hajnal JV, Doran M, Hall AS, Collins AG, Oatridge A, Pennock JM, Young IR, Bydder GM. MR imaging of anisotropically restricted diffusion of water in the nervous system: technical, anatomic, and pathologic considerations. *J Comput Assist Tomogr* 1991;**15**:1-18.

111. Anderson AW, Zhong J, Petroff OA, Szafer A, Ransom BR, Prichard JW, Gore JC. Effects of osmotically driven cell volume changes on diffusion-weighted imaging of the rat optic nerve. *Magn Reson Med* 1996;**35**:162-167.

112. Sevick RJ, Kanda F, Mintorovitch J, Arieff AI, Kucharczyk J, Tsuruda JS, Norman D, Moseley ME. Cytotoxic brain edema: assessment with diffusion-weighted MR imaging. *Radiology* 1992;**185**:687-690.

113. Zhong J, Petroff OA, Prichard JW, Gore JC. Changes in water diffusion and relaxation properties of rat cerebrum during status epilepticus. *Magn Reson Med* 1993;**30**:241-246.

114. Righini A, Pierpaoli C, Alger JR, Di Chiro G. Brain parenchyma apparent diffusion coefficient alterations associated with experimental complex partial status epilepticus. *Magn Reson Imaging* 1994;**12**:865-871.

115. Latour LL, Hasegawa Y, Formato JE, Fisher M, Sotak CH. Spreading waves of decreased diffusion coefficient after cortical stimulation in the rat brain. *Magn Reson Med* 1994; **32**:189-198.

116. Zhong J, Petroff OA, Prichard JW, Gore JC. Barbiturate-reversible reduction of water diffusion coefficient in flurothyl-induced status epilepticus in rats. *Magn Reson Med* 1995;**33**:253-256.

117. Nakasu Y, Nakasu S, Morikawa S, Uemura S, Inubushi T, Handa J. Diffusion-weighted MR in experimental sustained seizures elicited with kainic acid. *Am J Neuroradiol* 1995;**16**:1185-1192.

118. Ebisu T, Rooney WD, Graham SH, Mancuso A, Weiner MW, Maudsley AA. MR spectroscopic imaging and diffusion-weighted MRI for early detection of kainate-induced status epilepticus in the rat. *Magn Reson Med* 1996;**36**:821-828.

119. Wang Y, Majors A, Najm I, Xue M, Comair Y, Modic M, Ng TC. Postictal alteration of sodium content and apparent diffusion coefficient in epileptic rat brain induced by kainic acid. *Epilepsia* 1996;**37**:1000-1006.

120. Zhong J, Petroff OAG, Pleban LA, Gore JC, Prichard JW. Reversible, reproducible reduction of brain water apparent diffusion coefficient by cortical electroshocks. *Magn Reson Med* 1997;**37**:1-6.

121. Lynch LA, Lythgoe DJ, Haga EK, Smart SC, Beech JS, Millan M, Kinchesh P, Meldrum BS, Williams SCR. Temporal evolution of CNS damage in a rat model of chronic epilepsy. Proceeding of the International Society for Magnetic Resonance in Medicine, fourth scientific meeting. ISMRM, Berkeley, CA 1996:521.

Chapter 2

Fluid Attenuated Inversion Recovery prepared (FLAIR) Imaging in Epilepsy

2.1 FLAIR Imaging

2.1.1 Introduction

Conventional T2-weighted spin echo MR imaging (fig. 2.1) has been a mainstay of the evaluation of many pathologic processes of the brain.[1] Most of these processes (eg multiple sclerosis, infarction) increase the T2 relaxation times of the affected tissue, causing the lesion to have a signal intensity intermediate between those of CSF and normal grey or white matter on T2-weighted images. This intermediate signalintensity usually necessitates the acquisition of both T2- and proton density-weighted images for accurate interpretation, particulary when these lesion are close to CSF. A technique called fluid-attenuated inversion-recovery (FLAIR) (Picker, Cleveland, Ohio)[2,3,4] has been developed to solve this problem. FLAIR produces heavily T2-weighted CSF-nulled images by coupling an inversion pulse followed by long inversion time (TI), to a long echo time (TE) readout (fig.2.2). With nulling of the CSF, a tissue abnormality usually becomes the brightest object in these images, thereby enhancing its conspicuity. Furthermore, while the length of the TE used in T2-weighted SE imaging is limited by the increasing artifact and partial voluming effects of CSF as the TE is increased,[5] these longer TEs can be used in FLAIR, and images can thus be acquired with greater T2-weighting, because the CSF signal is nulled out. Although FLAIR has had great success in displaying lesion not seen with conventional T2-weighted sequences,[6] it has been limited by long acquistion times caused by the long TIs and long repetition times (TRs) required to both null CSF and allow non-CSF tissues adequate signal recovery before readout. For example, 13 minutes is required to

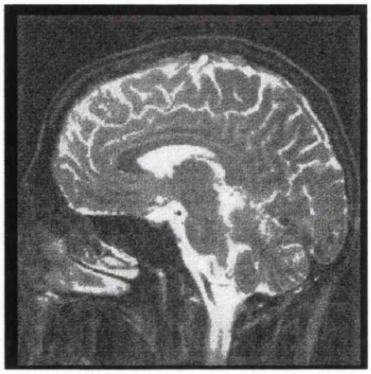

Figure 2.1 - sagittal FSE T2-weighted image of a normal control subject. CSF returns a high signal on the FSE T2-weighted images.

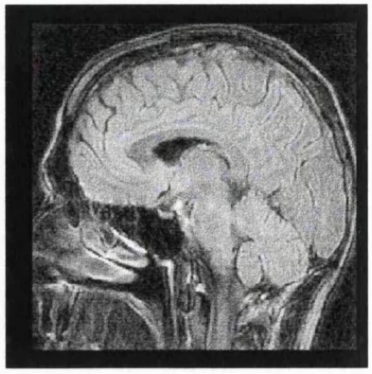

Figure 2.2 - Fast FLAIR images of the same control subject as in fig. 2.1. The signal from CSF is suppressed ("nulled").

obtain 10 images with a resolution of 128 x 256 with use of a 6000/160/2100 (TR msec/TE msec/TI msec) sequence. However, the FLAIR technique has been constantly improved since the first publications in 1992. The acquisition time has been reduced with the rapid acquisition with relaxation enhancement (RARE) readout in fast FLAIR (1994),[7] with interleaved inversion pulses in OIL FLAIR (1996)[8] and with echo-planar imaging (EPI) FLAIR (1997).[9] The constrast has been optimized for the detection of lesions (1995).[10] A 3D version of FLAIR (1997)[11] providing thin slices without interslice gap has been developed at the Institute of Neurology. We evaluated 2D fast FLAIR in epilepsy using a large group of patients from a tertial referral centre for epilepsy,[12] and applied the new 3D FLAIR version on 10 selected patients with typical structural abnormalities to obtain inital experience.[13]

Imaging in Epilepsy with a fast FLAIR sequence

2.2.1 Introduction

In a small study using the original version of FLAIR in patients with partial epilepsy several additional abnormalities had been detected.[14] However, the long acquisition time of this version of FLAIR limited the application to highly selected

patients who were motivated and able to cooperate. With fast FLAIR images covering the whole head can be acquired in 8 minutes, which makes the application of FLAIR possible in virtually all patients with epilepsy. The aim of our study was to assess the diagnostic value of this fast FLAIR sequence in epilepsy. We compared fast FLAIR with a protocol of sequences which has been especially developed in recent years for patients with epilepsy.

2.2.1 Material and methods

2.2.1.1 Patients and controls

One-hundred and twenty-eight consecutive adult patients attending a tertiary referral centre for epilepsy were included in the study. Classification of the epileptic seizures was based on electro-clinical data.[15] Twenty patients had epilepsy with generalized seizures, 98 had epilepsy with partial seizures and 10 had non-classified epilepsy. Ten normal control subjects were also evaluated.

2.2.1.2 MR imaging

We used a 1.5-Tesla GE signa scanner (GE Medical Systems, Milwaukee, WI) and scanned all subjects with the following sequences: 1. Spin echo (SE) T1- weighted (TR/TE/NEX 620/16/1) sagittal sequence, 256 x 256 matrix and 24 x 24 cm field of view (FOV), 5 mm slice thickness, 2.5 mm interslice gap. 2. Inversion recovery prepared fast spoiled gradient echo (IRSPGR) (predominantly) T1- weighted (TR/TE/TI/NEX 17.4/ 4.2/ 450/1, flip angle 20^0) coronal sequence, 256 x 192 matrix, 24 x 18 cm FOV, 1.5 mm slice thickness, 3 dimentioned acquisitions. 3. Fast spin echo (FSE) mild and heavily T2-weighted (TR/TEef1/TEef2/NEX 2000/38/95/1) coronal sequence, 256 x 192 matrix, 24 x 18 cm FOV, 5 mm slice thickness, no gap (81 patients, all controls) or spin echo (SE) (TR/TE1/TE2/NEX 2000/30/120/1) weighted coronal sequence, 256 x 192 matrix, 24 x 18 cm FOV, 5 mm slice thickness, no gap (47 patients, 2 controls). Images were obtained perpendicular to an axis drawn from the orbitofrontal cortex to the splenium,

which is approximately parallel to the long axis of the hippocampus. 4. Fast FLAIR (TR/TEef/TI/NEX 11000/164/2600/1) coronal sequence, 256 x 192 matrix and 24 x 18 cm FOV with 5 mm slice thickness, no gap. Forty two images covering the whole brain were obtained in 8 minutes. Images were obtained using the same plane as in 3. Volumetric measurements of the hippocampi and the intra-cranial space were performed on the IRSPGR T1-weighted images and the hippocampal volume was corrected for the intracranial volume using methods described previously.[16] Clear-cut unilateral hippocampal sclerosis (HS) was defined as asymmetry of more than 20%. Borderline hippocampal atrophy was defined as asymmetry between 10% and 20%. Hippocampal volumes were corrected for intra-cranial volume to identify bilateral HS. Bilateral HS was defined as a volume more than 2 standard deviations smaller than the mean hippocampal volume of a normal control group on both sides.[17] IRSPGR T1-weighted images with 1.5 mm slices, SE-, or FSE-images along with the volumetric measurements were regarded as the "standard protocol". Images of all sequences were compared by an unblinded neuroradiologist (J.S.) and a neurologist (U.W.). In addition, two blinded independent raters (S.F., A.E.) inspected only the fast FLAIR images of 40 subjects. Twenty subjects had abnormal hippocampal volumes on measurement, 17 had unilateral small hippocampal volumes with asymmetry >10%, 2 had bilateral symmetrical small hippocampal volumes and 1 had bilateral small volumes in addition to asymmetry. Twenty subjects had normal hippocampal volumes on measurement (10 control subjects and 10 patients) to evaluate the detectability of HS on fast FLAIR images. To evalute the conspicuity of HS on fast FLAIR images they compared fast FLAIR and T2-weighted FSE and SE T2-weighted images of 23 patients with known HS (detected by volumetric measurement) on a different day.

2.2.2 Results

2.2.2.1 Controls

The standard protocol was normal in all 10 control subjects. On fast FLAIR images

the temporo-mesial structures returned a higher signal than the cortex of the cerebral convexities in 7 of 10 controls. Two of these 7 control subjects were rated as abnormal by the blinded raters when they rated fast FLAIR images in isolation from other data. Although CSF suppression was generally excellent, high signal was present around the basal cisterns, the wall of the ventricles and the aqueduct. In 4 control subjects the whole third ventricle returned a high signal. The white matter adjacent to the occipital horn and the CSF adjacent to the choroid also returned a high signal. The gray matter/white matter contrast was generally lower than on T1- or T2- weighted images. The white matter returned a more heterogenous signal on fast FLAIR, with a higher signal being evident in 9 controls in the expected position of the cortico-spinal tract.

2.2.2.2 Patients

2.2.2.2.1 Neocortical lesions detected by the standard protocol

A non-dysgenetic neocortical lesion was shown in 22 patients by the standard protocol. (traumatic damage (n=5), presumed glioma (n=2), non-specific damage (n=10), temporal lobectomy (n=3), Sturge-Weber Syndrome (n=1), cyst (n=1), additional HS was present in 4 patients.) The lesions were more conspicuous on fast FLAIR images and the extent of the lesion was clearly shown. However, similar information could be obtained from conventional T1- and T2-weighted images when viewed in combination.

2.2.2.2.2 Dysgenetic lesions detected by the standard protocol

In 13 patients a probable dysgenetic lesion was visible (presumed band heterotopia (n=3), presumed nodular subependymal heterotopia (n=3) one with additional borderline hippocampal atrophy, polymicrogyria (n=1), schizencephaly (n=1), frontal pachgyria (n=1), presumed hypothalmic hamartoma (n=2), presumed dysembryoplastic neuroepithelial tumour (DNT) (n=2)). The schizencephaly was evident on every sequence. On fast FLAIR images hypothalamic hamartoma and

DNT returned a high signal (fig. 2.3). Both were more conspicuous on fast FLAIR than on IRSPGR T1-weighted images. However, band heterotopia and nodular subependymal heterotopia were less conspicuous on fast FLAIR than on coronal IRSPGR T1-weighted images with 1.5 mm slices or proton-density weighted images and could have easily been overlooked (fig. 2.4 and fig. 2.5). Polymicrogyria and pachgyria were also less conspicuous on fast FLAIR.

2.2.2.2.3 Normal standard MR imaging

The standard images of 58 patients were reported as normal. In 3 out of these 58 patients a small area of high signal was detected on fast FLAIR images. In all 3 patients slight signal changes were also identified on the proton-density and T2-weighted images but considered not to be clearly abnormal. In one case the area of signal change agreed with the clinical and EEG localization of seizure onset (fig. 2.6). In the other cases the epilepsy had been classified as generalized.

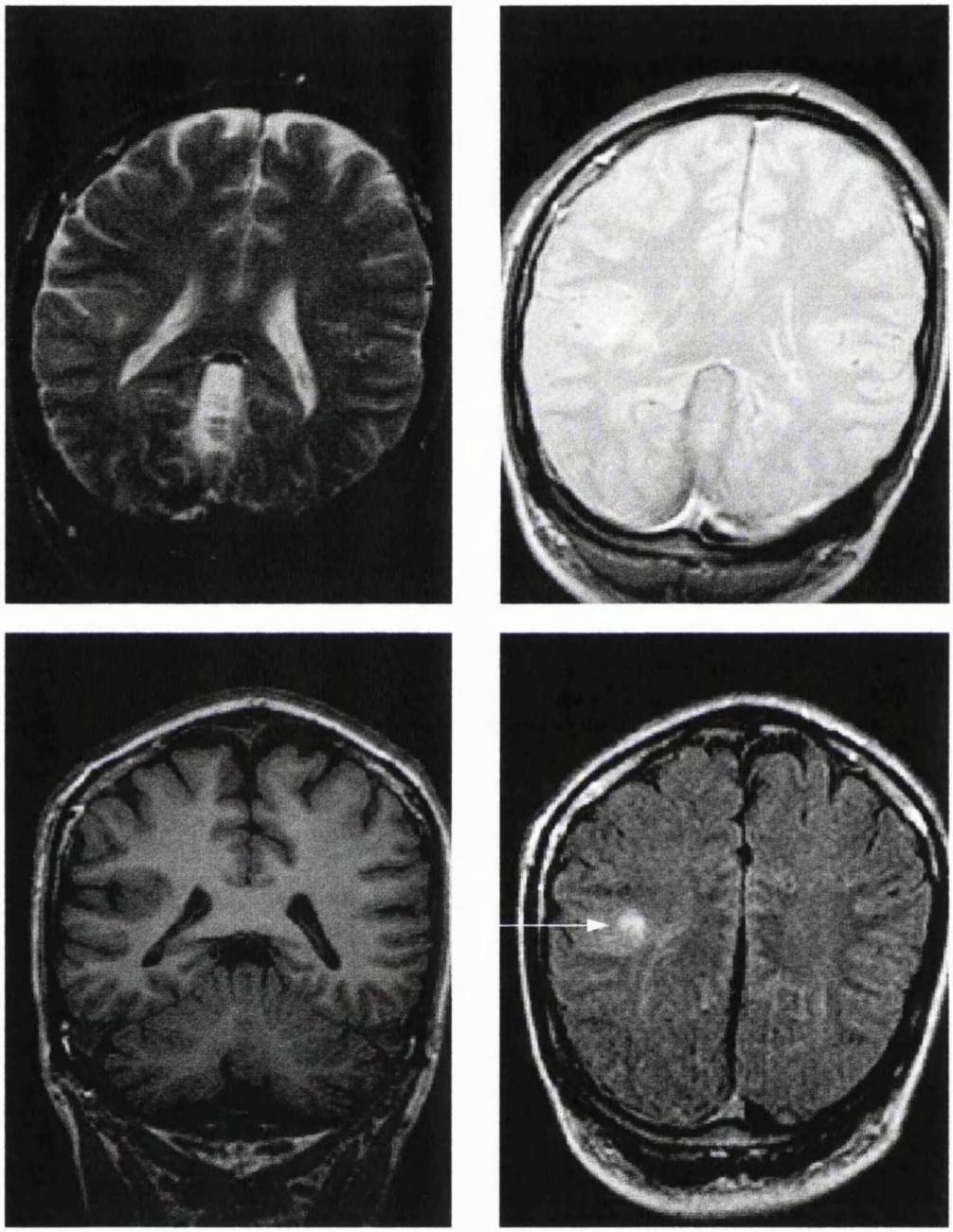

Figure 2.3 - Presumed DNT. Coronal spin echo T2-weighted image (top left), proton density weighted image (top right), T1-weighted image (bottom left) and fast FLAIR image (bottom right). A small cortical mass is shown in the right posterior temporal lobe. The signal intensity change is most conspicuous on fast FLAIR. The patient had partial epilepsy.

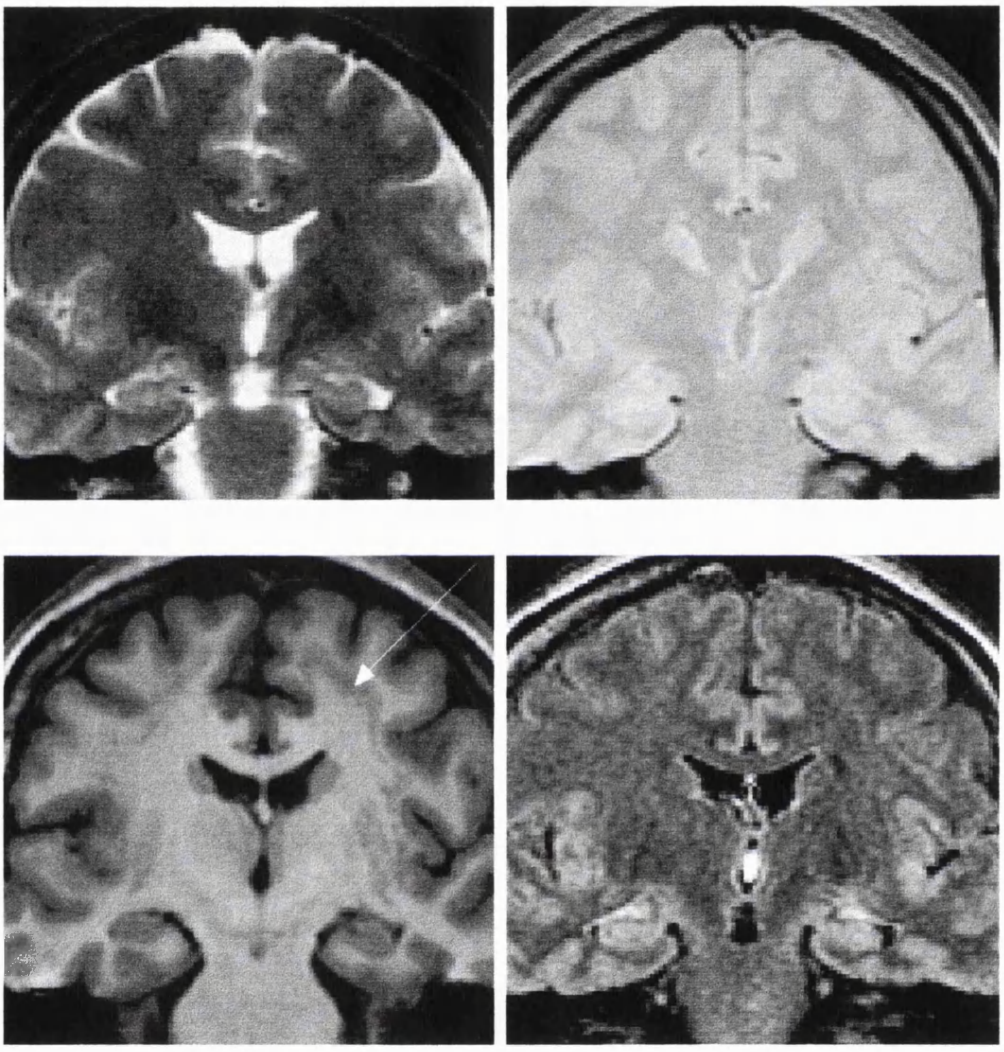

Figure 2.4 - BAND HETEROTOPIA. Coronal spin echo T2-weighted image (top left), proton density weighted image (top right), T1-weighted image (bottom left) and fast FLAIR image (bottom right). A band of ectopic grey matter underlying the cortex ("double cortex") is shown (arrow). The abnormality is bilateral and fairly symmetric. The heterotopic grey matter is most conspicuous on the T1-weighted image and could be overlooked on fast FLAIR. The patient had partial epilepsy.

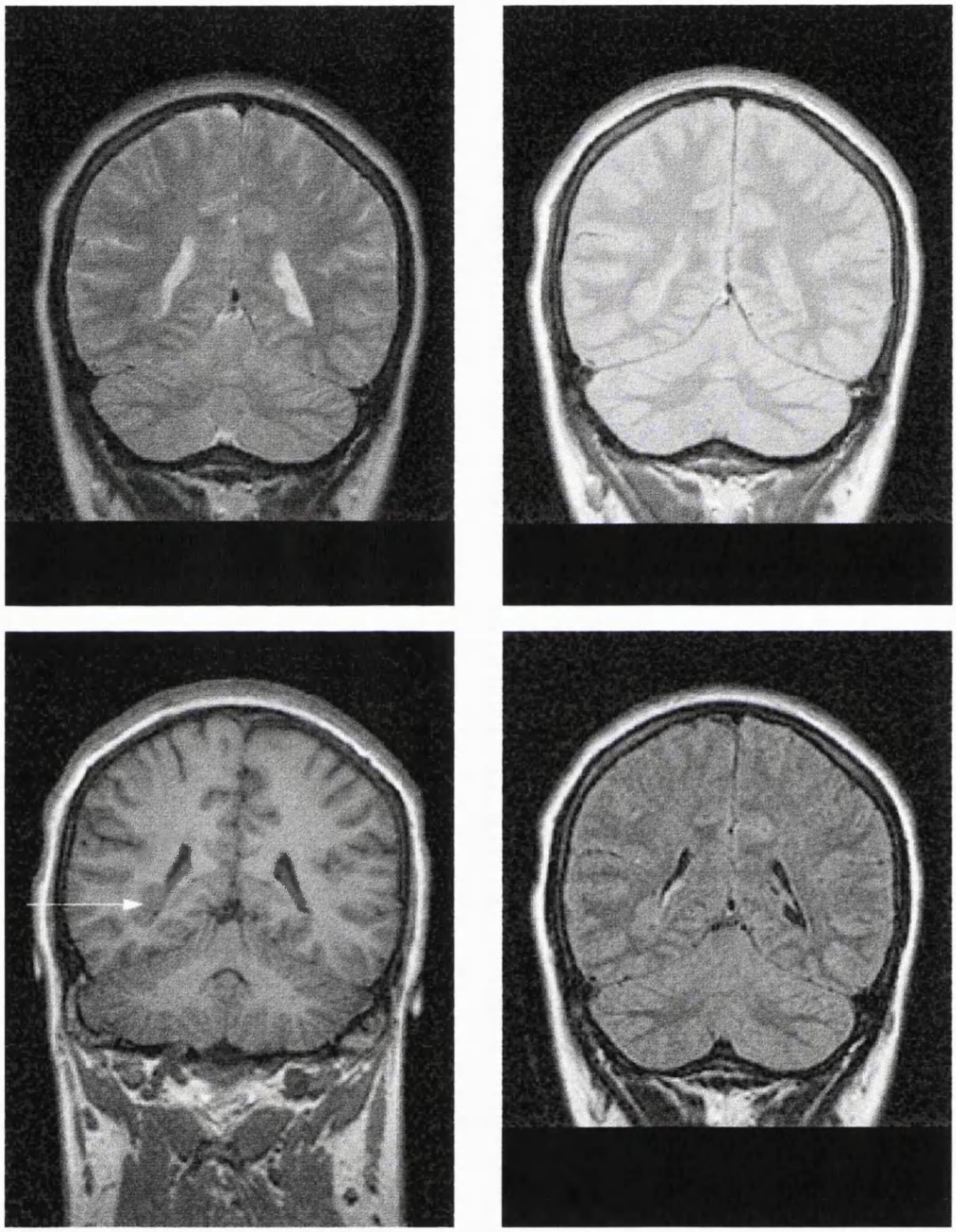

Figure 2.5 - NODULAR SUBEPENDYMAL HETEROTOPIA. Coronal spin echo T2-weighted image (top left), proton density weighted image (top right), T1-weighted image (bottom left) and fast FLAIR image (bottom right). Ectopic grey matter is shown adjacent to the right ventricle (arrow). The signal intensity of the ectopic grey matter is similar to normal greymatter and not more conspicuous on fast FLAIR. The patient had partial epilepsy.

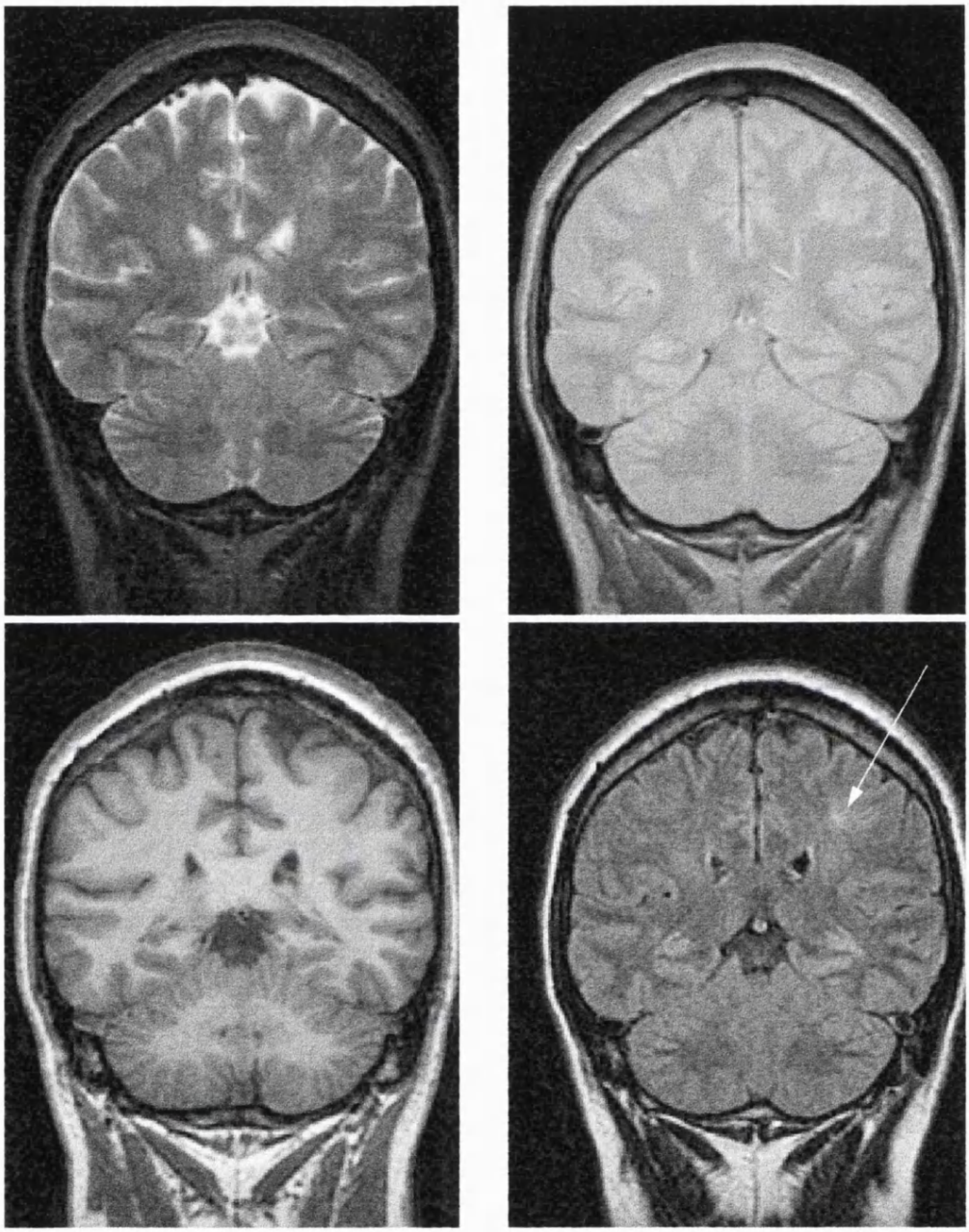

Figure 2.6 - NORMAL STANDARD IMAGING. Coronal spin echo T2-weighted image (top left), proton density weighted image (top right), T1-weighted image (bottom left) and fast FLAIR image (bottom right). A small area returning a high signal is visible on fast FLAIR (arrow). Slight signal changes on the proton-density and T2-weighted images in this area are not clearly abnormal. The patient had frequent simple partial seizure with tingling on the right side, the EEG changes were in keeping with a left seizure focus.

2.2.2.2.4 Hippocampal sclerosis

The volumes of 35 patients were abnormally small suggesting hippocampal sclerosis (HS). (28 patients had unilateral clear-cut HS, four patients had unilateral borderline hippocampal atrophy, 3 patients had bilateral HS). On fast FLAIR images the sclerotic hippocampus returned a high signal and was usually more conspicuous than on SE-T2 weighted images because the CSF of the temporal horn was suppressed (fig 2.7 and fig 2.8). However, the CSF suppression was not complete in every case and the choroid plexus often also returned a high signal. In addition, both mesio-temporal regions were brighter than the neocortex in normal control subjects as well as in the patients. We assessed detectability of HS with the help of two blinded raters (SF, AE) using the images of 20 randomly chosen HS cases (13 clear-cut HS, 4 borderline atrophy and 3 bilateral HS) and 20 normal cases (10 normal controls and 10 patients, all with normal hippocampal volumes) were rated. The raters detected all but one of the clear-cut HS cases. The case they missed had also a normal signal on SE T2-weighted images to visual inspection. They missed all cases with borderline hippocampal atrophy, one rater missed one bilateral case and both raters had 2 false-positive results. To assess the conspicuity of HS on fast FLAIR images the 2 blinded raters compared fast FLAIR and FSE T2-weighted images of 23 randomly chosen HS cases (unilateral volume loss ranging from 20% to 53% in 22, one with bilateral HS) on a different day. In three cases the raters felt that visual assessment was difficult (the reasons were movement artefacts, bilateral HS and images not imaged in standard size) and the patients were excluded. In more than 50% of the remaing 20 patients HS was more conspicuous on fast FLAIR (rater A.E. 11 of 20, rater S.F. 18 of 20). There was agreement between the raters in 9 patients.

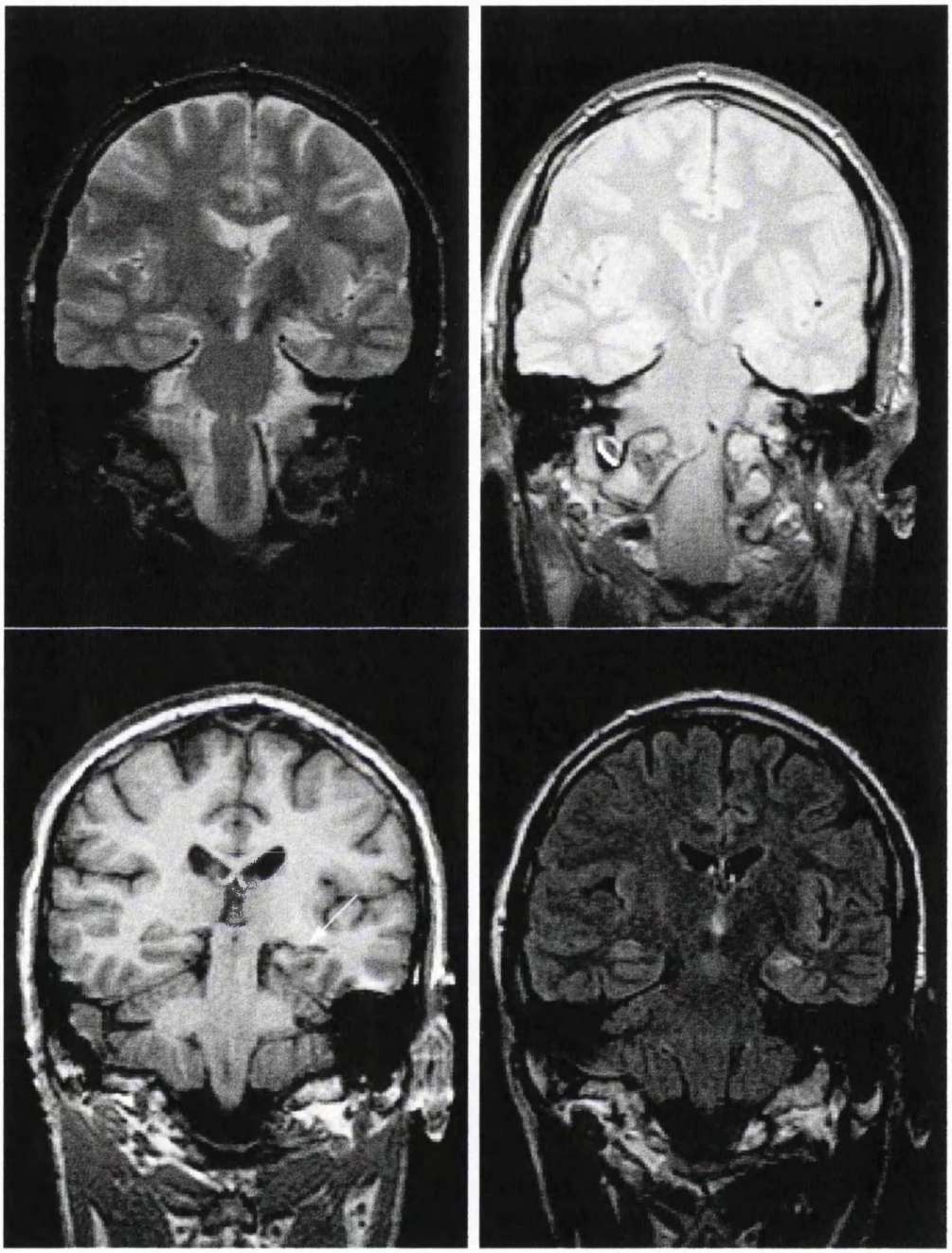

Figure 2.7 - Left HIPPOCAMPAL SCLEROSIS. Coronal images of the hippocampal body. Spin echo T2-weighted image (top left), proton density weighted image (top right), T1-weighted image (bottom left) and fast FLAIR image (bottom right). The left hippocampus (arrow) is smaller than the right and returns a high signal on T2-weighted images. This is most conspicous on fast FLAIR since CSF signal has been suppressed.

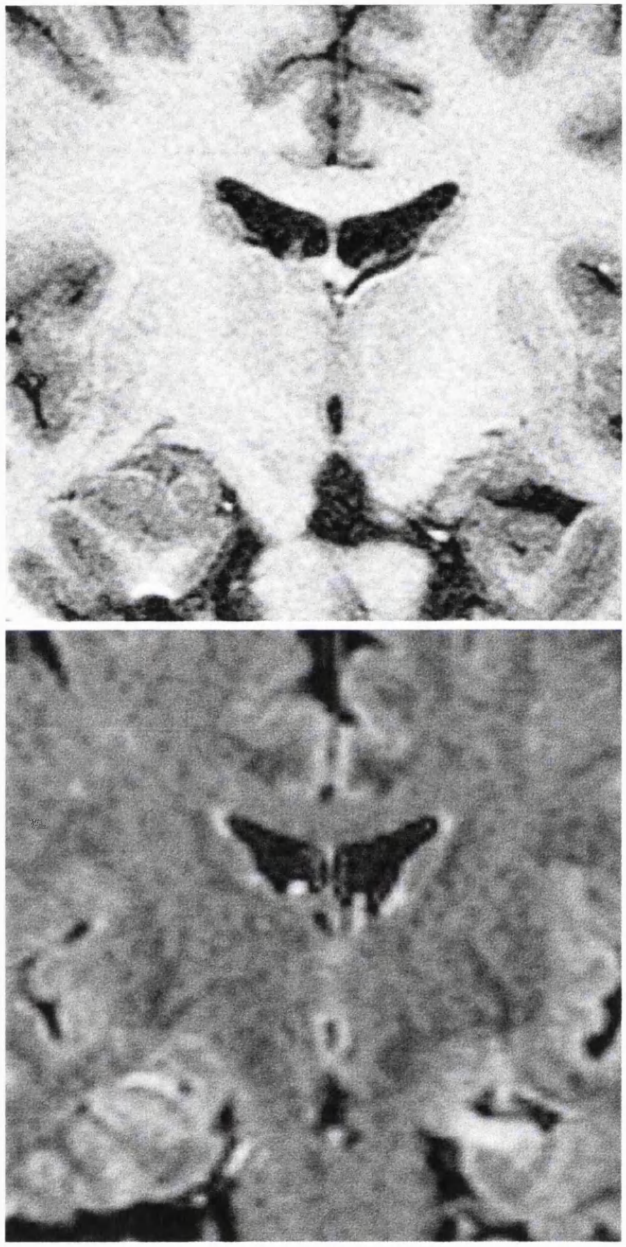

Figure 2.8 - Left HIPPOCAMPAL SCLEROSIS. Coronal images of the hippocampal head. High resolution T1-weighted images (upper) and fast FLAIR images (lower). The left hippocampus is smaller than the right and returns a high signal on fast FLAIR. The patient had temporal lobe epilepsy and later underwent a left temporal lobe ectomy. Hippocampal sclerosis was histological confirmed.

Tab. 2.1 Appearance of lesions associated with epilepsy on fast FLAIR

lesion	appearance on fast FLAIR
hypothalamic hamartomas	more conspicuous than SE-T2
DNT	more conspicuous than SE-T2
low grade glioma	more conspicuous than SE-T2
brain damage	more conspicuous than SE-T2
Sturge Weber Syndrome	cortical lesion conspicuous
clear-cut HS	high signal in all but one case
borderline hippocampal atrophy	signal similar to controls
schizencephaly	detectable, but not conspicuous
heterotopic gray matter	not conspicuous
pachygyria, polymicrogyria	difficult to detect

clear-cut HS = hippocampal sclerosis with asymmetry >20%, borderline hippocampal atrophy = with asymmetry of 10-20% on volumetric measurement. DNT = dysembryoplastic neuroepithelial tumour.

2.2.3 Discussion

The capability of fast FLAIR to demonstrate structural abnormalities varied considerably and depended on the aetiology. Neocortical brain damage and lesions diagnosed as presumed hamartomas and DNT were always more conspicuous on fast FLAIR. Takanashi et al reported a similar result for the detection of tubers in tuberous sclerosis.[18]

Fast FLAIR was inferior to coronal IRSPGR T1-weighted images with 1.5mm slices in detecting nodular subependymal heterotopia and laminar heterotopia because of the low grey-matter white-matter contrast, and fast FLAIR was inferior to IRSPGR T1-weighted images in detecting polymicrogyria and pachygyria because of the thicker slices. Heterotopia, polymicrogyria and pachygyria often

underlie apparent "cryptogenetic"epilepsy.[19] Heterotopia may be associated with HS,[20] as in one of our cases. The detection or exclusion of heterotopia is important in the presurgical evaluation since patients with heterotopia are often are not seizure free after temporal lobectomy,[21] Thus fast FLAIR cannot replace IRSPGR with thin slices in the investigation of patients with epilepsy.

Clear-cut HS (asymmetry > 20%) was detectable on fast FLAIR images in nearly all cases, because of the high signal returned by the sclerotic hippocampus. HS usually is associated with a high signal on T2-weighted images[22] making an abnormality on T2-weighted images an important diagnostic criterion for HS. In most, but not all, cases clear-cut HS was more conspicuous on fast FLAIR images than on SE or FSE T2-weighted images. In theory, a hippocampus with a high T2-signal should be the brightest (and most conspicuous) object on fast FLAIR images because the CSF signal of the temporal horn should be suppressed. On SE T2-weighted images the CSF of the temporal horn returns high signal which has to be distinguished from the hippocampal signal. Thus, HS should always be more conspicuous on fast FLAIR images compared to SE T2-weighted images. However, on some fast FLAIR images the CSF suppression was incomplete in the temporal horn and the choroid plexus also returned a high signal; in these cases the sclerotic hippocampus was not more conspicuous on fast FLAIR images than the T2-weighted images. One patient with clear-cut HS on volumetric measurements was missed by the two raters because the signal was not abnormal. This case had also a normal signal on visual inspection of SE-T2 weighted images but in fact yielded a measured T2 value on subsequent T2 mapping which was outside the normal range. Nevertheless, HS is not in every case associated with a change in T2 relaxation and an increased signal is not specific for sclerosis but may also occur in other types of pathology such as neoplasias and dysplasia. Therefore, the estimation of

hippocampal volume loss which is associated with HS, either visually or with volume measurements is equally important. Volume loss was not reliable assessable on fast FLAIR images because of the relatively low resolution and the large slice thickness (5mm). In addition to these problems the raters failed to recognize all cases of borderline hippocampal atrophy (asymmetry 10%-20%) on fast FLAIR images and called two false positive results. This may be explained by the fact that the mesio-temporal region was always brighter than the neocortex on fast FLAIR images and there was a high interindividual variability in signal intensity in control subjects making it difficult to decide whether the signal was pathological in borderline cases. HS is the most common lesion in temporal lobe epilepsy. The probability of a seizure-free outcome following temporal lobectomy is greater for patients with HS than for patients with normal histologic findings.[23] MRI with contiguous thin coronal T1-weighted images and coronal T2-weighted images[24] improves the sensitivity of detecting HS, and further improvement is possible using quantitative methods like volumetric measurements and T2-mapping.[25,26] Fast FLAIR increases the conspicuity of clear-cut HS but in this study it seemed not to be as sensitive as quantitative methods, and although fast FLAIR indeed may be useful for MRI units which lack the resources to carry out adequate quantitation, borderline hippocampal atrophy and bilateral HS will remain difficult to detect.

Usually, an abnormal fast FLAIR signal was associated with abnormalities on the other sequences. In only 3 cases fast FLAIR showed a clearly abnormal signal, when SE T2-weighted images were suspicious but not definitely abnormal. In contrast to this result, Bergin et al reported additional lesions detected by FLAIR in 30% of their cases. The different findings of the two studies may be explained by several factors. Firstly, Bergin et al implemented the sequence differently, using a 1.0 tesla Picker MR-scanner, their TR value was half as long as ours and they did not employ the RARE readout. The TR and TE values used in our sequence have been optimized for the detection of white matter lesions in multiple sclerosis but may have been suboptimal in the detection of lesions relevant in epilepsy. The echo-spacing of the RARE readout may also have been suboptimal in our sequence perhaps causing edge-related artefacts.[27] Secondly, Bergin et al in their smaller

study without control subjects described lesions in the amygdala and the adjacent hippocampus (accounting for 5 of 11 additional cases). With the fast FLAIR sequence we observed a high interindividual signal variation in the temporo-mesial region in control subjects. The temporo-mesial region also returned a higher signal than the neocortex on fast FLAIR images in control subjects. Consequently, slight signal changes in the amygdala were not regarded as abnormal in our study. Probably most important however, is that we compared the fast FLAIR with a different protocol of sequences than Bergin et al. We applied a volume acquisition sequence with a slice-thickness of 1.5 mm, performed hippocampal volumetric measurements and obtained the T2-weighted images perpendicular to the long axis of the hippocampus. Bergin et al used T1- and T2-weighted axial and coronal sequences with 6mm slice-thickness. The sensitivity for HS is higher on sequences with thin slices. Thus, the chance to detect additional HS with fast FLAIR was lower in our study.

2.2.4. Conclusion

The major advantages of fast FLAIR are increased conspicuity of neocortical lesions and clear-cut unilateral HS, fast FLAIR may also demonstrate lesions when other sequences are normal in a limited number of cases. Heterotopia, borderline hippocampal atrophy and subtle cortical dysplasia may be missed on fast FLAIR.

2.3 Fast Fluid-attenuated Inversion-Recovery Imaging: First Experience with a 3D Version in Epilepsy

2.3.1 Introduction

In the 2D implementation of the FLAIR technique the slice thickness was relatively large (3mm or more). It would be desirable to decrease the slice thickness since the yield of MRI in epilepsy can be increased if thin slices are used. In standard, 2D, FLAIR imaging the application of thinner slices is not only limited by crosstalk but also by the limitations of the CSF suppression technique. On thin slices inflowing unsuppressed CSF into the slice results in incomplete CSF

suppression. A 3D acquisition technique has certain advantages compared to a 2D technique. By phase-encoding in the slice direction the reduced gradient strength requirements of phase encoding relative to (thin) slice selection allow the "slice thickness" to be reduced and the 3D acquisition improves the signal to noise ratio.[28] Theoretically an inversion pulse applied to the whole slab rather than a slice will also reduce the artefacts of inflowing unsuppressed CSF. Unfortunately a "true" 3D FLAIR sequence acquiring all the data in one slab would have a very long acquisition time. Currently, a technique available for FSE obtains 3D data in a reasonable scan time using long echo train lengths (ETL) and a hybrid 2D/3D acquisition scheme.[29] Within a slab (of 10 "slices"), it can be thought of as a 3D technique, as phase-encoding is done in the z-direction. However, many slabs are excited (16 for the 96 slice version used here) within each TR period, in a 2D manner. These are concatenated in the z-direction in a similar manner to normal multi-slice data. The 3D FSE sequence was modified by our group to perform 3D fast FLAIR by implementing the Inversion Recovery pulses in an optimised interleaved scheme. The sequence has been described elsewhere.[30] Since a very long echo-time is desirable for contrast reasons in fast FLAIR, (unlike many FSE applications) the use of a long ETL with fast FLAIR is not a disadvantage. However, the implementation of the hybrid 2D/3D technique to fast FLAIR has certain implications. Like all 3D techniques, the hybrid 2D/3D technique is susceptible to "wraparound" artefacts, which means that some slices at each end of each slab have to be dropped. This gives a ~30% reduction in acquisition efficiency and may generate a bandlike artefact at slab interfaces on reformatted images.[31] Our current implementation of 3D fast FLAIR uses a relatively short TR (4600 ms) which makes the sequence more efficient with regard to scanning time. However, this affects the contrast, which may limit the usefulness of 3D fast FLAIR compared to the established 2D sequence with a long TR (11000 ms). To evaluate the usefulness of 3D fast FLAIR we scanned 10 patients with lesions on standard spin echo magnetic resonance imaging with the 3D fast FLAIR, 2D fast FLAIR and a "true" 3D gradient echo sequence.

2.3.2 Methods

Ten patients with focal epileptic seizures and known lesions on spin echo magnetic resonance images were included. The lesions were head injury n=1, hippocampal sclerosis n=2, low grade glioma n=2, dysembryoplastic neuroepithelial tumour (DNT) n=2, polymicrogyria n=1, perinatal infarct n=1, presumed thrombosed aneurysm n=1. In one patient with hippocampal sclerosis and one patient with DNT the diagnosis was histologically confirmed. MRI scans were performed on a 1.5 T scanner (Signa Horizon, Echospeed, GE Medical Systems, Milwaukee, WI). The 2D fast FLAIR images were obtained coronally oblique perpendicular to an axis from the orbitofrontal cortex to the splenium, which is approximately parallel to the long axis of the hippocampus. The 3D fast FLAIR images and the 3D IRSPGR images were obtained coronally. 3D fast FLAIR and 2D fast FLAIR images and 3D fast FLAIR and 3D IRSPGR images were compared. Lesion detectability, lesion conspicuity, contrast for tracts and cranial nerves, grey matter-white matter contrast, CSF suppression and artefacts were visually assessed by a neuroradiologist and a neurologist. In addition 3D fast FLAIR and 3D IRSPGR images were reformatted on a separate workstation to visualize the extent of lesions (Advantage Windows, GE Medical Systems, Milwaukee, WI). The standard SE MRI sequences were a sagittal spin echo (SE) T1-weighted sequence (TR/TE/NEX 620/16/1), FOV 24 x 24 cm, matrix 256 x 256, slice thickness 5 mm, interslice gap 2.5 mm and a coronal oblique SE T2-weighted sequence (TR/TE1/TE2/NEX 2000/30/120/1), matrix 256 x 192, FOV 24 x 18 cm, contiguous 5 mm thick slices. The T2 weighted images were obtained in the same orientation as the 2D fast FLAIR images. Table 2.2. shows the scanning parameters of 2D and 3D FLAIR and IRSPGR.

Table 2.2. Scanning parameters

	2D fast FLAIR	3D fast FLAIR	3D IRSPGR
TR[ms]	11000	4600	17.4
TE[ms]	144(eff)	136(eff)	4.2
TI[ms]	2600	1739	450*
ETL	8	24	na
bandwidth[kHz]	7.81	31.8	10.4
number of slices	42	96	124
number of slabs	na	16(in 2 acquisitions)	1
slices per slab	na	10(6 used)	128(124 used)
slicethickness[mm]	5	1.5	1.5
FOV[cm]	24x18	25x25	24x18
matrix	256x192	256x192	256x192
pixel dimensions[mm]	0.9375x0.9375	0.9766x1.302, acquired 0.9766x0.9766, reconstructed	0.9375x0.9375
NEX	1	1	1
scan time [min]	8	12	8

* Note that this is not a FLAIR CSF suppression pulse, but gives increased T1-weighting. TR=repetition time, TE = echo time, (eff) = effective, TI = inversion time, ETL = echo train length, FOV = field of view, NEX = number of excitations, na = not applicable.

2.3.3 Results

CSF suppression was excellent on both 2D and 3D fast FLAIR. The walls of the ventricles on the 3D fast FLAIR images returned a high signal, as on 2D fast FLAIR. On 3D fast FLAIR subtle bandlike "Venetian blind" artefacts were visible on slab interfaces in the skull on reformatted images orthogonal to the imaging plane. This is a recognised characteristic of multi-slab acquisition methods. However, only minor artefacts were visible within the brain. If the patient had moved between acquisitions images of first and second acquisition were not aligned, consequently reformatting resulted in artefacts which appeared as "steps" in the skull and distortion of anatomical structures. This problem occurred in one

patient. In the remaining patients reformatted images of diagnostic quality could be obtained. Grey matter-white matter contrast and the contrast for the myelinated tracts was higher on 2D than on 3D fast FLAIR. As reported previously the mesiotemporal region returned a higher signal than the neocortex on 2D fast FLAIR. This was not the case on 3D fast FLAIR. Fat returned a high signal on 3D fast FLAIR but a low signal on 2D fast FLAIR. Cranial nerves returned a low signal on both 3D and 2D fast FLAIR. The optic nerve was very conspicuous on 3D fast FLAIR because of the high contrast between nerve and the intraorbital fat. On 2D fast FLAIR the optic nerve was less conspicuous. The conspicuity of the trigeminal and acoustic nerves in their extra-cerebral course was low on both 2D and 3D fast FLAIR.

All lesions detected on standard SE MRI were also visible on 2D and 3D fast FLAIR. Tumours, hippocampal sclerosis and traumatic brain damage all returned a high signal on both 2D and 3D fast FLAIR. In the patient with presumed traumatic brain damage a second small area returning a high signal in the frontal lobe, presumably also of traumatic origin, was detectable on 3D fast FLAIR. This lesion was only retrospectively visible on 2D fast FLAIR images and had also been overlooked on the standard MRI images. The abnormal hippocampus in hippocampal sclerosis returned a high signal on both 2D and 3D FLAIR rendering hippocampal sclerosis more conspicuous on FLAIR than on IRSPGR images. However direct comparison of 2D and 3D FLAIR revealed that hippocampal sclerosis was less conspicuous on 3D than on 2D fast FLAIR. Tumours were the brightest object on both 2D and 3D fast FLAIR images rendering tumours more conspicuous than on standard spin echo and IRSPGR images. The tumours were better demarcated on 3D FLAIR than on the T1-weighted 3D IRSPGR sequence.

On reformatted 3D IRSPGR the extent was difficult to assess because the signal intensity of tumours and grey matter was similar (fig. 2.9). The extent of the abnormal signal could be visualized in all dimensions on reformatted 3D fast

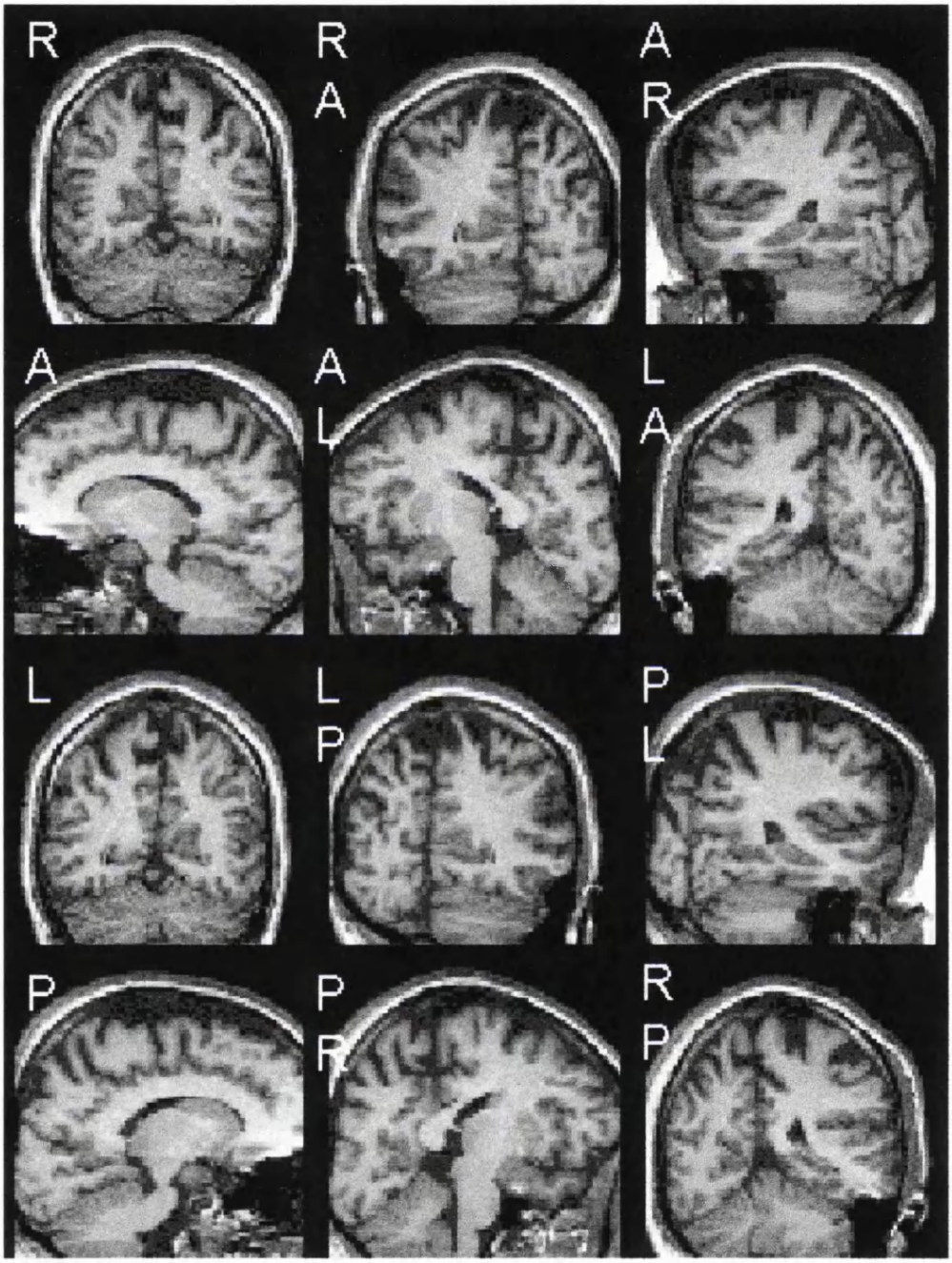

Figure 2.9 - REFORMATTED 3D IRSPGR images (predominantly T1-weighted); the 3D data set has been rotated 360° in steps of 30° around the vertical axis. The cortex around the right calcarine sulcus is thicker than the cortex around the left calcarine sulcus but no clear-cut abnormality is visible. R=right, L=left, A=anterior, P=posterior

FLAIR images (fig. 2.10). In a tumour with a cystic appearance on standard imaging 3D fast FLAIR allowed to distinguish between CSF-filled cyst and non CSF-filled lesion (fig. 2.11).The consequences of a perinatal infarct with loss of brain tissue and cerebral atrophy was visible on both 3D and 2D fast FLAIR.

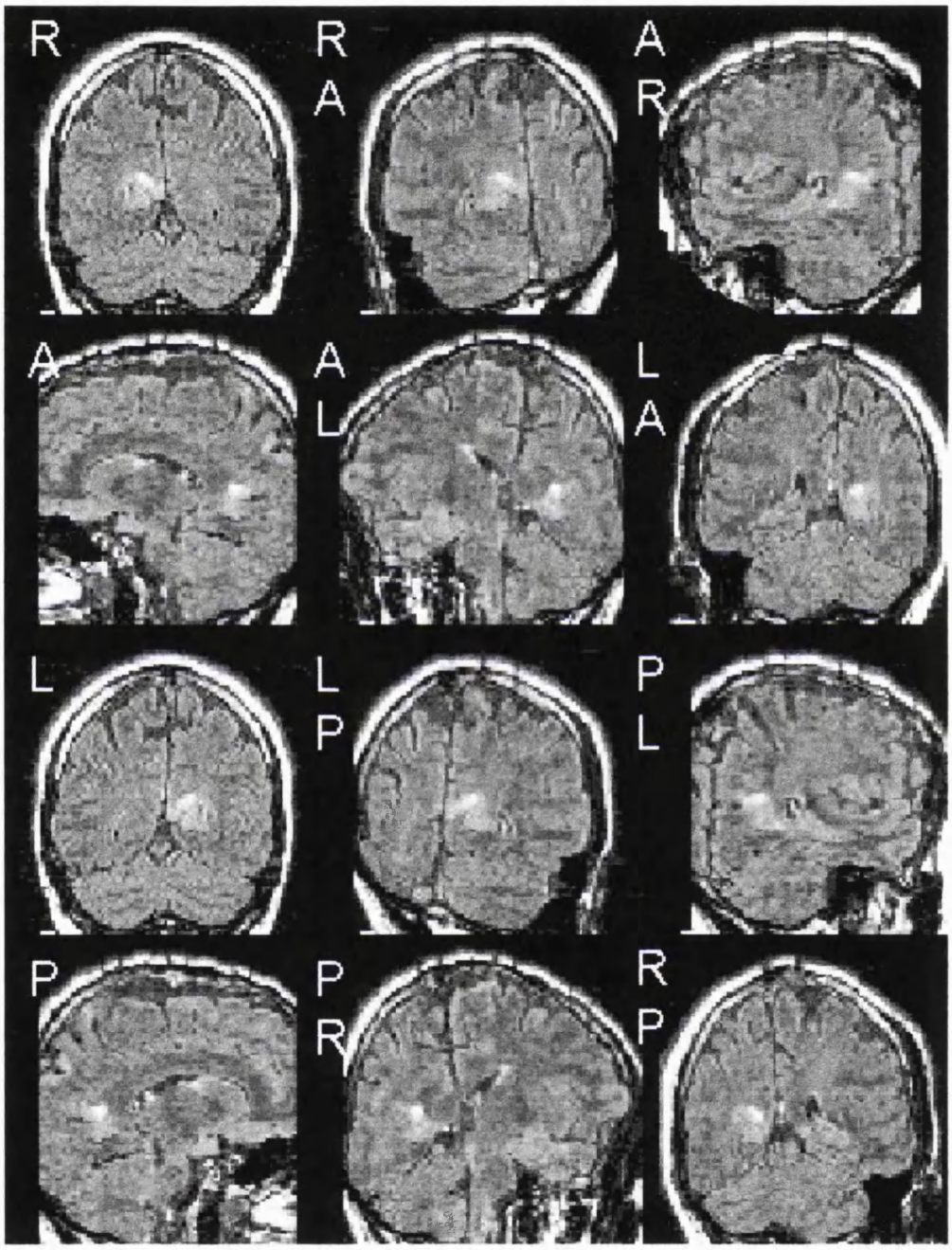

Figure 2.10 - REFORMATTED 3D fast FLAIR of the same patient. A lesion is clearly visible in the cortex above the anterior extremity of the right calcarine sulcus involving the isthmial gyrus. Note also Venetian blind artefacts at slab interfaces (best visible on reformatted images in the sagittal plane, which is orthogonal to the imaging plane).

Thickened cortex and polymicrogyria in cortical dysgenesis was less conspicuous on both 3D and 2D fast FLAIR than on the 3D IRSPGR images because of the lower grey matter white matter contrast of fast FLAIR. In this patient the white matter underlying the area of dysplastic cortex returned a high signal on T2 weighted images. This signal change was visible on both 3D and 2D fast FLAIR.

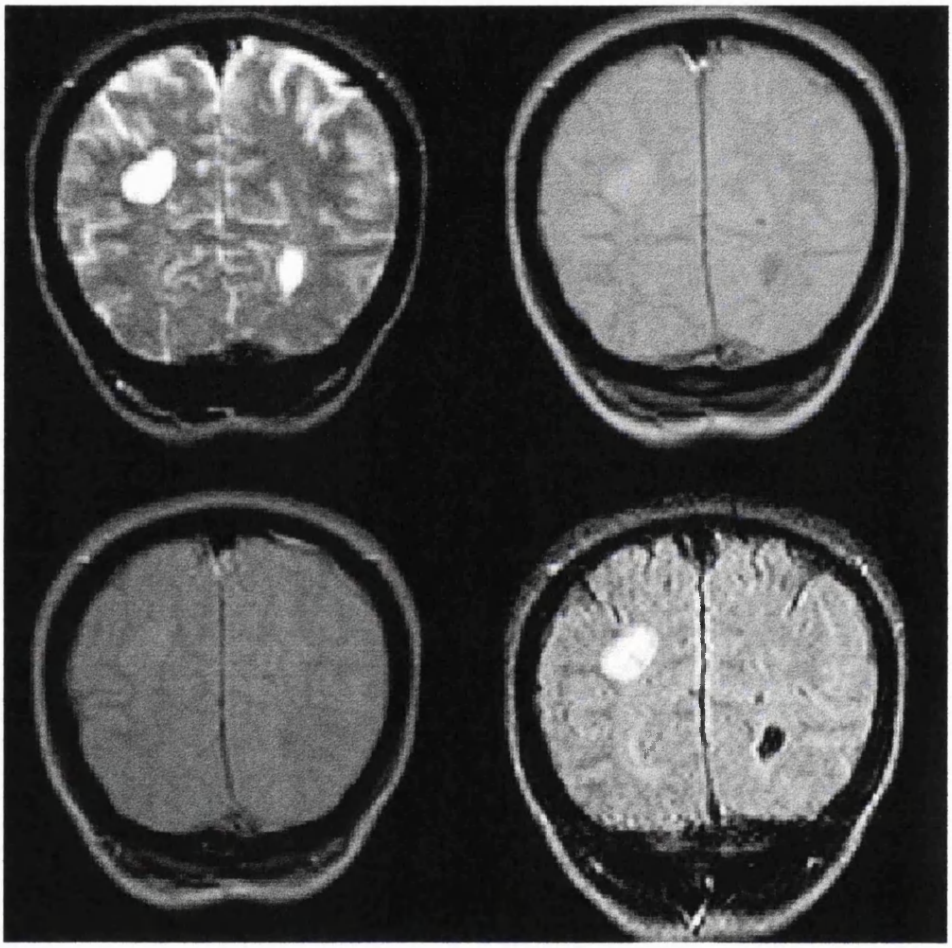

Figure 2.11 - ADDITIONAL INFORMATION ON TUMOUR TEXTURE obtained with 3D fast FLAIR. Spin echo T2-image (top left), proton density weighted image (top right), T1-weighted image (bottom left) and 3D fast FLAIR image (bottom right). A lesion is shown in the right parietal lobe. Contrast is low on the proton density weighted image, T1- and T2-weighted images provide high contrast. However, both lesion and CSF (for example in the occipital horn of the left lateral ventricle) have similar signalintensities (low on T1- and high on T2-weighted images). FLAIR provides a high contrast for the lesion. The fact that the signal from the lesion is not suppressed on FLAIR indicates that the lesion is not a CSF filled cavity but a solid tumour. The patient had partial epilepsy.

The conspicuity of the presumed thrombosed aneurysm was similar on 3D and 2D fast FLAIR and IRSPGR images.

2.3.4 Discussion

The 3D fast FLAIR sequence is an innovative pulse sequence which provides images with FLAIR contrast and thin slices which are suitable for postprocessing including reformatting. Our study showed that the sequence was useful in epilepsy patients. All lesions in this pilot study, which represented the typical spectrum of lesions in epilepsy,[32] were detectable on 3D fast FLAIR images. 3D fast FLAIR provided a higher conspicuity for DNT and other low grade tumours than IRSPGR or standard spin echo images. In addition 3D fast FLAIR improved the detectability of lesions in our study. One small, presumedly traumatic, lesion which had been overlooked on standard spin echo images was first detected on 3D fast FLAIR and only retrospectively identified on 2D fast FLAIR. 3D fast FLAIR had advantages in the investigation of patient with tumours. Tumour margins were difficult to assess on 3D IRSPGR images because the signal intensity was similar to the signal intensity of grey matter on this predominantly T1-weighted sequence. 3D fast FLAIR images allowed visualization of the extent of abnormal signal in all directions. In low grade tumours the extend of the abnormal signal is likely to represent the extent of the tumour because there is only minor or no perifocal oedema.[33] Thus 3D fast FLAIR may also provide a better estimation of tumour size. This is of particular importance in epilepsy. Low grade glial neoplasms are often the cause of epilepsy. Complete resection of the tumour is more often associated with a seizure free outcome than subtotal resection,[34] so assessment of the tumour margins is therefore important in the presurgical work up. Reformatted 3D fast FLAIR images may provide useful information when the extent of the resection is planned. 3D fast FLAIR can also provide additional information on tumour texture: in a lesion with a cystic appearance on standard imaging in our study 3D fast FLAIR allowed to distinguish between CSF-filled cyst and non CSF-filled lesion. Although overall the contrast of 3D and 2D fast FLAIR was similar,

the contrast for hippocampal sclerosis was lower on 3D fast FLAIR than on 2D fast FLAIR. The difference in contrast is likely to be caused by the different repetition time. The TR of the 3D fast FLAIR sequence was 4600ms, less than half of the TR of the 2D fast FLAIR sequence. Visibly lower contrast between sclerotic hippocampus and neighbouring brain tissue on the 3D fast FLAIR resulted in lower lesion conspicuity of hippocampal sclerosis on 3D fast FLAIR compared to 2D fast FLAIR. There was also a lower contrast between grey and white matter and between myelinated tracts and surrounding white matter on 3D fast FLAIR than on 2D fast FLAIR images. In most studies reporting high contrast for a variety of lesions[35] and for myelinated tracts[36] on FLAIR images a TR of 6000ms or longer was used. In one study using a TR of only 3000ms the FLAIR sequence provided still high lesion conspicuity for plaques in multiple sclerosis.[37] However, contrast optimization studies have shown that contrast between a sclerotic plaque in multiple sclerosis and surrounding white matter is optimal with a TR exceeding 10000ms. It is likely that this is also true for hippocampal sclerosis. The relatively short TR used in our 3D fast FLAIR may have been suboptimal. In our small series hippocampal sclerosis was still detectable on 3D fast FLAIR. However, larger studies are required to assess the detectability and conspicuity. Cortical dysplasia with thickened cortex was less conspicuous on both 3D and 2D fast FLAIR than on T1-weighted images because of the lower grey matter-white matter contrast of fast FLAIR. The same would apply for many cases of heterotopic grey matter since the T2- relaxation time of the heterotopic grey matter is often similar to normal grey matter. As on 2D fast FLAIR heterotopic grey matter may therefore be overlooked on 3D fast FLAIR. The 3D IRSPGR sequence remains the sequence of choice to detect cortical dysplasia. Neither 2D nor 3D fast FLAIR provided additional information in the patient with the giant aneurysm. More patients with small aneurysms are required to evaluate the use of 3D fast FLAIR in the detection of this type of lesion. Calcified lesions may also be less conspicuous on both 2D and 3D fast FLAIR than on T2*-weighted sequences.

2.3.5 Conclusion

In recent years several sequences have been developed including gradient echo imaging,[38] fast spin echo imaging,[39] magnetization transfer imaging[40,41] short tau inversion recovery (STIR) imaging[42] and diffusion imaging.[43] All have advantages compared to standard spin echo magnetic resonance imaging in certain special applications. 3D fast FLAIR provides a high contrast for lesions with long T2 relaxation time in combination with thin slices which results in high conspicuity and good demarcation of tumours. Thus, 3D fast FLAIR may be a useful diagnostic tool in the presurgical work up of patients with non enhancing tumours where assessment of the tumour margins with standard imaging is difficult.

2.4 References

1. Brant-Zawadaki M, Norman D, Newton TH. Magnetic resonance imaging of the brain: the optimal screening technique. *Radiology* 1984;**152**:71-77.

2. White SJ, Hajnal JV, Young IA, Bydder GM. Use of fluid-attenuated inversion-recovery pulse sequences for imaging the spinal cord. *Magn Reson Med* 1992;**28**:153-162.

3. De Coene B, Hajnal JV, Gatehouse P, Longmore DB, White SJ, Oatridge A, Pennock JM, Young IR, Bydder GM. MR of the brain using fluid-attenuated inversion recovery (FLAIR) pulse sequences. *Am J Neuroradiol* 1992; **13**:1555-1564.

4. Hajnal JV, Bryant DJ, Kasuboski L, Pattany PM, De Coene B, Lewis PD, Pennock JM, Oatridge A, Young IR, Bydder GM. Use of fluid attenuated inversion recovery (FLAIR) pulse sequences in MRI of the brain. *J Comput Assist Tomogr* 1992;**16**:841-844.

5. De Coene B, Hajnal JV, Pennock JM, Bydder GM. MRI of the brain stem using fluid attenuated inversion recovery pulse sequences. *Neuroradiology* 1993;**35**: 327-331.

6. Thomas DJ, Pennock JM, Hajnal JV, Young IR, Bydder GM, Steiner RE. Magnetic resonance imaging of spinal cord in multiple sclerosis by fluid-attenuated inversion recovery. *Lancet* 1993;**341**:593-594.

7. Rydberg JN, Hammond CA, Grimm RC, Bradley JE, Jack CR, Huston J, Riederer SJ. Initial clinical experience in MR-imaging of the brain with a Fast Fluid-attenuated Inversion-Recovery Pulse Sequence. *Radiology*

1994;**193**:173-180.

8. Listerud J, Mitchell J, Bagley L, Grossman R. OIL FLAIR: optimized interleaved fluid-attenuated inversion recovery in 2D fast spin echo. *Magn Reson Med* 1996;**36**:320-325.

9. Falconer JC, Narayana PA. Cerebrospinal fluid-suppressed high-resolution diffusion imaging of human brain. *Magn Reson Med* 1997;**37**:119-123.

10. Rydberg JN, Riederer SJ, Rydberg CH, Jack CR. Contrast optimization of fluid-attenuated inversion recovery (FLAIR) imaging. *Magn Reson Med* 1995;**34**:868-877.

11. Barker GJ, MacManus DG, Bartlett P. 3D fast FLAIR - a CSF-nulled 3D fast spin echo pulse sequence. ISMRM 5th scientific meeting, book of abstracts. Vancouver 1997:284.

12. Wieshmann UC, Free SL, Everitt AD,Bartlett PA, Barker GJ, Tofts PS, Duncan JS, Shorvon SD, Stevens JM. MR imaging in epilepsy with a fast FLAIR sequence. *J Neurol Neurosurg Psychiatry* 1996:**61**:357-361.

13. Wieshmann UC, Barker GJ, Symms MR, Bartlett PA, Shorvon SD. Fast Fluid-attenuated Inversion-Recovery Imaging: First Experience with a 3D Version in Epilepsy. *Neuroradiology* 1998;**40**:483-489.

14. Bergin PS, Fish DR, Shorvon SD, Oatridge A, deSouza NM, Bydder GM. Magnetic resonance imaging in partial epilepsy: additional abnormalities shown with the fluid attenuated inversion recovery (FLAIR) pulse sequence. *J Neurol Neurosurg Psychiatry* 1995;**58**:439-443.

15. Commission on classification and terminology of the international league against epilepsy: proposal for revised clinical and electroencephalographic classification of epileptic seizures. *Epilepsia* 1981;**22**:489-501.

16. Cook MJ, Fish DR, Shorvon SD, Straughan K, Stevens JM. Hippocampal volumetric and morphometric studies in frontal and temporal lobe epilepsy. *Brain* 1992;**115**,1001-1015.

17. Free SL, Bergin PS, Fish DR, Cook MJ, Shorvon SD, Stevens JM. Methods for normalization of hippocampal volumes measured with MR. *Am J Neuradiol* 1995;**16**:637-643.

18. Takanashi J, Sugita K, Fujii K, Niimi H. MR evaluation of tuberous sclerosis: increased sensitivity with fluid-attenuated inversion recovery and relation to severity of seizures and mental retardation. *Am JNeuroradiol* 1995; **16**:1923-1928.

19. Raymond AA, Fish DR, Sisodiya SM, Alsanjari N, Stevens JM, Shorvon SD. Abnormalities of gyration, heterotopias, tuberous sclerosis, focal cortical

dysplasia, microdysgenesis, dysembryoplastic neuroepithelial tumour and dysgenesis of the archicortex in epilepsy. Clinical, EEG and neuroimaging features in 100 adult patients. *Brain* 1995;**118**:629-660.

20. Raymond AA, Fish DR, Stevens JM, Cook MJ, Sisodiya SM, Shorvon SD. Association of hippocampal sclerosis with cortical dysgenesis in patients with epilepsy. *Neurology* 1994;**44**:1841-1845.

21. Li LM, Dubeau F, Andermann F, Fish DR, Watson C, Cascino GD, Berkovic SF, Moran N, Duncan JS, Olivier A, Leblanc R, Harkness W. Periventricular nodular heterotopia and intractable temporal lobe epilepsy: poor outcome after temporal lobe resection. *Ann Neurol* 1997;**41**:662-668.

22. Van Paesschen W, Sisodiya S, Connelly A, Duncan JS, Free SL, Raymond AA, Grünewald RA, Revesz T, Shorvon SD, Fish DR, Stevens JM, Johnson CL, Scaravilli F, Harkness WFJ, Jackson GD. Quantitative hippocampal MRI and intractable temporal lobe epilepsy. *Neurology* 1995;**45**:2233-2240.

23. Duncan JS, Sagar HJ. Seizures characteristics, pathology, and outcome after temporal lobectomy. *Neurology* 1987;**37**:405-409.

24. Stevens JM. Imaging in epilepsy. *Clinical MRI* 1995;**5**:14-23.

25. Jackson GD, Connelly A, Duncan JS, Grünewald RA, Gadian DG. Detection of hippocampal pathology in intractable partial epilepsy: increased sensitivity with quantitative magnetic resonance T2 relaxometry. *Neurology* 1993;**43**:1793-1799.

26. Grünewald RA, Jackson GD, Connelly A, Duncan JS. MR detection of hippocampal disease in epilepsy: factors influencing T2 relaxation time. *AmJ Neuroradiol* 1994;**15**:1149-1156.

27. Elster AD. Questions and answers in magnetic resonance imaging. St. Louis: Mosby-Year Book Inc, 1994:233-237.

28. Frahm J, Haase A, Matthaei D. Rapid three dimensional MR imaging using the FLASH technique. *J Comput Assist Tomgr* 1986;**10**:363-368.

29. Murakami JW, Weinberger E, Tsuruda JS, Mitchell JD, Yuan C. Multislab three-dimensional T2-weighted fast spin-echo imaging of the hippocampus: sequence optimization. *J Magn Reson Imaging* 1995;**5**:309-315.

30. Barker GJ, MacManus DG, Bartlett P. 3D fast FLAIR - a CSF-nulled 3D fast spin echo pulse sequence. *Proceedings of the International Society for Magnetic Resonance in Medicine, fifth scientific meeting.* ISMRM, Berkeley, CA 1997:284.

31. Le Roux P, Sun Y. Slab Boundary Artefact Reduction in 3DFSE. *Proceedings of the International Society for Magnetic Resonance in Medicine, fourth scientific meeting.* ISMRM, Berkeley, CA 1996:112.

32. Li LM, Fish DR, Sisodiya SM, Shorvon SD, Alsanjari N, Stevens JM. High resolution magnetic resonance imaging in adults with partial or secondary generalised epilepsy attending a tertiary referral unit. *J Neurol Neurosurg Psychiatry* 1995;**59**:384-387.

33. Kuroiwa T, Bergey GK, Rothman MI, Zoarski GH, Wolf A, Zagardo MT, Kristt DA, Hudson LP, Krumholz A, Barry E, Numaguchi Y. Radiologic appearance of the dysembryoplastic neuroepithelial tumor. *Radiology* 1995;**197**:233-238.

34. Britton JW, Cascino GD, Sharbrough FW, Kelly PJ. Low-grade glial neoplasms and intractable partial epilepsy: efficacy of surgical treatment. *Epilepsia* 1994;**35**:1130-1135.

35. Takanashi J, Sugita K, Fujii K, Niimi H. MR evaluation of tuberous sclerosis: increased sensitivity with fluid-attenuated inversion recovery and relation to severity of seizures and mental retardation. *Am J Neuroradiol* 1995;**16**:1923-1928.

36. Hajnal JV, De Coene B, Lewis PD, Baudouin CJ, Cowan FM, Pennock JM, Young IR, Bydder GM. High signal regions in normal white matter shown by heavily T2-weighted CSF nulled IR sequences. *J Comput Assist Tomogr* 1992;**16**:506-513.

37. Boggild MD, Williams R, Haq N, Hawkins CP. Cortical plaques visualised by fluid-attenuated inversion recovery imaging in relapsing multiple sclerosis. *Neuroradiology* 1996;**38**:S10-13.

38. Winkler ML, Ortendahl DA, Mills TC, Crooks LE, Sheldon PE, Kaufman L, Kramer DM. Characteristics of partial flip angle and gradient reversal MR imaging. *Radiology* 1988;**166**:17-26.

39. Constable RT, Anderson AW, Zhong J, Gore JC. Factors influencing contrast in fast spin-echo MR imaging. *Magn Reson Med* 1992;**10**:497-511.

40. Wolff SD, Balaban RS. Magnetization transfer imaging: practical aspects and clinical applications. *Radiology* 1994;**192**:593-599.

41. Gass A, Barker GJ, Kidd D, Thorpe JW, MacManus D, Brennan A, Tofts PS, Thompson AJ, McDonald WI, Miller DH. Correlation of magnetization transfer ratio with clinical disability in multiple sclerosis. *Ann Neurol* 1994;**36**:62-67.

42. Thorpe JW, MacManus DG, Kendall BE, Tofts PS, Barker GJ, McDonald WI, Miller DH. Short tau inversion recovery fast spin-echo (fast STIR) imaging of the spinal cord in multiple sclerosis. *Magn Reson Imaging* 1994;**12**:983-989.

43. LeBihan D, Breton E, Lallemand D, Grenier P, Cabanis E, Laval-Jeantet M. MR imaging of intravoxel incoherent motions: application to diffusion and

perfusion in neurologic disorders. *Radiology* 1986;**161**:401-407.

Chapter 3

Diffusion Imaging in Epilepsy

3.1 Introduction

3.1.1 Principles of diffusion

Diffusion imaging allows the quantitative measurement of a single physical process, the random molecular motion of water. Diffusion can be accurately mathematically described and plays an important role in the physiology of biological systems. Therefore MR diffusion imaging is an interesting tool in imaging. The interpretation of quantitative diffusion measurements is more straightforward than the interpretation of T1- and T2-imaging or off-resonance imaging, which depend on several different complex physical processes including dipole-dipole interaction of molecules, J coupling, chemical exchange, chemical shift anisotropy and others.[1] In the following paragraphs the mathematical description of diffusion is shown and the measurement of diffusion in MR imaging is explained.

Diffusion is a process by which matter is transported from one part of a system to

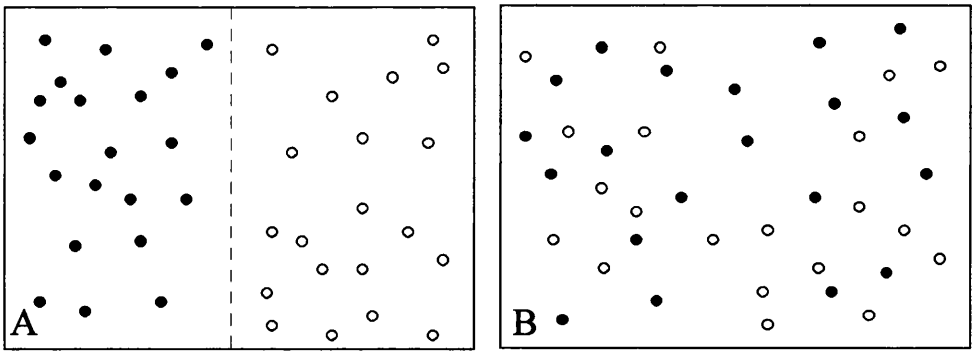

Figure 3.1 - Classic description of diffusion.

another as a result of random molecular motion. In the classic description of diffusion, a system is considered which contains two compartments separated by a barrier, as shown in fig. 3.1. The compartments contain two different fluid molecular species separated by a barrier (A). When the barrier is removed, the

molecules mix together (B). The microscopic, transitional motion is due to the thermal energy possessed by the molecule, causing them to constantly move in a random fashion and interact with one another. In a homogeneous fluid of infinite extent (which is known as an isotopic substance), diffusion is a truly random phenomenon. The mathematical theory of diffusion in isotropic substances is based on the hypothesis that the rate of transfer of diffusing substance through unit area of a section is proportional to the concentration gradient measured normal to the section. The equation which describes this is

$$J = - D \frac{\partial C}{\partial x} \qquad (3.1)$$

where J is the rate of transfer per unit area of section, C is the concentration of the diffusing substance, x is the co-ordinate chosen perpendicular to a reference surface through which the substance diffuses and D is the coefficient of diffusion of the substance under consideration. (Fick's laws of diffusion.) Fick's laws apply equally well to a single molecular species (usually water in MR imaging) and such considerations are referred to as self-diffusion. From these equations it is possible to calculate how far a diffusing particle has travelled in time t. For a single measurement, a molecule may have travelled a range of distances. It is more appropriate to consider the average displacement during a time, t.

For a single molecule the probability p(x)dx for a displacement between x and x+dx during time t, can be calculated.[2]

$$p(x)dx = \frac{1}{(4\pi D t)^{1/2}} \exp\left[\frac{-x^2}{4 D t}\right] dx \qquad (3.2)$$

where t is the diffusion time and D the diffusion coefficient. The mean square of displacement, $\langle x^2 \rangle$ is

$$\langle x^2 \rangle = 2Dt \qquad (3.3)$$

If displacements in three dimensions are considered then the displacement is

$$\langle r^2 \rangle = 6Dt \qquad (3.4)$$

This is commonly referred to as the Einstein equation[3] which may be interpreted as a description of molecules undergoing a random walk. The probability that a given molecule travels a distance x in time t is given by a Gaussian distribution. The diffusion coefficient D is a measure of the mobility of the molecules in the diffusing medium. D is dependent on the substance and the temperature. For pure water at 37°C the diffusion coefficient has a value of ~3.0 x 10^3 mm^2/s.[4] In this case, the root mean square (RMS) displacement for a diffusion time of 30 ms is about 20 μm.

3.1.2 Effect of diffusion on the NMR signal

Signal reduction of spin echoes by diffusion was considered by Hahn[5] and others[6,7] before the advent of imaging. In the presence of a spatially varying magnetic field, random motion of protons in diffusing water results in irreversible dephasing of the MR signal, producing a reduction of its amplitude. Since spatially varying magnetic fields are used for slice selection and spatial encoding in all MR images, diffusion of water molecules results in a reduction in signal intensity in all images, although the effect is normally quite small. By deliberately applying large magnetic field gradients in particular directions, diffusion can be made the dominant image contrast mechanism, enabling variations in diffusion to be visualised, including their directional dependence.

3.1.3 Pulsed gradient spin echo technique

Early measurements of diffusion employed a Hahn spin echo collected in the

presence of a constant applied gradient. The nominal diffusion time Td is equal to TE/3 with this sequence, forming an undesirable link between contrast due to restricted diffusion and that due to T2-relaxation. In 1965 Stejskal and Tanner introduced the pulsed gradient spin echo (PGSE) technique, in which sensitivity to diffusion was provided by gradient pulses placed on either side of the 180° refocussing pulse.[8]

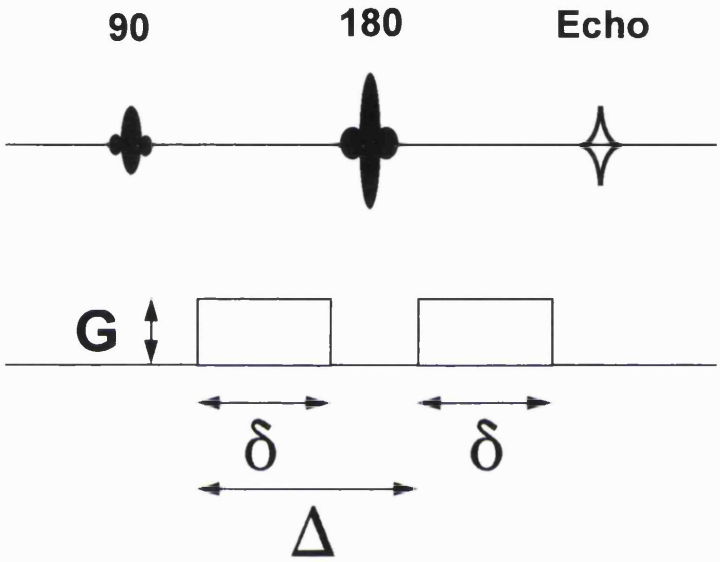

Figure 3.2 - Pulsed gradient spin echo sequence. Diffusion gradients are applied before and after the 180° pulse. The gradient strength G, the duration of the gradient δ and the time between the leading edges of the diffusion gradients Δ determine the diffusion weighting of the sequence.

Neglecting terms due to small conventional slice selecting and spatial encoding gradients, the diffusion attenuation S/S_0 with this sequence is then given by

$$S/S_0 = \exp\left[-\gamma^2 G^2 \delta^2 \left(\Delta - \frac{\delta}{3}\right) D\right] \qquad (3.5)$$

where γ is the gyromagnetic ratio, G is the amplitude of the gradient pulses, delta is their duration, DELTA is the time between their leading edges and D is the diffusion coefficient. For the PGSE sequence, Td=DELTA-delta/3. The composite parameter b (the diffusion sensitivity parameter)[9] is given as

$$b = G^2 \delta^2 \left(\Delta - \frac{\delta}{3}\right) \qquad (3.6)$$

b determines the overall signal attenuation (in conjunction with the D) and has units of seconds per millimetres squared (fig.3.3). It has to be kept in mind that equation 3.6 is a simplification. The b-value is also affected by the ramp time of the diffusion gradients by imaging gradients and background gradients arising as a result of susceptibility variations in the sample or poor magnetic field homogeneceity. Equation 3.5 can also be written as

$$ADC = - \frac{\ln(S/S_0)}{b_{max}} \qquad (3.7)$$

The PGSE technique has a number of advantages. It decouples diffusion contrast from T2 dependent contrast, since S/S_0 no longer depends on TE. In addition, by using very narrow pulses (making delta small in comparison to the average time required to diffuse between barriers), it enables the diffusion time to be determinated accurately.

In order to obtain a sufficient b values strong gradients are necessary, in particular if a short delta is chosen. In experimental scanners with strong gradients sufficient

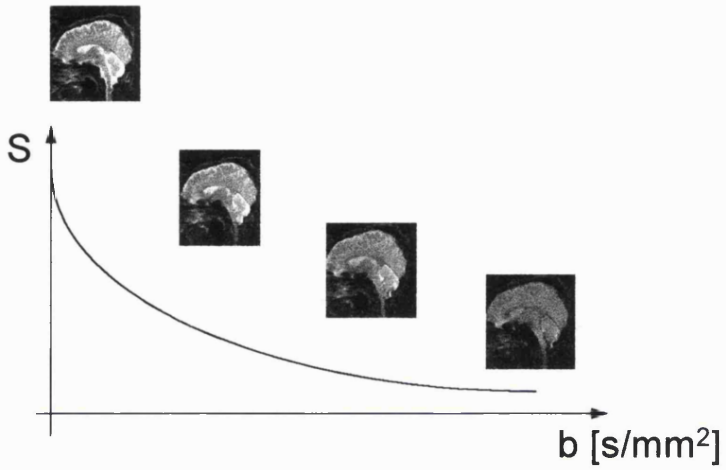

Figure 3.3 - Spin echo EPI sequence with pulsed diffusion gradients. Sagittal images of a control subject were acquired with increasing b values. Increasing b values results in signal attenuation. Signal attenuation is highest in regions of high diffusion (the CSF filled spaces). The slope of the curve represents the diffusion coefficient D (which becomes the apparent diffusion coefficient D* in biological systems, see *3.1.4.3*).

b values can be obtained with very short δ which allows measurements at varying Td for the determination of barrier spacing. Because of the limited gradient strength in clinical scanners measurements are usually performed with a fixed and long Td which is not suitable for measurements of barrier spacing but which allows accurate measurements of the apparent diffusion coefficient.

Other less commonly used methods of measuring diffusion include stimulated echo technique, the gradient echo technique and diffusion measurements with B1 field gradients.[10]

3.1.4 Diffusion in bounded systems

3.1.4.1. Restricted and hindered diffusion

The diffusional motion of molecules in a medium consisting of boundaries, which behave as barriers to diffusion, modifies the RMS displacement of the diffusing species as a function of time over which the diffusion is observed. This phenomenon is referred to as restricted or hindered diffusion.[11,12,13,14,15] If the barriers are completely impenetrable (restricted diffusion), molecules which reach the barriers are reflected back into the medium. In this case the diffusion distance no longer increases indefinitely with diffusion time, but saturates and reaches a plateau when all the molecules have reached the boundary (fig. 3.4).

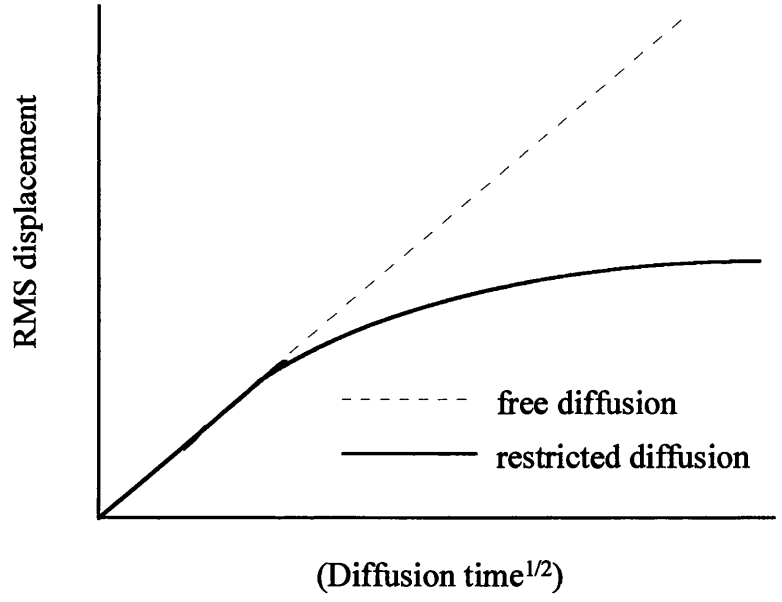

Figure 3.4 - Free and restricted diffusion.

The value of the restricted diffusion asymptote is a measure of the spacing between the barriers. In the case of hindered diffusion, the boundaries may be semi-permeable so that interactions with the barrier hinder the progress of the diffusing molecules passing through. In this case the diffusion characteristics become more complicated. If the barrier spacing is known, it is then possible to estimate the barrier permeability.[16] However, the geometrical arrangement of the medium is generally unknown in biological systems. The Stejskal Tanner sequence can be used to study the effect of restricted or hindered diffusion by obtaining measurements of the diffusion coefficient at a range of diffusion times by altering the value $t_d=(\Delta-\delta/3)$. The effects of restricted or hindered diffusion may be reduced by decreasing the diffusion time to a value to such a value that few diffusing molecules reach the boundaries.

3.1.4.2. Anisotropic diffusion and the diffusion tensor

The case of a medium consisting of barriers orientated in a given direction may result not only in restricted or hindered, but anisotropic diffusion. If the degree of restriction is orientationally dependant the molecular mobility of the diffusing species will not be the same in all directions. Thus, diffusion anisotropy reflects the directionality and structural anisotropy of the material giving rise to restricted or hindered diffusion. Mathematically, the appropriate description of anisotropic diffusion is provided by a tensor quantity which is referred to as the diffusion tensor. In this case equation (3.1) may be re-written as

$$\begin{vmatrix} J_x \\ J_y \\ J_z \end{vmatrix} = - \begin{bmatrix} D_{xx} D_{xy} D_{xz} \\ D_{yx} D_{yy} D_{yz} \\ D_{zx} D_{zy} D_{zz} \end{bmatrix} \begin{bmatrix} \partial C/\partial x \\ \partial C/\partial y \\ \partial C/\partial z \end{bmatrix} \quad (3.8)$$

Where J_x is the rate of transfer per unit area (or flux) and $\partial C/\partial x$ the concentration in the x direction. The diagonal elements of the diffusion tensor scale fluxes and concentration gradients in the same direction and off-diagonal elements couple fluxes and concentration gradients in orthogonal directions. For a medium in which self-diffusion is isotropic, such as water, the off-diagonal elements of the diffusion tensor are zero.

3.1.4.3 Diffusion in biological systems

The theory developed in this chapter has been used to describe diffusion in simple isotropic systems. Having then considered restricted and anisotropic diffusion, the subject of diffusion in biological systems will now be considered. The description of diffusion in biological systems presents a formidable task, since tissue is heterogeneous, containing multiple subcompartments (tissue microstructure). The diffusion process may be restricted by impermeable membranes,[17] hindered by semi-permeable membranes and may also be affected by the presence of macromolecules around which diffusing water molecules may execute a tortuous path. Diffusion in tissue may be anisotropic, as for example is the case in white matter[18,19,20,21] or peripheral nerves. Anisotropy in peripheral nerves is determinated by axons and, if present, by myelin.[22,23] Evidence for time dependent diffusion has been demonstrated in rat liver,[24] frog muscle[25] and human red blood cells.[26,27] In the case of water diffusion, Fick's law no longer applies, but the theory concerning the attenuation of the MR signal may be utilised by replacing the diffusion coefficient D by the apparent diffusion coefficient (ADC) in equation (3.5) and specifying the direction of the diffusion sensitising gradients and stating the diffusion time, t_d. The most complete description requires the evaluation of the diffusion tensor. In order to reflect the influence of tissue structure and diffusion time on the diffusion tensor, the term apparent diffusion tensor ($\mathbf{D}^{app}$) is used. Attenuation of the NMR signal in tissue may be caused by processes other than those of diffusion. These processes include the flow of spins in the blood or CSF out of the image slice, signal losses due to tissue motion and the microcirculation

within the typical dimensions of a voxel, microcirculation can be modified as a pseudo-diffusion process.[28,29]

3.1.5 MR diffusion imaging

3.1.5.1 History of diffusion imaging

The earliest diffusion-weighted MR images were obtained in 1985 by applying diffusion sensitising gradients (as described by Stejskal and Tanner) to spin echo[30,31] and stimulated echo[32] imaging sequences. However, the suggestion that is was theoretically feasible to combine diffusion pulsed gradient experiments and Fourier NMR imaging was raised earlier by Mansfield[33] and studies of the effect of diffusion on conventional MR images investigated by Wesbey et al.[34] Calculated diffusion maps[35] may be constructed from sets of diffusion weighted images, with different degrees of diffusion weighting (by altering the gradient b factor for each image), and the diffusion coefficients obtained by fitting the natural logarithm of the attenuated signal against the gradient b factor according to equation (3.5) on a pixel by pixel basis. Thus, the resultant map represents the spatial distribution of diffusion coefficients in the object, where regions of high (fast) diffusion are bright and those of areas of low (slow) diffusion are dark. The maps are independent from T1- and T2-relaxation.

3.1.5.2 Diffusion tensor imaging

Methods for the estimation of the apparent diffusion tensor $\mathbf{D}^{app}$ using MR imaging (diffusion tensor imaging or DTI), were developed by Basser et al.[36] The six elements of $\mathbf{D}^{app}$ may be determinated from seven measurements of the NMR signal, with diffusion sensitisation along seven non-collinear directions. (Note that in theory, six diffusion-weighted images are the minimum number required to estimate $\mathbf{D}^{app}$).[37] For a given estimation of the $\mathbf{D}^{app}$ in a voxel, a local orthogonal co-ordinate system may be constructed (which is referred to as the principal co-

ordinate axes) along which the diffusive fluxes and concentration gradients are decoupled (that is the off-diagonal elements of $\mathbf{D}^{app}$ are zero). The three diffusion coefficients which correspond to these principal directions are referred to as the principal diffusivities. The three eigenvectors of $\mathbf{D}^{app}$, ε_1 ε_2 and ξ, define the directions of the principal co-ordinate axes and the three eigenvalues λ_1, λ_2 and $\lambda_{3,}$, represent the principal diffusivities within the voxel. In other words, the eigenvector associated with the largest eigenvalue defines the direction of the tissue fibre tract axis. In summary, DTI allows measurements of the magnitude and directionality of diffusion in a three dimensional space.

3.1.5.3 Measurements of magnitude and directionality of diffusion

For clinical studies of water diffusion in tissue, it is often desirable to measure a quantity that is independent of tissue fibre orientation. The average ADC (ADC_{av}) is defined as

$$ADC_{av} = \frac{(ADC_x + ADC_y + ADC_z)}{3} \tag{3.9}$$

where x, y and z are the orthogonal directions of the diffusion measurements. The ADC_{av} is measured in mm^2/s. ADC_{av} can be used as a first approximation but is not rotationally invariant. A rotationally invariant measure is the mean diffusivity $\langle \mathbf{D}^{app} \rangle$

$$\langle \mathbf{D}^{app} \rangle = \frac{(\lambda_1 + \lambda_2 + \lambda_3)}{3} \tag{3.10}$$

$(\lambda_1,+\lambda_2+\lambda_3)/3$ is the trace of the diffusion tensor. Like ADC_{av}, $\langle \mathbf{D}^{app} \rangle$ is measured in mm^2/s.

Diffusion anisotropy may be indicated qualitatively by inspecting diffusion-weighted images obtained with diffusion sensitivity in different directions. In order to describe diffusion anisotropy in voxels containing tissue, an anisotropy index

may be calculated based on measurement of scaler diffusion coefficients in each direction. A scalar anisotropy index, the standard deviation index (AI), that is proportional to the standard deviation of three ADCs measured in three mutually perpendicular directions, divided by their mean value was proposed by van Gelderen.[38]

$$AI = \sqrt{\frac{1}{6}} \frac{\sqrt{(ADC_x - ADC_{av})^2 + (ADC_y - ADC_{av})^2 + (ADC_z - ADC_{av})^2}}{ADC_{av}} \quad (3.11)$$

This index scales from 0 (isotropic medium) to 1 (maximum anisotropy). AI has the advantage that measurements are only required in three direction. However, this anisotropy index does ignore the off-diagonal elements of the diffusion tensor and is therefore not strictly quantitative.

A rotationally invariant quantitative index of anisotropy is the fractional anisotropy index (FA) proposed by Basser and Pierpaoli[39]

$$FA = \sqrt{\frac{3}{2}} \frac{\sqrt{\underline{\underline{\boldsymbol{D}}}:\underline{\underline{\boldsymbol{D}}}}}{\sqrt{\underline{\underline{\mathbf{D}}}:\underline{\underline{\mathbf{D}}}}} \quad (3.12)$$

diffusion deviatoric of $\underline{\underline{\mathbf{D}}}$ (bold not italicized) and $\underline{\underline{\boldsymbol{D}}}:\underline{\underline{\boldsymbol{D}}}$ is the tensor dot product of $\underline{\underline{\boldsymbol{D}}}$. Like AI, the FA index scales from 0 (isotropic medium) to 1 (maximum anisotropy).

FA overestimates anisotropy if the SNR is low. There are other indices for the measurement of anisotropy. One of them, the lattice index is less noise sensitive than the FA.[40]

3.1.5.4 Problems of in vivo diffusion imaging

Diffusion imaging has met with a number of difficulties. Most notably, is the problem of motion artefacts. In diffusion imaging one attempts to measure movements of water molecules over very short distances, typically less than 100 μm. Not surprisingly, diffusion imaging is extremely sensitive to any macroscopic

motion. Motion can be caused by head movements in uncooperative subjects. Pulsatile brain motion caused by the inflow of blood into the skull is the other important source of motion artefacts in diffusion imaging. Brain motion is largest during the first 300 ms of the cardiac cycle.[41] In MR sequences where k-space is filled over several cardiac cycles uncorrected diffusion weighted images are degraded by ghosts. This affects conventional spin echo, fast spin echo and multishot EPI imaging techniques. In single shot EPI imaging k-space is filled in about 100 ms. Therefore, only diffusion weighted images which are acquired during the first 300ms of the cardiac cycle are affected (fig. 3.5 and 3.6). This results in an overestimation of the apparent diffusion coefficient in regions where the brain motion was parallel to the diffusion gradient. There are at least five ways of reducing artefacts from brain motion. Restraining the head, applying sequences with short acquisition times, such as single shot EPI,[42] using cardiac gating,[43] correcting motion artefacts using a second non-phase-encoded navigator echo,[44] or, with single shot EPI, oversampling and rejecting outliers.[45] Other problems of diffusion imaging include the estimation of the contribution of flow and perfusion to the diffusion measurements, the exact calculation of the contribution of imaging gradients to the b-value, the optimal number of b-values steps, the optimum b value and the optimum signal to noise ratio.[46] In clinical studies a compromise has to been made between reasonable acquisition time and the available scanner hardware and software. It has to be kept in mind that this compromise may affect the accuracy of measurements. Other factors potentially affecting quantitative measurements are scanner stability and other artefacts. This has to be taken into consideration when clinical images and quantitative maps are interpreted. Regular measurements of diffusion in a water phantom at a known temperature can be used as a quality assessment. At the same time scanning of normal control subjects and the interpretation of their scans is important.

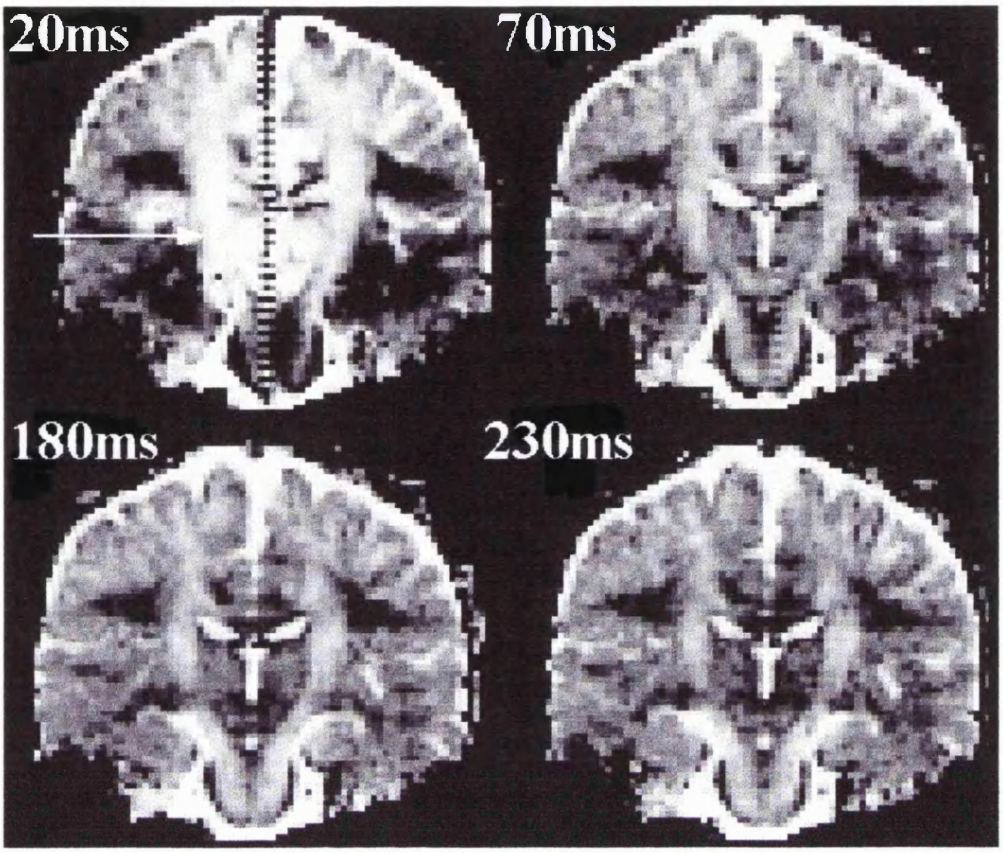

Figure 3.5 - Experiment illustrating the influence of pulsatile brain motion on the apparent diffusion coefficient (ADC). A single shot EPI diffusion sequence was gated from the right common carotid artery. The diffusion sensitising gradient was applied in the frequency encoding (superior-inferior) direction. Average ADC maps of 24 experiments of a control subject are shown for different trigger delays (20ms, 70ms, 180ms, 230ms). For short trigger delays the ADC is artificially high in midline structures (arrow).

3.1.5.5 Single shot EPI in diffusion imaging

We used single shot EPI for the tensor imaging studies in the thesis. Single shot EPI has the advantage of being the least motion sensitive technique and fastest MR acquisition technique. However, single shot EPI has number of disadvantages. The hardware requirements for EPI imaging are severe.[47] Susceptibility artefacts in the orbito-frontal and temporal region and parts of the brainstem make these regions inaccessible to single shot EPI. Single shot EPI is prone to image distortions due to eddy currents. These distortions change when diffusion gradients are applied which results in misregistration of images acquired with and

without diffusion gradients causing inaccurate calculations of diffusion parameters. Corrections, for example co-registration, are usually required.[48] Individual single shot EPI images have a low SNR. Averaging techniques, using a low resolution or filtering are all suitable to increase the SNR, but there are obvious trade-offs.

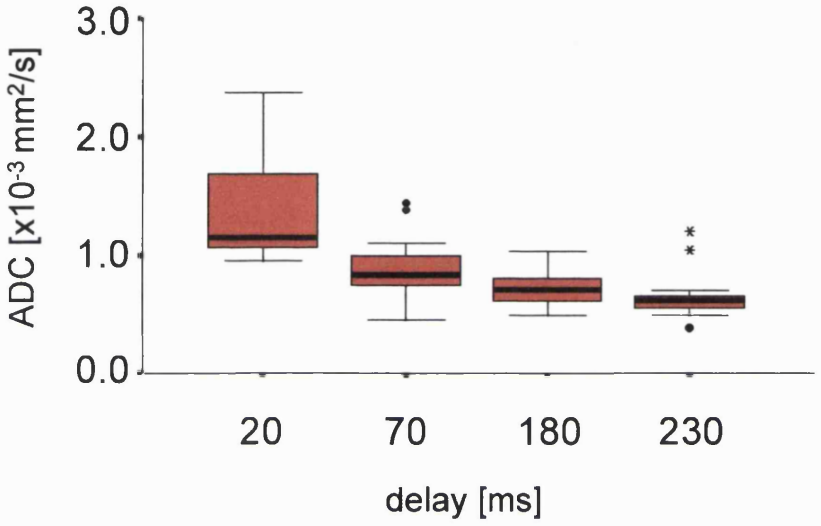

Figure 3.6 - Box plots of the 24 measurements of the ADC in a region of interest (arrow in fig.4.5). Scanning parameters as in figure 3.5. For short trigger delays the ADC is artificially high due to the pulsatile motion. For trigger delay 230ms the measured ADC equals the expected value (0.7 x 10^{-3} mm^2/s).

3.2. Diffusion Imaging of Neurological Disease

3.2.1. Experimental studies

Experimental studies have observed diffusion changes in biological systems in a number of pathological conditions. These include models of stroke and experimental cytotoxic oedema, models of excessive electric discharges and models of nerve damage. In all models changes in diffusion were observed (tab.3.1).

Table 3.1

Experimental models of nervous disease and development associated with diffusion changes

Disease/development	Model	Diffusion change
stroke and cytotoxic oedema	acute experimental stroke[49,50,51]	decreased ADC
	acute global ischemia[52,53,54]	decreased ADC
	experimental brain oedema[55]	decreased ADC
status epilepticus, seizures, epilepsy and migraine	experimental status epilepticus (kainic acid,[56,57,58,59] bicuculline,[60] flurothyl[61] induced) electroshocks,[62] spreading depression(KCL induced or in ischemia),[63,64,65,66]	decreased ADC (reversible if treated)
	chronic models of epilepsy[67]	initially decreased, later increased ADC
hypoglycaemia	acute severe experimental hypoglycaemia[68]	decreased ADC
traumatic head injury	severe trauma[69,70]	increase followed by decrease in ADC
various acute nervous disorders	osmotically driven cell volume changes in nerves [71]	increased cell volume decreased ADC and vice versa
wallerian degeneration	experimental nerve damage[72]	decreased anisotropy
brain development	serial scanning[73]	increasing anisotropy

The theoretical considerations and experimental studies discussed so far have important implications for the clinical use of water diffusion imaging. 1. Measurements of water diffusion are quantitative and independent of T1- and T2-relaxation. 2. Water diffusion in biological systems provide information on tissue microstructure including the density of the tissue (reflected by the restriction of water diffusion), the asymmetrical organisation (reflected by the anisotropy of water diffusion) and the main direction of diffusion (reflected by the principal

eigenvector). 3. Pathophysiological changes are associated with water diffusion changes.

3.2.2 Clinical applications of diffusion imaging

Currently, the main clinical application of diffusion imaging is the early detection of ischemia in stroke. During the early stages of ischemia (less than 2 hours), diffusion is reduced which has been interpreted as cytotoxic oedema.[74,75,76,77] The current understanding is that the extracellular space where diffusion is less restricted shrinks and water is trapped in cells resulting in an overall reduction of diffusion. The licensing of the recombinant tissue plasminogen activator (rtPA) for thrombolysis in human stroke in the USA has kindled the interest in techniques sensitive for the early detection of ischemia such as diffusion imaging.[78,79,80] There are only few studies using diffusion imaging in other conditions including multiple sclerosis,[81,82] brain tumours,[83,84] trauma[85] and Pelizaeus Merzbacher disease,[86] Alzheimers disease,[87,88] and Creutzfeldt-Jakob disease.[89]

In the following we are describing our application of diffusion imaging.

3.3 Water Diffusion in the Human Hippocampus in Epilepsy

3.3.1 Introduction

Animal models of chronic epilepsy following status have demonstrated that persistent ADC changes can develop (tab.3.1). These persistent ADC changes are likely to reflect the microstructural damage in such animals which include widened extracellular space, low neuronal densities, reduced dendritic branching and loss of cellular organization. In humans the hippocampus plays a central role in the generation and propagation of seizures in complex partial seizures. Hippocampal sclerosis (HS) is a common structural abnormality in patient with refractory temporal lobe epilepsy.[90,91] The aim of this study was to investigate diffusion in the

hippocampus in epilepsy during the interictal stage. To evaluate the diffusion changes associated with HS in epilepsy we established a normal range and performed measurements in patients with and without the MR criteria of HS.

3.3.2. Methods

3.3.2.1 Subjects

Seventeen patients and six control subjects without a history of neurological disease were scanned. Three patients had to be excluded from further analysis because of severe motion artefacts resulting in 14 patients (4 female, 10 male, mean age 33 years, range 20-50 years) and six controls (2 female, four male, mean age 31 years, range 29-36 years). Patients were recruited from a tertiary referral centre for epilepsy, were investigated with EEG and standard MR imaging, and were interviewed and examined by the investigator. The following clinical data were collected: age, age at onset of epilepsy, duration of epilepsy, cause of epilepsy, seizure types, frequency of seizures, severity of epilepsy, history of status epilepticus, EEG findings, findings on standard MR imaging. Seizures and epilepsy were classified according to the proposals of the commission for the classification of seizures and epilepsies.[92,93] All patients had both partial and secondary generalized seizures. Presumed cause of epilepsy, predominant seizure type and the results of measurements are shown in tab. 3.2.

Table 3.2

Presumed aetiology of epilepsy, predominant seizure type and quantitative measurements.

Pat	presumed aetiology	seizure	HV r/l	T2 r/l	ADC_{av} r/l	AI r/l
1	prolonged FC	CPS	3061/1891	88/101	0.96/1.08	0.05/0.02
2	childhood meningitis	CPS	2801/2173	85/91	0.84/0.94	0.10/0.03
3	cryptogenic	CPS	2401/1584	86/95	0.84/0.93	0.13/0.06
4	cryptogenic	CPS	2972/3079	85/84	0.94/0.96	0.18/0.16
5	stroke in infancy	SPS	1274/1505	116/108	1.42/1.21	0.03/0.03

Pat	presumed aetiology	seizure	HV r/l	T2 r/l	ADC_{av} r/l	AI r/l
6	childhood meningitis	CPS	2125/3056	99/89	1.13/0.92	0.09/0.18
7	perinatal damage	CPS	2125/2050	104/100	1.14/0.99	0.07/0.08
8	perinatal damage	CPS	2975/2496	93/93	1.14/1.05	0.16/0.07
9	cryptogenic	CPS	2808/3313	87/88	0.95/0.92	0.06/0.02
10	cortical dysgenesis	SPS	2603/2746	88/87	0.89/0.85	0.03/0.02
11	cryptogenic	CPS	2625/1955	86/94	0.89/1.09	0.06/0.08
12	Rassmussens' enc	EPC	3012/819	92/103	1.27/1.53	0.06/0.03
13	cryptogenic*	CPS	255/2489	114/99	1.30/1.05	0.06/0.06
14	cryptogenic*	CPS	525/2492	107/88	0.96/0.72	0.04/0.11

Seizure = predominant seizure type, HV = hippocampal volume in mm^3, ADC_{av} = apparent diffusion coefficient in x 10^{-3} mm^2/s, AI = anisotropy index, l = left, r = right, FC = febrile convulsion, CPS = complex partial seizures, SPS = simple partial seizures, EPC = epilepsia partialis continua. * = patient had with previous anterior temporal lobe ectomy.

The neurological examination was normal in eight and abnormal in six patients (hemiparesis n=5, ataxia n=1). Standard MRI scans of all control subjects were normal, HS was detected in 11 patients (unilateral in 8 and bilateral in 3).

3.3.2.2 Measurement of ADC and AI

Subjects were scanned with a 1.5T Signa Horizon system (maximum gradient strength of 22 mT/m). We used a cardiac-gated (2RR), navigated, diffusion-weighted version of a conventional dual-echo spin-echo (TE1/TE2=75/103ms) sequence. Matrix 128 x 256, field of view 24 cm, slice thickness 5 mm. One to four slice positions at the level of pons were taken in the coronal plane. In three patients images were acquired in the axial plane to cover both hippocampi and the occipital area. Diffusion sensitising gradients were applied along all three gradient axes in turn (b=720 s/mm^2).[94] Motion correction, postprocessing and measurements were performed on a separate workstation (Sun Sparc 20). Motion correction was performed using the second non-phase-encoded navigator echo. The phase correction step was performed in the frequency domain after the first

Fourier transform of the data in the readout direction.[44] Images were visually inspected to control the effects of movement correction: after correction no movement artefacts were detectable by visual inspection in the mesio temporal region in all controls and in 14 of 17 patients. In three patients residual movement artefacts (ghosting and signal loss) remained after correction in at least one diffusion-weighted image. These patients were excluded from further analysis. ADC maps were generated using the Stejskal Tanner formula. A map of the mean ADC (ADC_{av}) was calculated on a pixel-by-pixel basis. The hippocampal ADC was measured in the anterior part of the hippocampal body in a region of interest (ROI) on maps of ADC_x, ADC_y and ADC_z and on the map of the ADC_{av} by a rater who had a detailed knowledge of the hippocampal anatomy (U.C.W). The ROI was carefully drawn to avoid partial volume effects from cerebro-spinal fluid and included CA_1-CA_4 and the dentate gyrus but excluded the alveus. The same technique has been successfully used by others to measure the T2 relaxation time.[95]

To estimate the diffusion anisotropy in the hippocampus we calculated the anisotropy index (AI) proposed by VanGelderen et al. (see 3.1.5.2). We calculated the AI in the hippocampus and for comparison in the corpus callosum, a structure which is known to be highly anisotropic[96] and in a water phantom which is isotropic.

3.3.2.2 Measurement of T2 relaxation time and hippocampal volume

For T2-relaxation time measurements, subjects were scanned with a dual-echo spin-echo T2-weighted sequence (TR/TE1/TE2/NEX=2000/30/120ms/1. Matrix 256 x 192, FOV 24 x 18, 5 mm thick contiguous slices.) T2-maps were generated and T2-measurements performed in a ROI in the hippocampus in a position corresponding to the ADC measurements. For hippocampal volume measurements subjects were scanned with an IRSPGR volume acquisition (TR/TE/TI/NEX=17.4/4.2/450/1, flip angle 20^0). Matrix 256 x 192, FOV 24x18

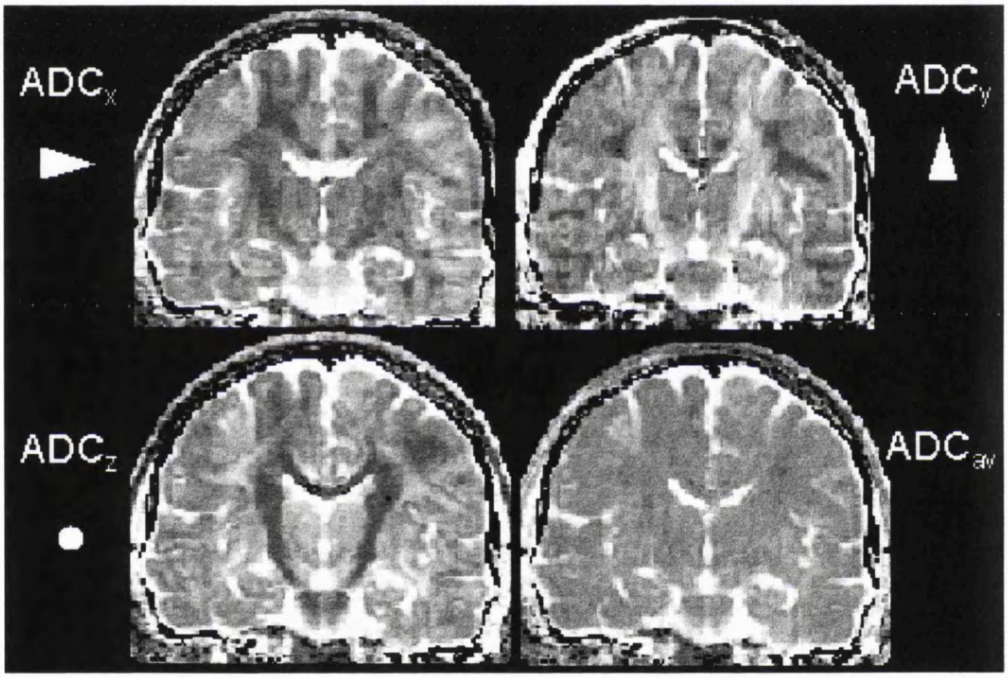

Figure 3.7 - Coronal maps of the apparent diffusion coefficient (ADC) of a control subject. Top left: ADC derived from measurements in the x-direction (ADC_x). Top right: ADC derived from measurements in the y-direction (ADC_y). Bottom left: ADC derived from measurements in the z-direction (ADC_z). Bottom right: Map of the mean ADC of ADÇ , ADÇ and ADÇ (ADC_{av}). The arrowhead indicates the gradient direction (direction is into the imaging plane on ADC_z).

cm, slices thickness 1.5mm. On each slice the hippocampus was manually outlined, the area calculated and the volume calculated by multiplying the sum of the area with the slice thickness. The hippocampal volume was corrected for intracranial

volume - the intracranial volume was estimated by outlining the cranium on 10 slices and multiplying the sum of the area by 15 mm. The methods of measurements hippocampal T2-relaxation time and hippocampal volume measurements and normal values are described in detail elsewhere.[97,98,99,100] Hippocampal sclerosis (HS) was assumed when the hippocampal volume was reduced (volume smaller than the mean minus 3 standard deviations (SD) of normal controls) and the T2-relaxation time prolonged (T2-relaxation time larger mean plus 2 SD of normal controls). In two patients an anterior temporal lobe-ectomy involving the hippocampal head had been previously performed and HS was histologically confirmed. In these patients measurements were performed in the sclerotic remnant.

3.3.2.3 Statistical analysis

ADC_{av} and AI were correlated with T2-relaxation time and hippocampal volume using Pearson's correlation coefficient. In addition, group comparisons were performed. Hippocampi were divided into the following three groups according to their volume and T2-relaxation time characteristics. 1. Hippocampi of patients which fulfilled the MR criteria for HS, 2. hippocampi of patients which did not fulfill the criteria for HS ("HS negative") and 3. hippocampi of normal controls. The mean ADC_{av} and the AI of the three groups were compared. A one way ANOVA (α=5%) was used to test the significance of differences between the three groups. SPSS 6.1 was used for all statistical calculations.

3.3.3 Results

3.3.3.1 Control subjects

The mean ADC_{av} was 0.91 x $10^{-3}mm^2/s$, the SD 0.03 x 10^{-3} mm^2/s, the coefficient of variation (COV) 4%. The mean AI in the hippocampus was 0.09 (SD 0.04, COV 46%). The mean AI in the corpus callosum was 0.55 (SD 0.10, COV 18%),

in the water phantom (theoretically 0) was <0.01. The mean hippocampal T2-relaxation time was 85.5 ms (SD 1.59ms, COV 2%). The mean hippocampal volume corrected for intracranial volume was 2941 mm^3 (SD 88 mm^3, COV 3%). Fig. 3.7 shows ADC maps in a control subject.

3.3.3.2 Patients

3.3.3.2.1 Correlation of T2 time and volume with ADC_{av} and AI

The hippocampal ADC_{av} was elevated (>mean + 2SD of control subjects) in eight patients (bilaterally in five and unilaterally in three)(fig.3.8). Hippocampal

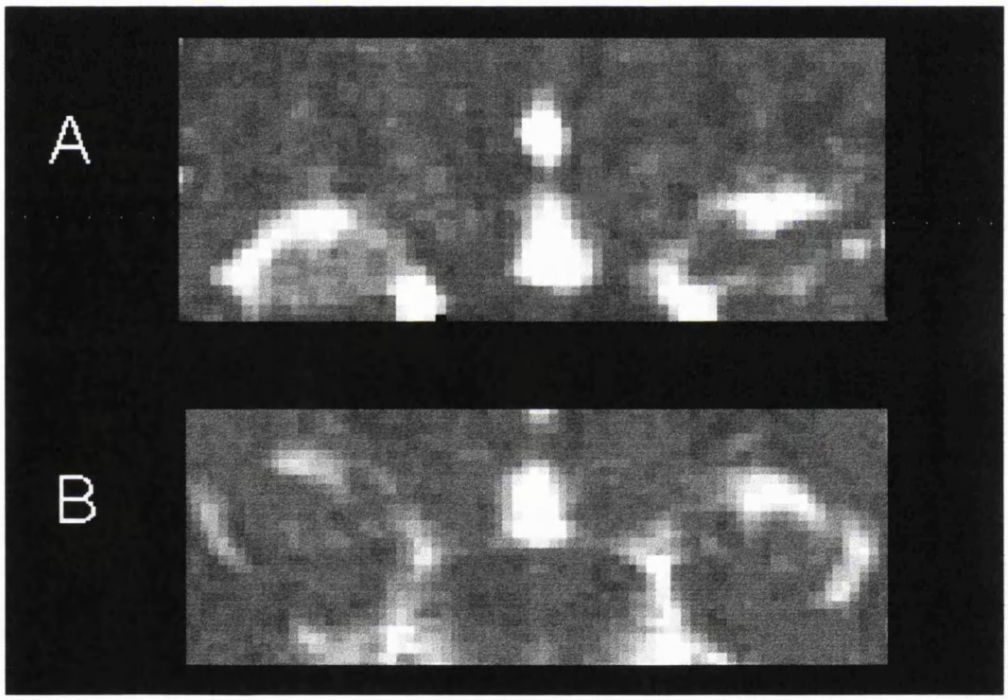

Figure 3.8 - Coronal maps of the ADC_{av} of the mesiotemporal region. A: patient with temporal lobe epilepsy, B: normal control. The signal is higher in the right hippocampus than in the left hippocampus in the patient, measurements revealed an elevated ADC_{av} on the right.

T2-relaxation time and hippocampal ADC_{av} and were positively correlated ($r=0.76$, $p<0.001$) (fig. 3.9). Hippocampal volume and hippocampal ADC_{av} were negatively correlated ($r=-0.61$, $p<0.001$) (fig. 3.10). There was also a weak

correlation between hippocampal T2-relaxation time and hippocampal AI (r=-0.39, p=0.01) and hippocampal volume and hippocampal AI (r=0.37, p=0.02). Group comparisons ADC and AI in HS, HS negative hippocampi and controls. Fourteen hippocampi of 11 patients fulfilled the MR criteria for HS (8 had unilateral, three had bilateral HS). Fourteen hippocampi of patients did not fulfill MR criteria for HS ("HS negative"). In 12 hippocampi the T2-relaxation time and volume were both within normal limits, in two the T2-relaxation time was prolonged but the volume normal. All values of T2-relaxation time and volumes of control hippocampi were within the normal range.

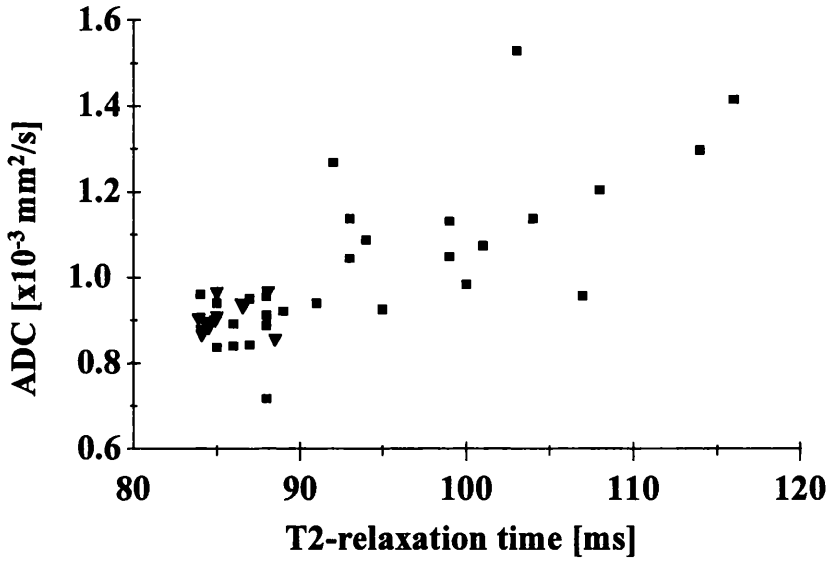

Figure 4.9 - Correlation of hippocampal T2-relaxation time and ADC_{av}. The triangles represent hippocampi of control subjects, the squares represent hippocampi of patients.

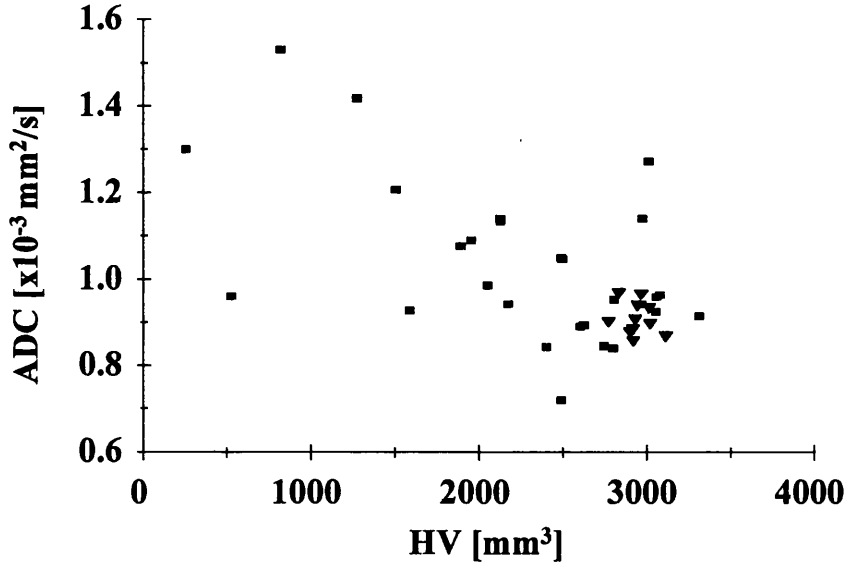

Figure 3.10 -Correlation of hippocampal volume and $ADC_{av.}$ The triangles represent hippocampi of control subjects, the squares represent hippocampi of patients.

The ADC_{av} was significantly increased in the HS group compared to the HS negative and the control group (p=0.0004, posthoc comparison with least mean square (LSD) and Bonferoni test). The mean ADC_{av} in the HS group was 1.13 x $10^{-3}mm^2/s$ (SD 0.17 x $10^{-3}mm^2/s$), in the HS negative group was 0.94 x $10^{-3}mm^2/s$ (SD 0.13 x $10^{-3}mm^2/s$), and in the control group was 0.91 x $10^{-3}mm^2/s$ (SD 0.03 x $10^{-3}mm^2/s$) (p=0.0004). (fig. 3.10).

The AI was significantly reduced in the HS group compared to the HS negative and the control group (p=0.04, posthoc comparison LSD). The mean AI in HS was 0.05 (SD 0.02), in HS negative hippocampi was 0.09 (SD 0.06), and in hippocampi of control subjects 0.09 (SD 0.04) (p=0.04) (fig. 3.12).

3.3.3.2.2 Outliers

In the HS negative group two hippocampi had outlying ADC_{av} values indicated as points in fig 4.11 Both had a normal hippocampal volume but a prolonged T2

relaxation time (patient 12 and patient 8). The AI in these patients was 0.06 and 0.16 respectively.

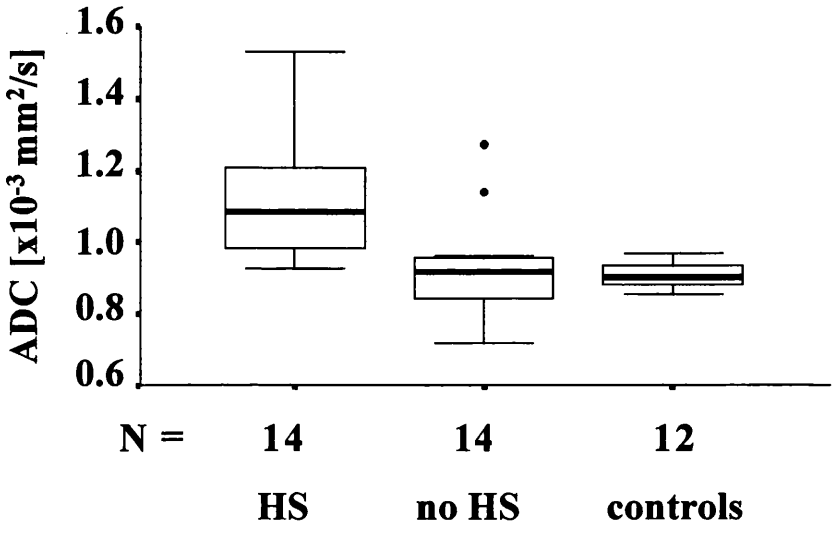

Figure 4.11 - Boxplot showing ADC_{av} in sclerotic hippocampi (HS), HS negative hippocampi of patients (no HS) and control hippocampi. Boxes contain the 50% of values falling between the 25th and 75th percentiles, and the "whiskers" lines that extend from the box to the highest and lowest values, outliers are indicated by dots. The line across the box is the median.

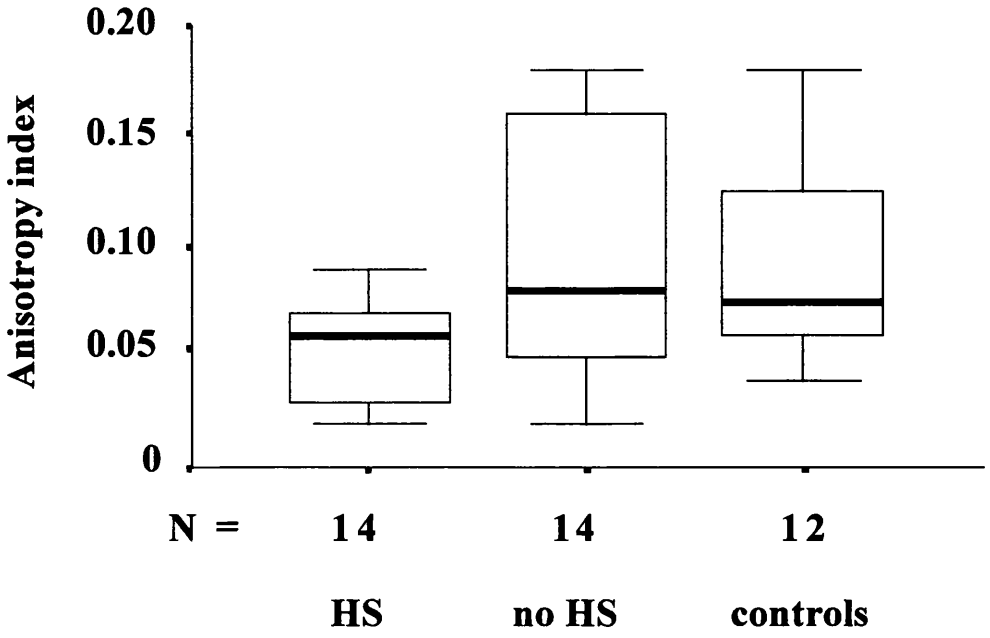

Figure 3.12 - Boxplot showing AI in sclerotic hippocampi (HS), HS negative hippocampi of patients (no HS) and control hippocampi. (For explanation see fig. 4.11)

3.3.4 Discussion

Our measurements showed that water diffusion is frequently abnormal in hippocampi of patients with epilepsy. We found a positive correlation of hippocampal T2-relaxation time and ADC_{av} and a negative correlation of hippocampal volume and ADC_{av}. This is in keeping with the observed trend of Zhong et al.[101] We also found a negative correlation of T2-relaxation time and AI and a positive correlation of hippocampal volume and AI. However, correlations for AI were weak and the coefficient of variation in control subjects of AI measurements was higher than the coefficient of variation of ADC_{av} measurements. AI measurements may be less robust than ADC_{av} measurements because they propagate noise differently. Both ADC_{av} and AI are not rotationally invariant.[40] Variation occurs if brains are not scanned in the same position, a condition which is in practice unlikely to be satisfied because of the interindividual

anatomical differences and variations of head position in the scanner. The measurements used here are therefore a relatively crude estimates. Other methods to quantify anisotropy which provide rotationally invariant measures. Despite the limitations, we found significant differences between normal and abnormal hippocampi for both ADC_{av} and AI. In hippocampi with reduced volume and prolonged T2-relaxation time diffusivity was significantly increased and anisotropy significantly reduced. The combination of reduced volume and prolonged T2-relaxation time in the context of epilepsy is predictive of HS.[102,103,104,105,106] Therefore it seems to be reasonable to assume that diffusivity is increased and anisotropy reduced in HS.

Our findings imply that the tissue texture in the sclerotic hippocampus must be compromised in a way that allows increased water mobility rather than restriction. Measurements using in vitro models have shown that both the expansion of the extracellular space and the increased permeability of membranes can cause an elevation of the ADC (see tab. 3.1). However, changes in membrane permeability only occur in severe and acute disturbance of cellular function, and the major factor for the increased diffusion in a chronic lesion like HS seems to be an expansion of the extracellular space. We interpret our findings as showing that the cells are not as densely packed and not as asymmetrically organized as in normal hippocampi. This information could not be derived from T2-measurements which are relatively nonspecific.[107] Our findings are likely to reflect neuronal loss and reduction of dendritic branching, microstructural changes believed to be the associated with epileptogenesis. For practical reasons the visual inspection of standard MR images including fast FLAIR will probably remain the method of choice to detect HS in a clinical setup.[108] However, quantitative measurements of diffusion may help to clarify cases where visual inspection, measurements of volumes and measurements of T2-relaxation time are not concordant. Interestingly in our study the ADC_{av} was elevated in two hippocampi with normal volume but prolonged T2-relaxation time which may suggest damage on the microstructural level in these hippocampi. Further studies correlating pathological (and clinical) parameters with T2-relaxation time and ADC_{av} are necessary to determine if

ADC_{av} or T2-measurements are more sensitive.

3.3.5 Conclusion

In summary we showed that hippocampal diffusion is frequently abnormal in patients with epilepsy. Our findings are compatible with an expansion of the extracellular space in HS.

3.4 Diffusion-weighted MRI Demonstrates Abnormal Pyramidal Tract in Hemiparesis

3.4.1 Introduction

The main clinical application of DWI so far has been the early detection of the cytotoxic oedema in stroke.[109,110,111] However, DWI can also be used as a tool to investigate the microstructural organization of white matter. Diffusion in the white matter is anisotropic, water molecules travel predominantly parallel but not perpendicular to tracts (tab. 3.1). Therefore DWI provides information on tracts. We used DWI in patients with longstanding hemiparesis to investigate the pyramidal tract.

3.4.2 Methods

3.4.2.1 Subjects

Six control subjects (2 female, four male, mean age 31 years, range 29-36 years) without a history of neurological disease and normal neurological examination and two patients with a right sided hemiparesis were investigated.
Patient one was a 38 year old left-handed man who developed partial epilepsy, a right hemiparesis and aphasia after an encephalitic illness age 8. Symptoms

partially resolved in the month after the disease but he developed epilepsy and was treated with polypharmacotherapy. EEG examinations had shown left sided abnormalities. At the time of the DWI investigation he was functioning intellectually below average (non verbal reasoning test IQ=75). The clinical examination showed a mild aphasia of Broca's type, a right spastic hemiparesis (power 4/5) with impaired fine finger movements on the right. The Edinburgh Inventory showed that the patient was strongly left handed (13 activities out of 13 performed with the left hand).

Patient two was a 37 year old man who developed epilepsia partialis continua at age 6 with jerking in the right face and hand. Subsequently he developed a right sided hemiparesis, hemianopia to the right and global aphasia, and declined intellectually but his deficit has been stable for the last 15 years. He had episodes of generalized tonic clonic status epilepticus and was treated with polypharmacotherapy. EEG examinations had shown left sided abnormalities. He was functioning intellectually at borderline level. On examination he had the following findings: a mild global aphasia, intermitted jerking in the right side of his face, a spastic right hemiparesis more pronounced in the arm, (the power was 3/5 in the arm and 4/5 in the leg, fine finger movements were impaired), a hemianopia to the right, sensory disturbances on the right side. The Edinburgh Inventory showed that the patient was strongly left handed (13 activities out of 13 performed with the left hand) at the time of DWI but there was evidence that he was right handed as a child. His syndrome was compatible with Rassmussen's encephalitis.

3.4.2.2 MR imaging

We used a 1.5T Signa Horizon system (maximum gradient strength of 22 mT/m). All subjects were scanned with the following standard sequences:

1.Spin echo (SE) T1- weighted sagittal localizer (TR/TE/NEX=620/16/1), 256x256 matrix and 24x24 field of view (FOV), 5mm slices, 2.5mm interslice gap. 2.Inversion recovery prepared 3 dimensional fast spoiled gradient echo (IRSPGR) (predominantly) T1- weighted sequence (TR/TE/TI/NEX=17.4/ 4.2/ 450/1, flip angle 20^0), 256 x 192 matrix, 24x18 FOV, 1.5mm slices. 3.SE T2-weighted

sequence (TR/TE1/TE2/NEX=2000/30/120/1), 256 x 192 matrix, 24x18 FOV, 5mm contiguous slices. Sequence 2 and 3 were obtained in the coronal plane. For DWI we used a cardiac-gated, navigated, diffusion-weighted version of a conventional dual-echo spin-echo (TE1/TE2=75/103ms) sequence. The sequence was triggered by every second R wave detected by a periphal pulse oximeter attached to the index finger. Matrix 128 x 256, FOV 24 cm, slice thickness 5mm. One to four slice positions at the level of the pons were taken in the coronal plane. Care was taken to position both patients and controls straight in the scanner. Diffusion sensitising gradients were applied along all three gradient axes in turn (b=720 s/mm^2).[112] Motion correction, postprocessing and measurements were performed on a separate workstation (Sun Microsystems, Palo Alto CA). Motion correction was performed using the second non-phase-encoded navigator echo.[11] Images were visually inspected to check the success of motion correction: after correction no movement artefacts were detectable by visual inspection in any subject. Maps of the ADC_x, ADC_y and ADC_z and of the mean ADC (ADC_{av}) were generated. A map of the anisotropy was calculated using the index proposed by Van Gelderen et al. ADC_{av} measurements were performed in a region of interest in structurally abnormal regions and in corresponding regions in control subjects. All images and maps were visually inspected and the appearance of DWI images compared with the known anatomy.[113,114]

3.4.3. Results

3.4.3.1 Standard MR imaging

All six control subjects had normal standard MR images. In both patients standard MR images revealed a diffuse left hemispheral damage with consecutive enlargement of the ventricles.

3.4.3.2 DWI

In control subjects structures which were undetectable on standard MR images were visible within the white matter on DWI. The location of these structures corresponded well with the known location of tracts (fig.3.12). Prominent tracts were the corpus callosum, the superior longitudinal (arcuate) fasciculus, the cingulum and the pyramidal tract. The direction of diffusion on diffusion weighted images also corresponded with the known orientation of the tracts: on diffusion weighted images with the direction of the diffusion gradient from left to right the corpus callosum appeared dark indicating high diffusion from left to right parallel to the main orientation of the corpus callosum. On diffusion weighted images with the direction of the diffusion gradient from superior to inferior the pyramidal tract appeared dark indicating high diffusion from superior to inferior parallel to the main orientation of the pyramidal tract on coronal images. And finally, on diffusion weighted images with the direction of the diffusion gradient from anterior to posterior the cingulum and superior longitudinal fasciculus appeared dark indicating high diffusion from anterior to posterior parallel to the main orientation of the these pathways on coronal images. On anisotropy maps tracts appeared bright regardless of their orientation because of the calculation of the anisotropy index effectively removes directional information. In all controls the appearance of tracts was symmetrical.

In both patients a gross asymmetry between left and right hemispheres was present on standard imaging but tracts were not detectable. On anisotropy maps the pyramidal tract appeared to be disrupted and anisotropy reduced on the clinically affected side. In addition in both patients the left arcuate fasciculus was abnormal. Measurements of the ADC in structurally abnormal regions in the left hemisphere revealed abnormally high values ($ADC_{av} > 1.0 \times 10^{-3} mm^2/s$, mean ADC_{av} in control subjects $0.90 \times 10^{-3} mm^2/s$, SD $0.03 \times 10^{-3} mm^2/s$).

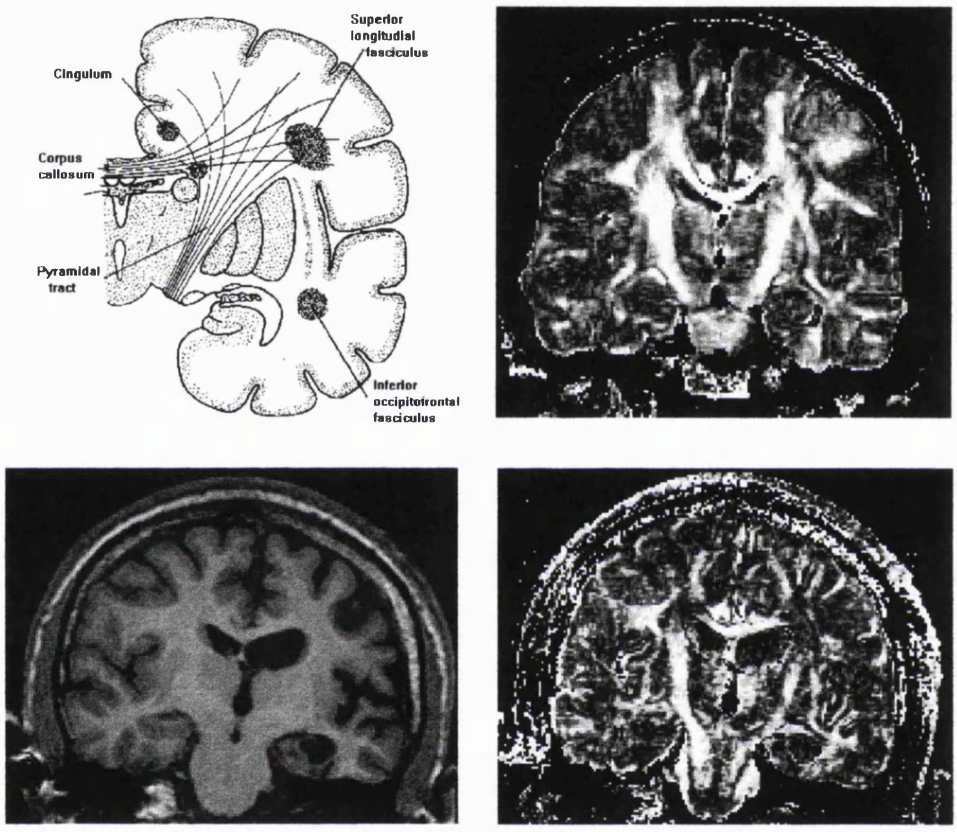

Figure 3.13 - Top left: schematic drawing of a coronal section through the hemisphere. The pyramidal tract consists of projection fibres and forms the posterior limb of the internal capsule. Top right: Anisotropy map of a normal control subject. Bottom left: T1-weighted image of a patient with hemiparesis. Bottom right: Anisotropy map of the same patient showing the abnormal pyramidal tract.

3.4.4 Discussion

DWI provided high contrast for structures within the human white matter which are undetectable with standard MR imaging. These structures detectable by DWI corresponded with the known anatomy of white matter tracts. This finding together with similar observations by other groups,[115,116,117] strongly suggests that DWI is capable of demonstrating the principal tracts in the human white matter. The capability of DWI to give contrast for tracts can be explained by considering the physical properties of water diffusion in the brain. It has been established that diffusion in the white matter is anisotropic: water molecules can move more in some directions than in others. The underlying mechanisms of anisotropic diffusion are not fully understood but there is evidence that the parallel orientation of myelinated fibres in the stem of tracts is an important factor. Water molecules can diffuse parallel but only to a limited extent perpendicular to myelinated tracts.[118] Unmyelinated tracts appear to impair diffusion less than myelinated tracts.[119]

The pyramidal tract is known to be a highly myelinated tract.[120] Our patients had neurological signs including weakness and impaired fine finger movements which indicated a dysfunction of the pyramidal tract.[121] We showed with DWI that the anisotropy was reduced in the clinically dysfunctional pyramidal tract. This implies that the movement of water molecules perpendicular to the dysfunctional tract was increased. Loss of axons and myelin may explain this finding. Experimental models of Wallerian degeneration showed that anisotropy is reduced in damaged fibres with myelin breakdown.[122]

The second abnormal structure on DWI in both patients was the left arcuate fasciculus. Both patients had impaired language functions. The arcuate fasciculus is a major association tract connecting the speech centres of Broca's and Wernicke's area. Damage to the arcuate fasciculus or secondary degeneration of the fasciculus would be compatible with the clinical findings.

Our finding suggests that DWI and in particular anisotropy measurements can be used as a tool to visualize abnormal tracts and hence connectivity as a

morphological correlate of dysfunction. This would be of interest for a better understanding of the relationship between structure and dysfunction. Anisotropy measurements depend on the parameters of the DWI sequence. The spin echo sequence used in our study for DWI had a slightly higher resolution and a higher signal to noise ratio than typical ultra fast echo planar imaging sequences, giving a theoretical advantage in particular in regions with complex anatomy and crossing fibres. However, the anisotropy index used here is not rotationally invariant and ignores the off diagonal elements of the diffusion tensor. Therefore anisotropy in certain regions (in particular in tracts diagonal to the diffusion gradients) may have been underestimated. However, our technique was sufficient to demonstrate the gross abnormality of the pyramidal tract in our patients. Technical improvements of DWI may allow the investigation of more subtle anisotropy changes and may enable us to apply the method in conditions where the changes are likely to be smaller.

3.4.5 Conclusion

We have shown that DWI is superior to standard MR imaging in the visualization of the normal white matter tracts in vivo. Furthermore we showed that DWI can visualize the morphological correlate of a clinically dysfunctional pyramidal tract in two patients with longstanding hemiparesis.

3.5 Anisotropy of Water Diffusion in Corona Radiata and Cerebral Peduncle in Patients with Hemiparesis - a Diffusion Tensor Imaging Study

3.5.1 Introduction

Diffusion tensor imaging (DTI) is a new imaging technique which allows the measurement of magnitude and directionality (anisotropy) of water diffusion in a 3 dimensional space (see chapter 3.1.5.2). Measurements of the anisotropy of water diffusion potentially provides valuable information on white matter tracts. The aim of this study was to assess the association between dysfunctional tracts and anisotropy of water diffusion using DTI. As a model for a dysfunctional tract we chose the pyramidal tract in patients with hemiparesis. We measured fractional anisotropy index (FA) in the expected position of the pyramidal tract at two levels (corona radiata and cerebral peduncle) and compared measurements of patients with chronic hemiparesis (n=10) and normal controls (n=10).

3.5.2. Methods

3.5.2.1 Subjects

Ten control subjects and 10 patients with hemiparesis were included. The mean age in control subjects was 33 years (range 29-39 years) in patients 38 years (range 19-54 years). The mean age when the hemiparesis was acquired was 4.5 years (range 0-16 years). The cause of the hemiparesis was perinatal brain damage (n=5), traumatic brain damage (n=1), surgical and radiation related brain damage (n=1) cortical dysgenesis (n=2), mitochondrial cytopathy (n=1). All patients had partial epilepsy. Three patients had a severe hemiparesis with severe impairment of the function of the affected hand. Seven patients had a mild hemiparesis. All patients had supratentorial structural abnormalities on standard T1- and T2-weighted magnetic resonance imaging affecting the primary motor area.

3.5.2.2 DTI parameters

Scans were performed on a 1.5T Horizon Echospeed scanner (GE, Milwaukee,USA). Maximum gradient strength = 22 mT/m, slew rate = 120 T/m/s. We used a single shot diffusion-weighted spin echo planar sequence (TR = 2700 ms, TE = 78 ms, FOV 24 cm, acquisition matrix 96 x 96, reconstruction matrix 128 x 128, 5mm slice thickness, 5mm interslice gap). Pulsed unipolar diffusion gradients were used for diffusion sensitisation (delta= 28 ms DELTA= 35 ms). Four linearly increasing b-values were applied in 7 non-collinear directions (xx, yy, zz, xy, xz, yz, xyz) at 6 slice positions (b_{max} = 703 s/mm^2). Four averages were acquired per series, 2 interleaved series were obtained. Images were transferred to a separate workstation (Sun Microsystems). Image distortion due to eddy current from the diffusion gradients were corrected by coregistration. Movement artefacts caused by brain pulsation, were reduced by using a filter algorithm which rejects outlying pixels. From the measured signal on T2-weighted and diffusion weighted images, and the b matrix calculated from the pulse sequence parameters, we estimated the effective diffusion tensor, in each voxel using the method of Basser et al.[36] The diffusion tensor matrix was diagonalised to give the three eigenvalues and their associated eigenvectors.[36] From this information the fractional anisotropy index (FA) was derived, on a pixel by pixel basis as described by Basser and Pierpaoli and calculated images (maps) generated.[39] Thus we obtained images with a T2-weighted contrast, diffusion weighted images and maps of FA and mean diffusivity in 12 axial slice positions. The appearance of structures on images and maps was compared with the known anatomy.[123] Measurements of FA were performed in regions of interest (ROI) using the DispImage software.[124] This software calculates mean and standard deviation (SD) of pixel values of pixels included in the ROI. Regions were drawn in the cerebral peduncle and the corona radiata in the white matter underlying the precentral gyrus on FA maps. For measurements in the corona radiata the central sulcus and the precentral gyrus were identified. The ROI was placed in the subcortical white matter underlying the precentral gyrus in the expected position of the corona radiata. Visual qualitative

inspection had revealed an increased signal intensity on T2-weighted images in all patients in this region. The cerebral peduncle was identified by its characteristic shape. On visual inspection of T2-weighted images the cerebral peduncle to not return a clearly increased signal in any patient but appeared to be smaller on the affected side in 2 patients. All measurements were performed by one investigator who has detailed anatomical knowledge (U.C.W.). The size of the ROI was adjusted to the size of the given structure for each measurement. Only ROI with a SD 0.05 or less were accepted to minimize the contamination of the ROI by neighbouring structures or CSF. To establish a normal range the mean FA and the SD for all 10 normal controls was calculated for both corona radiata and cerebral peduncle. Measurements in patients outside mean ± 3SD of control subjects were considered as abnormal.

3.5.3 Results

3.5.3.1 T2-weighted images and mean diffusivity maps

In all patients the structurally abnormal supratentorial regions returned an abnormally high signal on T2-weighted images and had increased mean diffusivity values. This included the Corona radiata where the FA measurements were performed. The brain stem was asymmetrical in two patients, signal intensities were within the normal limits in all patients.

3.5.3.2 FA measurements

In control subjects the range of FA values was narrow in both corona radiata (CR) and cerebral peduncle (CP) (the coefficient of variation (COV) in CR was 12%, the COV in CP was 4%). The mean FA in control subjects was 0.74 in CR and 0.86 in CP. This difference was statistically significant ($p<0.001$ T-test, $\alpha = 5\%$). There was no difference between left and right side in either CR or CP in control subjects (FA in the right CR=0.74, in the left CR=0.72 p=0.6, FA in the right

CP=0.87, in the left CP=0.86, p=0.5). In all patients FA was significantly reduced (<mean-3SD) in CR contralateral to the clinically affected side in the supratentorial lesion. In CP FA measurements were within the normal range in seven patients and abnormally low contralateral to the clinically affected side in three patients. All three had a severe hemiparesis. In all patients measurements in CR and CP contra lateral to the clinically normal side were within the normal range. The mean diffusivity was elevated in structurally abnormal regions. Fig. 3.14 shows maps of a normal control subject and a patient. Fig. 3.15 and tab. 3.3 show measurements of FA in CR and CP in control subjects and patients.

Tab. 3.3

Mean fractional anisotropy in Corona Radiata and Cerebral Peduncle

	Corona Radiata	Cerebral Peduncle
Control Subjects	0.74 (0.09)	0.86 (0.03)
Functional Pyramidal Tract in Patients	0.73 (0.08)	0.86 (0.03)
Dysfunctional Pyramidal Tract in Patients	0.36 (0.08)	0.76 (0.08)

The standard deviation is given in brackets.

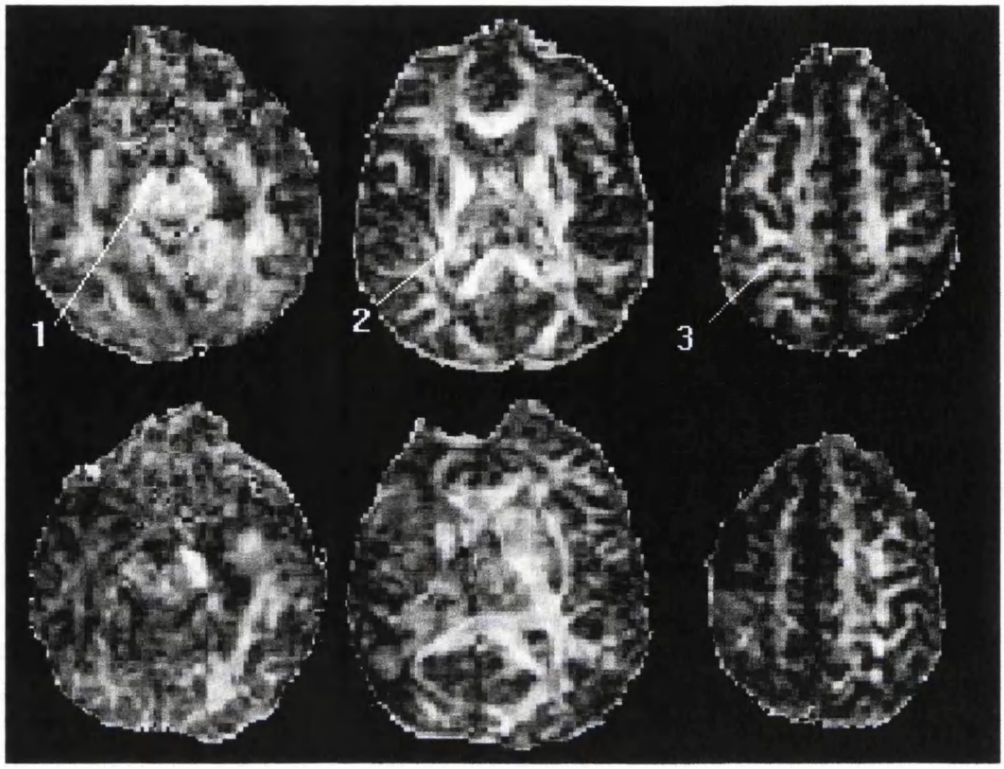

3.14 - Axial fractional anisotropy maps at three slice positions (midbrain level, through the basal ganglia and through the corona radiata). Top row: control subject. Bottom row: patient with a left hemiparesis. Myelinated structures are symmetrical in the control subject. 1 = right cerebral peduncle, 2 = right posterior limb of the internal capsule, 3 = subcortical white matter in the expected position of the right corona radiata. In the patient with a left sided hemiparesis anisotropy is reduced in the right cerebral peduncle, the right posterior limb of the internal capsule, and the right corona radiata.

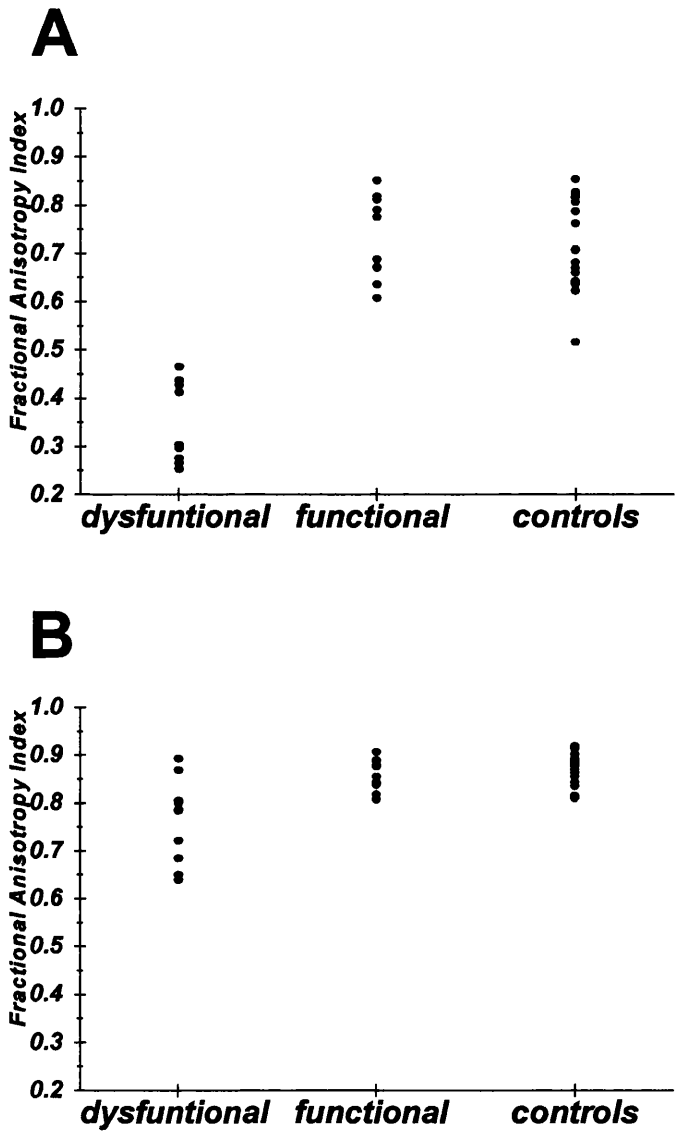

Figure 3.15 - Fractional anisotropy measurements in the corona radiata (A) and the cerebral peduncle (B) in patients in dysfunctional and functional pyramidal tract and in control subjects. The anisotropy is reduced in the dysfunctional pyramidal tract in the corona radiata. At the level of the cerebral peduncle the anisotropy is significantly reduced only in three patients in the dysfunctional tract. All three had a severe hemiparesis.

3.5.4 Discussion

We measured the anisotropy of water diffusion in the human corona radiata and cerebral peduncle in the expected position of the pyramidal tract in normal controls and patients with hemiparesis. In subjects with normally functioning pyramidal tract the anisotropy was high indicating directional movements of water molecules. Our measurements were in agreement with the measurements of Pierpaoli et al. performed in a healthy control subject. The range of anisotropy measurements in our study was relatively narrow, indicating that there is small interindividual variability of the internal microstructural organisation of the tract. Histological studies support both findings. Most fibres are myelinated (>90%) allowing the water molecules to move only parallel to tracts, there is only little interindividual variability of the myelination (SD 7.14%) in the normal pyramidal tract.[125] There was a small but significant increase in FA from corona radiata to cerebral peduncle in normal controls suggesting that directionality of diffusion increases from rostral to caudal. This is in keeping with the known anatomy of the pyramidal tract. In the corona radiata the fibres are not parallel orientated resulting in a relatively lower directionality of diffusion. In addition they are crossed by u-fibres. Directionality increases as pyramidal fibres converge in the cerebral peduncle (fig.3.16).

In all patients with chronic hemiparesis anisotropy was reduced in the area which appeared abnormal on T2-weighted images in the expected position of the corona radiata on the side contra lateral to the hemiparesis. This reduction implies a loss of directionality of the molecular motion of water molecules. Loss of myelin was one explanation for the reduction of anisotropy in the tract. A possible explanation is the replacement of myelinated fibres with less structurally organized tissue including glia cells or, in the patients with dysgenesis, an abnormal (structurally disorganized) development. In patients with severe hemiparesis a measurable reduction of anisotropy was also detected remote from the supratentorial lesion in the cerebral peduncle. A possible explanation is wallerian degeneration of fibres

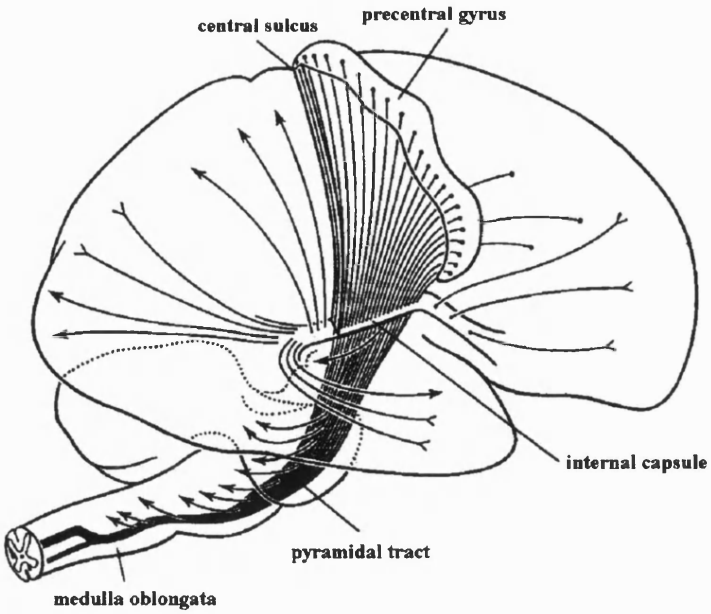

Figure 3.16 - Schematic drawing of the right pyramidal tract (right posterior view). (Adapted from Ferner and Staubesand with permission).

secondary to the supratentorial lesion. Wallerian degeneration (degeneration of the axon with secondary disappearance of the fibre, including the myelin sheet) is associated with reduced anisotropy.

Our experimental results are in keeping with a recent study of Pierpaoli et al. who also demonstrated a reduction of anisotropy in the midbrain and medulla oblongata in stroke patients with a chronic supratentorial infarction.[126] These and our results suggest that DTI may be useful to study the consequences of lesions on the structural integrity of nerve fibres remote to the lesion. Previously, standard T1 and T2 weighted MR techniques have been used to study wallerian degeneration qualitatively.[127] DTI has the advantage that measurements are quantitative and that there are good experimental models concerning the underlying mechanisms. Measurements of anisotropy should be performed in regions with coherent orientation of fibres like the cerebral peduncle. Anisotropy measurements are of limited value in regions with crossing fibres like the pons. In the majority of patients the anisotropy of water diffusion was within the normal range in the cerebral peduncle. In these patients with relatively circumscribed supratentorial damage to the pyramidal tract remaining normal fibres of the pyramidal tract may constitute the majority of fibres in the region of interest in the cerebral peduncle, the average anisotropy in the region of interest may be thus

within the normal variation. Use of a pixel by pixel approach and higher resolution may improve the sensitivity of DTI to detect anisotropy changes in regions distant to lesions.

3.5.5 Conclusion

Our findings suggest that reduced anisotropy is associated with chronic hemiparesis, sometimes distant to the structural abnormality. Measurements of anisotropy may be used in other neurological syndromes to investigate the structure - (dys-) function relationship.

3.6 Wallerian Degeneration in the Optic Radiation after Temporal Lobectomy Demonstrated in vivo with Diffusion Tensor Imaging

3.6.1 Introduction

Temporal lobectomy is the most common surgical procedure performed for medically refractory symptomatic epilepsy. The optic radiation can be damaged during surgery resulting in visual field defects. The clinical consequences of temporal lobectomy with regard to visual field defects range from quadrant anopia, which is commonly seen in en bloc resections, to hemianopia, if the resection extends more posteriorly.[128] The aim of this study was to investigate the microstructural changes in the optic radiation after temporal lobectomy. We used diffusion tensor imaging (DTI) which is a new magnetic resonance (MR) technique suitable for the visualization of tracts (MR tractography).[129]

3.6.2 Methods

3.6.2.1 Subjects

One patient with homonymous hemianopia and two patients with clinically full visual fields were selected for this study to compare the optic radiation of patients with and without clinical deficit after surgery. Twenty two control subjects (14 male and 7 female subjects, mean age 30 years, range 19-45 years) without a history of neurological disease were also studied. All three patients were operated for the treatment of medically intractable temporal lobe epilepsy, all had a normal neurological examination prior to surgery. One patient (patient 1; male, age 20) had an amygdalo-corticectomy 6 months prior to scanning. Two patients (patient 2; female age 50 and patient 3; female, age 32) had standard en block resections of the temporal lobe more than 5 years prior to surgery. Patient 3 developed a homonymous hemianopia after surgery. Patient 1 and patient 2 had clinically full visual fields.

3.6.2.2 DTI parameters

Scans were performed on a 1.5 T Horizon Echospeed scanner (GE, Milwaukee, USA). We used a diffusion weighted sequence based on a single shot fluid attenuated inversion recovery prepared (FLAIR) spin echo planar imaging sequence (TR = 5000 ms, TE = 78 ms, TI = 1835 ms, FOV 24 cm, acquisition matrix 96 x 96, reconstruction matrix 128 x 128, 5 mm slice thickness, 5 mm interslice gap). Two b-values were applied in 7 non-collinear directions at 14 slice positions (b_{max}=703 s/mm^2). Two interleaved series with five averages each were acquired, resulting in 28 contiguous slice positions. Images were transferred to a Unix workstation (Sun Microsystems, Palo Alto CA). Diffusion weighted images affected by movement artefacts caused by brain pulsation, were identified as outliers and rejected using a statistical comparison of the five averages (about 5%). The diffusion tensor was calculated from the diffusion weighted images and the fractional anisotropy index (FA) and the mean diffusivity were derived.[36,39]

3.6.2.3 Quantitative assessment of tracts (MR Tractrography)

Quantitative assessment of the motion of water molecules provides information about the tissue microstructure. In white matter water molecules exhibit diffusion which is anisotropic ie. high parallel with tracts but low perpendicular to tracts (see discussion). Calculated images (maps) of the diffusion anisotropy of water diffusion like FA maps delineate myelinated tracts. We spatially normalized diffusion maps and statistically compared the diffusion anisotropy of patients with the diffusion anisotropy in normal controls to detect areas of significantly abnormal diffusion anisotropy. For spatial normalization, we used an automatic iterative registration algorithm based on the maximization of the cross-correlation of the voxel intensities (MRreg).[130,131] The images with FLAIR contrast were matched to a model with nine degrees of freedom including translation, rotation and linear scaling. The spatial transformations were transferred to the maps of FA and mean diffusivity. FA and mean diffusivity of control subjects were generated

from spatially normalized controls and the standard deviation (SD) and the coefficient of variation (COV) maps were also calculated on a pixel by pixel basis, a reduction of > mean ± 2 SD being considered as significant. Averaged spatially normalized maps of FA of control subjects were overlayed with significantly lowered regions of diffusion anisotropy of the patients. The results were compared with the known anatomy.

3.6.3 Results

3.6.3.1 Standard MR imaging

Standard imaging in patient 1 showed a right anterior medial temporal resection. In patient 2 and patient 3 an extensive en bloc resection of the temporal lobe was shown (about 6 cm of lateral cortex, the uncus the amygdala and 4 cm of the anterior hippocampus, in patient 2 on the right in patient 3 on the left side). FLAIR images showed an increased signal at the margins of the resection in all patients and in patient 2 and 3 high signal in the posterior temporal lobe and occipital lobe ipsilateral to the resection.

3.6.3.2 DTI

The normal range for mean diffusivity and fractional anisotropy measured in regions of interest was narrow in the white matter of the occipital lobe (mean diffusivity: mean 0.79 x 10^{-3} mm^2/s, SD 0.06 x 10^{-3} mm^2/s, fractional anisotropy: mean 0.68, SD 0.05). These values are very similar to diffusion measurements by Pierpaoli et al.[2] There was no significant difference between left and right side. ($p = 0.06$ for mean diffusivity and $p = 0.19$ for fractional anisotropy (t-test, $\alpha = 5\%$). In all patients the mean diffusivity was higher than normal around the margin of resection in the temporal lobe. In patient 1 and 2 diffusion in the occipital lobe was normal, in patient 3 mean diffusivity was increased (mean diffusivity in patient 3 in this area about 1.5 x 10^{-3} mm^2/s) and the FA index reduced (0.45).

3.6.3.3 MR Tractography

Patient 1 did not show significant reductions. In patient 2 a small area of reduced diffusion anisotropy in the posterior part of the temporal lobe was noted. This may have been a direct effect of the resective surgery and affected only the most mesial fibres of the right optic radiation. The majority of fibres appeared to be intact which was in keeping with the lack of clinical signs. However, a significant reduction of diffusion anisotropy was shown in the left optic radiation in patient 3 affecting both Meyer's loop and the more superior parts of the left optic radiation. (fig.3.17).

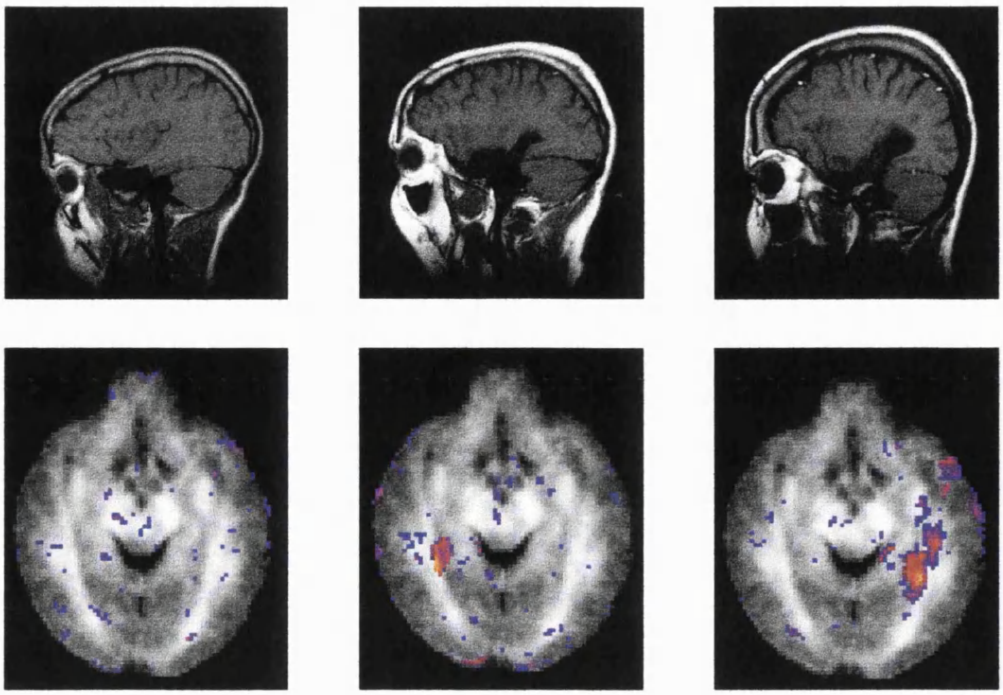

Figure 3.17 - Top: Sagittal T1-weighted images. Bottom: Axial averaged maps of the fractional anisotropy of normal controls, showing myelinated pathways including the optic radiation overlayed with regions of significantly reduced anisotropy in the patients (scaled from blue = 2SD to yellow = 2SD-200). Left: patient 1, right amygdalo-cortiectomy, no visual field defects. The optic radiation is normal. Middle: patient 2, right standard resection, clinically no visual field defect. Only the most medial fibres of the optic radiation are affected. Right: patient 3, left standard resection, clinically hemianopia to the right. Significant reductions of the anisotropy suggesting a breakdown of myelin are visible in the left optic radiation exceeding the resection line. (Note that patients left is right on axial images.)

3.6.4. Discussion

Using MR tractography we demonstrated, to our knowledge for the first time, a significant reduction of diffusion anisotropy in combination with an increased mean diffusivity in the optic radiation in the patient with hemianopia. Our finding can be interpreted by considering the physical properties of water diffusion in the brain. MR tractography utilizes information from the diffusion tensor which is a mathematical description of the magnitude and directionality (anisotropy) of the molecular movements of water in a 3 dimensional space. In the brain the molecular movement of water is restricted by membranes. In white matter diffusion is directional (anisotropic): water molecules move more or less freely parallel to tracts and are restricted or hindered in their movement perpendicular to tracts.[132,133] Experimental data suggest that myelin is an important factor for anisotropic diffusion. Breakdown of myelin in wallerian degeneration leads to a reduction of diffusion anisotropy because water molecules are less hindered in their movement perpendicular to tracts resulting in less directional (more isotropic) diffusion (tab. 3.1). Fibre degeneration has been identified in stroke patients in vivo using DTI.[134] Traditionally, wallerian degeneration caused by artificial or natural occurring lesions has been used to study the origin and course of nerve fibres in the brain postmortem. Using quantitative diffusion measurements in the described way we were able to use the same approach in vivo. Previously, T2-weighted MR sequences or FLAIR techniques were used to study tracts. Wallerian degeneration was assumed in the presence of qualitative and non specific signs such as an increase in signal intensity in the expected position of the optic radiation.[135] However, qualitative criteria are known to be rater dependent which is a major disadvantage of this approach. MR tractography provides superior contrast for tracts and allows a rater independent quantitation of the microstructural integrity of tracts. Neither of these can be obtained with standard MR imaging. The disadvantages of current implementations of DTI include a lower resolution than most standard MR images and distortions. Low resolution and thick slices as used in our study can affect the accuracy of diffusion anisotropy

measurements, in particular in regions with crossing fibres. However, this is merely a technical problem which is likely to be solved with new fast DTI techniques. Increased resolution and reduced artefacts will narrow the range of the diffusion anisotropy measurements in normal controls and thus increase the sensitivity of the method.

MR tractography using DTI is an exciting new technique which offers the opportunity to address other important questions in the context of epilepsy surgery. These include not only the correlation of postsurgical deficit (clinical and subclinical) and morphological changes which has been addressed in this study but also the correlation of outcome with damage to certain tracts such as the uncinate fascicle. This may assist in our understanding of seizure spread and also of the morphological consequences of seizures.

3.6.5 Conclusion

Our findings show that MR tractography maybe used to demonstrate wallerian degeneration in the optic radiation after temporal lobectomy in patients with hemianopia thus enabling us to visualize the morphological correlate of dysfunctional pathways after epilepsy surgery in vivo.

3.7 Reduced Anisotropy of Water Diffusion in Structural Cerebral Abnormalities demonstrated with Diffusion Tensor Imaging

3.7.1 Introduction

During phylogenetic development the structural complexity of the brain increases reflect the level of organization of the brain.[136] The microstructural organization of the brain can be investigated in vivo with diffusion weighted imaging. In this study our aim was to investigate the anisotropy of water diffusion in long standing structural abnormalities of different aetiology.

3.7.2 Methods

3.7.2.1 Patients

Eighteen patients (mean age 35 years, range 17-49 years) with partial epilepsy of more than 5 years and a structural abnormality on standard T1- and T2-weighted magnetic resonance images and 10 control subjects (mean age 33 years, range 29-39 years) without a history of neurological disease were scanned with DTI. Patients were recruited from a tertial referral centre for epilepsy and were interviewed and examined by the investigator. The neurological defict was stable, all patients were investigated with DTI in the interictal stage. The diagnosis of the structural abnormality was based on the appearance on standard imaging and the clinical data. The structural abnormalities could be divided in three principal groups, brain damage (lesions without mass effect), dysgenesis (characterized by abnormal gyral pattern and or heterotopic grey matter) and tumours (lesions with mass effect). Brain damage included postsurgical brain damage, nonspecific brain damage, perinatal brain damage, perinatal infarct, ischemic infarct, perinatal hypoxia, traumatic brain damage (n=3), mitochondrial cytopathy with the A117786 mutation and mesiotemporal sclerosis. Dysgenetic structural abnormalities included focal cortical dysplasia in combination with subcortical high signal, widespread cortical dysplasia and heterotopia in combination with cortical dysgenesis. Tumours included meningeoma (n=2), hypothalamic hamartoma and a glioma. Tab. 4.4 shows the location, diagnosis and diffusion measurements of the structural abnormalities.

3.7.2.2 DTI parameters

Scans were performed on a 1.5T Horizon Echospeed scanner (GE, Milwaukee,USA). Maximum gradient strength = 22 mT/m, slew rate = 120 T/m/s. We used a single shot diffusion-weighted spin echo planar sequence (TR = 2700ms, TE = 78ms, FOV 24 cm, acquisition matrix 96 x 96, reconstruction

matrix 128 x 128, 5mm slice thickness, 5mm interslice gap). Pulsed unipolar diffusion gradients were used for diffusion sensitisation (delta = 28ms DELTA = 35ms, diffusion time Td = 26ms). Four linearly increasing b-values were applied in 7 non-collinear directions at 6 slice positions (b_{max}=703 s/mm^2). Four averages were acquired.

Images were transferred to a separate workstation (Sun Microsystems, Palo Alto CA), and converted into UNC format for postprocessing. Image distortion due to the diffusion gradients were corrected with a co-registration program. Movement artefacts were reduced by using a filter algorithm which rejects outlying pixels. Maps of the mean diffusivity and the fractional anisotropy (FA) were generated using the method proposed by Basser and Pierpaoli[39] on a pixel by pixel basis. The mean diffusivity is a measure of the magnitude of diffusion in mm^2/s. The FA index is a rotationally invariant scalar index of anisotropy which scales from 0 (isotropic medium) to 1 (maximum anisotropy). Structural abnormalities were identified on standard MR images and measurements were performed in regions of interests using the DispImage software. The ROI was automatically transferred from mean diffusivity maps to the corresponding region on FA maps to ensure that measurements were performed in identical regions. Normal values were established by measuring FA and mean diffusivity in 2 locations (left and right) in 10 control subjects in the subcortical white matter. Differences between values of patients and of control subjects were statistically tested with a t-test (alpha 5%). Individual measurements in patients outside mean ± 3SD of normal controls were considered to be abnormal.

3.7.3 Results

FA maps provided contrast for myelinated tracts in normal controls. In the subcortical white matter of normal controls the mean FA in the white matter was 0.76 (SD 0.05). The mean diffusivity maps were uniform with values of 0.75 x 10^{-3} mm^2/s (SD 0.05 x10^{-3}mm^2/s). In structural abnormalities FA was significantly reduced ($p<0.0001$) and mean diffusivity significantly increased ($p<0.0001$)

compared to normal subcortical white matter (fig.3.18). Despite this finding the correlation between FA and mean diffusivity was poor (r = -0.1). In structural abnormalities of five patients the mean diffusivity was inside mean plus 3SD of normal control subjects. Two patients had dysgenetic lesions and three patients brain damage. All FA measurements in structural abnormalities were outside mean minus 3SD of normal control subjects regardless their aetiology (fig.3.19). Table 3.4 shows diagnosis and diffusion measurements.

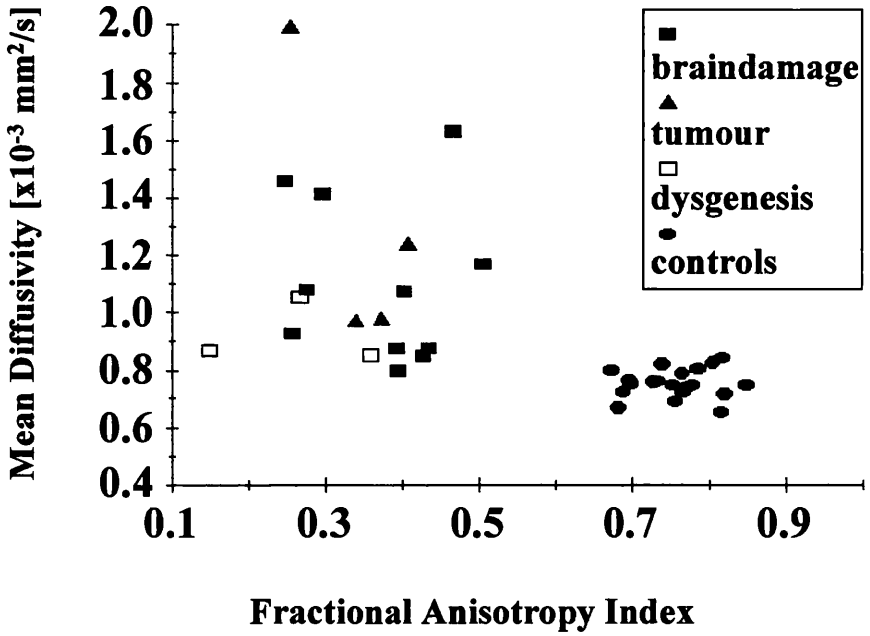

Figure 3.18 - Fractional anisotropy and mean diffusivity in structural abnormalities and in the white matter of control subjects.

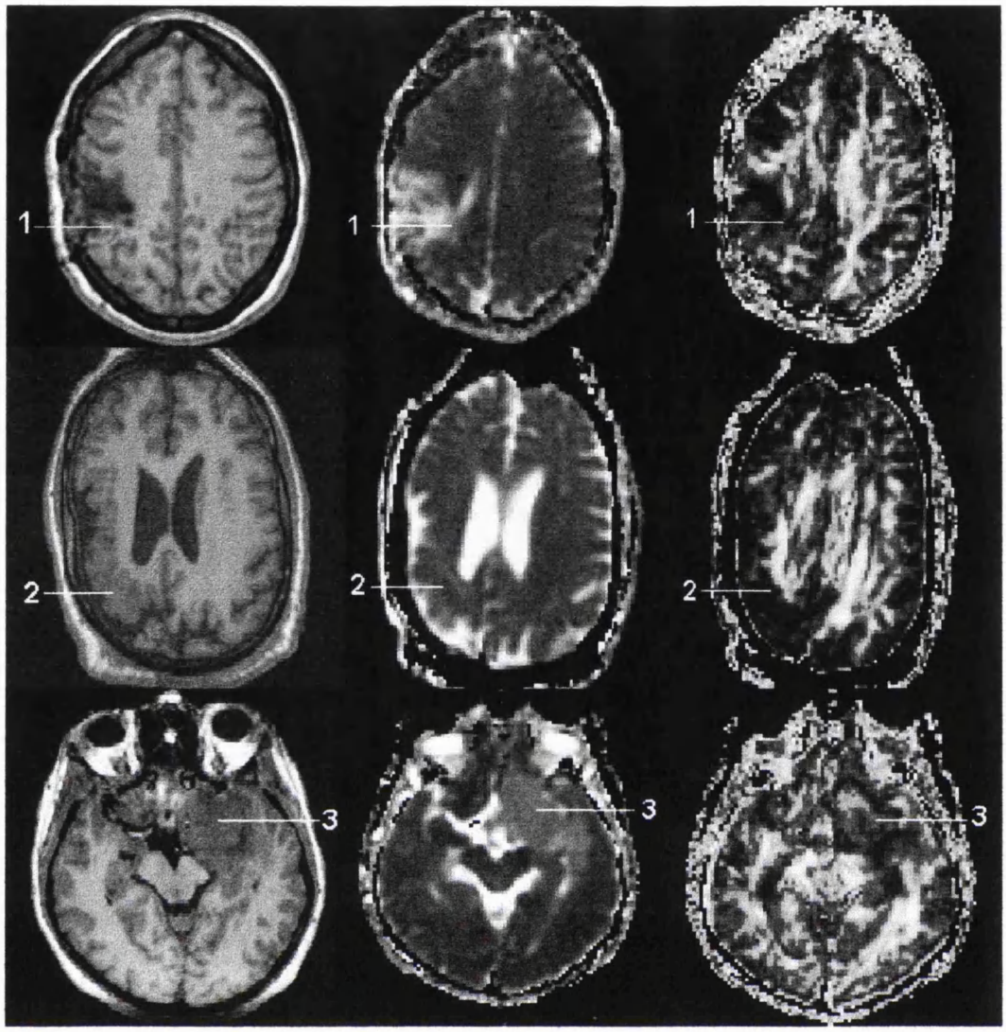

Figure 3.19 - Structural abnormalities on DTI. T1-weighted images (left), maps of mean diffusivity (middle) and fractional anisotropy (right) are shown. Top row: A patient with traumatic brain damage affecting the right parietal and frontal lobe (1). Middle row: A patient with polymicrogyria affecting the right hemisphere (2). Bottom row: A patient with a left temporal meningeoma (3). The fractional anisotropy is reduced in all structural abnormalities. However, mean diffusivity is only mildly increased in the patient with polymicrogyria.

Table 3.4 DTI measurements in structural abnormalities

Pat	standard MR imaging	diagnosis	FA	$\langle D^{app} \rangle$
1	right temporal lesion	postsurgical brain damage	0.47	1.63
2	left frontal lesion	nonspecific brain damage	0.39	0.87
3	left hemispheral lesion	perinatal brain damage	0.39	0.79
4	left fronto-parietal lesion	perinatal infarct	0.26	0.92
5	left occipital lesion	ischemic infarct	0.40	1.07
6	subcortical WML	perinatal infarct	0.44	0.87
7	left hemispheral lesion	traumatic brain damage	0.28	1.08
8	right fronto-parietal lesion	traumatic brain damage	0.30	1.41
9	right subcortical lesion	traumatic brain damage	0.42	0.85
10	WML and atrophy	mitochondrial cytopathy	0.25	1.46
11	hippocampal atrophy	mesiotemporal sclerosis	0.50	1.17
12	abnormal gyrification	cortical dysplasia	0.27	1.05
13	abnormal gyrification	cortical dysplasia	0.15	0.86
14	abnormal gyrification	cortical dysplasia	0.36	0.85
15	bilateral occipital mass	meningeoma	0.37	0.98
16	left temporal mass	meningeoma	0.40	1.24
17	hypothalamic mass	hypothalamic hamartoma	0.25	1.99
18	right mesio temporal mass	glioma	0.34	0.97

FA = fractional anisotropy, $\langle D^{app} \rangle$ = mean diffusivity, WML = white matter lesion, GM = grey matter.

3.7.4 Discussion

The main finding of our study was a reduction of anisotropy of water diffusion in a wide range of different structural abnormalities. In the majority of abnormalities (72%) the reduction of anisotropy was also associated with an increased diffusivity. Our finding can be interpreted by considering the physical properties of water diffusion in the brain. In the brain the molecular movement of water is restricted by membranes. Pathological processes resulting in microstructural

changes including cell swelling, shrinkage or widening of the extracellular space or the loss of tissue organization all result in transient or permanent changes of diffusion. It has also been established that water diffusion is anisotropic: water molecules can move more freely in some directions than in others. The underlying mechanisms of anisotropic diffusion are not fully understood but there is evidence that the parallel orientation of myelinated fibres in the stem of tracts is an important factor. Water molecules can diffuse parallel but only to a limited extent perpendicular to myelinated tracts. Unmyelinated tracts appear to impair diffusion less than myelinated tracts. A reduction of anisotropy in lesions implies that the water molecules have more freedom of movement in structurally abnormal tissue than in normal cerebral white matter. This suggests a loss of organization on the microstructural level. Experimental models of wallerian degeneration for example showed that anisotropy is reduced because the damaged fibres allow perpendicular diffusion. Our finding of a reduced anisotropy implies that a reduction of the organisation is the common finding in structural abnormalities. Our finding suggests that anisotropy measurements can be a sensitive although nonspecific tool for the detection of abnormal tissue in the white matter. Further studies are necessary to assess if abnormalities can be detected in patients with normal standard MR imaging. In our study measurements of anisotropy and mean diffusivity did not correlate suggesting that both parameters maybe independent measures. In about 30% of all abnormalities a reduced anisotropy was associated with a normal mean diffusivity implying that the structural organization was different (less directional) than in normal white matter (resulting in reduced anisotropy) but the cells were still as densely packed as in normal brain tissue (resulting in normal mean diffusivity). This combination seems to be possible in gliosis (as the consequence of brain damage) and dysgenesis and may distinguish these pathologies from for example tumours. Preliminary studies in stroke,[137] multiple sclerosis,[138,139] other white matter disorders,[140,141] malformations of cortical development[142] and ageing[143] have all shown a reduction in anisotropy suggesting that reduced anisotropy is associated with dysfunction independent of the underlying pathology. Anisotropy may even be mildly reduced in

schizophrenia[144] and possibly ageing.[145]

3.7.5. Conclusion

A reduced anisotropy reflecting a loss of the microstructural organisation appears to be the common denominator in structural cerebral abnormalities of different aetiologies.

3.8 Blunt Head Trauma associated with widespread Water Diffusion Changes

3.8.1 Introduction

Blunt head trauma is a major cause of disability giving rise to neurological deficits, neuropsychological deficits and epilepsy. Postmortem studies have identified surface contusion and lacerations, diffuse axonal injury, affecting predominantly central myelinated structures, and ischemia as main mechanisms of damage.[146] To localise damaged regions and quantitate the damage in vivo we used diffusion tensor imaging (DTI).

3.8.2 Methods

3.8.2.1 Patient

We investigated a 42 year old man who had suffered from a severe blunt head trauma in a road traffic accident with skull fracture and right fronto-temporal extra dural haemorrhage 9 years ago. He was comatose for 2 days and suffered from impaired memory, left quandrantanopia and epilepsy as the consequence of the accident. Standard MR imaging showed damage to the right temporal lobe, atrophy and multiple small juxacortical and a few deeper white matter lesions.

3.8.2.2 DTI parameters

DTI (TR = 5000 ms, TE = 78 ms, TI = 1835 ms, FOV 24 cm, acquisition matrix 96 x 96, reconstruction matrix 128 x 128, 5 mm slice thickness, 2 b-values applied in 7 non-collinear directions at 28 slice positions (b_{max}=703 s/mm^2)) showed widespread abnormalities involving both hemispheres. Statistical pixel by pixel comparison of spatially normalized diffusion maps of the patient with diffusion maps of 22 control subjects was performed.

3.8.3 Results

The statistical comparison with the 22 control subjects showed a significant *increase* of the magnitude of diffusion right temporal, frontal and bilateral occipital (mean diffusivity > mean + 2 standard deviations, >1.0 x 10 $^{-3}$ mm^2/s). Furthermore there was a significant *decrease* of the directionality of diffusion (fractional anisotropy < mean - 2 standard deviations, <0.3 [dimensionless]) in myelinated structures including the right optic radiation, corresponding to the quandrantanopia, and the corpus callosum (fig. 3.20).

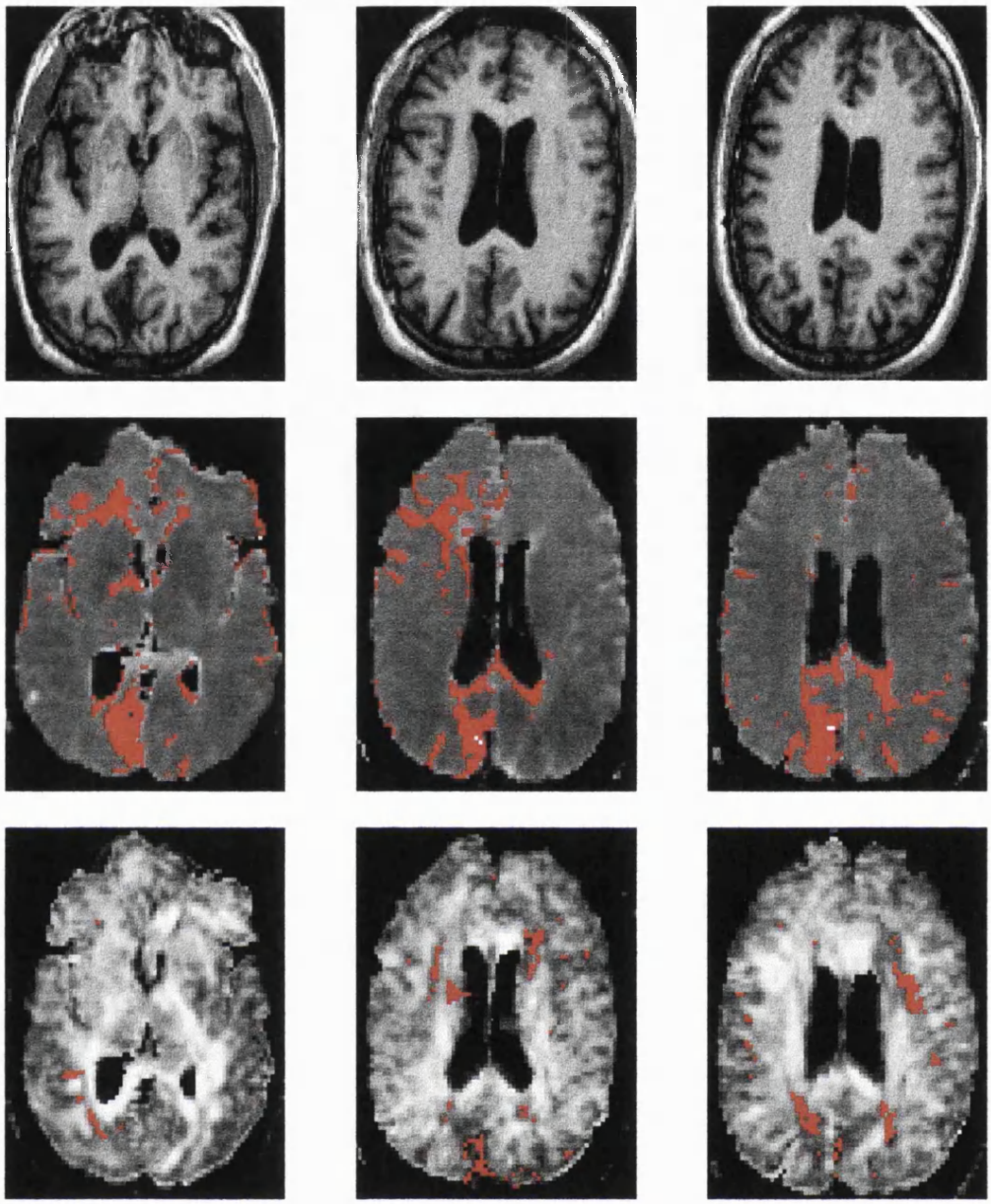

Figure 3.20 - Diffusion tensor imaging and standard T1 weighted images in traumatic brain damage causing right quadrant anopia, impaired memory and epilepsy. T1-weighted images (top row) show brain atrophy. Maps of the mean diffusivity show widespread increase of the magnitude of diffusion (pixels with significantly *increased* mean diffusivity are shown in red). Maps of the anisotropy of diffusion (bottom row) show a decrease of the directionality of diffusion in myelinated structures including the right optic radiation (bottom left) and the forceps major of the corpus callosum (bottom right), (pixels with significantly *decreased* anisotropy are shown in red).

3.8.4 Discussion

Diffusion changes reflect an abnormal microstructural organization of tissue. The magnitude of diffusion increases if microstructural changes cause a widening of the extracellular space. The directionality (anisotropy) of water diffusion changes if nerves or fibres are damaged (tab. 3.1). Cell loss and incomplete replacement resulting in a widened extracellular space would explain the increased magnitude of diffusion in our case. Diffuse axonal injury and secondary wallerian degeneration would explain the reduced anisotropy in central white matter structures.

3.8.5. Conclusion

Our finding suggests that DTI can be a sensitive tool for the detection of abnormalities after blunt head trauma thus allowing the in vivo quantitation of damage in this disabling condition.

3.9 Diffusion changes in status epilepticus

3.9.1 Introduction

During status epilepticus transient signal changes on standard T2-weighted MR images have been reported.[147,148,149,150,151,152] However, these changes were non-specific and involved both grey and white matter. Diffusion weighted imaging (DWI) is a MR method sensitive for diffusion of water and provides a contrast different from T1- and T2-relaxation. The apparent diffusion coefficient (ADC), a measure of diffusion, can be calculated. The ADC may provide different information about the pathophysiological changes in the investigated tissue. Diffusion is a fundamental biological process and is likely to be altered in stages of neuronal dysfunction. DWI has been used to investigate brain ischemia. In the

early stages of brain ischemia diffusion is reduced in the ischemic area involving both cortex and white matter. In the later stages of ischemia, after cell death, diffusion increases. In experimental status epilepticus similar diffusion changes have been demonstrated (see tab.3.1). The diffusion first decreased in the piriform cortex and amygdala in kainic acid induced status, this was followed in the later stages of the status. However, the application of DWI in humans during status has previously been hampered by hardware and software limitations of MR scanners, particularly by the long image acquisition time required. We used a diffusion weighted echo planar imaging (EPI) sequence which is fast enough to make the technique applicable to the investigation of humans during status to investigate a 51 year old female patient during and after focal status epilepticus.

3.9.2 Methods

3.9.2.1 Patient

The patient's condition was characterized by bilateral optic neuritis and recurrent focal status epilepticus but the underlying diagnosis of her condition remained unknown. Intensive investigations for metabolic, autoimmune and genetic disorders including muscle biopsy had been negative. The current status continued for 22 days and consisted of intermittent myoclonus in the right leg affecting predominantly the right tibialis anterior and quadriceps muscle. The status was followed by a Todd's paresis that persisted for several days.

3.9.2.2 DWI parameters

A General Electric Horizon Echospeed 1.5T scanner with SR120 gradients was used (gradient strength 22 mT/m, slew rate 120 T/m/s). For DWI a single-shot EPI sequence modified with pulsed diffusion gradients has been designed. EPI parameters were TR 2RR (about 2s) for gated EPI, TE 95 ms, matrix size 128 x 128, field of view 24 cm, slice thickness 5 mm, receiver bandwidth 91 kHz. Four

diffusion weighted steps (b=0 s/mm^2, b=107 s/mm^2, b=427 s/mm^2, b=960 s/mm^2) were repeated approximately every 8 seconds, depending on the patients heart rate, 24 times in three slices. Diffusion weighted gradients were applied in phase, frequency and slice select direction. The accuracy and the repeatability of the sequence were previously assessed.[43] The patient had been scanned in the same position in both scans. The resulting images were averaged to increase the signal to noise ratio and ADC maps were generated using least square fitting routine for each direction x, y, z. A map of the mean ADC was generated. The mean ADC is approximately the same as one third of the trace of the diffusion tensor, a property that is truly invariant under rotations of the tissue structure.[153] Measurements on ADC maps were performed in regions of interests (ROI) on mean ADC maps. The size of the ROI was 20 pixels for measurements in the white matter and 10 pixels for measurements in the grey matter. The mean signal intensity in the ROI and the standard error (standard deviation of signal intensities divided by the square root of the number of pixels) were calculated for each measurement. For standard imaging we used a spin echo T_1-weighted sequence (TR/TE/NEX 620/16/1) and a fast spin echoT_2-weighted sequence (TR/TEef/NEX 4500/92/2).

3.9.3 Results

A T_2-weighted MRI scan performed 15 days after the onset of status showed a non-specific high signal in the left paracentral lobule. Two DWI investigations were performed, the first during status (day 15) and the second four days after it ended. During status the motor cortex of the right leg returned a high signal on DWI indicating a decrease in water diffusion (fig.3.21). The change was independent of the direction of diffusion gradient. The underlying white matter returned a low signal on DWI, independent of the direction of the diffusion gradient. EPI images without diffusion weighting showed a high signal in both grey and white matter in this area. Four days after the clinical end of the status, when the patient still had a Todd's paresis, the abnormal signal on both DWI and

EPI images without diffusion weighting had almost resolved. Quantification of the ADC changes revealed a cortical ADC of 0.74 x 10^{-3} mm^2/s in the clinically affected area during status and of 0.99 x 10^{-3} mm^2/s after status. (A relative decrease of 27% during status). The ADC of the subcortical white matter was 0.98 x 10^{-3} mm^2/s during status and of 0.74 x 10^{-3} mm^2/s after status. (A relative increase of 31% during status). The ADC in the unaffected contra lateral grey matter was 0.84 x 10^{-3} mm^2/s during status and 0.91 x 10^{-3} mm^2/s after status. The ADC in the contra lateral white matter was 0.65 x 10^{-3} mm^2/s during status and 0.62 x 10^{-3} mm^2/s after status. ADC values in the clinically non affected areas were within the range of our normal controls.

3.9.4 Discussion

We found an interesting pattern of diffusion changes in our 51 year old female patient with during focal status epilepticus. DWI during status showed a decreased diffusion in the motor cortex of the right leg (relative decrease in ADC of 27%). Surprisingly, the diffusion was increased in the subcortical white matter (relative

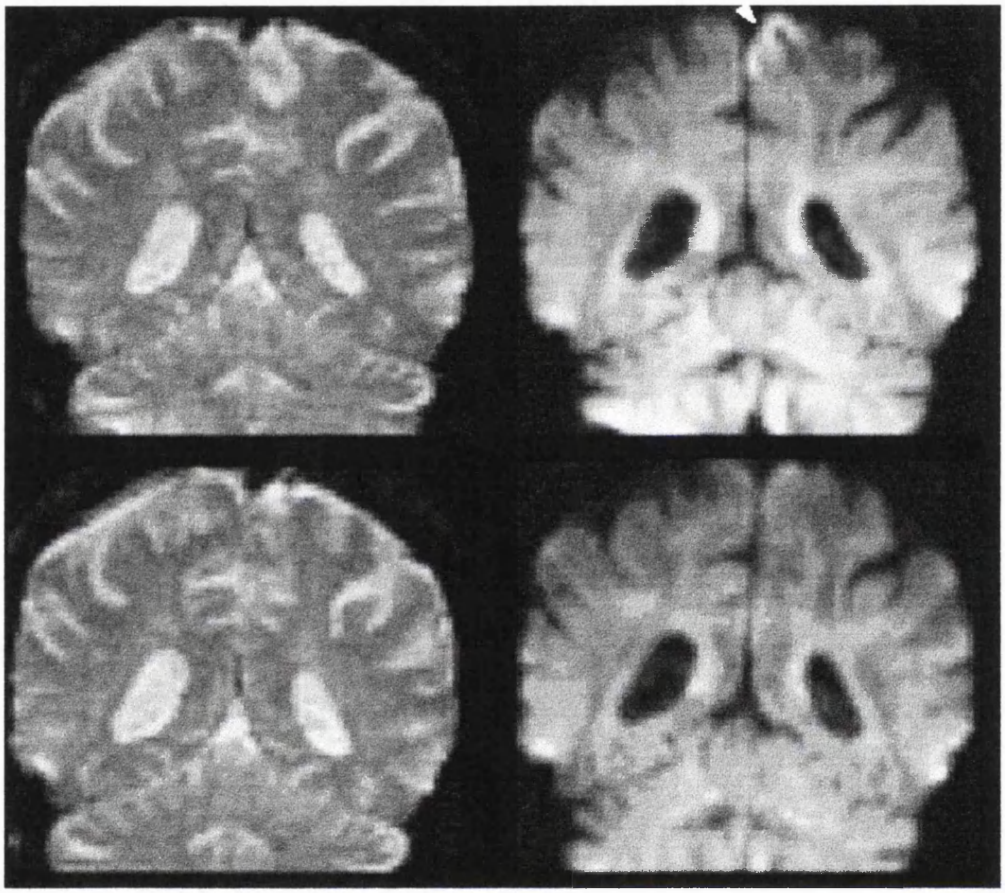

Figure - 3.21 DWI during and after status. The status affected the right leg (left on images is patient's right). Top left: T2-weighted images during status. Top right: DWI during status. Bottom left: T2-weighted image after status. Bottom right: DWI after status. On DWI during status a high signal in the motor cortex of the right leg (indicating a decreased diffusion, arrow head) and a low signal in the subcortical white matter (indicating an increased diffusion) is visible. Both changes resolved after status.

increase in ADC of 31%). On the T2-weighted image both cortex and subcortical white matter of the corresponding region returned a high signal similar to previously reported cases. After the cessation of the status, during the period of

the transient paresis, repeat DWI and T2-weighted imaging demonstrated resolution of these abnormalities. Resolution of diffusion changes preceded functional recovery. To our knowledge this is the first reported case of human focal status epilepticus investigated with DWI. The pattern of diffusion changes observed by us differed from the changes observed so far in brain ischemia and experimental status since the decrease in cortical diffusion was associated with an increased diffusion in the subcortical white matter. A possible explanation for the pattern of diffusion changes are water shifts associated with protracted epileptic activity. During epileptic activity the extracellular space (ES) shrinks due to a water flux into cells at the area of maximal neuronal activity (in the cortex). At the same time, the ES expands in areas remote to the neuronal activity.[154] This may explain the decrease in diffusion in the cortex and increase in diffusion in the subcortical white matter.

3.9.5. Conclusion

Our results imply that diffusion changes in status epilepticus differ from those observed in ischemia and that they are not inevitably followed by cell death.

3.10 EEG-correlated diffusion-weighted fMRI in epilepsy - a preliminary study

3.10.1 Introduction

Diffusion-weighted imaging (DWI) has been shown to be sensitive to the cellular changes occurring following stroke. DWI detects diffusion changes in the animal brain in epileptic events, but there are many difficulties in humans. These are mainly associated with the extreme motion-sensitivity of the diffusion sequence which effectively precludes study of any ictal events in which there is movement. Cardiac gating is normally used to mitigate these effects, however epileptic seizures are associated with cardiac arrythmia and the resulting variable TR renders this approach ineffective for snap-shot EPI-based DWI. We have detected diffusion changes in diffusion in both the grey and white matter in a patient in simple partial status (see 4.9), but a more robust approach is needed to study less severe ictal events. We have developed a method of recording EEG safely in the scanner[155] and used EEG-correlated fMRI to reproducibly localise areas of epileptic activity.[156] Here we report our preliminary results of EEG-triggered DWI.

3.10.2 Methods

We investigated a 47-year old woman with a 7-year history of complex partial seizures. EEG-correlated fMRI was performed (matrix 128 x 128 FOV 24 cm, TE 40 ms, TR 30 s, 10 5mm slices in 4 s), with a typical delay of 2s between the EEG event (spike or rest) and the start of gradient-echo EPI acquisition. In a separate study, EEG-correlated DWI was performed with similar timings and parameters except as noted (matrix 64 x 64, FOV 24 cm, TE 78 ms, TR 30 s, delta 28 ms, DELTA 35 ms, b 700 s/mm^2, 10 5mm slices in 2.5 s). The data were transferred to an off-line workstation for processing. 3D-registration with through-plane spin-history correction was used to motion-correct and detrend the data.[157]

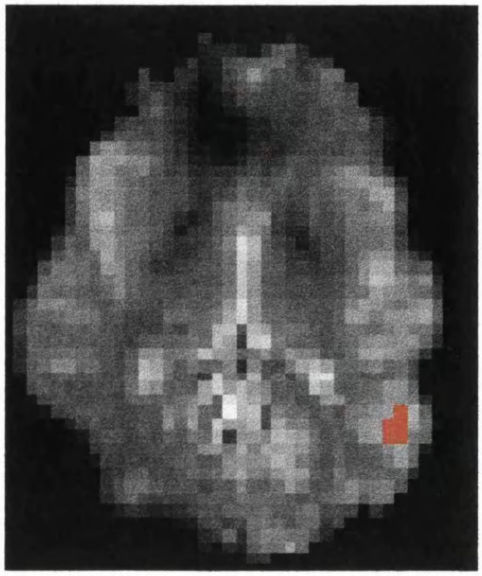

Figure - 3.22 fMRI (BOLD) activation map. Pixels with significant change are shown in red.

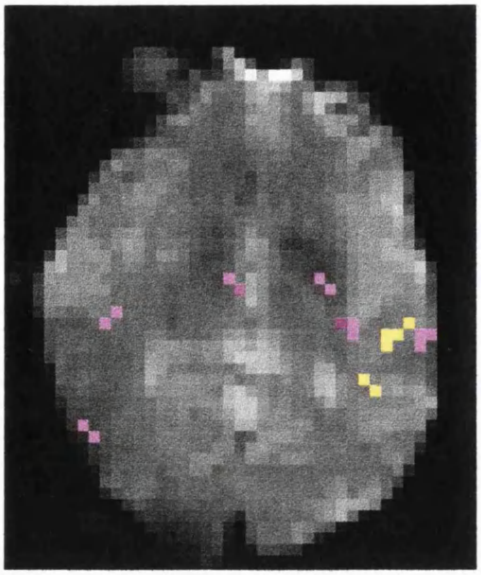

Figure - 3.23 DWI (right) activation map. Pixels with significant change are shown in yellow (increased diffusion) and pink (decreased diffusion).

A t-test was used to detect areas of significant change between those epochs identified as having EEG spikes and those having no spikes. In-plane clustering was applied to remove small activations that were unlikely to be of biological significance.

3.10.3 Results

Activation maps for the gradient-echo and DWI exams are shown in fig. 3.22 and fig. 3.23 at a confidence level of 95%. The slice shown for both studies contains an area of activation in the left temporal region that was identified from the fMRI study as being strongly correlated with the area localised by the EEG. In spite of the larger variation in the DWI data, similar areas were activated in the left temporal region.

3.10.4 Discussion and conclusion

While the delay associated with the Haemodynamic Response Function facilitates concurrent acquisition of EEG and MRI data for an EEG-correlated fMRI experiment, it is likely that the diffusion changes associated with epileptiform events follow a different time-scale. Simultaneous EEG and MRI acquisition would be needed to observe more rapid changes. Using the approach to data acquisition and processing developed for fMRI, EEG-correlated DWI offers the possibility of detecting changes in diffusion reflecting shrinkage of extracellular cell space or neuronal swelling, and this information, particularly taken in combination with other functional data, may lead to new insights about the mechanisms of seizures in epilepsy. More studies are necessary to confirm that DWI is sensitive for the detection of changes after single spikes and to establish whether there is a relationship between DWI and fMRI.

4.11 References

1. Fullerton GD. Physiologic basis of magnetic relaxation. In: Stark DD, Bradley WG Jr eds. *Magnetic resonance imaging*, second ed. Mosby-Year Book, St Louis 1992:88-108.

2. Crank J. *The mathematics of diffusion.* Oxford 1975.

3. Einstein A. *Ann Physik* 1905;**17**:549.

4. Mills R. Self-diffusion in normal and heavy water in the range 1-45°. *J Phys Chem* 1973;**77**:685-688.

5. Hahn E. Spin echoes. *Phys Rev* 1950;**80**:580-594.

6. Carr HY, Purcell EM. Effects of diffusion on free precession in nuclear magnetic resonance experiments. *Phys Rev* 1954;**94**:630-638.

7. Woessner DE. Effects of diffusion on nuclear magnetic resonance experiments. *J Chem Phys* 1961;**34**:2057-2061.

8. Stejskal EO, Tanner JE. Spin diffusion measurements: spin echoes in the presence of time-dependent field gradient. *J Chem Phys* 1965;**42**:288-292.

9. LeBihan D, Breton E, Lallemand D, Grenier P, Cabanis E, Laval-Jeantet M. MR imaging of intravoxel incoherent motions: application to diffusion and perfusion in neurologic disorders. *Radiology* 1986;**161**:401-407.

10. LeBihan D, Basser PJ. Molecular diffusion and nuclear magnetic resonance. In: LeBihan D, ed. *Diffusion and perfusion magnetic resonance imaging.* Raven Press, New York 1995:5-17.

11. Stejskal EA. Use of spin echos in a pulsed magnetic field gradient to study restricted diffusion and flow. *J Chem Phys* 1965;**43**:3597-3603.

12. Wayne RC, Cotts RM. Nuclear magnetic resonance study of self-diffusion in a bounded medium. *Phys Rev* 1966;**151**:264-272.

13. Tanner JE, Stejskal EO. Restricted self diffusion of protons in colloidal systems by the pulsed gradient spin echo method. *J Chem Phys* 1968;**49**:1768-1777.

14. Neuman CH. Spin echo of spins diffusing in a bounded medium. *J Chem Phys* 1974;**60**:4508-4511.

15. Callaghan PT. Pulsed field gradient nuclear magnetic resonance as a probe of liquid state molecular organization. *Aust J Phys* 1984;**37**:359-387.

16. Von Meerwall E, Ferguson RD. Interpreting pulsed-gradient spin-echo diffusion experiments with permeable membranes. *J Chem Phys* 1981;**74**:6956-6959.

17. Hansen JR. Pulsed NMR study of water mobility in muscle and brain tissue. *Biochim Biophys Acta* 1971;**230**:482-486.

18. Moseley ME, Cohen Y, Kucharczyk J, Mintorovitch J, Asgari HS, Wendland M, Tsuruda J, Norman D. Diffusion-weighted MR imaging of anisotropic water diffusion in cat central nervous system. *Radiology* 1990;**176**:439-445.

19. Doran M, Hajnal JV, Van Bruggen N, King MD, Young IR, Bydder GM. Normal and abnormal white matter tracts shown by MR imaging using directional diffusion weighted sequences. *J Comput Assist Tomogr* 1990;**14**:685-873.

20. Hajnal JV, Doran M, Hall AS, Collins AG, Oatridge A, Pennock JM, Young IR, Bydder GM. MR imaging of anisotropically restricted diffusion of water in the nervous system: technical, anatomic and pathological considerations. *J Comp Assist Tomogr* 1991;**15**:1-18.

21. Moseley ME, Kucharczyk J, Asgari HS, Norman D. Anisotropy in diffusion weighted MRI. *Magn Reson Med* 1991;**19**:312-326.

22. Beaulieu C, Allen PS. Determinants of anisotropic water diffusion in nerves. *Magn Reson Med* 1994;**31**:394-400.

23. Beaulieu C, Allen PS. Water diffusion in the giant axon of the squid: implications for diffusion-weighted MRI of the nervous system. *Magn Reson Med* 1994;**32**:579-583.

24. Copper RL, Chang DB, Young AC, Martin CJ, Ancker-Johnson B. Restricted diffusion in biophysical systems. *Biophys J* 1974;**14**:161-177.

25. Tanner JE. Self diffusion of water in frog muscle. *Biophys J* 1979;**28**:107-116.

26. Tanner JE. Intracellular diffusion of water. *Arch Biochem Biophys* 1983;**224**:416-428.

27. Latour LL, Svoboda K, Mitra PP, Sotak CH. Time-dependent diffusion of water in a biological model system. *Proc Natl Acad Sci USA* 1994;**91**:1229-1233.

28. Le Bihan D, Breton E, Lallemand D, Aubin M, Vignaud J, Laval-Jenatet M. Separation of diffusion and perfusion in intravoxel incoherent motion MR imaging. *Radiology* 1988;**168**:497-505.

29. Le Bihan D, Turner R. The capillary network: a link between IVIM and classical perfusion. *Magn Reson Med* 1992;**27**:171-178.

30. Le Bihan D, Breton E. Imagerie de diffusion in-vivo par resonance magnetique nucleaire. *C R Acad Sci III* 1985;301:1109-1112.

31. Taylor DG, Bushell MC. The spatial mapping of translational diffusion coefficients by the NMR imaging technique. *Phys Med Biol* 1985;**30**:345-349.

32. Merboldt KD, Hanicke W, Frahm J. Self-diffusion NMR imaging using stimulated echoes. *J Magn Reson* 1985;**64**:479-486.

33. Mansfield P, Morris PG. NMR imaging in biomedicine. In: Waugh JS ed: *Advances in Magnetic Resonance Imaging.* New York, Academic Press 1982.

34. Wesbey GE, Moon K, Crooks L, Arakawa M, Brash R. Proton T2 reduction due to spin diffusion through pulsed-gradients in spin-echo NMR imaging. Imaging implications and applications. *Magn Reson Med* 1984;**1**:273.

35. Wesbey GE, Moseley ME, Ehman RL. Translational molecular self-diffusion in magnetic resonance imaging II. Measurement of the self diffusion coefficient. *Invest Radiol* 1984;**19**:491-498.

36. Basser PJ, Le Bihan D, Mattiellllo J. Estimation of the effective self-diffusion tensor from the NMR spin echo. *J Magn Reson B* 1994;**103**:247-254.

37. Conturo TE, McKinstry RC, Akbudak E, Robinson BH. Encoding of anisotropic diffusion with tetrahedral gradients: a general mathematical diffusion formalism and experimental results. *Magn Reson Med* 1996;**35**:399-412.

38. Van Gelderen P, de Vleeschouwer MHM, DesPres D, Pekar J, van Zijl PCM, Moonen CTW. Water diffusion and acute stroke. *Magn Reson Med* 1994;**31**:154-163.

39. Basser PJ, Pierpaoli C. Microstructural and physiological features of tissues elucidated by quantitative-diffusion-tensor MRI. *J Magn Reson B* 1996;**111**:209-219.

40. Pierpaoli C, Basser PJ. Toward a quantitative assessment of diffusion anisotropy. *Magn Reson Med* 1996;**36**:893-906.

41. Poncelet BP, Wedeen VJ, Weiskoff RM, Cohen MS. Brain parenchyma motion: measurement with cine echo-planar MR imaging. *Radiology* 1992;**185**:645-651.

42. Turner R, Le Bihan D, Maier J, Vavrek R, Hedges LK, Pekar J. Echo-planar imaging of intravoxel incoherent motion. *Radiology* 1990;**177**:407-414.

43. Wieshmann UC, Franconi F, Symms MR, Clark CA, Barker GJ, Shorvon SD. The variability and accuracy of the apparent diffusion coefficient in diffusion weighted EPI. *Proceedings of the International Society for Magnetic Resonance in Medicine, fifth scientific meeting.* ISMRM, Berkeley, CA 1997:1748.

44. Anderson AW, Gore JC. Analysis and correction of motion artefacts in diffusion weighted imaging. Magn Reson Med 1994;**32**:379-387.

45. Wieshmann UC, Lemieux L, Symms MR, Franconi F, Clark CA, Barker GJ, Shorvon SD. Oversampling rejecting averaging correction algorithm for non-gated single shot diffusion weighted EPI. *Proceedings of the International Society for Magnetic Resonance in Medicine, sixth scientific meeting.* ISMRM, Berkeley, CA 1998:1230.

46. Xing D, Papadakis NG, Huang CL, Lee VM, Carpenter TA, Hall LD. Optimised diffusion-weighting for measurement of apparent diffusion coefficient (ADC) in human brain. *Magn Reson Imaging* 1997;**15**:771-784.

47. Wielopolski PA, Edelman RR. Echo planar imaging. *Electromedica* 1995;**63**:18-25.

48. Symms MR, Barker GJ, Franconi F, Clark CA. Correction of eddy-current distortions in diffusion-weighted echo-planar images with a two-dimensional registration technique. *Proceedings of the International Society of Magnetic Resonance in Medicine, fifth scientific meeting.* ISMRM, Berkeley, CA 1997:1723.

49. Mancuso A, Karibe H, Rooney WD, Zarow GJ, Graham SH, Weiner MW, Weinstein PR. Correlation of early reduction in the apparent diffusion coefficient of water with blood flow reduction during middle cerebral artery occlusion in rats. *Magn Reson Med* 1995;**34**:368-377.

50. Back T, Hoehn-Berlage M, Kohno K, Hossman KA. Diffusion nuclear magnetic resonance imaging in experimental stroke: correlation with cerebral metabolites. *Stroke* 1994;**25**:494-500.

51. Dreher W, Kuhn B, Gyngell ML, Busch E, Niendorf T, Hossmann KA, Leibfritz D. Temporal and regional changes during focal ischemia in rat brain studied by proton spectroscopic imaging and quantitative diffusion NMR imaging. *Magn Reson Med* 1998;**39**:878-888.

52. Bizzi A, Righini A, Turner R, LeBihan D, DesPres D, Di Chiro G, Alger JR. MR of diffusion slowing in global cerebral ischemia. *Am J Neuroradiol* 1993;**14**:1347-1354.

53. Fischer M, Bockhorst K, Hoehn-Berlage M, Schmitz B, Hossmann KA. Imaging of the apparent diffusion coefficient for the evaluation of cerebral metabolic recovery after cardiac arrest. *Magn Reson Imaging* 1995;**13**:781-790.

54. Pierpaoli C, Alger JR, Righini A, Mattiello J, Dickerson R, Des Pres D, Barnett A, Di Chiro G. High temporal resolution diffusion MRI of global cerebral ischemia and reperfusion. *J Cereb Blood Flow Metab* 1996;**16**:892-905.

55. Sevick RJ, Kanda F, Mintorovitch J, Arieff AI, Kucharczyk J, Tsuruda JS, Norman D, Moseley ME. Cytotoxic brain edema: assessment with diffusion-weighted MR imaging. *Radiology* 1992;**185**:687-690.

56. Righini A, Pierpaoli C, Alger JR, Di Chiro G. Brain parenchyma apparent diffusion coefficient alterations associated with experimental complex partial status epilepticus. *Magn Reson Imaging* 1994;**12**:865-871.

57. Nakasu Y, Nakasu S, Morikawa S, Uemura S, Inubushi T, Handa J. Diffusion-weighted MR in experimental sustained seizures elicited with kainic acid.

Am J Neuroradiol 1995;**16**:1185-1192.

58. Ebisu T, Rooney WD, Graham SH, Mancuso A, Weiner MW, Maudsley AA. MR spectroscopic imaging and diffusion-weighted MRI for early detection of kainate-induced status epilepticus in the rat. *Magn Reson Med* 1996;**36**:821-828.

59. Wang Y, Majors A, Najm I, Xue M, Comair Y, Modic M, Ng TC. Postictal alteration of sodium content and apparent diffusion coefficient in epileptic rat brain induced by kainic acid. *Epilepsia* 1996;**37**:1000-1006.

60. Zhong J, Petroff OA, Prichard JW, Gore JC. Changes in water diffusion and relaxation properties of rat cerebrum during status epilepticus. *Magn Reson Med* 1993;**30**:241-246.

61. Zhong J, Petroff OA, Prichard JW, Gore JC. Barbiturate-reversible reduction of water diffusion coefficient in flurothyl-induced status epilepticus in rats. *Magn Reson Med* 1995;**33**:253-256.

62. Zhong J, Petroff OAG, Pleban LA, Gore JC, Prichard JW. Reversible, reproducible reduction of brain water apparent diffusion coefficient by cortical electroshocks. *Magn Reson Med* 1997;**37**:1-6.

63. Latour LL, Hasegawa Y, Formato JE, Fisher M, Sotak CH. Spreading waves of decreased diffusion coefficient after cortical stimulation in the rat brain. *Magn Reson Med* 1994;**32**:189-198.

64. Hasegawa Y, Latour LL, Formato JE, Sotak CH, Fisher M. Spreading waves of a reduced diffusion coefficient of water in normal and ischemic rat brain. *J Cereb Blood Flow Metab* 1995;**15**:179-187.

65. Busch E, Hoehn-Berlage M, Eis M, Gyngell ML, Hossmann KA. Simultaneous recording of EEG, DC potential and diffusion-weighted NMR imaging during potassium induced cortical spreading depression in rats. *NMR Biomed* 1995;**8**:59-64.

66. De Crespigny A, Rother J, van Bruggen N, Beaulieu C, Moseley ME. Magnetic resonance imaging assessment of cerebral hemodynamics during spreading depression in rats. *J Cereb Blood Flow Metab* 1998;**18**:1008-1017.

67. Lynch LA, Lythgoe DJ, Haga EK, Smart SC, Beech JS, Millan M, Kinchesh P, Meldrum BS, Williams SCR. Temporal evolution of CNS damage in a rat model of chronic epilepsy. *Proceedings of the International Society of Magnetic Resonance in Medicine, fourth scientific meeting.* ISMRM, Berkeley 1996:521.

68. Hasegawa Y, Formato JE, Latour LL, Gutierrez JA, Liu KF, Garcia JH, Sotak CH, Fisher M. Severe transient hypoglycaemia causes reversible change in the apparent diffusion coefficient of water. *Stroke* 1996;**27**:1648-1655.

69. Unterberg AW, Stroop R, Thomale UW, Kiening KL, Pauser S, Vollmann W. Characterisation of brain edema following "controlled cortical impact injury" in rats.

Acta Neurochir Suppl (Wien) 1997;**70**:106-108.

70. Barzo P, Marmarou A, Fatouros P, Hayasaki K, Corwin F. Contribution of vasogenic and cellular edema to traumatic brain swelling measured by diffusion-weighted imaging. *J Neurosurg* 1997;**87**:900-907.

71. Anderson AW, Zhong J, Petroff OA, Szafer A, Ransom BR, Prichard JW, Gore JC. Effects of osmotically driven cell volume changes on diffusion-weighted imaging of the rat optic nerve. *Magn Reson Med* 1996;**35**:162-167.

72. Beaulieu C, Does MD, Snyder RE, Allen, PS. Changes in water diffusion due to Wallerian degeneration in periphal nerve. *Magn Reson Med* 1996;**36**:627-631.

73. Baratti C, Barnett A, Pierpaoli C. Comparative MRI study of brain maturation using T1, T2, and the diffusion tensor. *Proceedings of the International Society of Magnetic Resonance in Medicine, fifth scientific meeting.* ISMRM, Berkeley 1997:504.

74. Warach S, Chien D, Li W, Ronthal M, Edelman RR. Fast magnetic resonance diffusion-weighted imaging of acute human stroke. *Neurology* 1992;**42**:1717-1723.

75. Schlaug G, Siewert B, Benfield A, Edelman RR, Warach S. Time course of the apparent diffusion coefficient (ADC) abnormality in human stroke. *Neurology* 1997;**49**:113-119.

76. DeCrespigny AJ, Marks MP, Enzmann DR, Moseley ME. Navigated diffusion imaging of normal and ischemic human brain. *Magn Reson Med* 1995;**33**:720-728.

77. Lutsep HL, Albers GW, DeCrespigny A, Kamat GN, Marks MP, Moseley ME. Clinical utility of diffusion-weighted magnetic resonance imaging in the assessment of ischemic stroke. *Ann Neurol* 1997;**41**:574-580.

78. Vuadens P, Bogousslavsky J. Diagnosis as a guide to stroke therapy. *Lancet* 1998;**352**:(suppl III):5-9.

79. Koroshetz WJ, Gonzalez G. Diffusion-weighted MRI: An ECG for "brain attack". *Ann Neurol* 1997;**41**:565-566.

80. Zivin JA. Diffusion-weighted MRI for diagnosis and treatment of ischemic stroke. *Ann Neurol* 1997;**41**:567-568.

81. Horsfield MA, Lai M, Webb SL, Barker GJ, Tofts PS, Turner R, Rudge P, Miller DH. Apparent diffusion coefficients in benign and secondary progressive multiple sclerosis by nuclear magnetic resonance. *Magn Reson Med* 1996;**36**:393-400.

82. Christiansen P, Gideon P, Thomsen C, Stubgaard M, Henriksen O, Larson HB. Increase water self-diffusion in chronic plaques and in apparently normal white matter in patients with multiple sclerosis. *Acta Neurol Scand* 1992;**87**:195-199.

83. Tien RD, Felsberg GJ, Friedman H, Brown M, MacFall J. MR imaging of high-grade cerebral gliomas: value of diffusion-weighted echoplanar pulse sequences. *Am J Roentgenol* 1994;**162**:671-677.

84. Tsuruda JS, Chew WM, Moseley ME, Norman D. Diffusion-weighted MR imaging of the brain: value of differentiating between extraaxial cysts and epidermoid tumors. *Am J Neuroradiol* 1990;**11**:925-931.

85. Werring DJ, Clark CA, Barker GJ, Miller DH, Parker GJM, Brammer MJ, Bullmore ET, Giampietro VP, Thompson AJ. The structural and functional mechanisms of motor recovery: complementary use of diffusion tensor and functional magnetic resonance imaging in a traumatic injury of the internal capsule. *J Neurol Neurosurg Psychiatry* 1998;**65**:863-869.

86. Pierpaoli C, Choi B, Schiffmann R, Di Chiro G. Diffusion tensor MRI in Pelizaeus-Merzbacher disease. *Proceedings of the International Society of Magnetic Resonance in Medicine, fifth scientific meeting.* ISMRM, Berkeley 1995:664.

87. Hanyu H, Sakurai H, Iwamoto T, Takasaki M, Shindo H, Abe K. Diffusion-weighted MR imaging of the hippocampus and temporal white matter in Alzheimer's disease. *J Neurol Sci* 1998;**156**:195-200.

88. Sandson TA, Felician O, Edelman RR, Warach S. Diffusion-weighted magnetic resonance imaging in Alzheimer's disease. *Dement Geriatr Cogn Disord* 1999;**10**:166-171.

89. Demaerel P, Baert AL, Vanopdenbosch L, Robberecht W, Dom R. Diffusion-weighted magnetic resonance imaging in Creutzfeldt-Jakob disease. *Lancet* 1997; **349:** 847.

90. Mathern GW, Babb TL, Leite JP, Pretorius JK, Yeoman KM, Kuhlman PA. The pathogenic and progressive features of chronic human hippocampal epilepsy. *Epilepsy Res* 1996;**26**:151-161.

91. Wieser, GH. Selective amygdalo-hippocampectomy for temporal lobe epilepsy. *Epilepsia* 1988;**29**(suppl.2):S100-S113.

92. Commission on classification and terminology of the international league against epilepsy. Proposal for revised clinical and electroencephalographic classification of epileptic seizures. *Epilepsia* 1981;**22**:489-501.

93. Commission on classification and terminology of the international league against epilepsy. Proposal for revised classification of epilepsies and epileptic syndromes. *Epilepsia* 1989;**30**:389-399.

94. Clark CA, Droogan A, Anderson AW, Barker GJ, Tofts PS. Diffusion imaging of multiple sclerosis plaques using a navigated PGSE. Proceedings of the International Society of Magnetic Resonance in Medicine, fifth scientific meeting. ISMRM,

Berkeley, CA 1997:1715.

95. Grünewald RA, Jackson GD, Connelly A, Duncan JS. MR detection of hippocampal disease in epilepsy: factors influencing T2 relaxation time. *Am J Neuroradiol* 1994;**15**:1149-1156.

96. Pierpaoli C, Jezzard P, Basser PJ, Barnett A, Di Chiro G. Diffusion tensor MR imaging of the human brain. *Radiology* 1996;**20**:637-648.

97. Cook MJ, Fish DR, Shorvon SD, Straughan K, Stevens JM. Hippocampal volumetric and morphometric studies in frontal and temporal lobe epilepsy. *Brain* 1992;**115**:1001-1015.

98. Duncan JS, Bartlett P, Barker GJ. Technique for measuring T2 relaxation time. *Am J Neuroradiol* 1996;**17**:1805-1810.

99. Wieshmann UC, Free SL, Stevens JM, Shorvon SD. Image contrast and hippocampal volumetric measurements. *Magn Reson Imaging* 1998;**16**:13-17.

100. Free SL, Bergin PS, Fish DR, Cook MJ, Shorvon SD, Stevens JM. Methods for normalization of hippocampal volumes measured with MR. *Am J Neuroradiol* 1995;**16**:637-643.

101. Zhong J, Petroff OA, Spencer S, Gore JC. T2 and ADC maps of hippocampi in patients with complex partial seizures. Proceedings of the International Society of Magnetic Resonance in Medicine, fourth scientific meeting. ISMRM, Berkeley, CA 1996:227.

102. Jackson GD, Berkovic SF, Tress BM, Kalnins RM, Fabinyi GC, Bladin PF. Hippocampal sclerosis can be reliably detected by magnetic resonance imaging. *Neurology* 1990;**40**:1869-1875.

103. Cascino GD, Jack CR, Parisi JE, Sharbrough FW, Hirschhorn KA, Meyer FB, Marsh WR, O'Brien PC. Magnetic resonance imaging-based volume studies in temporal lobe epilepsy: pathological correlations. *Ann Neurol* 1991;**30**:31-36.

104. Bronen RA, Cheung G, Charles JT, Kim JH, Spencer DD, Spencer SS, Sze G, McCarthy G. Imaging findings in hippocampal sclerosis: correlation with pathology. Am J Neuroradiol 1991;**12**:933-940.

105. Kim JH, Tien RD, Felsberg GJ, Osumi AK, Lee N, Friedman AH. Fast spin-echo MR in hippocampal sclerosis: Correlation with pathology and surgery. *Am J Neuroradiol* 1995;**16**:627-636.

106. Van Paesschen W, Revesz T, Duncan JS, King MD, Connelly A. Quantitative Neuropathology and quantitative magnetic resonance imaging of the hippocampus in temporal lobe epilepsy. *Ann Neurol* 1997;**42**:756-766.

107. Morris PG. *Nuclear magnetic resonance imaging in medicine and biology.* Oxford University Press, Oxford 1986:257-374.

108. Wieshmann UC, Free SL, Everitt AD, Bartlett PA, Barker GJ, Tofts PS, Duncan JS, Shorvon SD, Stevens JM. MR imaging in epilepsy with a fast FLAIR sequence. *J Neurol Neurosurg Psychiatry* 1996;**61**:357-361.

109. Warach S, Gaa M, Siewert B, Wielopolski P, Edelman RR. Acute human stroke studied by whole brain echo planar diffusion-weighted magnetic resonance imaging. *Ann Neurol* 1995;**37**:231-241.

110. Baird AE, Benfield A, Schlaug G, Siewert B, Lövblad KO, Edelman RR, Warach S. Enlargement of human cerebral ischemic lesion volumes measured by diffusion-weighted magnetic resonance imaging. *Ann Neurol* 1997;**41**:581-589.

111. Marks MP, DeCrespigny A, Lentz D, Enzmann DR, Albers GW, Moseley ME. Acute and chronic stroke: navigated spin-echo diffusion-weighted MR imaging. *Radiology* 1996; **199**:403-408.

112. Clark CA, Droogan A, Anderson AW, Barker GJ, Tofts PS. Diffusion imaging of multiple sclerosis plaques using a navigated PGSE. *Proceedings of the International Society of Magnetic Resonance in Medicine, fifth scientific meeting.* ISMRM, Berkeley 1997:1715.

113. Barr ML, Kierman JA. *The human nervous system. An anatomical viewpoint.* Philadelphia: Harper & Row,1983:242-251.

114. Talairach J, Tournoux P. *Referentially oriented cerebral MRI anatomy.* Stuttgart: Georg Thieme Verlag, 1993:202.

115. Doran M, Hajnal JV, Van Bruggen N, King MD, Young IR, Bydder GM. Normal and abnormal white matter tracts shown by MR imaging using directional diffusion weighted sequences. *J Comput Assist Tomogr* 1990;**14**:865-873.

116. Pierpaoli C, Jezzard P, Basser PJ, Barnett A, Di Chiro G. Diffusion tensor MR imaging of the human brain. *Radiology* 1996;**20**:637-648.

117. Makris N, Worth AJ, Sorensen AG, Papadimitriou GM, Wu O, Reese TG, Wedeen VJ, Davis TL, Stakes JW, Caviness VS, Kaplan E, Rosen BR, Pandya DN, Kennedy DN. Morphometry of in vivo human white matter association pathways with diffusion-weighted magnetic resonance imaging. *Ann Neurol* 1997;**42**:951-962.

118. LeBihan D. Anisotropic diffusion of brain white matter revisited: restriction, permeability and tortuosity. *Proceedings of the International Society of Magnetic Resonance in Medicine, fourth scientific meeting.* ISMRM, Berkeley, CA 1996:1324.

119. Baratti, C., Barnett, A., Pierpaoli, C. Comparative MRI study of brain maturation using T1, T2, and the diffusion tensor. *Proceedings of the International Society of Magnetic Resonance in Medicine, fifth scientific meeting.* ISMRM, Berkeley

1997:504.

120. DeMyer, W. Number of axons and myelin sheaths in adult human medullary pyramids. *Neurology* 1959;**9**:42-47.

121. Davidoff, RA. The pyramidal tract. *Neurology* 1990;**40**:332-339.

122. Beaulieu C, Does MD, Snyder RE, Allen, PS. Changes in water diffusion due to Wallerian degeneration in periphal nerve. *Magn Reson Med* 1996;**36**:627-631.

123. Ferner H, Staubesand J. *Sobotta Atlas der Anatomie des Menschen.* Urban & Schwarzenberg, München 1982.

124. Plummer DL. DispImage, a display and analysis tool for medical images. *Rev. Neuroradiol.* 1992;**5**:489-495.

125. DeMyer W. Number of axons and myelin sheaths in adult human medullary pyramids. *Neurology* 1959;**9**:42-47.

126. Pierpaoli C, Barnett A, Virta A, Penix L, Chen R. Diffusion MRI of wallerian degeneration. A new tool to investigate neural connectivity in vivo? *Proceedings of the International Society of Magnetic Resonance in Medicine, sixth scientific meeting.* ISMRM, Berkeley, CA 1998:1247.

127. Kuhn MJ, Johnson KA, Davis KR. Wallerian degeneration: evaluation with MR imaging. *Radiology* 1988;**168**:199-202.

128. Doyle WK, Spencer DD. Anterior temporal resections. In: Engel J Jr, Pedley TA, eds. *Epilepsy.* Philadelphia: Lippincott-Raven Publishers, 1997:1807-1817.

129. Wieshmann UC, Symms MS, Lemieux L, Franconi F, Clark CA, Barker GJ, Shorvon SD. MR tractography using diffusion tensor imaging and normalization to Talairach space. *J Neurol Neurosurg Psychiatry* 1999;**66**:271.

130. Lemieux L, Wieshmann UC, Moran NF, Fish DR, Shorvon SD. The detection and significance of subtle changes in mixed-signal brain lesions by serial MRI scan matching and spatial normalisation. *Medical Image Analysis* 1998;**2**:227-242.

131. Lemieux L, Barker GJ. Measurement of small inter-scan fluctuations in voxel dimensions in magnetic resonance images Using registration. *Medical Physics* 1998;**25**:1049-1054.

132. Chenevert TL, Brunberg JA, Pipe JG. Anisotropic diffusion in human white matter: demonstration with MR techniques in vivo. *Radiology* 1990;**177**:401-405.

133. Douek P, Turner R, Pekar J, Patronas N, LeBihan D. MR color mapping of myelin fiber orientation. *J Comput Assist Tomogr* 1991;**15**:923-929.

134. Pierpaoli C, Barnett A, Penix L, De Graba T, Basser PJ. Identification of fiber degeneration and organized gliosis in stroke patients by diffusion tensor MRI. *Proceedings of the International Society for Magnetic Resonance in Medicine, fourth scientific meeting.* Berkeley, CA 1996:563.

135. Renowden SA, Matkovic Z, Adams CB, Carpenter K, Oxbury S, Molyneux AJ, Anslow P, Oxbury J. Selective amygdalohippocampectomy for hippocampal sclerosis: postoperative MR appearance. *Am J Neuroradiol* 1995;16:1855-1861.

136. Creutzfeldt OD. *Cortex cerebri.* Springer Verlag, Berlin 1983:7-13.

137. Flood N, Zelaya F, Chalk J, Doddrell D. Improved delineation of ischemic lesion volume in human brain by combination of diffusion contrast, diffusion tensor trace and anisotropy images. *Proceedings of the International Society of Magnetic Resonance in Medicine, sixth scientific meeting.* ISMRM, Berkeley, CA 1998:1238.

138. Graham GD, Zhong J, Guarnaccia JB, Gore JC. Echo-planar imaging of water directional diffusion and diffusion anisotropy within multiple sclerosis plaques. *Proceedings of the International Society of Magnetic Resonance in Medicine, third scientific meeting.* ISMRM, Berkeley, CA 1995:278.

139. Werring DJ, Clark CA, Barker GJ, Symms MR, Franconi F, Thompson AJ, Miller DH. The structural properties of multiple sclerosis (MS) lesions demonstrated by diffusion tensor imaging. *Proceedings of the International Society of Magnetic Resonance in Medicine, sixth scientific meeting.* ISMRM, Berkeley, CA 1998:119.

140. Pierpaoli C, Choi B, Schiffmann R, Di Chiro G. Diffusion tensor MRI in Pelizaeus-Merzbacher disease. *Proceedings of the International Society of Magnetic Resonance in Medicine, fifth scientific meeting.* ISMRM, Berkeley, CA 1997:664.

141. Barker P, Ulug AM, Raymond GV, Moser H, Van Zijl PCM. Diffusion tensor imaging in x-linked adrenoleukodystropy. *Proceedings of the International Society of Magnetic Resonance in Medicine, sixth scientific meeting.* ISMRM, Berkeley, CA 1998:1338.

142. Wieshmann UC, Symms MR, Franconi F, Clark CA, Barker GJ, Shorvon SD. Reduced diffusion anisotropy in malformations of cortical development. *Proceedings of the International Society of Magnetic Resonance in Medicine, sixth scientific meeting.* ISMRM, Berkeley, CA 1998:1245.

143. Virta A, Barnett A, Pierpaoli C. Diffusion anisotropy changes in normal aging. A study of the descending projection pathways at the level of the cerebral peduncle. *Proceedings of the International Society of Magnetic Resonance in Medicine, sixth scientific meeting.* ISMRM, Berkeley, CA 1998:1347.

144. Buchsbaum MS, Tang CY, Peled S, Gudbjartsson H, Lu D, Hazlett EA, Downhill J, Haznedar M, Fallon JH, Atlas SW. MRI white matter diffusion anisotropy and PET metabolic rate in schizophrenia. *Neuroreport* 1998;**16**:425-430.

145. Virta A, Barnett A, Pierpaoli C. Diffusion anisotropy changes in normal aging. A study of the descending projection pathways at the level of the cerebral peduncle. *Proceedings of the International Society of Magnetic Resonance in Medicine, sixth scientific meeting.* ISMRM, Berkeley, CA 1998:1347.

146. Graham DI, Lantos PL (eds.) *Greenfield's neuropathology* sixth ed. Arnold, London, 1997:208-243.

147. Riela AR, Sires BP, Penry JK. Transient magnetic resonance imaging abnormalities during partial status epilepticus. *J Child Neurol* 1991;**6**:143-145.

148. Henry TR, Drury I, Brunberg JA, Pennell PB, McKeever PE, Beydoun A. Focal cerebral magnetic resonance changes associated with partial status epilepticus. *Epilepsia* 1994;**35**:35-41.

149. Cox JE, Mathews VP, Santos CC, Elster AD. Seizure-induced transient hippocampal abnormalities on MR: Correlation with positron emission tomography and electroencephalography. *Am J Neuroradiol* 1995;**16**,1736-1738.

150. Tien RD, Felsberg GJ. The hippocampus in status epilepticus: demonstration of signal intensity and morphologic changes with sequential fast spin-echo MR imaging. *Radiology* 1995;**194:**249-256.

151. Chan S, Chin SSM, Kartha K, Nordli DR, Goodman RR, Pedley TA. Reversible signal abnormalities in the hippocampus and neocortex after prolonged seizures. *Am J Neuroradiol* 1996;**17**:1725-1731.

152. Meierkord H, Wieshmann UC, Lehmann R, Niehaus L. Functional and structural consequences of status epilepticus demonstrated with MR imaging. *Acta Neurol Scand* 1997;**96**:127-132.

153. Basser P J, Mattiello J, Le Bihan D. MR diffusion tensor spectroscopy and imaging. *Biophys J* 1994;66:259-267.

154. Lux HD, Heinemann U, Dietzel I. Ionic changes and alterations in the size of the extracellular space during epileptic activity. In: Delgado-Escueta AV, Wasterlain CG, Treiman DM, Porter RJ (eds.) *Advances in Neurology* Raven Press, New York, 1986; **44:** 619-639.

155. Lemieux L, Allen PJ, Franconi F, Symms MR, Fish DR. Recording of EEG during fMRI experiments: patient safety. *Magn Reson Med* 1997;**38**:943-952.

156. Symms MR, Allen PJ, Woermann FG, Polizzi G, Krakow K, Barker GJ, Fish DR, Duncan JS. Reproducible localization of interictal epileptiform discharges using EEG-correlated fMRI. *Proceeding of the International Society for Magnetic Resonance in Medicine, sixth scientific meeting.* ISMRM, Berkeley 1998:168.

157. Bullmore E, Brammer M, Williams SC, Rabe-Hesketh S, Janot N, David A, Mellers J, Howard R, Sham P. Statistical methods of estimation and inference for

functional MR image analysis. *Magn Reson Med* 1996;**35**:261-277.

Chapter 4

More MR Imaging of the Hippocampus

4.1 Introduction

There has been considerable interest in scanning the hippocampus in epilepsy (see chapter 1.3.3.1). In this chapter we will describe three studies which we have conducted to study the hippocampus. The first study is on image contrast and the repeatability of hippocampal volumteric measurements. The second is a serial study of hippocampal measurements and the third study investigates hippocampal layers.

4.2 Image contrast and hippocampal volumetric measurements

4.2.1 Introduction

The hippocampus is a mesio-temporal structure[1] which is frequently affected in epilepsy. The hippocampal volume can be measured on magnetic resonance (MR) images. This technique is of particular interest in epilepsy because the underlying structural cause of epilepsy is frequently hippocampal sclerosis which is associated with hippocampal volume loss.[2] However, the quality of measurements depends on the ability of the investigator to identify the anatomical boundaries of the hippocampus. The detectability of the boundaries depends on resolution and grey matter-white matter contrast. A number of different sequences with different contrast have been used to measure the hippocampus including spin echo,[3,4,5] fast spin echo,[6] inversion recovery[7] and gradient echo [8,9,10] sequences (tab.4.1). However, the influence of the image contrast on hippocampal volumetric measurements has not been systematically evaluated. One way of evaluating hippocampal measurements is to assess the repeatability of measurements. The objective of this study was to compare the repeatability of hippocampal volumetric

measurements on two sequences with identical resolution but different contrast. We compared spoiled GRASS gradient echo (SPGR) 3D acquisition with inversion recovery prepared spoiled GRASS (IRSPGR) 3D acquisition.

Table 4.1 MR sequences used for hippocampal volumetric measurements

author	sequence	scanner
Cook et al 1992	GRE 3D TR/TE/FA 35/5/35	GE 1.5T
Jack et al 1990	SE TR/TE 500/20	GE 1.5T
Bronen et al 1991	SE TR/TE 400/20	GE 1.5T
Watson et al 1992	GRE 3D TR/TE/FA 75/16/60	PH 1.5T
Bartzokis et al 1993	IR TI/TR/TE 600/2500/30	PI 1.5T
Tien et al 1993	FSE TR/TEef/ET 4000/100/16	GE 1.5T
Yoneda et al 1994	SE TR/TE 600/15	SI 1.0T
Van Paesschen et al 1996	mpGRE 3D TI/TR/TI/FA 200/10/4/12	SI 1.5T

SE=spin echo, GRE=gradient echo acquisition, mpGRE=magnetization prepared gradient echo, IR=inversion recovery, FSE=fast spin echo, GE=General Electrics, SI=Siemens, PH=Philips, PI=Picker MR scanner. FA=flip angle, TR=relaxation time (ms), TE=echo time (ms).

4.2.2. Methods

We used a 1.5 T Signa scanner (GE Medical Systems,Milwaukee, WI, USA) in our study. Thirteen subjects without a history of neurological disease were included. In each subject two consecutive scans were performed without changing the position of the head. The subjects were first scanned with a spoiled GRASS volume acquisition (SPGR) (TR/TE/NEX 35/5/1, flip angle 35^0). The second scan was performed with an inversion recovery prepared spoiled GRASS volume acquisition (IRSPGR) (TR/TE/TI/NEX 17.4/4.2/450/1, flip angle 20^0). Spoiling was accomplished by semirandomly changing the phase of the RF carrier from view to view (RF spoiling) in SPGR and IRSPGR sequence. For the SPGR sequence the slicethickness was 1.5 mm, the field of view (FOV) was 25 x 18 cm, the matrix was 256 x 128 (acquired pixel dimensions 0.9375 x 1.40625 mm, reconstructed pixel dimension 0.9375 x 0.9375 mm). For the IRSPGR sequence the slicethickness was 1.5 mm, the FOV was 24 x 18 cm, the matrix was 256 x 192, (pixel dimensions 0.9375 x 0.9375 mm). One hundred twenty four coronal images were obtained in 9:31 minutes with the SPGR sequence and in 6:56 minutes with the IRSPGR sequence.

4.2.2.1 Hippocampal measurements

All measurements were performed by one rater (U.W.) who had a detailed knowledge of the hippocampal anatomy. The method for hippocampal volumetric measurements has been described in detail elsewhere. Images were transferred to a separate workstation (Advantage Windows, GE Medical Systems, Milwaukee, WI, USA). The hippocampus was manually outlined on each slice with a mouse driven tracer thus defining 20-25 cross sectional regions of interest (ROI) of the hippocampus. The area of the ROI was calculated by pixel counting. All areas were added and the sum multiplied with the slice-thickness (1.5mm) to obtain the hippocampal volume. Each hippocampus was measured two times on SPGR and two times on IRSPGR images. Repeated measurements were performed on

different days (more than 2 days apart) and in a randomized order on SPGR and IRSPGR images to eliminate training effects. When the repeated measurements were performed the rater was blinded to the results of the first measurement.

4.2.2.2 Repeatability

To analyse our data we assessed the repeatability coefficient by calculating the standard deviation of the mean difference of repeated measurement in analogy to Bland et al.[11] Calculations were performed in the following steps: For each hippocampus the difference of the two measurements was calculated by subtracting the second measurement from the first measurement. The difference (first minus second measurement) was plotted against the mean of first and second measurement for each hippocampus to visualize the repeatability (fig.4.1). After that, we calculated the mean difference $\bar{d}_v$:

$$\overline{d_v} = \sum_{i=1}^{n} \frac{(HV1_i - HV2_i)}{n} \qquad (4.1)$$

where HV1 is the first and HV2 is second measurement and n the number of measurements. Since the difference could have positive or negative values $\bar{d}_v$ was small. In the absence of systematic measurement errors $\bar{d}_v$ is zero. The standard deviation SD_v was used as a measure of the repeatability due to the tracing technique:

$$SD_v = \sqrt{\frac{\sum_{i=1}^{n} (\overline{d_v} - d_{v_i})^2}{n}} \qquad (4.2)$$

If all the difference $d_v = 0$, then $\bar{d}_v = 0$ and $SD_v = 0$. Hence, the smaller SD_v, the smaller the variability. 95% of all differences (in this case due to the tracing technique) are within 2 SD_v.

In addition we calculated the mean of the *absolute* differences as a percentage of the mean hippocampal volume to compare our data with other groups.[12] For each hippocampus the smaller hippocampal volume was subtracted from the larger (to obtain absolute differences), the difference ($d_{(abs\%)}$) was given as a percentage of the mean hippocampal volume:

$$d_{(abs\%)}=[(HV_{larger}-HV_{smaller})/HV_{mean}]\cdot 100 \qquad (4.3)$$

Where HV_{mean} is the mean of HV_{larger} and $HV_{smaller}$. Finally, we calculated the mean absolute difference ($\bar{d}_{(abs\%)}$) of all the $d_{(abs\%)}$. The same calculations were performed for repeated IRSPGR measurements.

3.2.2.3 Contrast

Signal to noise measurements were performed in five subjects on both SPGR and IRSPGR images on corresponding slices. Signal intensity measurements were performed in a ROI including at least 36 pixels in the hippocampus ($S_{hippocampus}$) and the white matter (S_{wm}) (in the corona radiata). The standard deviation of the noise (SD_{noise}) was measured in a ROI outside the head which contained at least 100 pixels. To avoid artificially high noise values the windowing was changed to visualize artefacts outside the head from eye movements and flow and the ROI was placed in a location which was artefact free. The contrast to noise ratio (CNR) was calculated as:[13]

$$CNR=(S_{wm}-S_{hippocampus})/SD_{noise} \qquad (4.4)$$

Measurements were repeated on four consecutive slices and the mean CNR calculated. The mean CNR of SPGR and IRSPGR of each subject were compared. We used the CNR rather than the difference between signal intensities because the noise can affect the ability to distinguish anatomical structures especially on images with low signal to noise ratio and the signal intensity is lower of IRSPGR images than on SPGR images because of the inversion pulse. Our method to measure the signal to noise ratios is widely used. It may provide less accurate values than other methods[14] but was sufficient to show the relative difference between SPGR and IRSPGR.

3.2.3 Results

The mean hippocampal volume of all 26 hippocampi was 2683 mm^3 for first SPGR measurements, 2725 mm^3 for second SPGR measurements, 2750 mm^3 for first IRSPGR measurements and 2781 mm^3 for second IRSPGR measurements. Despite the similarity of these values there were considerable differences between first and second measurement in individual hippocampi. Differences of repeated measurements were larger on SPGR than on IRSPGR measurements. The repeatability coefficient was 238.60 mm^3 for SPGR and 134.49 mm^3 for IRSPGR. Fig. 4.1 shows the differences (first minus second measurement) plotted against the mean of first and second measurements for each hippocampus for measurements to visualize the repeatability. (Top: SPGR measurements. Bottom: IRSPGR measurements). The low repeatability of SPGR measurements was also reflected by the second statistical method we applied. Here the mean *absolute* difference as a percentage of the mean hippocampal volume $\bar{d}_{(abs\%)}$ was 7.4% for SPGR and 3.3% for IRSPGR hippocampal volumetric measurements.

The CNR (hippocampal grey matter and extrahippocampal white matter) were between 1.92 to 1.41 times higher on IRSPGR than on SPGR images (tab.4.2 and fig.4.2).

Table 4.2 Contrast to noise ratios of grey matter and white matter on SPGR and IRSPGR images

subjects	CNR SPGR	CNR IRSPGR	CNR IRSPGR/ CNR SPGR
subject 1	15.62	29.98	1.92
subject 2	12.81	22.64	1.77
subject 3	19.33	30.02	1.55
subject 4	13.59	25.70	1.89
subject 5	12.88	18.14	1.41
mean	14.85	25.30	1.70

CNR=contrast to noise ratio (arbitrary units)

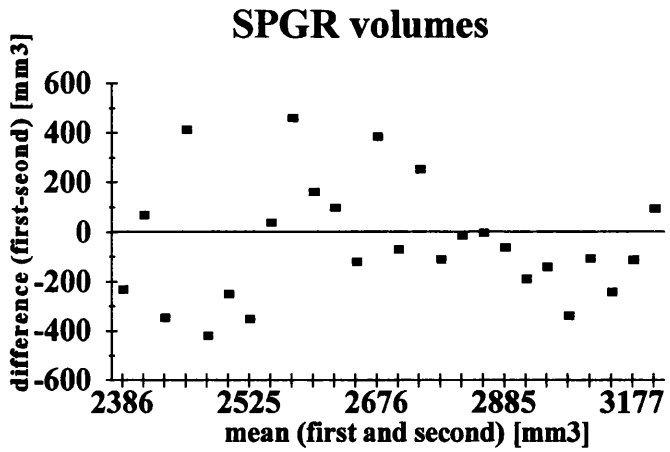

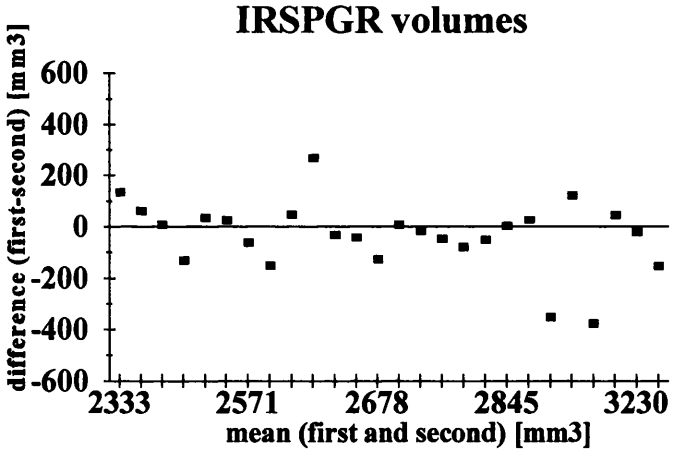

Figure 4.1 - Repeatability of hippocampal volumetric measurements. The difference (first minus second measurement) is plotted against the mean of both measurement for each hippocampus. Top: SPGR measurements. Bottom: IRSPGR measurements.

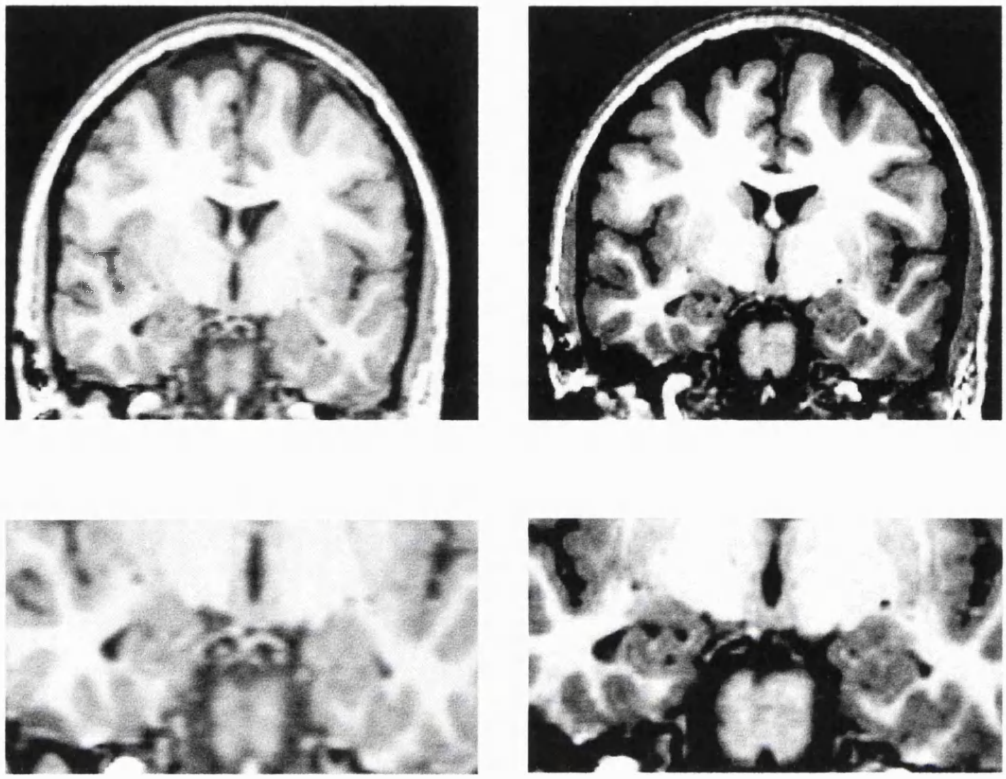

Figure 4.2 - Coronal SPGR (left) and IRSPGR (right) image taken though the hippocampal head. The inset (approximately 1.5 x magnification) shows mesio temporal structures. Note the higher grey matter-white matter contrast and the higher conspicuity of the alveus on IRSPGR.

4.2.4 Discussion

In our study higher grey matter-white matter contrast was associated with improved repeatability of hippocampal measurements. The most likely explanation for the improved repeatability of measurements was the improved detectability of hippocampal boundaries, especially in the hippocampal head. The hippocampal head is the largest part of the hippocampus,[1] precise outlining of the hippocampal head is crucial for the measurement. However, the hippocampal head is the part which is most difficult to outline.[6,7,9] Hippocampal head and amygdala are joined together.[1] The structure which allows distinction between hippocampal head and amygdala is the alveus, a thin white matter structure.[2] The alveus is usually visible on SPGR on most slices. However, there are often one or two slices in the hippocampal head where the alveus can be difficult to identify on SPGR images. On IRSPGR images the alveus is often more conspicuous on these slices (fig.4.2) which allows to outline the hippocampus more precisely.

Despite this improvement hippocampal volumetric measurements are still limited by the tracing technique. The repeatability in our study was within the range of reported repeatabilities.[3,7,8,10,12] Using our approach the standard deviation of the differences can be used to obtain information about the probability of a given measurement to be a measurement error. It can be expected that 95% of all errors due to the tracing technique are within 2 standard deviations. On IRSPGR the repeatability coefficient was 134.49 mm^3 (2 standard deviations 270 mm^3) Thus, a difference of more than 270 mm^3 (2 standard deviations) between two measurements would only have a 5 % chance to be an error due to the tracing technique. However, a difference of less than 270 mm^3 between two hippocampal volumes may not reflect a true biological difference but a measurement error due to the tracing technique. This has to be taken into consideration when the measurements of a patient are interpreted. The measurement error affects also intergroup comparisons although, depending of the sample size, differences of less than 270 mm^3 may be statistically significant.

4.2.5 Conclusion

It has been demonstrated that the measurement skills of the rater[10] and reformatting the hippocampi in a specific plane[15] affect hippocamal volumetric measurements. Our data suggest that grey matter-white matter contrast also affects hippocampal volumetric measurements and that improved contrast improves the repeatability.

4.3 The development of hippocampal atrophy; a serial MRI study in a patient who developed epilepsy after generalized status epilepticus

4.3.1 Introduction

Status epilepticus can be associated with hippocampal atrophy.[16] However, it is unknown whether chronic epilepsy is associated with progressive hippocampal atrophy. With serial magnetic resonance imaging (MRI) this question can be addressed. By performing serial MRI scans changes of the brain over time can be monitored. Co-registration and substraction of serial MRI scans may help to detect subtle changes.[17,18,19,20] The hippocampal volume can be quantified on MRI images. We performed a serial MRI study over almost five years to investigate hippocampal volume changes in a patient who developed chronic epilepsy after tonic clonic status epilepticus.

4.3.2.Case report

A thirty-year-old woman developed generalized tonic clonic status epilepticus in the beginning of September 1991 following low grade fever for one week. Two days after the onset of status, CSF examination showed a pleocytosis of 72 cells/mm^3, normal blood sugar and oligoclonal bands against HSV1. The serum HSV1 antibody titre rose from 20 to 160 between the third and fourth weeks of

the illness. Chest X-ray, brain CT and intravenous DSA and muscle biopsy were normal. The status persisted for two weeks despite intensive therapy including intravenous thiopentone.Two months after the onset of the illness she was well enough to commence neurorehabilitation but she had developed memory deficits and habitual epilepsy with frequent secondary generalized seizures that remained refractory to medical treatment. The seizure semiology was compatible with a frontal onset with secondary spread to the temporal lobes. There was evidence of continuing neuropsychological decline with the Warrington recognition test for words and faces dropping from 46/50 and 46/50 respectively to 37/50 and 35/50 over the four years following the illness. The IQ was unchanged (79).

4.3.3. Methods

4.3.3.1 Scanning parameters

Scans during status were performed with a 0.5 T Picker machine (Picker International, Cleveland, Ohio). Spin echo (SE) T1-weighted (TR/TE/NEX 380/20/4) and T2-weighted and proton density-weighted (TR/TE1/TE2/NEX 2080/60/120/2) images were obtained. Scans after status were performed with 1.5 T GE Signa machines (GE Medical Systems, Milwaukee, WI). 3D spoiled GRASS (SPGR) (TR/TE/NEX/FA 35/5/1/35^0) and SE T2-weighted images were obtained (TR/TE1/TE2/NEX 2000/32/80/1 on the 11.11.1991, 2800/32/90/1 on the 20.8.1992 and 2000/30/120/1 on the 26.7.1996).
All images were reviewed by a senior neuroradiologist (JS) who has a special interest in the neuroradiological findings in epilepsy.

4.3.3.2 Quantification of hippocampal volumes

The hippocampal volume were measured on 3D spoiled GRASS (SPGR) images using a previously described method on a Sun Sparc 20 workstation using the Xdispim Image Analysis software.[21] All hippocampi were measured by one of us

(UW) in 1996 and corrected for intracranial volume. The normal range for hippocampal volumes had been previously established using 20 healthy volunteers. Our repeatability studies for hippocampal volumetric measurements on SPGR images showed that a difference of more than 480 mm^3 has only a 5% chance to be a measurement error (chapter 4.2). Our repeatability was similar to previously published repeatabilities.

4.3.3.3 Co-registration and substraction of serial MRI scans

3D SPGR images were co-registered using a locally-developed program (MRreg). The processing steps included brain extraction from the skull, global signal-intensity matching of first and second brain, co-registration of first and second brain to match scans and subtraction of first from the second scan to visualize subtle signal changes in the brain. Using our convention (first image subtracted from second) low signal intensity on the subtraction image implies signal loss (suggesting volume loss) between the first and second scan. Unchanged brain structures appear grey (image noise) on subtraction images. The skull was not co-registered and therefore remains visible on subtracted images due to movement of the brain relative to the skull. The program adjusted for variations in pixel dimensions.

4.3.4 Results

4.3.4.1 Visual inspection of MRI images

During status epilepticus on the 13.9.1991 and on the 30.9.1991 both mesio-temporal regions returned a high signal on T2-weighted images, the hippocampi were enlarged, consistent with focal oedema (fig. 4.3). There was no contrast enhancement. Two month after the onset of the status, on the 11.11.1991 both hippocampi were reduced in size and returned a high signal on T2-weighted images indicating hippocampal sclerosis.

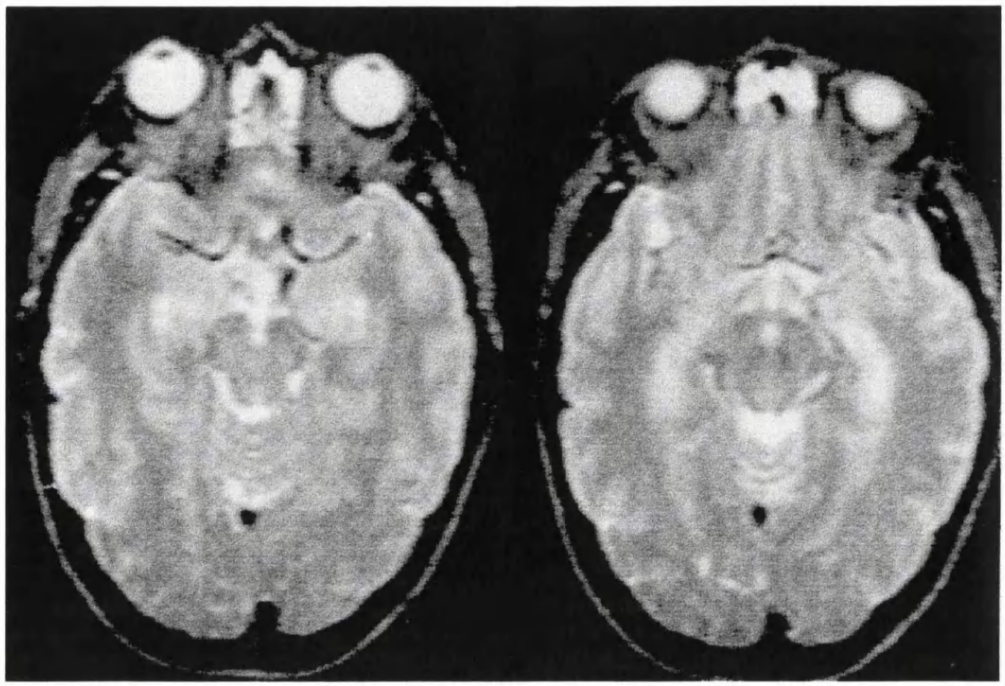

Figure 4.3 - Axial T2-weighted images obtained during status in 1991. An abnormally high signal is visible in the mesio-temporal region bilaterally.

4.3.4.2Quantification of hippocampal volumes

Hippocampal volumes on the 11.11.1991, two month after the onset of the status, showed bilateral hippocampal atrophy. There was further atrophy between first and second and second and third scan (table 4.3).

Table 4.3 Hippocampal volumetric measurements

	rightHV	leftHV
1991	2243	2273
1992	1890	1863
1996	1409	1406

Hippocampal volumes (HV) corrected for intracranial volume in mm^3

(Normal range (mean ± 2SD) 2700 mm^3 -3700 mm^3)

4.3.4.3. Co-registration and substraction of serial MRI scans

Registration of first SPGR (11.11.91) and second SPGR (20.8.92) and of second SPGR (20.8.92) and third SPGR (26.7.96) was performed. On substraction images signal change consistent with progressive hippocampal atrophy was detected (fig.4.4). Mild ventricular enlargement and cortical atrophy was also noted.

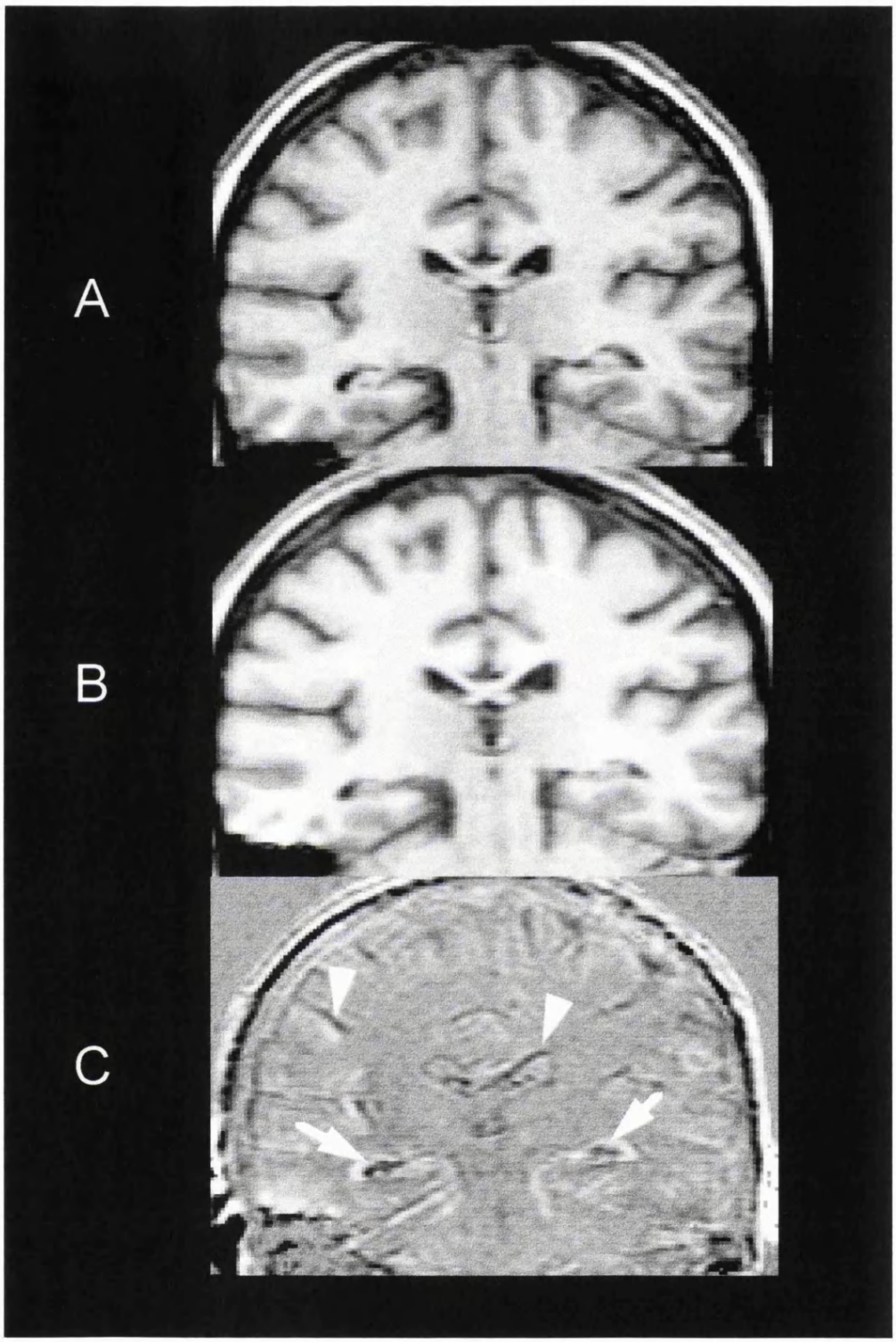

Figure 4.4 - Registration of brain scans using Mrreg. A Coronal T1-weighted image obtained 1 year after status epilepsy. B Coronal T1-weighted image obtained 4 years later and registered to A. C Difference image (B minus A). Dark pixels indicate loss of signal intensity (atrophy) between A and B. Atrophy is visible in both hippocampi (arrow). There is also mild ventricular expansion (arrowhead). Only minor neo-cortical and ventricular changes are visible (arrowhead). Windowing in C: level=0, width=100.

4.3.5 Discussion

We demonstrated progressive hippocampal volume loss in our patient who developed chronic epilepsy after status epilepticus, probably due to herpes encephalitis. It is known that the hippocampus can be damaged in such patients. However, our finding suggests that hippocampal atrophy is a process which can continue long after the end of the acute disease. We first detected hippocampal atrophy two months after the onset of status which is in keeping with other reports.[22] In addition we detected, to our knowledge for the first time, progressive hippocampal atrophy during the follow-up period of 58 months. Progressive atrophy was demonstrated by two independent MRI methods. Manual volumetric hippocampal measurements revealed a volume loss of more than 700 mm^3 between November 1991 (one month after the status) and July 1996 (58 months after the status). This difference has only a 5% chance of being due to a measurement error. The largest change was detected in the first year after the acute disease. Co-registration which is an automatic qualitative technique to detect change on serial MR images confirmed the presence of progressive atrophy. The atrophy may have been a consequence of the inflamatory process. Alternatively it may have been caused by the excessive epileptic activity. Progressive hippocampal damage has been reported in an animal model of chronic epilepsy after status epilepticus.[23] In humans epilepsy can be associated with mental deterioration which suggests progressive brain damage.[24] However, MRI detectable hippocampal sclerosis and clinically obvious mental deterioration do not invariably occur after prolonged ictal activity.[25,26] A possible explanation for this discrepancy is that these patients have had less severe epilepsy than our patient.

4.3.6 Conclusion

Obviously on the basis of a single case report it is impossible to distinguish whether the ongoing atrophy in our patient was a result of repeated seizure activity or was more directly related to the previous encephalitic illness. Still, our

observation suggests that progressive hippocampal atrophy may occur in adults long after the end of an acute episode of status, at least in a subgroup of patients who suffer from chronic epilepsy.

4.4 Hippocampal Layers on High Resolution Magnetic Resonance Images: Real or Imaginary?

4.4.1 Introduction

The hippocampus is a complex mesiotemporal structure consisting of several layers (fig. 4.5). The hippocampus plays an important role in the aetiology of dementia, psychosis and epilepsy. In temporal lobe epilepsy hippocampal sclerosis is the most common underlying structural abnormality.[27] Histologically hippocampal sclerosis is characterized by cell loss and gliosis affecting mainly the pyramidal cell layer in sector CA1 (or Sommers' sector).[28] With magnetic resonance (MR) imaging the hippocampus can be visualized and severe hippocampal sclerosis can be reliably detected.[29] Visualizing the internal structure of the hippocampus on MR images to detect more subtle abnormalities has been of interest in the context of epilepsy research. On coronal MR images lines within the hippocampus can sometimes be identified. These lines have been interpreted as the internal structure of the hippocampus. Disruption of the internal structure has been interpreted to be a sign of hippocampal sclerosis.[30,31] To evaluate whether these lines do reflect layers within the hippocampus, we have performed MR experiments at different field strength using a hippocampal anatomical specimen and on a volunteer.

4.4.2. Methods

An anatomical specimen of the hippocampus was obtained by dissecting the hippocampus from a formalin fixed brain. The volunteer was a 34 years old man without a history of neurological disease.

4.4.2.1 MR experiments

4.4.2.1.1 Scanning a hippocampal specimen at 7 Tesla

The formalin fixed hippocampal specimen was scanned in air using a small bore 7 Tesla scanner and a RF saddle coil with 3.5 cm diameter. We used a spin echo T2 weighted sequence. Images were acquired in the coronal plane perpendicular to the longitudinal axis. Scanning parameters were: relaxation time (TR)/ echo time (TE)/ number of excitations (NEX) = 3030 ms/60 ms/100. The field of view (FOV) was 16.5 mm, the matrix 256 x 256, resulting in an in plane resolution of 0.064 x 0.064 mm. The slice thickness was 1 mm (voxel size 0.004 mm^3)

4.4.2.1.2 Scanning a hippocampal specimen at 1.5 Tesla

The hippocampal specimen was placed in the centre of a small container (about 3 x 3 inch) filled with formalin using a plastic hook. Scanning was performed with a 1.5 Tesla scanner which is used for human studies (GE Signa Horizon) using two 3 inch phased array surface coils positioned at the top and bottom of the container. Images were acquired in the coronal plane perpendicular to the longitudinal axis. We used a spin echo T2 weighted sequence (TR/TE/NEX =6000 ms/80 ms/32, FOV = 80 mm, matrix 512 x 512, with an in plane resolution 0.156 x 0.156 mm, slice thickness 1 mm (voxel size 0.024 mm^3).

4.4.2.1.3 Scanning the hippocampus in vivo at 1.5 Tesla

The volunteer was scanned twice using the same 1.5 Tesla scanner as in 2. using a circularly polarized headcoil and a T2 weighted fast spin echo (FSE) sequence. Scanning parameters were TR/effectiveTE/ETL/NEX = 4500 ms/75 ms/16/2, FOV 240 mm, matrix 512 x 512, giving in plane resolution 0.47 x 0.47 mm and a slice thickness of 2 mm (voxel size 0.442 mm^3). Images were obtained

perpendicular to the longitudinal axis of the hippocampus. Phase and frequency encoding direction were swapped in the second scan to modify edge related artefacts.

4.4.2.1.4 Comparison with the histological appearance

The hippocampal specimen was cut in the same coronal orientation as in the scan, stained using a myelin stain and examined and compared with MR images.

4.4.3 Results

On the stained anatomical specimen 5 hippocampal layers (alveus, pyramidal cell layer, stratum radiatum, stratum lacunosum and stratum moleculare) and 3 layers in the dentate gyrus (stratum moleculare, granule cell layer and polymorphic layer) could be identified (fig. 4.9).

7 Tesla images: 5 hippocampal layers were visible in the hippocampal head. These were identified as 1. alveus (returning a low signal), 2. stratum oriens and pyramidal cell layer (returning a high signal), 3. stratum radiatum returning a low signal, 4. the stratum lacunosum returning a high signal and 5. stratum moleculare returning a low signal. In the hippocampal body, 4 hippocampal layers could be identified, stratum lacunosum and stratum moleculare could not be clearly separated. In the dentate gyrus the granule cell layer was clearly discernible as a thin dark line. The stratum moleculare of the dentate gyrus was visible as a layer returning a high signal (fig.4.6).

On 1.5 Tesla images of the specimen the hippocampal layers were again identified, but in the dentate gyrus the granule cell layer was not detectable (fig.4.7).

On 1.5 Tesla images of the hippocampus in vivo, 3 layers could be distinguished in the hippocampus on some slices in the hippocampal body. These were identified as mainly representing 1. alveus, 2. pyramidal cell layer and 3. stratum radiatum. A dark line consisting of a few pixels possibly represented the dentate gyrus (fig.4.8). Swapping phase and frequency encode direction did not change the

appearance of the layers, providing reasonable evidence that they were not primarily edge related artefacts.

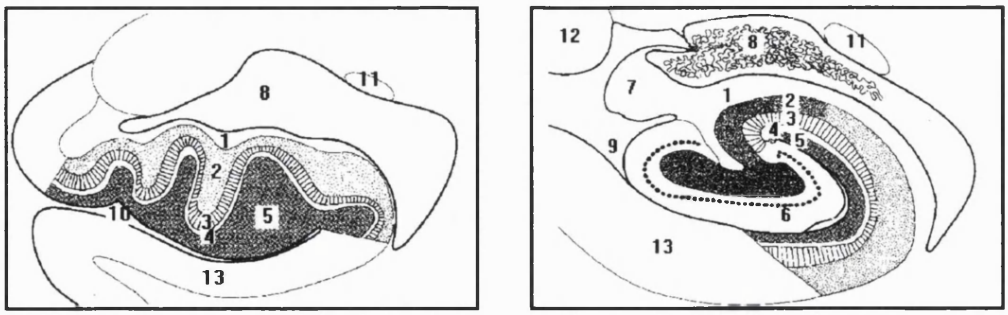

Figure 4.5 - Left: schematic drawing of the hippocampal head. Right: Schematic drawing of the hippocampal body. The numbers indicate: 1=alveus, 2=pyramidal cell layer, 3=stratum radiatum, 4=stratum lacunosum, 5=stratum moleculare, 6=dentate gyrus with granule cell layer, 7=fimbria, 8=temporal horn, 9=hippocampal fissure, 10=uncal fissure, 11=caudate nucleus, 12=lateral geniculate body, 13=subiculum.

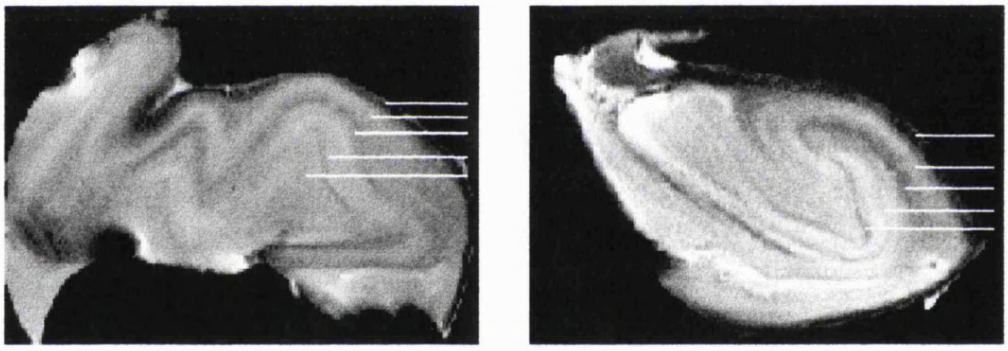

Figure 4.6 - High resolution imaging of the hippocampal specimen at 7T. (Voxel size 0.064 x 0.064 x 1 = 0.004 mm^3.) Left: coronal sections of the hippocampal head. The background is dark and there are susceptibility artefacts at the edges because the specimen was scanned in air. The lines indicate hippocampal layers (from top to bottom) alveus, pyramidal cell layer, stratum radiatum, stratum lacunosum, stratum moleculare).

Right: coronal sections of the hippocampal body. There is an artefact caused by air a small bubble. The lines indicate (from top to bottom) alveus, pyramidal cell layer, stratum radiatum, stratum lacunosum and stratum moleculare, granule cell layer of the dentate gyrus).

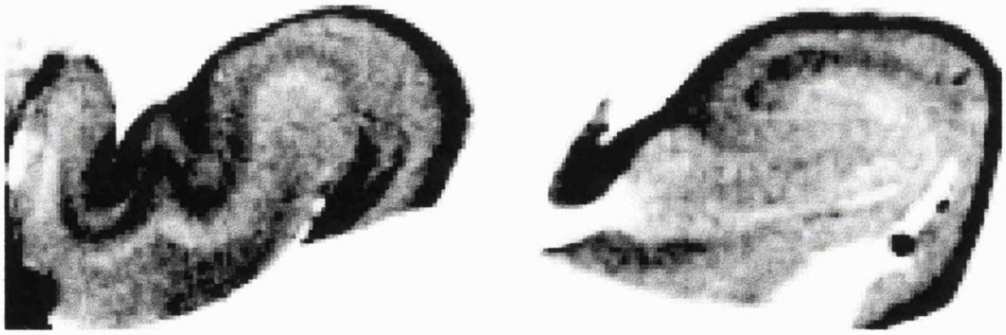

Figure 4.7 High resolution imaging of the hippocampal specimen at 1.5 T. (Voxel size 0.156 x 0.156 x 1 mm = 0.024 mm^3.) Left: coronal section of the hippocampal head. The background is white because the specimen was scanned in formalin. Hippocampal layers can be identified.
Right: coronal section of the hippocampal body. The background is white because the specimen was scanned in formalin. Hippocampal layers can be identified but the granule cell layer of the dentate gyrus is difficult to identify.

Figure 4.8 - High resolution imaging of the hippocampus in vivo at 1.5 T. (Voxel size 0.47 x 0.47 x 2 mm = 0.442 mm^3.) Coronal FSE image showing the hippocampal body. The horizontal lines indicate layers presumably mainly representing alveus, pyramidal cell layer and stratum radiatum. The oblique line indicates a few pixels which are possibly representing the dentate gyrus.

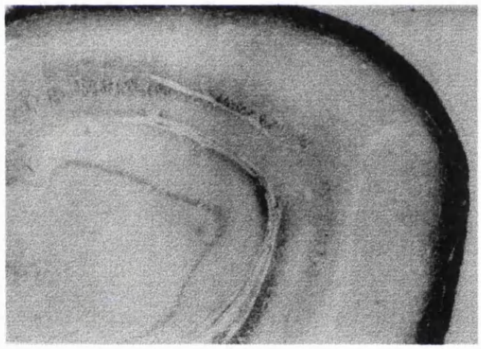

Figure 4.9 - Histological picture of the anatomical specimen showing the layers in the hippocampal body.

4.4.4 Discussion

We attempted to compare the appearance of hippocampal structures on MR images at different resolutions in vivo and in vitro. We chose a T2-weighted contrast in all experiments because the contrast of T2 weighted images in vivo and formalin fixed brains is similar.[32] Our results show that MR imaging can provide sufficient contrast to distinguish the microscopic layers in the hippocampus and illustrate the influence of spatial resolution on the detectability of layers. On high resolution images of the specimen, layers were detectable on both 1.5 Tesla and 7 Tesla images. Only the stratum oriens could not be distinguished from the pyramidal cell layer on MR images. On 7 Tesla images even the granule cell layer of the dentate was clearly visible. Interestingly, the contrast in hippocampus and dentate gyrus was different from the T2 weighted contrast seen in other regions of the brain. On T2 weighted images, both in vivo and in formalin fixed brains, structures which contain cell bodies of neurons like grey matter are usually brighter than myelin containing white matter. Our results show that neuron containing layers like the granule cell layer of the dentate and myelin containing white matter structures like the alveus both returned a low signal on MR images. This finding is in agreement with a study performed by Miller et al[33] but difficult to explain because the factors determining T1 and T2 relaxation are complex and there is no comprehensive theory to predict T1 and T2 relaxation in tissue.[34] Experimental studies using other MR techniques including diffusion imaging can elucidate the physical behaviour of protons in different hippocampal compartments[35] and may improve our understanding of contrast generation.

On 1.5 Tesla images of the hippocampus in vivo only 3 layers could be distinguished in the hippocampus on some slices in the hippocampal body. The main limiting factor for the detection of hippocampal layers on clinical MR images in vivo appeared to be the resolution. MR images are generated by measuring an induced signal from a small volume sample. The signal is converted to a grey level and displayed on a two-dimensional matrix in which each two-dimensional element or "pixel" has an intensity representing the amount of signal from the original

sample at that location. The resolution of an MR image is determined by the voxel size. Whilst preserving the principal contrast in all experiments in our study, shown by the fact that the alveus was dark in all three experiments, changing the resolution affected the detectability of layers. Our experiment allowed an estimate for the minimum resolution required for the detection of structures within the dentate gyrus and in the hippocampus. With a voxel size of 0.064 x 0.064 x 1 = 0.004 mm^3 even the granule cell layer of the dentate was detectable. For a voxel size of 0.156 x 0.156 x 1 mm = 0.024 mm^3 (or 6 times larger) which could be achieved on a clinical scanner the hippocampal layers were detectable but the granule cell layer was not. Using a voxel size of 0.47 x 0.47 x 2 mm = 0.442 mm^3 (or about 18 times larger than in the second experiment) only occasionally three main layers could be detected. (On slices where the hippocampus was cut perpendicular to its longitudinal axis). A potential limitation of our study was that we used a FSE sequence with a shorter TR for the investigation of the hippocampus in vivo. FSE imaging is faster than standard spin echo imaging, an important advantage of FSE imaging for vivo studies, but point spread function can produce blurring which may affect the detectability of small structures.[36] However, it is unlikely that this explains the fact that we could only detect 3 principal layers on FSE images in our in vivo study. Other in vivo MR studies of the hippocampus using different MR techniques (inversion recovery imaging or spoiled gradient echo imaging with T1-weighted contrast) have also failed to demonstrate internal hippocampal structures consistently. Our experimental results are in keeping with theoretical considerations. Hippocampal layers are between 0.1 mm (granule cell layer) and 0.5 mm (stratum radiatum) thick. Voxels must be at least as small as the object to permit its resolution, and usually much smaller to achieve an image without partial volume effects.[37] It is therefore not surprising that on images with a resolution of 0.469 x 0.469 x 2 mm only thick layers aligned with the pixel are visible.

In human in vivo studies the long acquisition time required for signal averaging currently precludes the use of the resolution required to visualize all hippocampal layers. High field scanners and special receiver coil design are alternative ways of

improving the signal to noise ratio without averaging and therefore allow the use of higher resolution without time penalty. In vivo studies of the human hippocampus using high field scanners[38] or 3 inch phased arrayed surface coils positioned over the temporal lobes[39] have already demonstrated an improved detectability of the thicker hippocampal layers, including alveus and pyramidal cell layer. The continuous technical development in MR imaging makes it likely that the higher resolution studies in vivo will be feasible in the future.

4.4.5 Conclusion

In summary our results show that the lines occasionally detected on clinical MR images are likely to represent real hippocampal layers. However, for a reliable detection of all hippocampal layers, an increase of the resolution currently used in clinical imaging by a factor of approximately 20 would be necessary.

4.5 References

1. Duvernoy HM. *The human hippocampus.* J.F. Bergmann Verlag, München 1988.

2. Cook MJ, Fish DR, Shorvon SD, Straughan K, Stevens JM. Hippocampal volumetric and morphometric studies in frontal and temporal lobe epilepsy. *Brain* 1992;**115**:1001-1015.

3. Jack CR, Bentley MD, Twomey CK, Zinsmeister AR. MR imaging-based volume measurements of the hippocampal formation and anterior temporal lobe: validation studies. *Radiology* 1990;**176**:205-209.

4. Yoneda Y, Mori E, Yamashita H, Yamadori. A MRI volumetry of medial temporal lobe structures in amnesia following herpes simplex encephalitis. *Eur Neurol* 1994;**34**:243-252.

5. Bronen RA, Cheung G, Charles JT, Kim JH, Spencer DD, Spencer SS, Sze G, McCarthy G. Imaging findings in hippocampal sclerosis: correlation with pathology. *Am J Neuroradiol* 1991;**12**:933-940.

6. Tien RD, Felsberg G, Campi de Castro C, Osumi AK, Lewis DV, Friedman AH, Crain B, Radtke RA. Complex partial seizures and mesial temporal sclerosis: evaluation with fast spin-echo MR imaging. *Radiology* 1993;**189**:835-842.

7. Bartzokis G, Mintz J, Marx P, Osborn D, Gutkind D, Chiang F, Phelan CK, Marder SR. Reliability of in vivo volume measures of hippocampus and other brain structures using MRI. *Magn Reson Imaging* 1993;**11**:993-1006.

8. Watson C, Andermann F, Gloor P, Jones-Gotman M, Peters T, Evans A, Olivier A, Melanson D, Leroux G. Anatomic basis of amygdaloid and hippocampal volume measurement by magnetic resonance imaging. *Neurology* 1992;**42**:1743-1750.

9. Van Paesschen W, Sisodiya S, Connelly A, Duncan JS, Free SL, Raymond AA, Grünewald RA, Revesz T, Shorvon SD, Fish DR, Stevens JM, Johnson CL, Scaravilli F, Harkness WFJ, Jackson GD. Quantitative hippocampal MRI and intractable temporal lobe epilepsy. *Neurology* 1995;**45**:2233-2240.

10. Free SL, Bergin PS, Fish DR, Cook MJ, Shorvon SD, Stevens JM. Methods for normalization of hippocampal volumes measured with MR. *Am J Neuroradiol* 1995;**16**:637-643.

11. Bland JM, Altman DG.Statistical methods for assessing agreement between two methods of clinical measurement. *Lancet* 1986;**1**(8476):307-310.

12. Cendes F, Andermann F, Gloor P, Evans A, Jones-Gotman M, Watson C, Melanson D, Oliver, A, Peters T, Lopes Cendes I, Leroux G. MRI volumetric measurement of amygdala and hippocampus in temporal lobe epilepsy. *Neurology* 1993;**43**:719-725.

13. Field SA, Wehrli FW. Image quality: effective choice of imaging parameters. *Signa applications guide* 1992;**1**:7-15.

14. Sijbers J, Scheunders P, Bonnet N, Van Dyck D, Raman E. Quantification and improvement of the signal-to-noise ratio in a magnetic resonance image acquisition procedure. *Magn Reson Imaging* 1996;**14**:1157-1163.

15. Hasboun D, Chantôme M, Zouaoui A, Sahel M, Deladoeuille M, Sourour N, Duyme M, Baulac M, Marsault C, Dormont D. MR Determination of hippocampal volume: comparison of three methods. *Am J Neuroradiol* 1996;**17**:1091-1098.

16. Shorvon SD. *Status epilepticus: its clinical features and treatment in children and adults.* Cambridge University Press, Cambridge 1994:152-158.

17. Lemieux L, Wieshmann UC, Fish DR. Application of co-registration of serial magnetic resonance imaging in subjects with epilepsy. *Epilepsia* 1996;**37**(suppl 5):201.

18. Hajnal JV, Saeed N, Oatridge A, Williams EJ, Young IR, Bydder GM. Detection of subtle brain changes using subvoxel registration and subtraction of serial MR images. *J Comput Assist Tomogr* 1995;**19**:677-691.

19. Hajnal JV, Saeed N, Oatridge A, Williams EJ, Young IR, Bydder GM. Detection of subtle brain changes using subvoxel registration and subtraction of serial MR images. *J Comput Assist Tomogr* 1995;**19**:677-691.

20. Fox NC, Freeborough PA, Rossor MN. Visualisation and quantification of rates of atrophy in Alzheimer's disease. *Lancet* 1996;**348**:94-97.

21. Plummer DL. DispImage, a display and analysis tool for medical images. *Rev Neuroradiol* 1992;**5**:489-495.

22. Tien RD, Felsberg GJ. The hippocampus in status epilepticus: demonstration of signal intensity and morphologic changes with sequential fast spin-echo MR imaging. *Radiology* 1995;**194**:249-256.

23. Lynch LA, Lythgoe DJ, Escott KJ, Haga K, Smart SC, Beech JS, Millan M, Kinchesh P, Meldrum BS, Williams SCR. Temporal evolution of CNS damage in a rat model of chronic epilepsy. *Proceedings of the International Society for Magnetic Resonance in Medicine. Fourth scientific meeting.* ISMRM, Berkeley, CA 1996:521.

24. Scholz W. Die Krampfschäden des Gehirns. In: Guhle HW, Spatz H, Vogel O, eds. *Monographien aus dem Gesamtgebiete der Neurologie und Psychiatrie.* Springer Verlag, Berlin, Heidelberg, Göttingen: 1951;**75**:1-116.

25. Chan S, Chin SSM, Kartha K, Nordli DR, Goodman RR, Pedley TA, Hilal SK. Reversible signal abnormalities in the hippocampus and neocortex after prolonged seizures. *Am J Neuroradiol* 1996;**17**:1725-1731.

26. Cockerell OC, Walker MC, Sander JW, Shorvon SD. Complex partial status epilepticus: a recurrent problem. *J Neurol Neurosurg Psychiatry* 1994;**57**:835-837.

27. Wolf HK, Campos MG, Zentner J, Hufnagel A, Schramm J, Elger CE, Wiestler OD. Surgical pathology of temporal lobe epilepsy. Experience with 216 cases. *Journal of Neuropathology and Experimental Neurology* 1993;**52**:499-506.

28. Meencke HJ, Veith G. Hippocampal sclerosis in epilepsy. In: Lüders H. ed. *Epilepsy surgery.* Raven Press, New York 1991:705-715.

29. Jackson GD, Berkovic SF, Tress BM, Kalnins RM, Fabinyi GC, Bladin PF. Hippocampal sclerosis can be reliably detected by magnetic resonance imaging. *Neurology* 1990;**40**,1869-1875.

30. Jackson GD, Berkovic SF, Duncan JS, Connelly A. Optimizing the diagnosis of hippocampal sclerosis using MR imaging. *Am J Neuroradiol* 1993;**14**:753-762.

31. Bronen R. MR of mesial temporal sclerosis: how much is enough? *Am J Neuroradiol 1998;***19**:15-18.

32. Tovi M, Ericsson A. Measurements of T1 and T2 over time in formalin-fixed human whole-brain specimens. *Acta Radiologica* 1992;**33**:400-404.

33. Miller MJ, Mark LP, Ho KC, Haughton VM. R appearance of the internal architecture of ammon's horn. *Am J Neuroradiol* 1996;**17**:23-26.

34. Elster AD. *Questions and answers in magnetic resonance imaging.* Mosby Year Book, St Louis: 1994.

35. Buckley DL, Bui JD, Phillips MI, Zelles T, Inglis BA, Plant HD, Blackband SJ. The effect of ouabain on water diffusion in the rat hippocampal slice measured by high resolution NMR imaging. *Magn Reson Med* 1999;**41**:137-142.

36. Constable RT, Gore JC.The loss of small objects in variable TE imaging: implications for FSE, RARE, and EPI. *Magn Reson Med* 1992;**28**:9-24.

37. Morris PG.*Nuclear magnetic resonance imaging in medicine and biology.* Oxford University Press, Oxford 1986.

38. Pan JW, Vaughan JT, Kuzniecky RI, Pohost GM, Hetherington HP. High resolution neuroimaging at 4.1T. *Magnetic Resonance Imaging* 1995;**13**:915-921.

39. Wieshmann UC, Free SL, Lemieux L, Bartlett PA, Stevens JM, Shorvon SD. Comparative assessment of phased array surface coils and standard headcoil in high resolution imaging of mesio-temporal structures. *Proceedings of the International Society for Magnetic Resonance in Medicine, fourth scientific meeting.* ISMRM, Berkeley, CA 1996:250.

Chapter 5

Conclusions

5.1 Introduction

MR imaging is a rapidly developing technique and the full potential has yet to be explored. This thesis focused only on three specialised techniques, FLAIR imaging, diffusion imaging and imaging of the hippocampus, and limited itself to one clinical application, epilepsy. However, it was impossible to cover all potential applications of these techniques in epilepsy. The techniques presented here were at a different levels of development. For example, there continues to be a rapid technical development in diffusion imaging. On the other hand, the technical development of FLAIR imaging has reached a plateau. As a result I was able to conduct sufficiently large studies to assess the clinical value of FLAIR imaging in epilepsy. In diffusion imaging (and in our study on serial imaging of the hippocampus) our initial results presented in this thesis allow the formulation new hypotheses which are currently tested in larger studies at the University College London.

5.2 Summary of thesis and future work

5.2.1 Epilepsy and magnetic resonance imaging

In Chapter one I described the clinical definition of epilepsy, associated structural abnormalities and the concepts of seizure generation. I referred to the imaging techniques and the role of neuroimaging techniques in epilepsy. In the second part I described the physical principles of MR imaging. I explained the methods of contrast modification in MR imaging which makes MR imaging a uniquely flexible imaging tool. I gave a brief introduction to standard MR imaging techniques. I explained the relationship between pixel size and signal to noise ratio and potential

sources of artefacts in MR imaging. I showed that there is an increasing interest in MR imaging in epilepsy research. At the same time, I mentioned the potential methodological shortcomings of MR research. I also pointed out that MR imaging is a developing technique and that the applications of MR imaging in research are constantly changing. I gave an overview on the current use of MR imaging in epilepsy. I described the appearance of structural abnormalities on MR images associated with epilepsy. I showed that the current role of MR imaging is the detection of structural abnormalities and the formulation of an epileptic syndrome. Moreover, I underlined the important implication of the detection of structural abnormalities on patient management and prognosis. In this context I emphasised that patients with hippocampal sclerosis detected in vivo by MR imaging have a far better chance to be seizure free after temporal lobectomy than patients without structural abnormality on MR imaging.

I then described the development of new MR techniques in recent years and their implication for epilepsy research and introduced the new MR techniques which are discussed in this thesis.

5.2.2 FLAIR imaging in epilepsy

In the second chapter I described our experience with FLAIR imaging in epilepsy. I explained that FLAIR is an imaging technique with was originally designed to increase lesion conspicuity by suppressing the bright signal from CSF on a T2-weighed scan. I showed that FLAIR imaging is one of the major new developments in MR imaging. FLAIR had reached the technical level necessary for the application in clinical imaging. However, as pointed out in the introduction to MR imaging in epilepsy, there is a risk that new MR techniques are introduced into clinical practice without rigorous assessments. Our study on fast FLAIR imaging in epilepsy aimed at assessing the clinical value of fast FLAIR in a large study. Our main finding was that fast FLAIR imaging increased the lesion conspicuity for a number of lesions relevant in epilepsy including hippocampal sclerosis, tumours and brain damage. In patients with normal standard MR images

additional lesions were only occasionally detected on fast FLAIR images. The main disadvantage of fast FLAIR imaging in epilepsy was that dysgenic lesions were less conspicuous on fast FLAIR images than on T1-weighted images and could be overlooked. Therefore, the fast FLAIR sequence is an useful addition to existing sequences but cannot replace them. The relatively short acquisition time of fast FLAIR makes it feasible to add the sequence to the MR investigation of patients. Other authors have confirmed our results since our publication in 1996.[1,2,3] FLAIR has been used in epilepsy research.[4] At the University College London fast FLAIR is routinely used as part of the protocol for the investigation of patients with epilepsy since 1995. Fast 2D FLAIR sequences are now available from all major MR vendors. Fast FLAIR, if not routinely added, should be used in patients with focal epilepsy, who are MR negative on standard imaging, since additional abnormalities can be detected in a minority of MR negative patients (5% in our study).

The FLAIR technique is a still developing technique. Our group developed a 3D version of FLAIR which allowed the acquisition of thin contiguous slices. In the next part of the FLAIR chapter I described our initial experience with this new technique in epilepsy. I scanned 10 patients with typical structural abnormalities and compared the 3D fast FLAIR with the 2D fast FLAIR version and a T1-weighted 3D gradient echo sequence. Our main finding was that reconstruction of 3D fast FLAIR datasets in any plane allowed the identification of structural abnormalities in all three dimensions. On T1-weighted reconstructed images tumour boundaries were difficult to detect because of the lower contrast between tumour and normal brain. 3D fast FLAIR may have a potential application in patients who are considered to be surgical candidates to accurately assess tumour boundaries. However, there were sources of artefacts due to the "slab" acquisition technique such as Venetian blind artefacts. In addition, lesion conspicuity was lower on 3D fast FLAIR than on 2D fast FLAIR, presumably due to the shorter TR in 3D fast FLAIR. This again shows the need of careful assessment of modified sequences. The main role of 3D fast FLAIR is likely to be in specialised applications. For example, in presurgical patients when the resection

of the lesion is planned 3D FLAIR may help visualising the extend of the lesion. Another potential application is the use of 3D FLAIR in serial MR studies since this technique allows the co-registration of serial scans.

The use on FLAIR is not limited to T2-weighted imaging. CSF suppression reduces the partial volume effect due to CSF contamination. This is of particular importance in images with low resolution such as single shot EPI where many pixels are bound to contain CSF from neighbouring CSF filled spaces. CSF suppression can be applied in diffusion imaging.[5] I used CSF suppression techniques for our diffusion tensor imaging studies in 3.6 and 3.8.

There are a number of applications of suppression techniques which still awaiting evaluation in epilepsy. These include CSF suppression techniques to reduce the partial volume effect on T2-quantitation in the hippocampus[6] and suppression of grey matter and suppression of white matter for segmentation.

5.2.4 Diffusion imaging in epilepsy

In Chapter three I described the principles of diffusion imaging and our applications of diffusion imaging. In the introduction I gave the basic formulas describing diffusion, explained how diffusion affects the MR signal and how MR imaging can be used to describe diffusion in a three dimensional space. I described how diffusion is changed in biological systems. I provided a list of experimental models of neurological disorders where diffusion changes have been described and discuss the main implications for diffusion imaging in humans.

In the following I presented our diffusion studies (3.3 to 3.10). The studies reflected the technical development of diffusion imaging. In our first study on hippocampal diffusion and diffusion in hemiparesis (studies 3.3 and 3.4) I used a navigated conventional spin echo diffusion weighted sequence. This technique has the advantage of providing images without distortions and relatively high resolution. However, the long acquisition time implied that only a few slices could be acquired and that diffusion measurements could only be performed in a limited number of directions. For example the acquisition time for figure 3.7 was 30

minutes. Because of the long acquisition times tensor imaging was not feasible with a conventional spin echo diffusion weighted sequence. Therefore, rotationally variant measures of anisotropy and the magnitude of diffusion had to be used. For the same reason the use of the sequence was also limited to co-operative patients and control subjects. Despite these limitations I was able to perform a limited study on patients with temporal lobe epilepsy (study 3.3) and demonstrated that the diffusion is increased in hippocampal sclerosis. This had important implications for the microstructural organisation in hippocampal sclerosis. An increased ADC suggests an expansion of the extracellular space and argues against a reduced water content in the sclerotic hippocampus. More "unbound" water would explain the increased T2 relaxation time in hippocampal sclerosis. This pattern of change may not be specific for epilepsy. Hanyu et al demonstrated hippocampal abnormalities in patients with Alzheimer's disease.[7] In the following study, I demonstrated that diffusion imaging is superior to standard imaging in demonstrating tracts and demonstrated in 2 patients with hemiparesis a reduced anisotropy in the pyramidal tract (study 3.4).

In the following studies I applied a single shot spin echo planar imaging sequence for diffusion imaging. The reduced acquisition time of this sequence made the acquisition of the full tensor feasible for clinical studies (diffusion tensor imaging, DTI) and enables us to acquire rotationally invariant measurements of diffusion. I continued our work on tracts with DTI and studied 10 patients with hemiparesis and supratentorial lesion. I measured the anisotropy in regions of interest using the fractional anisotropy index in the corona radiata in the lesion and in the cerebral peduncle (study 3.5). Anisotropy was reduced in all patients in the supratentorial lesion. In some the anisotropy was also reduced in the tract remote to the lesion which was compatible with wallerian degeneration.

In the next studies (study 3.6) I extended the work on tracts to an application more relevant to epilepsy. I studied 3 patients who underwent temporal lobectomies, one of which developed homonymous hemianopia. Compared to the previous study I introduced important modifications. I used a DTI version with CSF suppression to reduce partial volume effects from CSF and covered the

whole head with contiguous slices. I doubled our control group and used a statistically comparison of spatially normalised images of patients and control subjects. This method provided a rater-independent way of identifying potentially abnormal brain areas and is therefore less biased than a region of interest approach. However, spatial normalisation has potential problems which need to be addressed. The ability to identify structural abnormalities using this approach depends on the quality of the spatial normalisation. In regions with relatively little inter-individual anatomical variability like central white matter structures the normal variation will be narrow and the method sensitive to subtle changes. Our own data have shown that the coefficient of variation in central white matter structures can be as small as 5% on fractional anisotropy maps. However, in regions with high inter-individual variability like the temporal grey matter, spatial normalisation may be imperfect and the resulting normal range wider. Hence the sensitivity of the technique for subtle changes will be smaller. Another problem is that gross abnormalities such as ventricular enlargement and lobectomies cannot be corrected for by spatial normalisation. For example anisotropy will be significantly reduced in the CSF filled cavity after temporal lobectomy. Although this result is statistically correct it is not necessarily meaningful since it does not imply a reduction of anisotropy in the remaining brain. This problem becomes complicated if warping techniques are used for spatial normalisation because this can result in distortions of the remaining brain and "significantly" reduced pixels appear distant to the original lesion. To avoid misinterpretation of our statistical results in both study 3.6 (and study 3.8, where I used the same method) I limited our spatial normalisation to rotation, translation and linear scaling and did not use warping techniques. In addition, I used a method suggested by Prof A. Evans (personal communication): regions with statistically abnormal pixels were carefully checked on the raw data for potential artefacts and gross structural abnormalities. And measurements were performed in regions of interest on the raw data. A region was only accepted as being abnormal if all data consistently showed abnormal diffusion in brain tissue.

Our findings in study 3.6 provided an interesting insight in the consequences of

epilepsy surgery on tracts. I demonstrated that the patient with hemianopia had a markedly reduced anisotropy in the optic radiation involving Meyer's loop. This reduction was remote to the resection and compatible with wallerian degeneration. In this initial study I used highly selected patients and had a clear clinical hypothesis with regard to the expected abnormality. Our results show that DTI in association with spatial normalisation gives the opportunity to study tracts quantitatively in vivo. There are various applications in epilepsy research. The method can be used to study the consequences of epilepsy surgery but also to study structurally abnormal tracts in patients with epilepsy without surgery to gather information on dysfunctional tracts.

In study 3.7 I was investigating the microstructural abnormalities using DTI. In this study I used standard MR imaging as a goldstandard for structural abnormalities. The location of the structural was defined by standard imaging and therefore a region of interest approach straightforward. I was looking at 3 broad categories of lesion types, brain damage, tumours and dysgenesis. I compared our measurements in patients with the measurements in the white matter of controls. I found that anisotropy was lower than in normal white matter in all types of lesions whereas mean diffusivity was sometimes only mildly increased or within normal limits. Our data suggest a loss of the microstructural organisation which appears to be the common denominator in structural abnormalities. Our study has also important implications of the type of structural abnormalities. Whereas most chronic lesions have an increased mean diffusivity and a reduced anisotropy indicating a widened extracellular space and a reduced directional organisation, there are some lesion where the extracellular space appears to be normal (implying densely packed cells) but the tissue is not directionally organised. Possible reasons include the age when the lesion was acquired, nature of the lesion and the repair mechanisms all which have to be addressed in future studies. This is another example where diffusion imaging provides information which cannot be obtained with standard imaging.

In study 3.8 I was extending the study of microstructural abnormalities. Like in study 3.6. I was using spatial normalisation and a statistical approach to identify

abnormal regions. I studied a patient who had suffered a blunt head trauma. This patient had abnormalities on standard MR imaging including damage in the right temporal pole and juxacortical white matter lesion. However, DTI showed a more widespread damage. In particular there was a significant reduction of anisotropy in the right optic radiation which could explain the quadrant anopia. In addition there was reduced anisotropy in central white matter structures including the corpus callosum which are known to be affected by diffuse axonal injury. Abnormalities were bilateral, affecting all lobes. Again, there were regions where anisotropy was reduced but mean diffusivity was normal indicating a loss of directional organisation with preserved density of cell. A possible explanation is axonal loss and replacement with glia cell. On maps of fractional anisotropy were less significantly abnormal pixels than on maps of mean diffusivity. This may be due to the fact that there is a different noise propagation in fractional anisotropy and mean diffusivity resulting in a higher variability on fractional anisotropy maps and hence fewer significantly reduced pixels. Nevertheless, DTI showed abnormalities in regions where standard imaging was normal. The DTI finding were consistent with clinical findings and the known pathological changes. This opens the opportunity for more extensive studies of patients with neurological deficits and/or epilepsy but no abnormality on standard imaging.

In study 3.9 and 3.10 I was investigating transient changes in patients with excessive epileptic discharges. Studies in experimental status have shown a decrease in ADC during status and a smaller, short-lived decrease after mild electroshocks. The implementation of diffusion EPI made to possible to reduced the scanning time which makes the technique theoretically applicable in humans. However, experiments like this are still extremely difficult to perform. Only a small group of patients is suitable for this type of scanning. Many patients decline to be studied during seizures or postictally because of the additional distress. Excessive movements, in particular head movements and confusion makes patients unsuitable for scanning. Limiting logistic problems include transport, availability of the scanner and monitoring of vital functions.

Because of these difficulties our studies are extremely limited and the results are

preliminary. In study 3.9 I studied a patient during and after focal status epilepticus and demonstrated transient diffusion changes. As expected form animal experiments diffusion was decreased in the affected cortex. Surprisingly, the ADC was increased in the subcortical white matter. It is impossible to make a generalised statement about focal status epilepticus based on this single observation. It is possible that the underlying cause of the status, which remained unknown in our patient, rather than the epileptic discharges explain the diffusion changes. However, there have been several reports of diffusion changes during partial status epilepticus[8,9] and immediately after seizures[10] which confirmed a reduction of diffusion in the cortex as observed in our patient. An increased diffusion in the subcortical white matter was not reported in any of these patients. Taken together these data suggest that the cortical ADC decreases during human status epilepticus as it decreases in experimental status regardless the aetiology of the status. The most likely explanation is a flux of water from the extracellular to the intracellular space following the Na+ influx resulting in shrinkage of the extracellular space and neuronal swelling. Under physiological conditions the equilibrium is quickly restored by the Na+/K+ ATPase. This mechanism may fail if the electric discharges are prolonged or sustained.

It is unclear whether detectable changes occur after single seizures. Animal experiments have shown a short-lived change after mild electrical stimulation. The cause of the observed changes is not entirely clear. Stimulation of isolated nerve tissue has not resulted in diffusion changes and it has been hypothesised that the observed changes may be due to blood flow changes.[11]

After single seizures in humans I did not observe clear-cut diffusion changes with the single shot EPI diffusion sequence. I used the same sequence as in 4.9 postictally and interictally. In one patient who experienced a seizure in the scanner and was immediately scanned afterwards I observed a small decrease in ADC postictally compared to interictally. This patient has a lesion which was the potential cause of the seizures and the slice for diffusion imaging was placed at the margin of the lesion.[12] I failed to demonstrate any diffusion abnormalities in two patients who I scanned within ten minutes after a simple partial seizure. Both

patients had fully recovered at the time of the scan and no abnormality on standard MR imaging (unpublished data). However, our approach to perform EPI diffusion imaging postictally and interictally had several limitations. The delay between seizure and scan was likely to be too long (the electroshock models suggested that changes only persist for a few minutes). Our scans did not cover the whole head and I may have missed the epileptic focus, I was unable to use averaging techniques and there was no EEG correlation.

To improve these shortcomings I modified our approach in study 3.10. I scanned a patient with frequent focal spikes, performed EEG recordings while the patient was in the scanner and acquired EPI diffusion weighted images immediately after single interictal spikes (event related EEG triggered diffusion imaging). EEG-triggered "DW-fMRI" localised the same lobe as BOLD fMRI.

However, there was not a complete agreement. A spike is an electrographic event which involves the rhythmic discharge of thousands of neurons and involves also subcortical loops. The question whether single seizure or even interictal spikes produce a shift of water which is sufficient to generate detectable diffusion changes is at this state unanswered. However, our preliminary data suggest that this may be the case.

In summary, I presented 8 diffusion studies in epilepsy. I demonstrated increased diffusion in hippocampal sclerosis compatible with widening of the extracellular space. I showed that diffusion imaging provides superior contrast for myelinated tracts and demonstrated reduced anisotropy in hemiparesis and in homonymous hemianopia. I found anisotropy to be reduced in lesions of different aetiology suggesting a lost of directional organisation and demonstrated widespread abnormalities in regions which were normal on standard imaging.

I demonstrated a reduced cortical ADC during status epilepticus which has since been confirmed by other investigators and collected evidence of the possibility to detect diffusion changes after single seizure which remains however, at this stage hypothetical. The spike triggered approach has two main shortcomings (which apply for both fMRI with BOLD contrast and diffusion imaging). Interictal spikes may reflect activation of the irritative zone which may not identical with the

zone. Secondly, epileptic discharges in mesio temporal, orbito frontal, parasagittal, or occipital regions may not be recorded with surface EEG. Hence, epileptic discharges in these regions may not be used as triggers for the MR sequence. Consequently significant changes may not be detected. In the future, the design of an unbiased technique to detect significant change without relying on EEG would be desirable.

It has to be kept in mind that out of necessity the diffusion studies were small and that only cautious predictions with regard to the clinical applications can be made. However, three main applications for diffusion imaging appear to be likely. i.)The investigation of tracts and connectivity, ii.) the investigation of microstructure and iii.) the investigation of transient diffusion changes. Diffusion imaging is superior to any other imaging modality in the investigation of tracts.[13] Methods to visualise tract continue to be developed.[14,15,16,17] This is one of the most promising applications of diffusion imaging and has far reaching implications for neurological applications. The goal of future studies could be the creation of an atlas of human tracts and the comparison of tracts in patients with the normal brain. These studies could be conducted over the next 3 years and would require patients with different clinical conditions covering motor neuron diseases, extrapyramidal diseases, multiple sclerosis, stroke and devolepmental disorders. In epilepsy possible investigations of include studies of the optic radiation in patients with visual field defects, of the pyramidal tract and mirror movements and of Papez limbic circuit in patients with temporal lobe epilepsy.

Possible investigations of microstructure include studies of dysgenetic brains[18] (who may have a different connectivity resulting in abnormal anisotropy, see study 3.7), of the hippocampus (including studies of the anisotropy with improved high resolution DTI) and of patients with clear neurological findings but normal standard imaging. Diffusion imaging is likely to gain an important role together with spectroscopy and fMRI in multi parameter imaging to describe microstructure.[19] Finally, diffusion imaging may gain a role in the investigation of transient diffusion changes despite the current difficulties involved with such studies. Studies addressing these issues at currently underway at the University

College London.

5.2.3 More MR imaging of the hippocampus

In chapter four I presented three studies which I performed to investigate the hippocampus. The first study was a repeatability study on hippocampal volumetric measurements. I estimated the volume loss necessary to be detected by this technique and demonstrated that increasing the contrast improved the repeatability of volumetric measurements. This study was of importance for the interpretation of the following study. I presented a patient who had serial scans after a encephalitis complicated by a generalized status epilepticus. In this patient I detected progressive hippocampal atrophy in the 58 month after the status. Our finding suggested an ongoing cell loss after the end of the acute disease. If this finding can be confirmed, new therapeutic concepts aiming at the salvation of cells could be developed. Serial MR imaging is a developing field and various other clinical applications are in epilepsy are possible.[20] In the third study I correlated the MR appearance of the hippocampus with the histological appearance. Histopathological correlation plays an important role in the understanding of MR imaging. I showed that MR imaging can provide contrast for layers in the hippocampus. However, a substantial increase of the resolution currently used in standard MR imaging is necessary to detect layers reliably. Further high resolution studies using improved receiver coils for high resolution imaging are currently planned.

5.3 Conclusion

In this thesis, FLAIR imaging, diffusion imaging and imaging of the hippocampus were used in patients with epilepsy. For all three methods specific applications for the investigation of the brain in epilepsy have been identified. FLAIR increases the conspicuity of lesion relevant in epilepsy including hippocampal sclerosis. Serial imaging allows for the first time the visualisation of temporal changes and high

resolution imaging has the prospect of demonstrating hippocampal layers in vivo. Diffusion imaging has been shown to be superior to standard imaging techniques to visualise tracts which has far-reaching implications for neurological applications. Diffusion imaging also provides an exciting window to study cerebral microstructure in vivo.

In particular the following questions can be addressed in further studies with diffusion imaging in epilepsy:

1. How is the epileptogenic region connected with other parts of the brain?

Diffusion tensor imaging studies will allow to investigate the anisotropy of water diffusion as a marker for directionality/connectivity of fibres in the white matter of patients with partial epilepsy. This will be of particular interest in patients with mesio temporal lobe epilepsy where the connections of the epileptogenic temporal lobe may be abnormal. Diffusion tensor imaging will allow us to study the mayor limbic connections such as the Papez circuit.

2. How widespread are the abnormalities of connectivity in patients with epilepsy?

Studies using diffusion tensor imaging will also be able to demonstrate widespread abnormalities in regions which appear to be normal on standard MR imaging. Diffusion tensor imaging will provide further information about the microstructural organisation of dysgenetic tissue. It is possible that diffusion tensor imaging will show abnormalities in patients with epilepsy who are MR negative, in particular, when groups of patients are statistically compared with a normal control groups.

3. Is the diffusion abnormality associated with the epileptogenic zone or the functional deficit zone? Studies correlating neurological examination and neuropsychological testing with diffusion imaging will enable us to correlate diffusion abnormalities with the functional deficit zone.

Studies correlating diffusion imaging with functional investigations such as EEG studies including ictal depth electrode investigations and studies comparing

diffusion imaging with the outcome after surgical resection will allow us to correlate diffusion abnormalities with the epileptogenic zone.

4. Does connectivity change over time in patients who develop chronic epilepsy? Diffusion tensor imaging is a unique tool to study the connectivity of the brain in vivo. This will allow us for the first time to perform serial imaging studies of connectivity in patients who develop epilepsy. Serial diffusion tensor imaging would be in particular interesting in children who develop epilepsy. Studying abnormal connections may allows us to understand seizure spread. This may eventually enable us to modify surgical approaches targeting specific pathways. MR imaging is a constantly progressing technique. It is hoped that this thesis will help to formulate hypotheses for new MR experiments to study the relationship of dysfunction and structural abnormalities.

5.4 References

1. Jack CR, Rydberg CH, Krecke KN, Trenerry MR, Parisi JE, Rydberg JN, Cascino GD, Riederer SJ. Mesial temporal sclerosis: diagnosis with fluid-attenuated inversion-recovery versus spin-echo MR imaging. *Radiology* 1996;**199**:367-373.

2. Taillibert S, Oppenheim C, Baulac M, Dormont D, Marsault C, Cabanis EA, Tourbah. Yield of Fluid-Attenuated Inversion Recovery in Drug-Resistant Focal Epilepsy with Noninformative Conventional Magnetic Resonance Imaging. *A Eur Neurol* 1999;**41**:64-72.

3. Meiners LC, van Gils AD, De Kort G, Van Der Graaf Y, Jansen GH, Van Veelen CW. Fast fluid-attenuated inversion recovery (FLAIR) compared with T2-weighted spin-echo in the magnetic resonance diagnosis of mesial temporal sclerosis. *Invest Radiol* 1999;**34**:134-142.

4. Fernandez G, Effenberger O, Vinz B, Steinlein O, Elger CE, Dohring W, Heinze HJ. Hippocampal malformation as a cause of familial febrile convulsions and subsequent hippocampal sclerosis. *Neurology* 1998;**50**:909-917.

5. Falconer JC, Narayana PA. Cerebrospinal fluid-suppressed high-resolution diffusion imaging of human brain. *Magn Reson Med* 1997;**37**:119-123.

6. Melhem ER, Whitehead RE, Bert RJ, Caruthers SD. MR imaging of the hippocampus: measurement of T2 with four dual-echo techniques. *Radiology* 1998;**209**:551-555.

7. Hanyu H, Sakurai H, Iwamoto T, Takasaki M, Shindo H, Abe K. Diffusion-weighted MR imaging of the hippocampus and temporal white matter in Alzheimer's disease. *J Neurol Sci* 1998;**156**:195-200.

8. Lansberg MG, O'Brien MW, Norbash AM, Moseley ME, Morrel M, Albers GW. MRI abnormalities associated with partial status epilepticus. *Neurology* 1999;**52**:1021-1027.

9. Ross J, Sorensen G, Shaefer PW, Gonzalez RG, Cole AJ. Diffusion-weighted magnetic resonance imaging abnormalities of focal seizures: a novel localizing technique. *Epilepsia* 1997;**38**(suppl 8):140.

10. Diehl B, Najm I, Foldvary N, Mohamed A, Ruggieri P, Tkach J, Morris H, Wyllie E, Geller E, Bingaman W, Luders HO. Postictal diffusion weighted imaging for the localization of focal epileptogenic areas. *Epilepsia* 1998;**39**(suppl 6):140.

11. Gulani V, Iwamoto GA, Lauterbur PC. Apparent water diffusion measurements in electrically stimulated neural tissue. *Magn Reson Med* 1999;**41**:241-246.

12. Wieshmann UC, Franconi F, Symms MR, Barker GJ, Shorvon SD. Postictal changes of the apparent diffusion coefficient detect by diffusion weighted EPI - preliminary results. *Epilepsia* 1997;**38**(suppl 3):208.

13. Rye DB. Tracking neural pathways with MRI. *TINS* 1999;**22**:373-374.

14. Mori S, Crain BJ, Chacko VP, van Zijl PC. Three-dimensional tracking of axonal projections in the brain by magnetic resonance imaging. *Ann Neurol* 1999;**45**:265-269.

15. Nakada T, Nakayama N, Fujii Y, Kwee IL. Clinical application of three-dimensional anisotropy contrast magnetic resonance axonography. Technical note. *J Neurosurg* 1999;**90**:791-795.

16. Peled S, Gudbjartsson H, Westin CF, Kikins R, Jolesz FA. Magnetic resonance imaging shows orientation and symmetry of white matter tracts. *Brain Research* 1998;**780**:27-33.

17. Wieshmann UC, Parker GJM, Symms MR, Barker GJ, Shorvon SD. In vivo MR Tractography using Diffusion Tensor Imaging and Spatial Normalisation: Rotation of Eigenvectors into Talairach Space. *Proceedings of the International Society for Magnetic Resonance in Medicine, seventh scientific meeting.* ISMRM, Berkeley, CA 1999:958.

18. Eriksson SH, Symms MR, Barker GJ, Wieshmann UC, Woermann FG, Duncan JS. Diffusion Tensor Imaging demonstrates reduced anisotropy in a patient with cerebral dysgenesis. *Proceedings of the International Society for Magnetic Resonance in Medicine, seventh scientific meeting.* ISMRM, Berkeley, CA 1999:1778.

19. Krakow K, Wieshmann UC, Woermann FG, Symms MR, McLean MA, Allen PJ, Barker GJ, Fish DR, Duncan JS. Multi modal MR imaging: functional, diffusion

tensor and chemical shift imaging in a patient with localization-related epilepsy. *Epilepsia* 1999;**40**:1459-1462.

20. Lemieux L, Wieshmann UC, Moran NF, Fish DR, Shorvon SD. The detection and significance of subtle changes in mixed-signal brain lesions by serial MRI scan matching and spatial normalisation. *Medical Image Analysis* 1998; **2**: 227-242.

6 Appendix

Publications associated with this thesis

6.1 Publications associated with FLAIR Imaging in Epilepsy

6.1.1 Articles

1. Wieshmann UC, Free SL, Everitt AD,Bartlett PA, Barker GJ, Tofts PS, Duncan JS, Shorvon SD, Stevens JM. MR imaging in epilepsy with a fast FLAIR sequence. *J Neurol Neurosurg Psychiatry* 1996:**61**:357-361.

2. Wieshmann UC, Barker GJ, Symms MR, Bartlett PA, Shorvon SD. Fast Fluid-attenuated Inversion-Recovery Imaging: First Experience with a 3D Version in Epilepsy. *Neuroradiology* 1998;**40**:483-489.

6.1.2 Abstracts

1. Wieshmann UC, Free SL, Everitt AD, Bartlett PA, Barker GJ, Duncan JS, Shorvon SD, Stevens JM. MR imaging in epilepsy with a fast FLAIR sequence. *Proceedings of the International Society of Magnetic Resonance in Medicine, fourth scientific meeting.* ISMRM, Berkeley, CA 1998:228.

2. Wieshmann UC, Free SL, Everitt AD, Bartlett PA, Barker GJ, Duncan JS, Shorvon SD, Stevens JM. MR imaging in epilepsy with a fast FLAIR sequence. *Epilepsia* 1996;**37**(supp.4):38.

6.2 Publications associated with Diffusion Imaging in Epilepsy

6.2.1 Articles

1. Wieshmann UC, Clark CA, Symms MR, Barker GJ, Birnie KD, Shorvon SD. Water diffusion in the human hippocampus in epilepsy. *Magn Reson Imaging* 1999;**17**:29-36.

2. Wieshmann UC, Clark CA, Symms MR, Barker GJ, Bartlett PA, Shorvon SD. Diffusion-weighted MRI Demonstrates Abnormal Pyramidal Tract in Hemiparesis. *J Neurol Neurosurg Psychiatry* 1999;**66**:797-798.

3. Wieshmann UC, Clark CA, Symms MR, Franconi F, Barker GJ, Shorvon SD. Anisotropy of Water Diffusion in Corona Radiata and Cerebral Peduncle in Patients with Hemiparesis. *NeuroImage* 1999;**10**:225-230.

4. Wieshmann UC, Symms MR, Clark CA, Lemieux L, Franconi F, Parker GJM, Barker GJ, Shorvon SD. Wallerian degeneration in the optic radiation after temporal lobectomy demonstrated in vivo with diffusion tensor imaging. *Epilepsia* 1999;**40**:1155-1158..

5. Wieshmann UC, Clark CA, Symms MR, Franconi F, Barker GJ, Shorvon SD. Reduced Anisotropy of Water Diffusion in Structural Cerebral Abnormalities demonstrated with Diffusion Tensor Imaging. *Magn Reson Imaging* 1999;**17**:1269-1274.

6. Wieshmann UC, Symms MR, Clark CA, Lemieux L, Parker GJM, Barker GJ, Shorvon SD. Blunt Head Trauma associated with widespread Water Diffusion Changes. *Lancet* 1999;**353**:1242-1243.

7. Wieshmann UC, Symms MR, Shorvon SD. Diffusion changes in status

epilepticus. *Lancet* 1997;**350**(No. 9076):493-494.

6.2.2 Abstracts

1. Wieshmann UC, Franconi F, Symms MR, Clark CA, Barker GJ, Shorvon SD. The variability and accuracy of the apparent diffusion coefficient in diffusion weighted EPI. *Proceedings of the International Society of Magnetic Resonance in Medicine, fifth scientific meeting.* ISMRM, Berkeley, CA 1998:1748.

2. Wieshmann UC, Lemieux L, Symms MR, Franconi F, Clark CA, Barker GJ, Shorvon SD. Oversampling rejecting averaging correction algorithm for non-gated single shot diffusion weighted EPI. *Proceedings of the International Society of Magnetic Resonance in Medicine, sixth scientific meeting.* ISMRM, Berkeley, CA 1998, Book of abstracts:1230.

3. Wieshmann UC, Clark CA, Symms MR, Bartlett PA, Shorvon SD. Anisotropic diffusion in hippocampal grey matter. *14th Annual meeting of the ESMRM.* Brussels 1997:66.

4. Wieshmann UC, Clark CA, Symms MR, Birnie KD, Shorvon SD. Increased diffusion in hippocampal sclerosis: correlation with T2-relaxation. *14th Annual meeting of the ESMRM.* Brussels 1997:66.

5. Wieshmann UC, Clark CA, Symms MR, Barker GJ, Birnie KD, Shorvon SD. Quantitation of water diffusion in hippocampal sclerosis. *Proceedings of the International Society of Magnetic Resonance in Medicine, sixth scientific meeting.* ISMRM, Berkeley, CA 1998:1244.

6. Wieshmann UC, Clark CA, Symms MR, Barker GJ, Birnie KD, Shorvon SD. Water diffusion in the hippocampus in epilepsy. *Journal of Neurology*

1998;**245**:386.

7. Wieshmann UC, Clark CA, Symms MR, Birnie KD, Shorvon SD. Abnormal cortico-spinal tract in patients with hemiparesis demonstrated by diffusion-weighted MRI. *14th Annual meeting of the ESMRM.* Brussels 1997:69.

8. Wieshmann UC, Franconi F, Symms MR, Clark CA, Barker GJ. Visualization of cingulum and dentatothalamic tract using diffusion-weighted EPI. *The British Chapter of the Society of Magnetic Resonance in Medicine, second annual meeting.* London 1996:55.

9. Wieshmann UC, Symms MS, Lemieux L, Franconi F, Clark CA, Barker GJ, Shorvon SD. MR tractography using diffusion tensor imaging and normalization to Talairach space. *J Neurology Neurosurg Psychiatry* 1999;**66**:271.

10. Wieshmann UC, Symms MR, Lemieux L, Franconi F, Barker GJ, Clark CA, Shorvon SD. MR Hodography using diffusion tensor imaging and spatial normalization to Talairach space. *15th Annual meeting of the ESMRM.* Geneva 1998.

11. Wieshmann UC, Clark CA, Symms MR, Franconi F, Barker GJ, Birnie KD, Shorvon SD. Microstructural abnormalities in the brain detected with diffusion tensor imaging. *Journal of Neurology* 1998;**245**:386.

12. Wieshmann UC, Symms MR, Franconi F, Clark CA, Barker GJ, Birnie KD, Shorvon SD. Microstructural Abnormalities in Cerebral White Matter in Epilepsy detected with Diffusion Tensor Imaging. *J Neurol Neurosurg Psychiatry* 1998;**65**:421.

13. Wieshmann UC, Symms MR, Franconi F, Clark CA, Barker GJ, Shorvon SD. Reduced diffusion anisotropy in malformations of cortical development. *Proceedings of the International Society of Magnetic Resonance in Medicine, sixth scientific meeting.* ISMRM, Berkeley, CA 1998:1245.

14. MR Symms, K Krakow, UC Wieshmann, GJ Barker, DR Fish, JS Duncan. EEG-correlated diffusion-weighted fMRI in epilepsy. *Proceedings of the International Society of Magnetic Resonance in Medicine, seventh scientific meeting.* ISMRM, Berkeley, CA 1999, Book of abstracts:506.

6.3 Publications associated with MR Imaging of the Hippocampus

6.3.1 Articles

1. Wieshmann UC, Free SL, Stevens JM, Shorvon SD. Image contrast and hippocampal volumetric measurements. *Magn Reson Imaging* 1998;**16**:13-17.

2. Wieshmann UC, Woermann FG, Lemieux L, Free SL, Bartlett PA, Smith SJM, Duncan JS, Stevens JM, Shorvon SD. The development of hippocampal atrophy; a serial MRI study in a patient who developed epilepsy after generalized status epilepticus. *Epilepsia* 1997;**38**:1238-1241.

3. Wieshmann UC, Symms MR, Mottershead JP, MacManus DG, Barker GJ, Tofts PS, Revesz T, Stevens JM, Shorvon SD. Hippocampal layers on high resolution magnetic resonance images: real or imaginary? *J Anat* 1999,**195**:131-135.

6.3.2 Abstracts

1. Wieshmann UC, Free SL, Bartlett PA, Lemieux L, McManus DG, Smith S, Duncan JS, Shorvon SD, Stevens JM. Pattern of MRI signal changes in

encephalitis complicated by status epilepticus. *Epilepsia* 1996;**37**(supp.4):114.

2. Lemieux L, Wieshmann UC, Fish DR. Application of co-registration of serial magnetic resonance imaging in subjects with epilepsy. *Epilepsia* 1996;**37**(suppl 5):201.

3. Wieshmann UC, Free SL, Lemieux L, Bartlett PA, Duncan JS, Stevens JM, Shorvon SD. High resolution MR imaging of the mesio-temporal region. *Epilepsia* 1996;**37**(supp.4):114.

4. Wieshmann UC, Free SL, Lemieux L, Bartlett PA, Stevens JM, Shorvon SD. Comparative assessment of phased array surface coils and standard headcoil in high resolution imaging of mesio-temporal structures. *Proceedings of the International Society of Magnetic Resonance in Medicine, fourth scientific meeting.* ISMRM, Berkeley, CA 1998:250.

5. Wieshmann UC, Symms MR, Mottershead J, Barker GJ, Tofts PS, Stevens JM, Shorvon SD. Neuronal layers on high resolution magnetic resonance images - real or imaginary? *Epilepsia* 1997;**38**(suppl 3):207.

6.4 Publications associated with Conclusions

6.4.1 Articles

1. Krakow K, Wieshmann UC, Woermann FG, Symms MR, McLean MA, Allen PJ, Barker GJ, Fish DR, Duncan JS. Multi modal MR imaging: functional, diffusion tensor and chemical shift imaging in a patient with localization-related epilepsy. *Epilepsia* 1999;**40**:1459-1462.

2. Lemieux L, Wieshmann UC, Moran NF, Fish DR, Shorvon SD. The detection and significance of subtle changes in mixed-signal brain lesions by serial MRI

scan matching and spatial normalisation. *Medical Image Analysis* 1998; **2**: 227-242.

3. Wieshmann UC, Symms MR, Parker GJM, Clark CA, Lemieux L, Barker GJ, Shorvon SD. Diffusion tensor imaging demonstrates deviation of fibres in normal appearing white matter adjacent to a brain tumour. *J Neurol Neurosurg Psychiatry* (accepted for publication)

6.4.2 Abstracts

1. Lemieux L, Wieshmann UC. Combined T1 & T2-weighted Contrast visualization of low grade lesions by volume scan co-registration. *Proceedings of the International Society of Magnetic Resonance in Medicine, sixth scientific meeting.* ISMRM, Berkeley, CA 1998, Book of abstracts:2094.

2. Lemieux L, Wieshmann UC, Moran NF, Fish DR, Shorvon SD. The detection and significance of subtle changes in mixed-signal brain lesions by serial MRI scan matching and spatial normalization. *Proceedings of the International Society of Magnetic Resonance in Medicine, sixth scientific meeting.* ISMRM, Berkeley, CA 1998, Book of abstracts:2160.

3. Wieshmann UC, Franconi F, Symms MR, Barker GJ, Shorvon SD. Postictal changes of the apparent diffusion coefficient detect by diffusion weighted EPI - preliminary results. *Epilepsia* 1997;**38**(suppl 3):208.

4. Wieshmann UC, Woermann FG, Symms MR, Birnie KD, Bartlett PA, Shorvon SD. Residual hippocampal cavities on high resolution magnetic resonance imaging. *Epilepsia* 1997;**38**(suppl 3):207.

5. Wieshmann UC, Free SL, Bartlett PA, Shorvon SD. The contralateral hippocampus in hippocampal sclerosis. *Epilepsia* 1997;**38**(suppl 3):207.

6. Wieshmann UC, Bartlett PA, Kendall BE, Stevens JM. The yield of MRI in clinical epilepsy referrals. *Neuroradiology* 1997;**39**:151.

7. Everitt AD, UC Wieshmann, SL Free, JM Stevens, Sanders JWAS, Shorvon SD. MRI findings in a residential population of patients with severe epilepsy. *Epilepsia* 1996;**37**(supp.4):148.

8. Woermann FG, Wieshmann UC, Bartlett PA, Barker GJ, Free SL, Duncan JS, Shorvon SD. Hippocampal sclerosis in MRI: regional changes in T2-relaxation and volume. *Epilepsia* 1996;**37**(supp.4):36.

9. UC Wieshmann, GJM Parker, MR Symms, GJ Barker, SD Shorvon. In vivo MR Tractography using Diffusion Tensor Imaging and Spatial Normalisation: Rotation of Eigenvectors into Talairach Space. *Proceedings of the International Society for Magnetic Resonance in Medicine, seventh scientific meeting.* ISMRM, Berkeley, CA 1999:958.

10. Eriksson SH, Symms MR, Barker GJ, Wieshmann UC, Woermann FG, Duncan JS. Diffusion Tensor Imaging demonstrates reduced anisotropy in a patient with cerebral dysgenesis. *Proceedings of the International Society for Magnetic Resonance in Medicine, seventh scientific meeting.* ISMRM, Berkeley, CA 1999:1778.